Evaluation of Hybrid-Composite Beam for Use in Tide Mill Bridge

Shainur Ahsan

Thesis submitted to the faculty of the Virginia
Polytechnic Institute and State University in partial fulfillment of the requirements for the degree of

Master of Science
in
Civil Engineering

Thomas E. Cousins, Co-Chair
Carin L. Roberts-Wollmann, Co-Chair
Cristopher D. Moen

September 10, 2012
Blacksburg, Virginia

Keywords: Hybrid-Composite Beam, Tide Mill Bridge, Skewed Bridge, Distribution Factors

EVALUATION OF HYBRID-COMPOSITE BEAM FOR USE IN TIDE MILL BRIDGE

Shainur Ahsan

ABSTRACT

A test program for the Hybrid-Composite Beam (HCB) was conducted prior to its use for the replacement of a skewed, simply-supported bridge (Tide Mill Bridge). The HCB is an innovative combination of conventional materials and ideas in a structural beam. The beam consists of a concrete arch tied with prestressing strand that is placed within a Fiber-Reinforced Polymer (FRP) box. Behavior in individual HCB's and a three HCB-system was examined to determine the appropriateness of the current design methodology developed by John Hillman and the simplifying assumptions made within it. Such assumptions include strain compatibility and linear-elastic behavior. Three HCB's were tested at the structures laboratory at Virginia Tech. During individual beam tests, the predicted behavior of the FRP box and prestressing strand agreed with experimental results. The tests revealed the arch was susceptible to local bending and behaved far differently from predicted. Overall, the beams were shown to behave linearly. A final test was performed to apply the design live load to the system. Slight non-linear behavior was observed in the beams. Distribution factors for the system were also investigated and compared to AASHTO and Hillman's model. AASHTO factors were conservative for exterior girders but unconservative for interior girders. Hillman's factors were often conservative but were in agreement for the shear in the exterior girder. The current design procedure appeared to predict FRP and strand behavior well, but the behavior of the arch appeared to differ greatly from the other components of the HCB.

ACKNOWLEDGMENTS

I would like to greatly thank my committee members (Dr. Thomas Cousins, Dr. Carin Roberts-Wollmann, and Dr. Cris Moen) for the opportunity to be involved with research at Virginia Tech and their guidance and support throughout the duration of the project. I deeply appreciate their input and patience during our many lengthy research meetings. Their encouragement and relentless search for answers pushed me through the long, hard hours I spent on the project. I would like to also thank the faculty of the Structural Engineering and Materials Program for granting me an opportunity to pursue a Master's degree at Virginia Tech. I cannot describe how satisfied I have felt about the skills and knowledge I have received during my time here. I feel my education has prepared me to face any trials I may face in my professional career.

I am deeply grateful of the other students who were and continue to be on the project: Sasha Bajzek, Margaret Mascaro, and Stephen Van Nosdall. Without their help, setup and testing for the project would have been infinitely more difficult. I wish Sasha and Stephen the best of luck with future research. I also express gratitude to Brett Farmer, Dennis Huffman, and Dave Mokarem for their help and input in the setup for the project. Their help is often not emphasized enough for how critical it is to the completion of experimental research and everyday functions at the lab. I also could not have accomplished the major tasks on the project such as the deck pour without the help of my dear friends in the structures program. The last two years have been much more enjoyable and much less difficult because of their great camaraderie. Whether it was working on long and tiring homework assignments, studying for upcoming tests, or setting up and partaking in the many fun SEM events; they were always willing and able to take up the challenge.

I would also like to thank VDOT (both VCTIR and the Central Bridge Division) for taking the time to drive hours to Blacksburg and visit the lab. It was a pleasure to present updates on the project and to answer all your questions. Thank you to John Hillman and Mike Zicko for promptly responding to our questions about the beam. Much appreciation to Mike for coming to Virginia Tech and getting his hands dirty to help us with attaching the FRP lids. The opportunity to work on such a unique, innovative project has been incredible considering the conservative nature of our profession. I wish everyone luck in the design and construction of Tide Mill Bridge and all future HCB projects.

Finally, I would like to thank my family: Nazma, Mahbub, and Ronia Ahsan. Without their love and support, I would have felt much more discouraged to take on the obstacles I met while working on the project. They always checked in to make sure I was doing well and showed patience despite the long periods of time away from home.

All pictures were taken by the author in 2011 and 2012.

Table of Contents

1 Introduction 1

1.1. Project Description and Overview 1

1.2. Thesis Objective and Outline 2

2 Literature Review 5

2.1. Design Methodology 6

2.2. IDEA Test Program Results 9

2.2.1. Investigation of a Hybrid-Composite Beam System 9

2.2.2. Product Application of a Hybrid-Composite Beam System 16

2.3. Testing of Knickerbocker Bridge HCB 17

2.4. AASHTO Distribution Factors 22

2.4.1. Effects of Skew on Live Load Distribution Factors 23

2.4.2. Distribution Factors for Fiber-Reinforced Polymer Bridge Structures 25

2.5. Summary 28

3 Beam Fabrication and Instrumentation 30

3.1. HCB Construction 31

3.2. Strain Gages 36

3.2.1. Strain Gages on Tension Strand 36

3.2.2. Strain Gages on FRP Box 38

3.2.3. Strain Gages on Deck Reinforcement 40

3.3. Concrete Vibrating Wire Gages 42

3.4. Potentiometers 46

3.5. Load Cells 48

3.6. Linear Variable Differential Transformers 50
3.7. Dial Gages 53
3.8. Photogrammetry 54
3.9. Data Acquisition Systems 54
4 Methodology and Testing Procedures 56
4.1. Preparation for Phase I Testing 57
4.2. Phase I Testing 59
4.3. Preparation for Phase II 61
4.4. Phase II Testing 65
4.5. Preparation for Phase III Testing 68
4.6. Phase III Testing 76
5 Results and Discussion 80
5.1. Material Testing 80
5.1.1. Concrete Cylinder Testing 80
5.1.2. Prestressing Strand Calibration 83
5.1.3. Fiber-Reinforced Polymer Properties 88
5.2. Phase I Testing 88
5.2.1. Load-Deflection Behavior 89
5.2.2. Behavior of Fiber-Reinforced Polymer 96
5.2.3. Behavior of Prestressing Strand 98
5.2.4. Strain Profiles 100
5.2.5. Summary of Phase I Results 105

5.3. Phase II Testing 105
5.3.1. Load-Deflection Behavior 106
5.3.2. Behavior of Fiber-Reinforced Polymer 112
5.3.3. Behavior of Prestressing Strand 118
5.3.4. Behavior of Concrete Arch 123
5.3.5. Strain Profiles 134
5.3.6. Summary of Phase II Results 143
5.4. Phase III Testing 143
5.4.1. Component Material Behavior 144
5.4.1.1. Behavior of Fiber-Reinforced Polymer 144
5.4.1.2. Behavior of Prestressing Strand 148
5.4.1.3. Behavior of Concrete Arch 150
5.4.1.4. Summary of Component Material Behavior 158
5.4.2. System Behavior 158
5.4.2.1. Strain Profiles 159
5.4.2.2. Load-Deflection Behavior 166
5.4.2.3. Load Distribution Factors 172
5.4.2.4. Design Service Live Load Test 187
6 Conclusions and Recommendations 201
6.1. Conclusions 201
6.2. Recommendations 203

6.3. Recommendations for Future Work 204

References 206

Appendix A – Sample Calculations 208

Appendix B – Supplementary Phase I Results 231

Appendix C – Supplementary Phase II Results 236

Appendix D – Supplementary Phase III Results and Calculations 263

List of Tables

Table 2-1 2003 IDEA Program Test Matrix (Hillman 2003, Used with permission of John R. Hillman, HC Bridge Company) © 12

Table 2-2 AEWC Test Matrix 19

Table 3-1 Overview of HCB Instrumentation 31

Table 3-2 Strand Gage Labels 38

Table 3-3 FRP Strain Gage Labels 40

Table 3-4 Vibrating Wire Gage Labels 44

Table 4-1 A4 Concrete Mix Design (VDOT 2007) 71

Table 5-1 Material Testing Results for Arch Concrete 81

Table 5-2 Material Testing Results for Diaphragm Concrete 81

Table 5-3 Material Testing Results for Deck Concrete 81

Table 5-4 Specimen Mixture of Concrete Cylinders 83

Table 5-5 Compressive Strength for Arch Concrete Cylinders 83

Table 5-6 Experimental Modulus (with values zeroed) 87

Table 5-7 Material Properties for Fiber-Reinforced Polymer 88

Table 5-8 Maximum Deflection for Phase I Testing 90

Table 5-9 Comparison to Deflections Including Shear Deformations 93

Table 5-10 Stiffness Equations 94

Table 5-11 Comparison of Measured and Calculated Stiffness at Midspan 95

Table 5-12 Comparison of Midspan Strains for Test 7 97

Table 5-13 Comparison of Quarter Point Strains for Test 7 97

Table 5-14 Maximum Prestressing Strand Strain for Phase I Testing 98

Table 5-15 Updated Test Matrix for Phase II Testing 106
Table 5-16 Maximum Midspan Deflection for Point Load Tests 107
Table 5-17 Maximum Midspan Deflection for Quarter Point Load Tests 108
Table 5-18 Average Midspan Strains for Point Load Tests 113
Table 5-19 Average Quarter Point Strains for Quarter Point Loading 114
Table 5-20 Midspan FRP Gages for Point Load Tests 117
Table 5-21 Maximum Midspan Strain in Strand for Point Load Tests 119
Table 5-22 Maximum Midspan Strain in Strand for Quarter Point Load Tests 120
Table 5-23 Maximum Midspan Strain in Arch Top for Point Load Tests 124
Table 5-24 Maximum Midspan Strain in Arch top for Quarter Point Load Tests 124
Table 5-25 Summary of Maximum Measured FRP Strain in Bottom Flange 145
Table 5-26 Summary of Maximum Phase III Strand Strains 149
Table 5-27 Summary of Maximum Arch Strains 152
Table 5-28 Comparison of Midspan Neutral Axis Location 160
Table 5-29 Summary of Maximum Measured Deflections 167
Table 5-30 Deflection-Based Moment Distribution Factors 177
Table 5-31 Strain-Based Moment Distribution Factors 177
Table 5-32 Transverse Moment Distribution Factors 179
Table 5-33 Deflection-Based Shear Distribution Factors 181
Table 5-34 Strain-Based Shear Distribution Factors 181
Table 5-35 Transverse Shear Distribution Factors 183
Table 5-36 Critical Distribution Factors from Phase III Testing 184
Table 5-37 Comparison of Experimental to Lever Rule Distribution Factors 184

Table 5-38 Comparison of Experimental to Hillman Model 186

Table 5-39 Comparison of Measured to Ultimate Stresses in Strand 190

Table 5-40 Comparison of Measured to Predicted Stresses in Strand 190

Table 5-41 Comparison of Measured to Ultimate Stresses in FRP 192

Table 5-42 Comparison of Measured to Predicted Stresses in FRP 192

Table 5-43 Comparison of Measured to Ultimate Stresses in Arch 194

Table 5-44 Comparison of Measured to Predicted Stresses in Arch 195

Table 5-45 Distribution Factors for Test ST17 198

Table 5-46 Comparison of Experimental Distribution Factors to Lever Rule Factors 199

Table 5-47 Comparison of Experimental Distribution Factors to Hillman Model Factors 199

List of Figures

Figure 1-1 Tide Mill Bridge (VDOT 2011) 2

Figure 2-1 2003 IDEA Test Setup (Hillman 2003, Used with permission of John R. Hillman, HC Bridge Company) © 11

Figure 2-2 Load vs. Deflection for Test 7S (Hillman 2003, Used with permission of John R. Hillman, HC Bridge Company) © 13

Figure 2-3 Load vs. Deflection for Test 9S (Hillman 2003, Used with permission of John R. Hillman, HC Bridge Company) © 13

Figure 2-4 Concrete and Steel Strain for Test 7S (Hillman 2003, Used with permission of John R. Hillman, HC Bridge Company) © 15

Figure 2-5 Concrete and Steel Strain for Test 9S (Hillman 2003, Used with permission of John R. Hillman, HC Bridge Company) © 15

Figure 2-6 Knickerbocker Bridge Cross Section (MDOT 2009) 18

Figure 2-7 Knickerbocker HCB Section (MDOT 2009) 18

Figure 2-8 Skewed Bridge Terminology 24

Figure 3-1 HCB Naming Convention 30

Figure 3-2 Naming Convention for HCB Gages 31

Figure 3-3 Cut View of HCB (Hillman 2003, Used with permission of John R. Hillman, HC Bridge Company) © 32

Figure 3-4 Layup of FRP and Prestressing Strand 32

Figure 3-5 Foam Layup 33

Figure 3-6 Infusion Process 34

Figure 3-7 Completed HCB 35

Figure 3-8 Section View of Tide Mill HCB (VDOT 2011) 36
Figure 3-9 Elevation View of Tension Strand Instrumentation 37
Figure 3-10 Strain Gage on Individual Wire on Tension Strand 37
Figure 3-11 Strain Gage Installation on FRP 38
Figure 3-12 Elevation View of FRP Strain Gages 39
Figure 3-13 Section View of Strain Gages at Midspan 39
Figure 3-14 Section View of Strain Gages at Quarter Point 39
Figure 3-15 Section View of Strain Gages at Support 40
Figure 3-16 Deck Strain Gage Layout 41
Figure 3-17 Deck Strain Gage Labels 41
Figure 3-18 Deck Strain Gage Naming Convention 42
Figure 3-19 Geokon 4200 Vibrating Wire Gage 42
Figure 3-20 Geokon Readout Box 43
Figure 3-21 Elevation View of Concrete Arch Instrumentation 43
Figure 3-22 Installation of VWG on Bottom of Arch 44
Figure 3-23 Installation of VWG at Top of Arch 45
Figure 3-24 Installation of VWG at Top of Arch at Midspan 46
Figure 3-25 Potentiometer Layout for Phase I & II 47
Figure 3-26 Potentiometer Attached to HCB 47
Figure 3-27 Potentiometer Layout for Phase III 47
Figure 3-28 50 Kip Load Cell used for Phase II 49
Figure 3-29 300 Kip Load Cell used for Phase III 49
Figure 3-30 Support Load Cell Locations 50

Figure 3-31 Support Load Cell Construction..... 50
Figure 3-32 LVDT Mounted on HCB 1 at Midspan..... 51
Figure 3-33 LVDT Mounted at Acute Corner..... 52
Figure 3-34 LVDT Mounted to Mobile Support..... 53
Figure 4-1 Floor Layout..... 57
Figure 4-2 Screwjack Introducing Camber into HCB..... 58
Figure 4-3 Epoxy used to Glue FRP Lid..... 58
Figure 4-4 Pin and Roller Boundary Conditions..... 59
Figure 4-5 Placement of Steel Angles for Phase I Loading..... 60
Figure 4-6 Elevation View of Shear Connectors..... 61
Figure 4-7 Reinforcement Tied to Shear Connectors..... 61
Figure 4-8 Hole Locations in Lid of FRP..... 62
Figure 4-9 Plywood Cap at End of HCB..... 63
Figure 4-10 Cross Section of HCB System at North End..... 63
Figure 4-11 Concrete Pump Used for Arch Pour..... 64
Figure 4-12 Concrete Pumped into Hole at Quarter Point..... 65
Figure 4-13 Plywood Caps Sealed at HCB End..... 65
Figure 4-14 Plaster Placed in Channel of HCB..... 66
Figure 4-15 Clicker used to Synchronize Data Systems..... 67
Figure 4-16 Phase II Loading Schemes..... 67
Figure 4-17 Plan View of Diaphragm at South End..... 69
Figure 4-18 Plan View of Diaphragm at North End..... 70
Figure 4-19 Diaphragm Reinforcement..... 70

Figure 4-20 Roughened Diaphragm Surface 71
Figure 4-21 Deck Side Walls 72
Figure 4-22 Deck Reinforcement Layout 73
Figure 4-23 Deck Cross Section 73
Figure 4-24 Screeding of Deck 74
Figure 4-25 Finishing Done by Hand and Bullfloat 74
Figure 4-26 Edge of First Concrete Truckload 75
Figure 4-27 Actuators Placed under Diaphragm 76
Figure 4-28 Loading Configuration 77
Figure 4-29 Phase III Loading Configurations 78
Figure 5-1 Strand Test Specimen 84
Figure 5-2 Strand Calibration Test Setup 85
Figure 5-3 Load vs. Wire Strain for Test 2 86
Figure 5-4 Load vs. Deflection for Test 4 (Uniform Load) 90
Figure 5-5 Point Load vs. Deflection for Test 6 91
Figure 5-6 Load vs. Tension Strand Strain for Test 4 (Uniform Load) 99
Figure 5-7 Point Load vs. Tension Strand Strain for Test 6 99
Figure 5-8 Strain Profiles for Test 7 at Midspan 101
Figure 5-9 Strain Profiles for Test 7 at Quarter Point 103
Figure 5-10 Strain Profile for Test 8 at Midspan 104
Figure 5-11 Strain Profile for Test 8 at Quarter Point 105
Figure 5-12 Load vs. Deflection Plot for Test 1 109
Figure 5-13 Load vs. Deflection for Test 2 110

Figure 5-14 Load Deflection Plot for Test 3 111
Figure 5-15 Load Deflection Plot for Test 9 111
Figure 5-16 Load Deflection Plot for Test 10 112
Figure 5-17 Load vs. Strain for Bottom Flange for Test 1 115
Figure 5-18 Load vs. Strain for Top Flange at Quarter Point for Test 8 116
Figure 5-19 Load vs. Strain for Bottom Flange for Test 9 117
Figure 5-20 Load vs. Strand Strain for Test 1 121
Figure 5-21 Load vs. Strand Strain for Test 3 122
Figure 5-22 Load vs. Strand Strain for Test 7 122
Figure 5-23 Load vs. Concrete Strain for Test 1 126
Figure 5-24 Load vs. Concrete Strain for Test 2 127
Figure 5-25 Load vs. Concrete Strain for Test 5 128
Figure 5-26 Load vs. Concrete Strain for Test 3 129
Figure 5-27 Load vs. Concrete Strain for Test 4 130
Figure 5-28 Load vs. Concrete Strain for Test 11 131
Figure 5-29 Elevation View of FRP Sheet and Ties (VDOT 2011) 132
Figure 5-30 Midspan Spring Concept 133
Figure 5-31 Midspan Strain Profile for Test 1 136
Figure 5-32 North Quarter Strain Profile for Test 1 137
Figure 5-33 Midspan Strain Profile for Test 3 138
Figure 5-34 North Quarter Strain Profile for Test 3 139
Figure 5-35 Midspan Strain Profile for Test 11 140
Figure 5-36 North Quarter Strain Profile for Test 11 141

Figure 5-37 Loading Configurations for Phase III 144
Figure 5-38 Load vs. Strain for Test ST1 for HCB 1 147
Figure 5-39 Load vs. Strain for Test ST5 for HCB 3 147
Figure 5-40 Load vs. Strand Strain for Test ST1 150
Figure 5-41 HCB 1 Arch Strains for Test ST1 155
Figure 5-42 HCB 1 Arch Strains for Test ST7 156
Figure 5-43 HCB 2 Arch Strains for Test ST9 156
Figure 5-44 HCB 2 Midspan Strain Profile for Test ST3 161
Figure 5-45 HCB 2 Quarter Point Strain Profile for Test ST3 162
Figure 5-46 HCB 2 Midspan Strain Profiles for Test ST9 163
Figure 5-47 HCB 2 Quarter Point Strain Profiles for Test ST9 164
Figure 5-48 HCB 2 Midspan Strain Profiles for Test ST15 165
Figure 5-49 HCB 2 Quarter Point Strain Profiles for Test ST15 165
Figure 5-50 Load vs. Deflection for Test ST1 169
Figure 5-51 Load vs. Deflection for Test ST3 170
Figure 5-52 Load vs. Deflection for Test ST7 171
Figure 5-53 Load vs. Deflection for Test ST9 171
Figure 5-54 Direction of Distribution Factors 173
Figure 5-55 AASHTO vs. Experimental Exterior Wheel Line Placement 174
Figure 5-56 Loading Configuration for Test ST1 175
Figure 5-57 Load vs. Deflection for HCB 2 for Design Live Load Test 189
Figure 5-58 Load vs. Strand Strain for HCB 2 for Design Live Load Test 190
Figure 5-59 Load vs. Bottom Flange Strain for HCB 2 for Design Live Load Test 191

Figure 5-60 Load vs. Strain for HCB 2 Arch for Design Live Load Test 193

Figure 5-61 HCB2 Midspan Strain Profile for ST17 197

Figure 5-62 HCB2 Quarter Point Strain Profile for ST17 198

List of Equations

Equation 1 Correction for Moment Distribution Factor for Skewed Bridge for Concrete Box Beams 24

Equation 2 Correction for Shear Distribution Factor for Obtuse Corner in Skewed Bridge for Concrete Box Beams 24

Equation 3 Distribution Factor Formula 26

Equation 4 Flexural Deformation Term for Virtual Work 90

Equation 5 Shear Deformation Term for Virtual Work 90

Equation 6 Complete Deformation for Virtual Work 90

1 Introduction

As the number of structurally deficient bridges continues to increase, replacement of dilapidated structures has become a high priority. Much emphasis has been placed on research in rapid bridge replacement and in new methods to extend the lives of newly-built bridges. The Hybrid-Composite Beam (HCB) invented by John Hillman accomplishes both quick construction and increased durability. The HCB is a new type of beam that combines concrete, steel, and glass fiber-reinforced polymer in an efficient form (Hillman 2008). A concrete arch tied at the bottom with steel strand is encased inside of a polymer box. The polymer box protects the steel and concrete from corrosion and serves as formwork for the concrete arch. The beams have a great advantage in that they are much lighter than similar sized concrete and steel beams. This reduces transportation costs and facilitates movement of the beams at the construction site. The beams have already been deployed in bridges in Illinois, New Jersey, and Maine. Because of the novelty of the HCB, many aspects of the design process continue to require refinement.

1.1. Project Description and Overview

The Virginia Department of Transportation (VDOT) will finance the first bridge in Virginia to use the HCB. Tide Mill Bridge on state route 205 located in Colonial Beach, VA is to be replaced with a HCB bridge (Figure 1-1). The current bridge spans approximately 52 ft with a semi-integral abutment and is configured in a forty five degree skew. One advantage of the light weight of the HCB is that existing abutments can be reused for this bridge replacement.

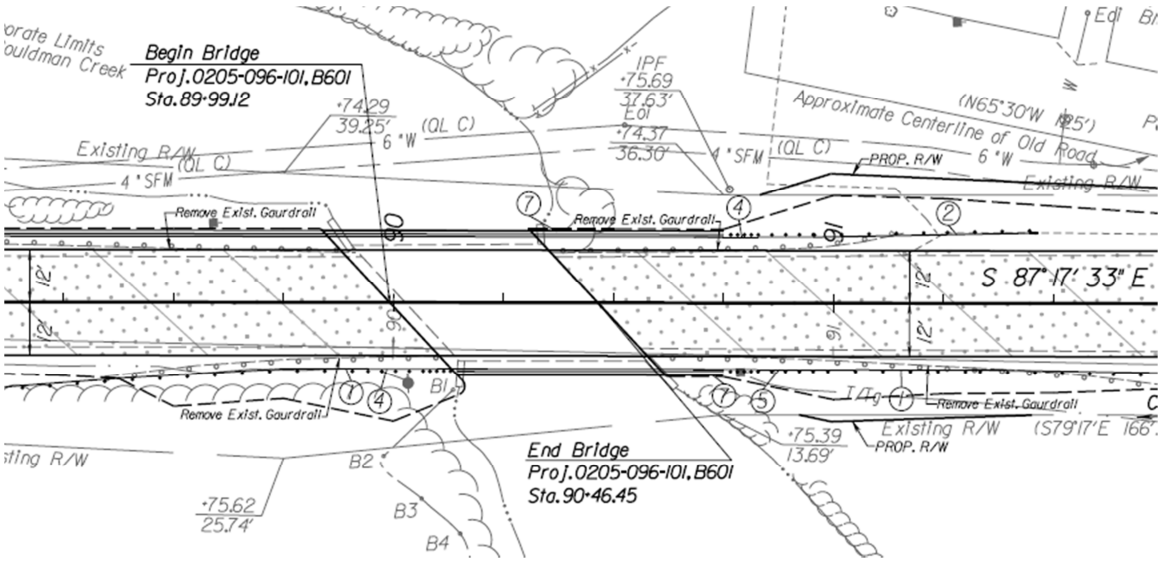

Figure 1-1 Tide Mill Bridge (VDOT 2011)

Because of the lack of experience with HCB design and the limited studies in the past, a research program was warranted to investigate the behavior of the HCB bridge system in a skew configuration and to develop design procedures for Tide Mill Bridge. Full-scale testing was performed on individual beams and a three-beam system configured in a forty five degree skew at the Structures Laboratory at Virginia Polytechnic Institute and State University. Analytical models of the HCB will be created and validated as data from the experimental testing becomes available. This thesis will focus on the experimental full-scale testing of both the individual HCB and the three girder system.

1.2. Thesis Objective and Outline

The understating of the behavior of the HCB both individually and in a three-girder forty-five degree skew system is the primary focus of this thesis. For each stage of testing, deflections and strains at critical locations were measured in order to determine the behavior of the HCB and to compare experimental results to predicted results from a simple HCB model developed by John Hillman. From the strain data, strain profiles were created for each phase of testing to evaluate the accuracy of the transformed section approach. The test data served as the basis for

evaluation of the appropriateness of the current design method. Additionally, for the final phase of testing (three-beam system) load distribution factors were examined. Ratios of deflection and bottom flange strain values at the quarter points and midspan were used to obtain experimental moment distribution factors. Load cells placed under the north supports were used to determine shear distribution factors. The experimental factors were used to compare with distribution factors used by HC Bridge, the design firm founded by John Hillman. In addition, the measured strains during all phase of testing and during the concrete placements were used to establish maximum observed strains from the experimental testing. The observed strains were then compared to the ultimate limit states provided either from the manufacturer's specifications, service limit states provided in the AASHTO LRFD specification, and the calculated strains using Hillman's model. The data from the experimental testing will become a basis for computational modeling as well as a design method for the Virginia Department of Transportation to use in the design of Tide Mill Bridge.

Additional research will be conducted to further study the behavior of the HCB and the three-HCB system. Out of plane movement of the fiber-reinforced polymer component of the HCB was examined using photogrammetry. The relative movement of the arch and the fiber-reinforced polymer box were also investigated. Computer models of the HCB and the deck and diaphragms were created simultaneously with the laboratory experiments to provide direction with loading schemes. The computer models consisted of finite element models created to better understand complex behavior of the beam itself. The deck and diaphragm were also modeled to understand the behavior of the system due to the flexible nature of the HCB's.

The study presented herein is divided into five main parts. The second chapter investigates existing literature on the Hybrid Composite Beam. Furthermore, research on live

load distribution factors in skewed bridges and bridges with low girder stiffness are considered. The third chapter describes the HCB fabrication process and instrumentation that occurred during fabrication and after delivery to Virginia Tech. The fourth chapter details the methodology used for the different phases of testing. This section describes both the steps used for testing and the preparations between each phase of testing. The fifth chapter discusses results from each phase of testing and provides some analysis of the behavior of the beam. The thesis concludes with a summary and conclusion and describes recommendations for future work. Additional information may be found in the appendices.

2 Literature Review

Current literature on the Hybrid Composite Beam is limited to a few studies that were focused on individual beam behavior. The design methodology assumed typical beam behavior to simplify the analysis. Results from previous testing showed agreement with assumptions. Evaluation of the HCB in a bridge system occurred during a portion of the Innovations Deserving of Exploratory Analysis (IDEA) program in which the prototype beams were developed, but distribution factors were not examined in depth. The HCB was deployed in highway bridge in Maine, New Jersey, and Illinois; but field testing has not yet been performed.

The HCB is to be used in a forty-five degree skewed bridge in Virginia. The AASHTO LRFD Specifications provide transverse distribution factors that reduce the analysis of a 3D structure to a 2D beam analysis. The determination of appropriate distribution factors is important in determining the critical design loads. The behavior of a skewed bridge can be much different than typical bridges due to the complex geometry. The understanding of load distribution in skewed bridge remains complex though the AASHTO code currently provides correction factors.

Because fiber composite structural members are relatively new, their adoption and use are far less common than traditional concrete and steel materials. As a result, the AASHTO code does not specifically provide guidance for bridge designs with FRP composite materials. New composite bridge designs typically require relation to one of the existing AASHTO bridge types or an alternate form of analysis which may be rigorous.

2.1. Design Methodology

Because the hybrid composite beam is constructed of three elements acting together, the analysis of the HCB is more complex than typical analysis although the same principles are applied. A design methodology was developed to check the critical limit states incorporated in a design spreadsheet. John Hillman made a number of simplifying assumptions in the design of the hybrid-composite beam. Such assumptions include linear-elastic behavior in the components of the HCB, that beam theory applies, and that plane sections before bending remain plane after bending.

Hillman proposed the use of the transformed section analysis to determine the behavior of the HCB (Hillman 2003). The concrete, steel, and fiber-reinforced polymer (FRP) components of the HCB are transformed into equivalent areas of the glass FRP composite. The components were transformed into the FRP rather than concrete because the material properties of the FRP remained linear-elastic until failure whereas material properties of concrete become non-linear at higher stresses (Hillman 2003). Section properties and stresses were calculated and checked at tenth points along the span of the beam (Hillman 2011). The arch shape of the concrete element was taken into consideration for the section properties. The centroid and moment of inertia was calculated separately for each of the components for the HCB and summed to obtain the overall properties. The foam used to shape the arch conduit is neglected in calculations. Also worth noting, the flanges of the FRP lid are ignored in calculations. Both non-composite (HCB only) and composite (including stiffness of bridge deck) section properties were generated.

The design loads for the calculations were generated using the governing code (AASHTO). The sheet also provided the option to use an internal shear and moment envelope generator or input shear and moment values from external structural analysis software (Hillman

2011). Dead load shear and moment envelopes are generated internally. The calculations use the HL-93 truck with lane loading for a simple span. The moment and shear values were multiplied by a dynamic load allowance and distribution factor. The calculation sheets use distribution factor formulas based on the lever rule according to the AASHTO LRFD Specification Section 4.6.2.2.1-1. Additional factors were calculated using guidelines for concrete box girders but did not control (Hillman 2011). The user was expected to verify the applicability of the distribution factor formulas. Envelopes for service and ultimate strength load cases were generated using the appropriate load factors for live load and dead load. The shear and moment values were calculated by shifting the location of the centroid of the HL-93 truck at tenth points along the beam span. The calculations include locations near the supports to generate maximum shear. The sheet also includes the calculations for the truck centroid location at 2.33 ft. off the beam centerline to generate maximum moment.

Section properties were calculated for the tenth points and traditional structural analysis methods were used to calculate the deflection of the HCB. Non-composite section (HCB with arch concrete but without deck concrete) deflections are used to determine the amount of camber to induce in the beams during fabrication. The camber was induced to ensure excessive deflections from dead load did not occur prior to placement of the deck. The composite section deflections are compared to limits given in AASHTO. Because of the low modulus of elasticity of the FRP material, the overall design of the HCB is typically governed by the corresponding deflection limit. The amount of prestressing strand in the bottom of the beam is increased until the applicable deflection limit is satisfied. All other limit states are checked after the design meets the deflection limits

The strength limit state is checked by using strain compatibility between components at midspan. The limiting compressive strain in the deck concrete is set to 0.003 με (Hillman 2003). The strain in the other components of the HCB was calculated using a linear strain profile through the beam depth. The resulting stresses and forces are calculated. Equilibrium of forces is taken at the tenth sections. The forces consist of the deck concrete, arch concrete, steel, and FRP capacities. The moment arm for each of the components is calculated from the centroid and used to sum the moment capacity. A phi factor of 0.81 was used based on the typical phi factor of 0.9 multiplied by the additional factor of 0.9 for FRP strength according to ACI 440 (Hillman 2011). The strength limit state is also checked for the non-composite section. Hillman's model assumes strain compatibility and linear elastic material properties in each of the components. Because the design was governed by deflection criteria, a large amount of strength reserve was present in the HCB. Because there is reserve capacity, the stresses and strains in the components are assumed to be within the linear-elastic range for the strength limit state.

The shear limit state was calculated by taking the maximum allowable shear stress of the glass fiber polymer composite used in the webs and multiplying by the web area. The allowable shear stress for the FRP was experimentally determined to be 7.5 ksi after a safety factor of 2 was applied (Hillman 2003). Hillman assumed the shear in the webs was partially reduced by a component of force carried by the arch. Because of the parabolic profile of the concrete, the arch force was decomposed into vertical and horizontal components. The vertical component was subtracted from the factored shear load (Hillman 2003). This reduced shear load was then compared to the shear capacity of the FRP webs of the box. If the capacity was greater than the shear load, then the design was satisfactory. From observations made during tests, elastic buckling of the FRP webs was not a concern due to the bond between the FRP and the internal

foam (Hillman 2003). Thus, no reduction was made to the shear capacity of the webs for buckling.

The following assumptions were examined in this study:

- Linear-elastic behavior of HCB components (FRP, strand, concrete arch)
- Presence of deformations after beam's were loaded and unloaded with service loads
- Linear strain profile throughout depth of HCB section to determined applicability of strain compatibility which is necessary for the validity of the transformed area approach.

Additionally, predicted values from Hillman's model were compared to experimental results. Such values included strain magnitudes and location of the neutral axis. An example set of calculations are presented in Appendix A.

2.2. IDEA Test Program Results

Prototypes of the Hybrid Composite Beam (HCB) were tested as part of the Innovations Deserving Exploratory Analysis (IDEA) program sponsored by the Transportation Research Board. Two studies were generated during the program. The focus of the first study was to determine the feasibility of the hybrid composite beam. Hillman's design methodology was presented in this report and was discussed in the previous section. A second study was performed to test the application of the HCB in a field setting. A 30 ft span railroad bridge constructed of eight HCB's was placed in the Transportation Technology Center at Pueblo, CO. The IDEA program provided the initial data describing the behavior of the HCB.

2.2.1. Investigation of a Hybrid-Composite Beam System

The first study conducted in 2003 focused on the discussion of feasibility as compared to concrete and steel bridge girders, constructability and selection of materials, design methodologies, and prototype performance. Hillman examined a national inventory of Class I

railroad bridges, and found that the majority of bridges that were being replaced consisted of 12-15 ft timber bridges (2003). Typically, the bridges were replaced with longer concrete bridges about twice as long as the existing bridge resulting in span lengths around 30 ft Hillman began to focus application of his beams towards short and medium span bridges. Based on these observations, cost metrics were performed on a 12 ft wide 30 ft span bridge using the HCB. The estimated cost per foot was found to be $2010/ft. (Hillman 2003). When compared to plate girder bridges, the cost was almost equal. The HCB was found to be slightly more expensive than prestressed and Cast-in-Place (CIP) bridges which ranged in cost from $1200-1300/ft (Hillman 2003). Hillman took the comparison further and examined the comparative costs as the span length varied. He found that for short span lengths (less than 30ft), the HCB was uneconomical. For longer span lengths (50 ft and greater), the cost of the HCB approached the cost of the prestressed and CIP girders (Hillman 2003). However, some of the life-cycle costs may be decreased by unique attributes of the HCB. Factors such as operation and maintenance costs must be included with the initial costs when examining lifecycle costs of the bridge.

Unique attributes of the HCB may reduce some lifecycle costs to offset the higher initial cost. Because the strand and concrete arch are within the FRP, additional protection against corrosion is provided (Hillman 2003). Also, speed of construction may also reduce costs due to the bridge being out of commission. When life cycle costs are analyzed for concrete, steel, and hybrid composite beams for 30 ft spans, the HCB is shown to be more favorable (Hillman 2003). The HCB had a lower initial cost than steel beams but was still higher than the concrete beams. However, Hillman suggests as the life cycle costs are observed over longer service lives, the HCB will become more economical.

A prototype HCB was tested at the University of Delaware as part of the study. The specimen consisted of a 20 ft beam with 24 in. height and a 12 in. width. The span length of the beam was 19 ft. The beam ends were placed on bearing pads. The HCB was constructed of quad-weave fibers infused in a vinyl ester resin; the quad-weave consisted of four layers of fiber oriented in 0/90° and +/-45° directions. The tension reinforcement was three 150 ksi post-tensioning bars. The arch material was a high strength Portland cement grout. The beam was tested without a deck. The instrumentation for the specimen included strain gages embedded in the concrete arch, strain gages adhesively bonded to the tension reinforcement, strain rosettes mounted to the FRP webs, and longitudinal adhesively bonded strain gages on the FRP (Figure 2-1). Six Linear Variable Displacement Transducers (LVDT) were placed to measure vertical deflections at various sections along the beam. Three LVDT's were used to monitor rotation at the beam end.

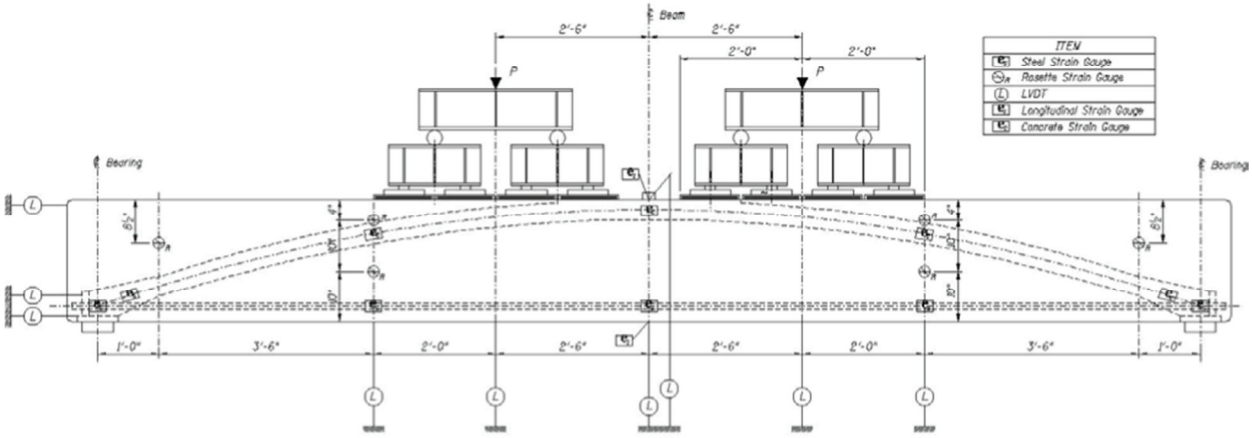

Figure 2-1 2003 IDEA Test Setup (Hillman 2003, Used with permission of John R. Hillman, HC Bridge Company) ©

Four point loads were applied using two levels of spreader beams and two actuators (Figure 2-1). The 2003 IDEA program consisted of nine tests (Table 2-1). The table shows values for force representing the load in kips at each actuator and the duration in minutes the load was applied. The first three tests consisted of symmetrical loading to represent the dead load

moment from the ballast and track weight and the maximum live load moment generated by a Cooper E-80 load including impact (Hillman 2003). Two unsymmetrical loading tests were conducted to create maximum shear representative of the dead load and live load used in the previous three tests. A cyclic test of 100,000 cycles was performed, but no data was collected. A symmetrical loading test was then conducted to determine if any fatigue damage occurred during the sixth test. For tests 3 and 7, AREMA load factors were used to increase the applied load. The last two tests were conducted to determine the ultimate strength of the specimen.

Table 2-1 2003 IDEA Program Test Matrix (Hillman 2003, Used with permission of John R. Hillman, HC Bridge Company) ©

Test	Force	Dur.	Force	Dur.	Force	Dur.	Force	Dur.	Force	Dur.	Force	Dur.	Force
1S	0	5	1.84	10	1.84	5	16.76	5	16.76	5	0	-	-
2S	0	5	21.46	0	0	-	-	-	-	-	-	-	-
3S	0	5	1.84	5	1.84	5	16.76	5	16.76	5	33.2	5	0
4U	0	5	1.84	5	1.84	5	16.76	5	16.76	1	0	-	-
5U	0	5	1.84	5	1.84	5	16.76	5	16.76	5	0	-	-
6C	100,000 cycles @ 2 Hz, symmetrical loading varying between 11.63 kips and 16.76 kips per actuator (2 each)												
7S	0	5	1.84	5	1.84	5	16.76	5	16.76	5	33.2	5	0
8S	0	14	45.81	-	-	-	-	-	-	-	-	-	-
9S	45.86	5	58.74	-	-	-	-	-	-	-	-	-	-

Results from testing provided the first data to determine the accuracy of the design methodology. The beams were described to behave linear elastic until near the ultimate load (Hillman 2003). Measured deflections during the service level tests were found to be 0.43 in. This was 23% higher than the expected deflection of 0.35 in. The difference between the values may have been attributed to differences in material properties or geometric dimensions between those used in the calculations and of the specimen (Hillman 2003). The measured deflection for the factored load was 0.88 in. whereas the expected value was 0.78. The differences may be due to the same reasons as for the service level tests. The data for tests 7S and 9S are presented within the report in Figure 2-2 and Figure 2-3. For test 7S, the load-deflection behavior was

linear suggesting the materials behaved linear elastically. As expected, the deflection at the midspan was greater than at the load point and quarter point (Figure 2-2). For the ultimate load (test 9S), the load-deflection behavior was linear up to the factored loading of 33 kips. However, at higher loads the relationship became non-linear (Figure 2-3).

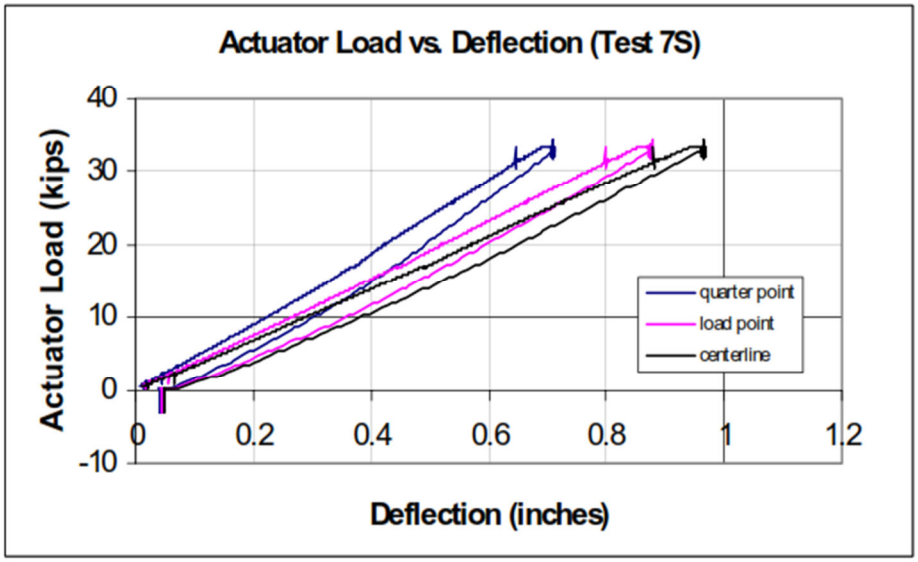

Figure 2-2 Load vs. Deflection for Test 7S (Hillman 2003, Used with permission of John R. Hillman, HC Bridge Company) ©

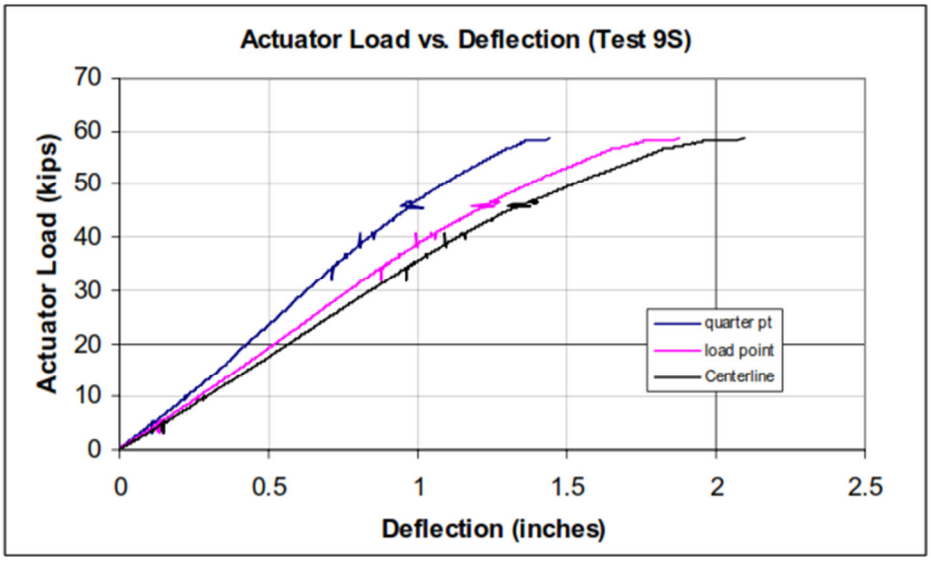

Figure 2-3 Load vs. Deflection for Test 9S (Hillman 2003, Used with permission of John R. Hillman, HC Bridge Company) ©

The beam behavior was examined for tests 7S and 9S as well. In test 9S, the beam carried the load beyond the factored loads (Hillman 2003). The beams were thought to behave as a tied arch system in which the arch would carry the loads to the supports and the resulting horizontal thrust would be equilibrated by the tension reinforcement (Hillman 2003). However, minimal strains in the arch and strand near the support suggested the FRP webs carried much of the load to the supports through shear (Hillman 2003). Data from instrumentation in the concrete arch and tension reinforcement provided evidence for this behavior. Gages were placed longitudinally at the midspan, quarter points, and near the support. For test 7S, the strain in the midspan of the arch was the highest at about -625 με for the maximum load applied (Figure 2-4 (a)). The strain at the quarter point was noticeably lower at -400 με. The strain measurements continue to decrease for the gages located at the anchor points which are located over the supports. The gage located on the eastern end of the beam had a reading of approximately -200 με and the western end was -50 με. Under tied arch behavior, the strain at each of the locations should be approximately the same. The tension reinforcement strain gages indicated that the strains in the midspan and quarter points of the beam were greater than those measured at the anchor points supports (Figure 2-4 (b)). The magnitude of strains at the midspan and the quarter points are in the range of 1200-1400 με. The magnitude of strains for the gages located near the anchor point was approximately 200 με. A noticeable difference in strain was observed between the midspan and the quarter points for the concrete gages, but strain measurements for the tension reinforcement was similar at the midspan and quarter points (Figure 2-4). Despite this irregularity, the data suggests the load was not carried by the concrete and steel at the beam ends.

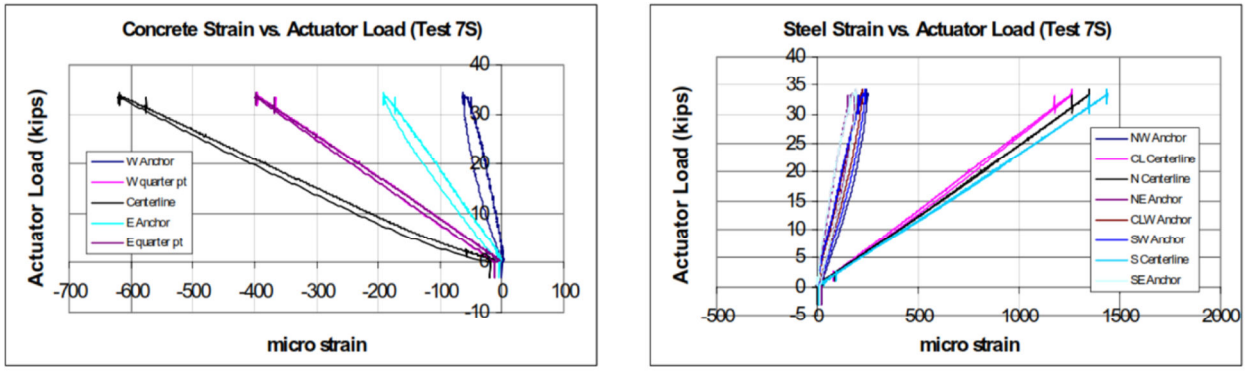

Figure 2-4 Concrete and Steel Strain for Test 7S (Hillman 2003, Used with permission of John R. Hillman, HC Bridge Company) ©

For the ultimate loading in test 9S, similar trends were observed for the gage locations. Non-linear behavior occurred in the gages located near the anchor points. This behavior was observed in both the concrete and steel components of the HCB (Figure 2-5). The behavior of the gages located at the midspan and quarter points appear to behave linearly with the exception of the concrete midspan gage. The data from test 9S as well as test 7S suggest the load was not completely carried by the concrete and steel components of the HCB. The only other component that could have carried the load was the FRP webs. Hillman noted as the load approached the maximum load, more of the load was distributed to the concrete and steel components (Hillman 2003). Thus a redundant load path was created to redistribute loads from the FRP at higher loads.

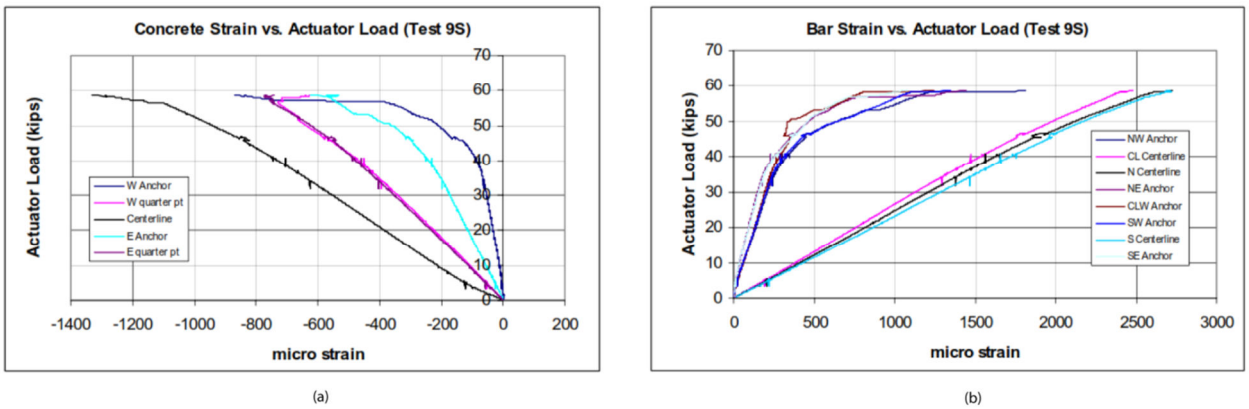

Figure 2-5 Concrete and Steel Strain for Test 9S (Hillman 2003, Used with permission of John R. Hillman, HC Bridge Company) ©

The study served to determine the feasibility of the HCB and to observe behavior of a prototype beam. The HCB was found to be economical for medium span bridges; the cost is usually less than an equivalent steel bridge and approaches the cost of a concrete bridge. Preliminary testing showed fair results. Deflections observed during testing were greater than anticipated, but Hillman suggested the error may be corrected. The data from the component testing suggests beam behavior within the service range which justifies the design methodology developed for the HCB. Though there were differences between observed and expected HCB behavior, the study provided a good basis to refine the initial design assumptions and calculations.

2.2.2. Product Application of a Hybrid-Composite Beam System

A second study was performed to test the application of the HCB in a field setting. A 30 ft span railroad bridge constructed of eight HCB's was placed in the Transportation Technology Center at Pueblo, CO. The prototype HCB's were assembled into two four-girder units that were tied together with threaded rods (Hillman 2008). A 4 in. slab and ballast curb was cast for both of the units. A track was laid across the top of the bridge with superelevation with the outside rail approximately 4 in. higher than the inside rail of the track. Because the bridge was on a curved section of the track, the track was placed slightly off-center on the bridge deck. Both static and live load test were performed on the bridge to determine the systems behavior using heavy axle railcars. Deflection and strain measurements were measured and corrected for the effects of track eccentricity and speed of the train.

The results showed higher distribution to the interior girders of the two units that made up the bridge. Compared to the interior girders, smaller deflections were typically observed for the exterior girders. The lower deflection was attributed to added stiffness from the ballast curbs.

The deflections were observed to decrease linearly from the interior to the exterior girder of each unit. The measured deflections were within a few hundredths of an inch of the expected values (Hillman 2008). Despite transverse variation in deflection, the maximum deflection was shown to satisfy the allowable limit of 0.54 in. Strain values taken at the bottom flange were also observed. Interior girder registered higher strain measurements. Lower strains were typically observed in the exterior girders. The strains were shown to be much less than their ultimate tensile strength (Hillman 2008). In general, measured response values were close to predicted values. The Hillman model approximated the HCB behavior for the IDEA tests effectively.

2.3. Testing of Knickerbocker Bridge HCB

Knickerbocker Bridge was constructed in Boothbay, Maine in the spring of 2010. The bridge consisted of eight straight, non-skewed spans with a total length of 540 ft and a width of 32 ft (Figure 2-6). The interior spans were 70 ft and the exterior spans were 60 ft Testing was performed prior to the construction of Knickerbocker Bridge at the Advanced Engineering Wood Composite (AEWC) lab at the Advanced Structures and Composites Center at the University of Maine. The AEWC center tested one HCB with a cast-in-place deck in addition to material-level coupon testing for the composites used prior to the construction of Knickerbocker Bridge (Snape 2009). Testing of the HCB included static and fatigue loading. The Knickerbocker (KB) HCB had a height of 33 in. with one layer of forty-two ½ in. diameter seven wire strands (Figure 2-7). The top lid of the KB HCB was infused in segments and spliced together. Also, the FRP lid was flat transversely which made the lid susceptible to buckling.

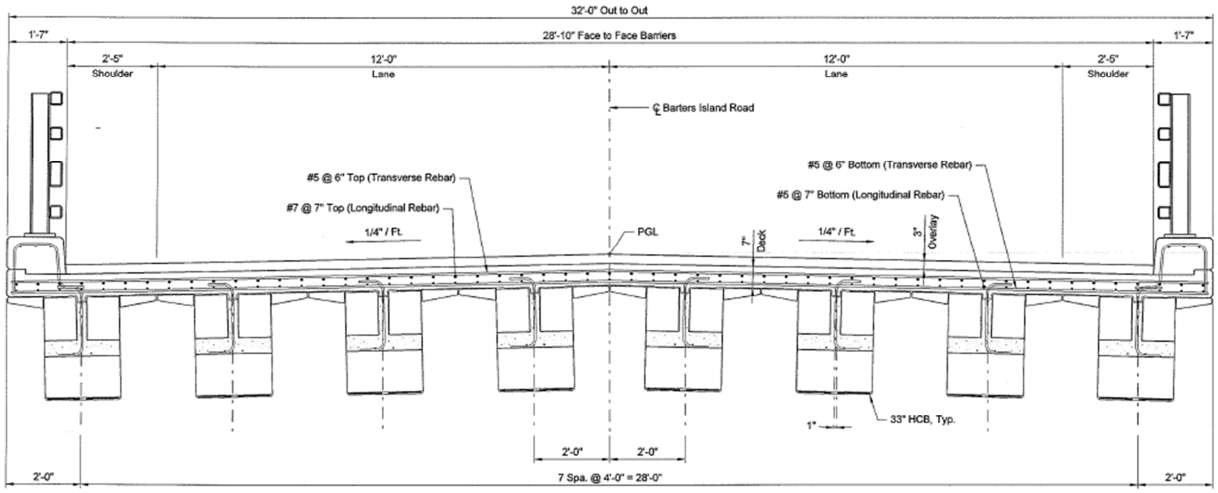

Figure 2-6 Knickerbocker Bridge Cross Section (MDOT 2009)

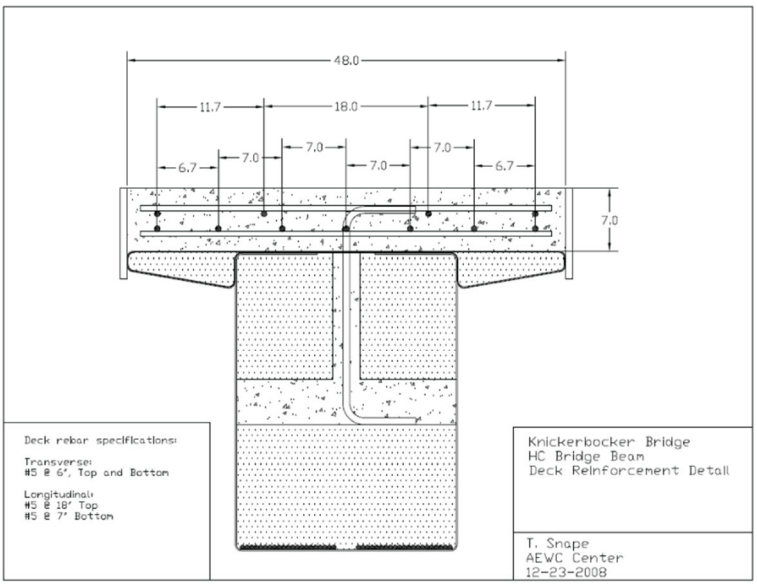

Figure 2-7 Knickerbocker HCB Section (MDOT 2009)

The instrumentation plan for the Knickerbocker HCB testing included strain gages, embedded strain gages, wirepots, LVDT's, and a load cell. In addition, the Aramis 3D optical deformation system was used to measure shear strains in the FRP. Instrumentation was primarily placed at five points: midspan, quarter points, and near the supports. Strain gages were placed in the concrete arch, on the FRP box, and on the steel tension strand.

Data set of the Knickerbocker testing consisted of the applied loads, the arch concrete placement, and the deck placement. The applied loading for the AEWC testing consisted of four-point bending tests for shear and moment. The AASHTO HL-93 truck loading was used to determine the magnitude of applied static and fatigue loads (Table 2-2). Service level tests for shear and moment were first performed. The beam was then subjected to 2,000,000 cycles of fatigue loading. The fatigue loading was interrupted periodically to perform service moment tests to observe any potential changes in beam behavior (Snape 2009). After the fatigue cycles were completed, factored shear and moment was applied. At the conclusion of the testing program, the beam was loaded to failure. The beam was loaded in a shear configuration up to the capacity of the actuator without failure of the beam. A final test was performed to apply a failure load in a bending configuration.

Table 2-2 AEWC Test Matrix

Test	Description	Load Configuration	Magnitude (kips)
1	Service Shear	Shear	100
2	Service Moment	Moment	65.6
3	Fatigue up to 2,000,000 cycles	Fatigue	16.6 - 41.4
-	Periodic Service Moment Tests	Moment	65.6
4	Factored Moment	Moment	133
5	Factored Shear	Shear	135
6	Max Shear	Shear	318
7	Max Moment	Moment	210

The results from testing and the concrete placements were compared to calculation sheets prepared by HC Bridge Company, the design firm founded by John Hillman. The strain data was used to establish a strain profile at midspan. The measured deflections from the arch and deck concrete placement were compared to the expected deflections from the calculation sheets. For the concrete arch placement, the measured midspan deflection was 1.68 in while the predicted

deflection was 2.65 in. An explanation offered for the differences seen for both the strain profile and deflection measurement was contribution of the "wings" that extend outward from the main body of the FRP. Hillman neglected the stiffness of the wings in his model. Snape et. al calculated a new predicted deflection of 1.52 in. including the unaccounted stiffness. Two explanations were offered for the difference between the new predicted deflection and the measured deflection. The FRP used for the top flange was spliced from shorter segments rather than being continuous along the length of the beam (Snape 2009). In addition, elastic buckling was observed in the flat top flange due to bending stresses. Hillman's model calculated the neutral axis location at 7.67 in. from the bottom extreme fiber for the arch placement, but the observed location was found at 5.59 in. (Snape 2009). The non-continuous FRP segments and buckling of the top flange were assumed to be the cause.

The deck was placed 12 days after the arch placement. Data for the deck placement was also analyzed. The test data showed the neutral axis location at 22.13 in. while the calculated location was at 22.89 in. from the bottom extreme fiber (Snape 2009). The measured midspan deflection was 1.44 in., and the predicted deflection was 1.75 in. The differences were attributed to the early age (12 days) and continuing strength gain of the arch concrete.

Results for an initial static shear test and bending test were presented. The tests consisted of four point bending scheme representative of HL-93 loads. Two 45 kip point loads were applied at 14 ft distance apart; for the shear tests the point load was placed 3.4 ft from the support. For the moment test, two 32.8 kip point loads were centered over the midspan. The shear test showed linear-elastic behavior for deflections measured at the midspan and 1/3 span point. The maximum measured deflection was 0.08 in. at the 1/3 point (Snape 2009). Test results from a static bending test showed the neutral axis to be located at 31.36 in. from the extreme

bottom fiber (Snape 2009). Hillman's model was in agreement with the results with a predicted location of 31.4 in. The load-deflection relationship was shown to be linear-elastic. Fatigue loading occurred for 2,000,000 cycles after these initial tests. A static bending test was performed after the fatigue loading, and identical stiffness and linear-elastic behavior was observed.

A factored static bending test, factored static shear test, and ultimate shear and bending tests were performed on the Knickerbocker HCB. For the factored tests, linear-elastic behavior was observed for the loading and unloading phases. The reported strains created a fairly linear strain profile through the composite HCB section. The beam was then loaded to 318.4 kips in the shear loading configuration; and failure of the beam did not occur (Snape 2009). The final test was performed to fail the HCB in bending. The load-deflection behavior was linear up to a load of approximately 120 kips. At higher loads, the HCB behaved non-linearly up to the failure load of 209 kips (Snape 2009). The failure mode consisted of the FRP box failing at the anchor point for the tension strand at the end support of the HCB.

From the provided comparisons between measured and predicted values, Hillman's model appeared to predict the behavior of the HCB well. The location of the neutral axis was in strong agreement with an interpolated profile from the measured strains. Because no predicted values were presented for the static shear and bending tests in the AEWC report, the validity of the model was not established for service level loads. From the reported data, linear-elastic behavior was observed for the service level tests. Strain profiles appeared to remain linear for the composite HCB section. For the ultimate bending test, non-linear behavior was observed at high loads. The Hillman model appeared to approximate strains and deflection well from the

presented data, but data from service level testing must be compared to predicted values from the model before the appropriateness of the model can be established.

2.4. AASHTO Distribution Factors

All bridges consist of a three-dimensional structure in which designing individual girders for exact live load moments and shears would be intensive. Though moment and shear envelopes have been established for the longitudinal direction of the bridge, the transverse placement of the load needs to be considered for a rigorous analysis. As 3D structural analysis is not typically viable for the large number of typical highway bridges, AASHTO Bridge Specifications provide a method for 2D beam-line analysis as long as specified guidelines are met. If bridge parameters fall outside of the limits, other forms of analysis such as Finite-Element (FE) analysis or the lever rule must be used (AASHTO 2008). The method entails the use of live load distribution factors that take into account transverse placement of load and transverse load distribution to adjacent girders (Barker 2007). The establishment and calibration of the live load factors for different bridge types and geometries have been and continue to be heavily researched topics.

Live load distribution factors were developed to predict worse case moments and shear distribution occurring in individual bridge girders. Originally, distribution factors in the AASHTO Standard Specifications were used for design (1996). The Standard method involved a simplified calculation using the ratio of girder spacing s and a constant D that is dependent on the bridge type and geometry. However, extensive research efforts have shown the Standard Specification formulas can lead to highly conservative or highly unconservative designs (Huo 2004). Furthermore, the limits of its applicability are relatively unclear and effects of skew are ignored. The AASHTO LRFD Bridge Specifications present more complicated formulas developed by Zokaie that take into consideration additional design variables besides girder

spacing (Barker 2007). The new method also has limits of applicability, but the limits are expanded due to the consideration of more variables. The LRFD Specifications provide tabulated formulas for different girder types that have been calibrated against a database of FE analysis and field testing (Huo 2004). Though the LRFD formulas provided better prediction for transverse distribution, refinement and examination of the effect of varying factors on load distribution is ongoing.

2.4.1. Effects of Skew on Live Load Distribution Factors

The AASHTO Standard Specifications were created for typical straight span bridges (i.e. the longitudinal and transverse edges of the bridge are perpendicular to each other as in a rectangle). Due to restrictions from site geometry, many bridges cannot be built using straight spans. In many cases, the supporting abutments are placed at an angle to conform to site geometry. This results in a trapezoidal shape for the plan view of the bridge (Figure 2-8). The skew is measured as the angle between the transverse direction and the skew direction. Though the direction of traffic remains perpendicular to the transverse direction of the bridge, the bridge supports are aligned along the skew direction. The change of geometry from a typical bridge structure greatly affects the behavior under loading.

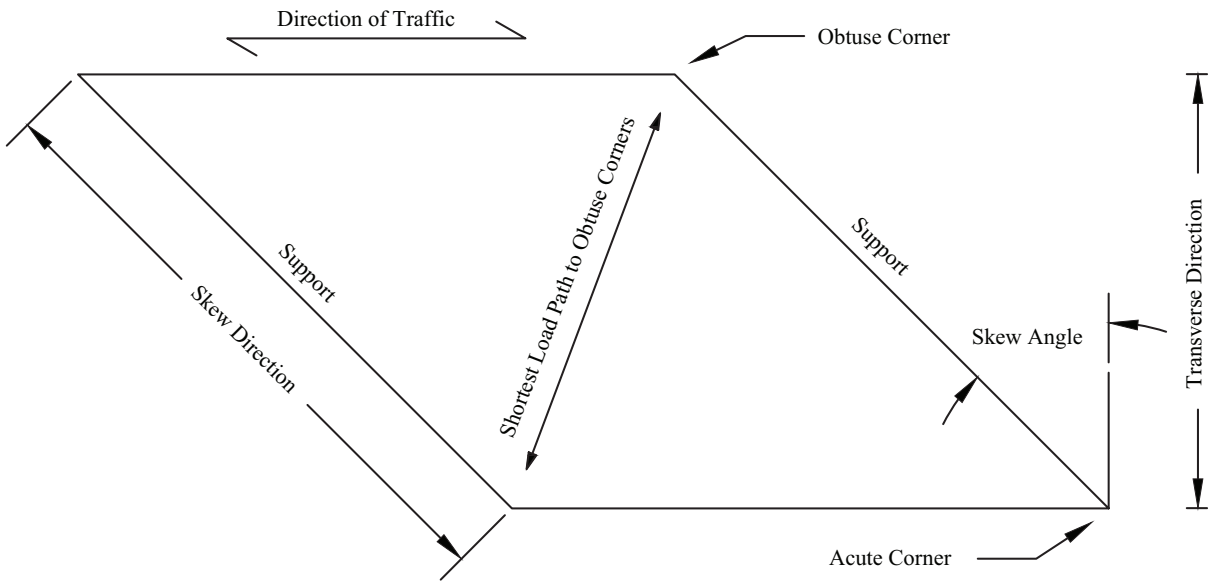

Figure 2-8 Skewed Bridge Terminology

Because of the irregular geometry, the behavior of skewed bridges can be unlike traditional straight span bridges. For skewed bridges, the load follows the shortest load path which is often to the girder supports closest to the obtuse corners (Figure 2-8). The load path results in lower moments but increased shear in the obtuse corners (PCI 2001). Khaloo and Mirzabozorg established the skew angle as the most important parameter on distribution in skewed bridges (2003). The moment distribution was shown to decrease approximately 24% for exterior girders and 26.4% for interior girders from straight span bridges (2003). Ebeido and Kennedy conducted experimental and analytical studies into the effects of different parameters on skewed-bridge behavior (1996). They determined the greatest deflections and strains occurred in the exterior girder. They also observed strains and deflections for all beams decreased as the skew angle increased. Ebeido also observed that a higher aspect ratio for the bridge may cause a decrease in the distribution factor (1996).

The effect on shear distribution is also influenced by skew angle. Ebeido and Kennedy determined skew angle to be the most critical factor on shear distribution (1995). They noted as

the skew angle increased the reactions at the obtuse corners increased and reactions at the acute corners decreased. Their results also showed the sensitivity of the bridge reactions to eccentric placement of the loads. Huo et. al confirmed that skew angle had an important effect on the shear distribution factor from FE analysis; other studies noted an increase in the distribution factor for the girder at the obtuse corner as the skew angle increased (2005). The most critical case was when the truck load is placed near an obtuse corner (Ebeido 1995).

As the Standard Specifications do not account for skew, bridge design with its guidelines may be highly conservative. The new guidelines presented in the LRFD Specifications present more complex formulas that take more geometric variable into consideration. Additionally, correction factors for moment (Eq. 1) and shear (Eq. 2) were developed for skewed bridges.

$$1.05 - 0.25 \tan\theta \leq 1.0 \qquad \text{(Eq. 1)}$$

$$1.0 + \frac{\sqrt{\frac{Ld}{12.0}}}{6S} \tan\theta \qquad \text{(Eq. 2)}$$

2.4.2. Distribution Factors for Fiber-Reinforced Polymer Bridge Structures

The use of fiber composites remain a nontraditional material in the civil engineering field despite progress made from their introduction many years ago. Adoption of the materials in structures has remained minimal compared to traditional building materials due to lack of widespread knowledge and unfamiliarity of design methodologies using composites. Their application to bridge structures represents such a case. The majority of bridges constructed using composite materials have been primarily for research programs where close attention was paid to the design and analysis of the bridge members. Due to the very small proportion of existing and planned composite bridges, the AASHTO Specifications do not specifically include provisions

for the design of composite girder bridges. For new composite bridge construction, engineers must make assumptions relating to existing bridge types in the AASHTO code or perform rigorous analysis for design.

Many have chosen to forgo rigorous analysis by relating composite girders to the existing bridge types in the AASHTO Specifications despite the difference in material. Often, guidelines for steel beams are used to determine distribution factors, but the use of such factors may be unconservative in some cases (Waldron 2001). Route 601 Bridge was constructed used 36 in. pultruded FRP girders. Distribution factors for steel girders with a timber deck were used for the design (S/4.5). The formulas for this bridge type were based on the older distribution formulas presented in the AASHTO Standard Specifications: $DF = s/D$. Though Zokaie updated the distribution formulas for the LRFD Specification, the formula for steel beams with timber decks remained in the simplified form (Restrepo 2002). Only the constant D was updated, but no other bridge parameters were included in the formula. Thus, the distribution factor calculation is largely dependent on girder spacing.

Restrepo used a formula developed by Stallings and Yoo to derive distribution factors from measured strains and deflections during a field test performed on Route 601 Bridge (1993). For differing girder stiffness', a weighting variable must be introduced into the formula:

$$GDF_i = \frac{M_i}{\sum_{j=1}^{k} M_j} = \frac{ES_i\varepsilon_i}{\sum_{j=1}^{k} ES_j\varepsilon_j} = \frac{\frac{S_i}{S_l}\varepsilon_i}{\sum_{j=1}^{k}\frac{S_j}{S_l}\varepsilon_j} = \frac{\varepsilon_i w_i}{\sum_{j=1}^{k}\varepsilon_j w_j} \qquad \text{(Eq. 3)}$$

M_i = bending Moment at ith girder
E = Modulus of Elasticity
S_i = Section Modulus of ith girder
S_l = typical interior section Modulus
ε_i = maximum bottom flange strain at ith girder
w_i = ratio of the section modulus of the ith girder to that of a typical interior girder
k = number of girders

The formula used for Route 601 Bridge was simplified by excluding the weighting variable as all girders had the same stiffness (Restrepo 2002). Stiffening for the exterior girder from the barrier rail was neglected. The worst case moments and strains were used to determine the controlling distribution factor of S/5.0 (Waldron 2001). The factor from the Standard Specification formula was shown to be conservative. The above formula was derived for steel girders and did not take into account shear deformations. Because the FRP materials have a high bending to shear modulus ratio, the effects of shear deformation are important. However, Kassner who tested the same bridge years later assumed the formula was still applicable (2004). For the deflection measurements, shear deformations are measured along with flexural deformations. For shear, only flexural strains are measured. Because the formula consists of a ratio of maximum response to girder response, the shear deformations in each term would have canceled (Kassner 2004). Kassner agreed with Waldron's distribution factors. Similar testing was performed for Tom's Creek Bridge which used similar pultruded girders to Route 601 Bridge. The distribution factor calculated from the AASHTO formula was found to be S/4.0. The experimental data agreed with the predicted factor (Hayes 2000). During a later test, Kassner confirmed the appropriateness of this factor (2004).

2.5. Summary

The Hybrid-Composite Beam (HCB) represents an innovative combination of traditional concrete and steel materials with a composite Fiber-Reinforced Polymer (FRP) material that is relatively new to the structural engineering field. The beam consists of a tied arch encased within a FRP box. Hillman has developed a model to analyze the HCB as a typical beam. Assumptions that plane sections before bending remain plane after bending and strain compatibility were used in its development. Early studies have shown linear strain profiles through the depth of the HCB section indicating these assumptions have some validity. The current design methodology is deflection controlled. The dimensions and properties of the HCB are modified until appropriate deflection limits are satisfied. As a result, a large amount of reserve capacity was observed compared to the ultimate design loads. The beam has been tested on a railroad test track and has already been used in a number of roadway bridges. Limited tests on individual beams have been conducted; many aspects of the beam's behavior need to be investigated. Additional data for individual beam behavior needs to be collected. Information about system behavior also must be collected to validate the model for use in Tide Mill Bridge.

The live load distribution factors for an HCB system need to be established for the widespread adoption of the beam. Distribution factors are used in the AASHTO Specification to reduce the 3D analysis of a bridge structure into a 2D beam-line analysis. Formulas have been developed that include many bridge parameters for many bridge types. Unfortunately, existing formulas do not apply to the HCB. Thus, bridge design with the HCB must involve rigorous analysis or relation to one of the existing bridge types in the AASHTO Specifications. Hillman's current model uses formulas for concrete spread box beams. Live load distribution factors can be largely affected by unusual geometry such as in skewed bridges. The complex geometry of a

skewed bridge can lead to complicated system behavior and transverse load distribution. The AASHTO LRFD specifications currently include a correction factor for moment and shear for exterior girders. Though skewed bridge are becoming more common due to geometric roadway restrictions, literature on skewed bridge behavior remains relatively uncommon. Furthermore, the combination of the HCB with a skewed geometry can lead to very complex behavior which may not be predicted by the any of the current AASHTO Specifications formulas. A research program was established to investigate behavior of the HCB in various stages of its life cycle and to observed system behavior of a scale skewed-three HCB bridge system.

3 Beam Fabrication and Instrumentation

The overall HCB layout and fabrication process are described in the following section. Instrumentation plans for the testing were developed based on the literature review placing emphasis on the AEWC report summarizing testing for the Knickerbocker Bridge. Instrumentation was placed on the tension strand, fiber-reinforced polymer box, and concrete arch to help determine the force distribution in each component of the hybrid-composite beam. The beams were numbered from west to east with the westernmost beam labeled as HCB1 (Figure 3-1). Table 3-1 describes the instrumentation associated with each phase for each HCB. A detailed description of the HCB construction and instrumentation is presented in the following sections. The naming convention for the gages was chosen to quickly determine which HCB component the instrumentation belonged to and which longitudinal location it was placed. The deck strain gages used a different naming convention that is explained in its respective section.

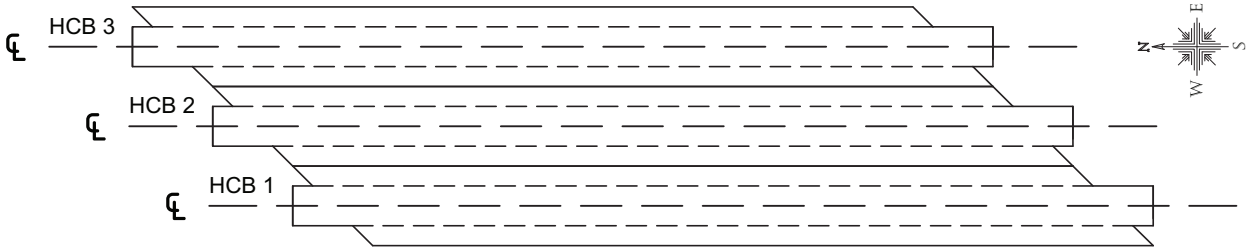

Figure 3-1 HCB Naming Convention

Table 3-1 Overview of HCB Instrumentation

	Phase I Hybrid Composite Beam Only (without arch concrete)	Phase II Hybrid Composite Beam (with arch concrete)	Phase III Skewed Three-HCB System with Diaphragm
HCB 1	Potentiometers, FRP Gages, Strand Gages, RAD Targets	Potentiometers, FRP Gages, Strand Gages, RAD Targets, Load Cell at Actuator, LVDT's, VWG's	Potentiometers, FRP Gages, Strand Gages, RAD Targets, Load Cell at Actuator, LVDT's, VWG's, Load Cells at N Support, Dial Gages at N&S Quarter and Midspan, Dial Gage at beam centerline perpendicular to midspan of HCB 2
HCB 2	Potentiometers and Strand Gages	Potentiometers, FRP Gages, Strand Gages, Load Cell at Actuator, VWG's	Potentiometers, FRP Gages, Strand Gages, Load Cell at Actuator, VWG's, Load Cells at N Support
HCB 3	Potentiometers and Strand Gages	Potentiometers, FRP Gages, Strand Gages, Load Cell at Actuator, VWG's	Potentiometers, FRP Gages, Strand Gages, Load Cell at Actuator, LVDT, VWG's, Load Cells at N Support, Dial Gage at beam centerline perpendicular to midspan of HCB 2

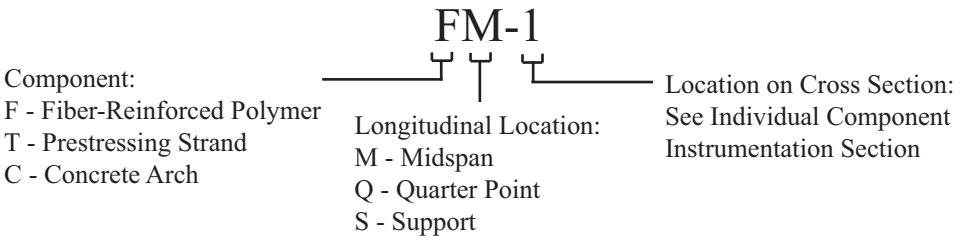

Figure 3-2 Naming Convention for HCB Gages

3.1. HCB Construction

The Hybrid-Composite Beam is constructed of three main components: a concrete arch, seven wire steel strand, and a glass fiber-reinforced polymer (FRP) box (Figure 3-3). The layup and infusion of the FRP box and steel strand was performed at the Harbor Technologies plant in Brunswick, ME.

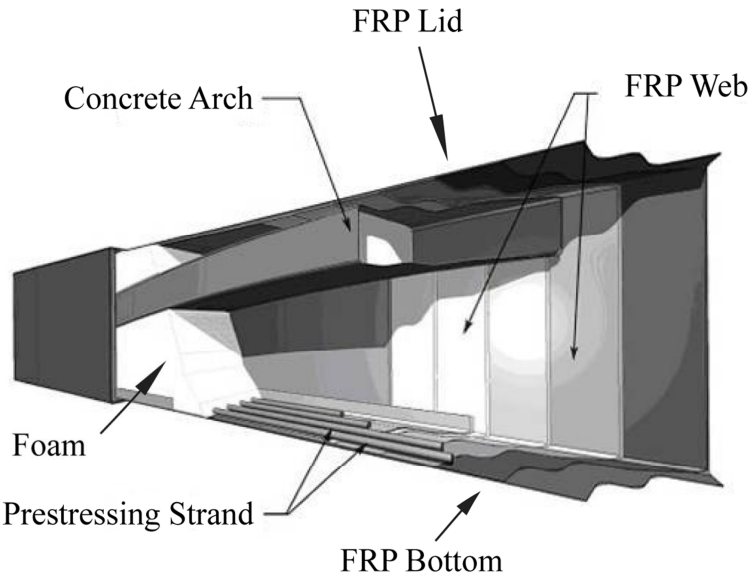

Figure 3-3 Cut View of HCB (Hillman 2003, Used with permission of John R. Hillman, HC Bridge Company) ©

The first step in the beam's construction was the layup of the glass fiber layers. The layup process consisted of fiber layers placed in a mold that forms the two sides and bottom of the beam box. Fiber layers for the lid were laid later using a standalone mold. The number and type of FRP layers depended on the design completed by HC Bridge Company, the design firm founded by John Hillman.

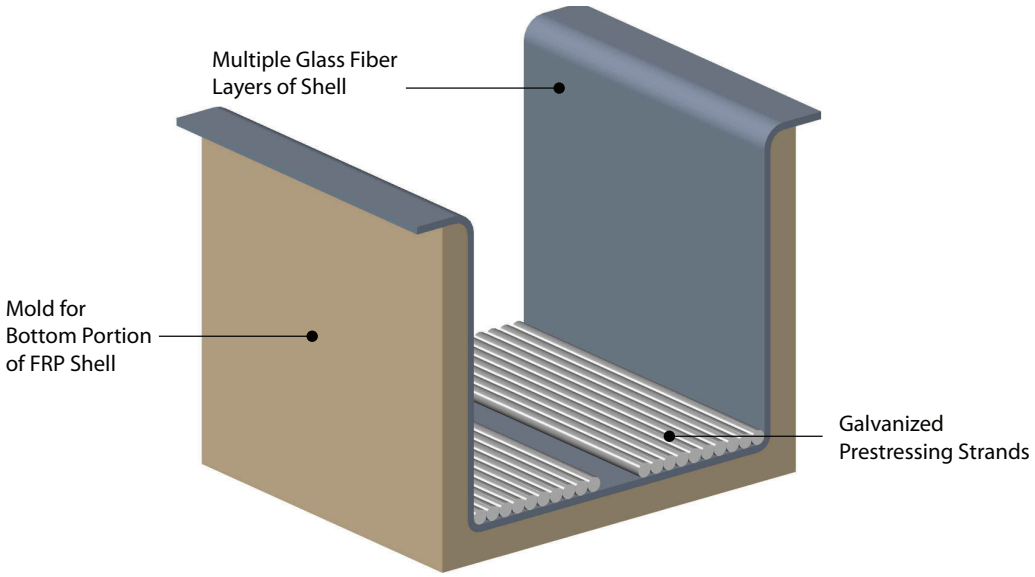

Figure 3-4 Layup of FRP and Prestressing Strand

After the fiber layers were placed in the bottom mold, ½ in. seven wire steel strand was placed on top of the fiber layers (Figure 3-4). The amount of strand depended on the design by HC Bridge Company. During the design process, strands were added to satisfy deflection limits. For the Tide Mill Bridge, one layer of twenty-two strands was used (Hillman 2003). Once the strands were placed, a bottom layer of foam was placed within the mold (Figure 3-5). The foam formed a parabolic arch shape that supported the concrete arch when it was poured at a future date. Additional strips of fiber were laid transversely on top of the foam and tied into the sides. The function of these pieces was to tie the two sides together and help prevent bulging of the FRP box during the arch concrete pour. A bag was placed on the bottom layer of foam and through the fiber cross-ties. This bag was inflated to keep the space for the concrete arch free and to prevent the collapse of the space during the infusion process. A layer of foam was placed on top of the bag that followed the top surface of the arch profile.

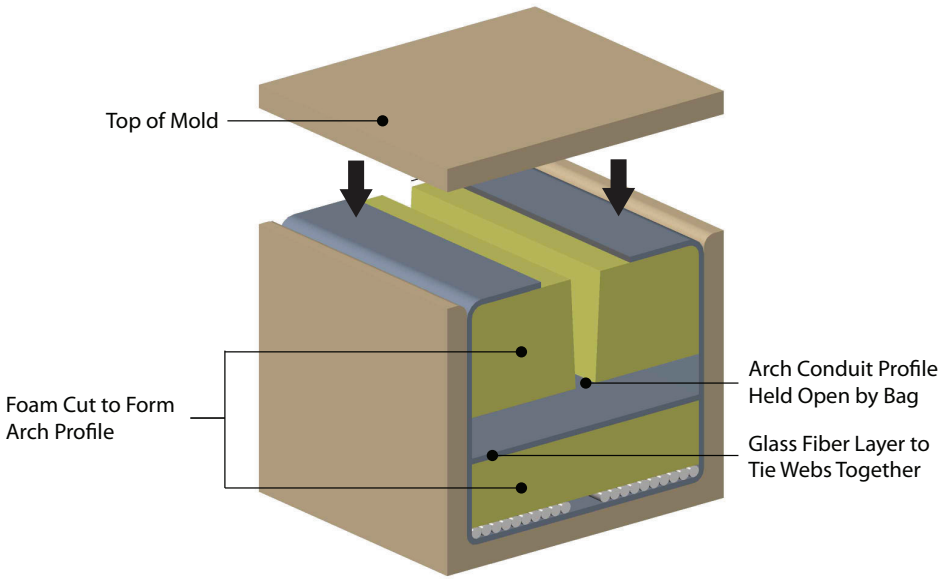

Figure 3-5 Foam Layup

The mold was closed and prepared for infusion. The infusion process consisted of using the Vacuum Assisted Resin Transfer Method (VARTM) to draw vinyl-ester resin into the mold and holding the mold under vacuum for approximately 24 hours (Figure 3-6). The resulting shell was then removed from the mold (Hillman 2003). The lid was infused independently in a separate mold.

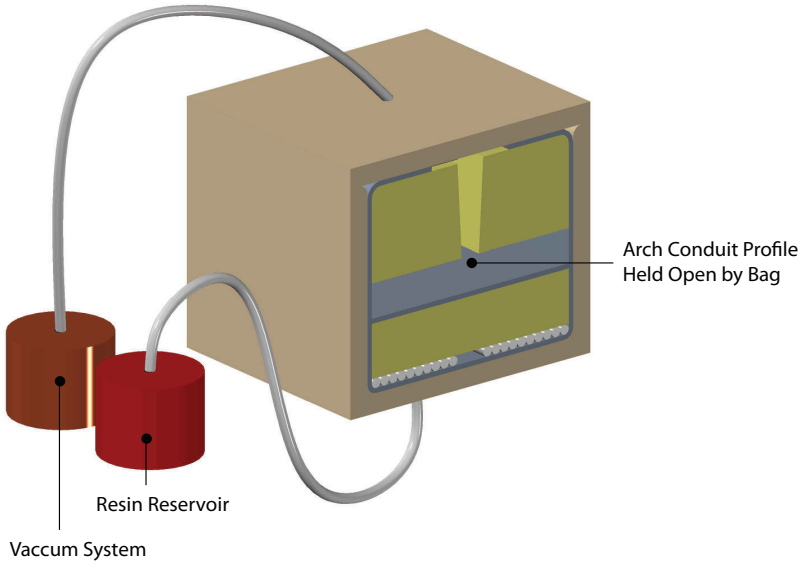

Figure 3-6 Infusion Process

Prior to the attachment of the lid to the bottom component of the shell, a specified camber was introduced into the bottom (Hillman 2003). This was usually accounted for by lifting the shell and placing a block at the center with the ends of the beams resting on the floor. Two ½ in. strands were placed inside of the arch cavity. Tie wires were attached to the strand along the lengths and fed through small drilled holes. These strands were used to help anchor the shear connectors at a later stage. A 1 in. bead of epoxy was placed along the top edge of the bottom component of the shell. The lid was aligned with the bottom shell and placed before the epoxy had set. Self-tapping screws were used to further connect the two elements. The beams were

cured for one day. Holes for the shear connectors and vents were cut into the lid (and through the foam at some locations). Once assembled, the beam was ready to be shipped to the construction site.

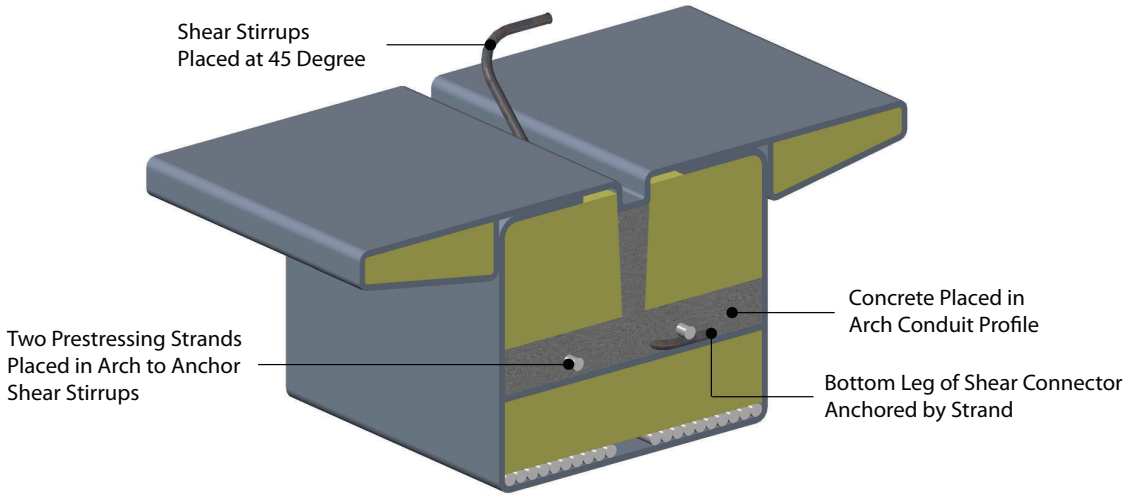

Figure 3-7 Completed HCB

The contractor can choose whether to pour the concrete arch before or after the HCB's are set in their final locations (Figure 3-7). Regardless, the shear connectors must be placed prior to the arch pour. C-shaped shear connectors were placed along the length of the beam at a forty-five degree angle with one leg inside of the arch cavity (Figure 3-7). The length of the shear connectors vary with the arch profile of the beam. The arrangement of the connectors alternate with the leg towards the left or right. The leg of the shear connector was placed underneath the loose prestressing strand on the respective side. This was accomplished by raising the strand with the tie wire. If rapid replacement was preferred, the concrete can be placed prior to setting the beam on its bearings. The concrete can thus gain strength while other construction activities are occurring. However, the beam is much heavier than without the concrete arch in place. If rapid replacement is not a high priority, the beam shells can be placed using a small crane or other

construction equipment. The concrete arch would then be placed with the beam in its final location. The Tide Mill Bridge was constructed using this process (Figure 3-8).

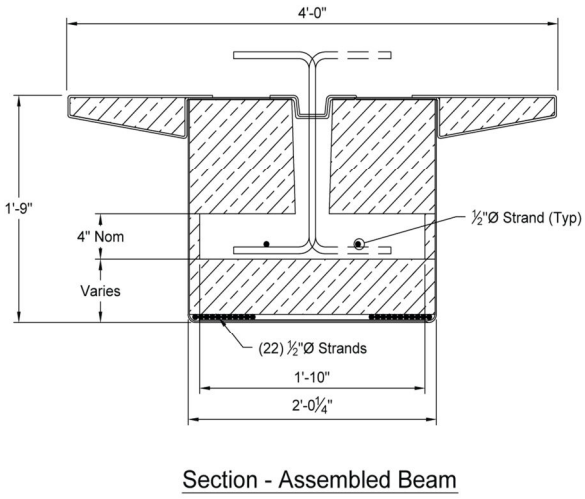

Figure 3-8 Section View of Tide Mill HCB (VDOT 2011)

3.2. Strain Gages

3.2.1. Strain Gages on Tension Strand

For phase I testing, 1/8 in. long electrical resistance strain gages were adhesively attached to one tension strand in each beam during fabrication. This was necessary because the tension strand is inaccessible inside the fiber-reinforced polymer box when the fabrication process is complete. Bonded strain gages were chosen because of the low cost and profile. The strand was expected to be heated to very high temperatures by the resin during the infusion process and could have damaged instrumentation. Also, other measurement devices investigated may have interfered with the infusion process due to bulky components. The selection of bondable gages made the instrumentation of all three beams feasible. Two strain gages were placed at the midpoint of the strand for redundancy (Figure 3-9). Only one gage was placed at the north quarter point. Because the strand consisted of seven wires, each strain gage was adhered to one

wire (Figure 3-10). Because the seven wires were coiled in a helical pattern, the wires were not aligned with the longitudinal direction of the overall strand. The strain gages were attached along the longitudinal direction of the individual wire. This also led to a problem with using the measured strains to calculate force in the strand. The strain measurement from the gage represented strain in the wire occurring in a direction parallel to the wire and not parallel to the overall strand. Testing was conducted at the Virginia Tech lab to determine the force conversion for the strain in the wire. The strand strain gage locations are presented in Table 3-2.

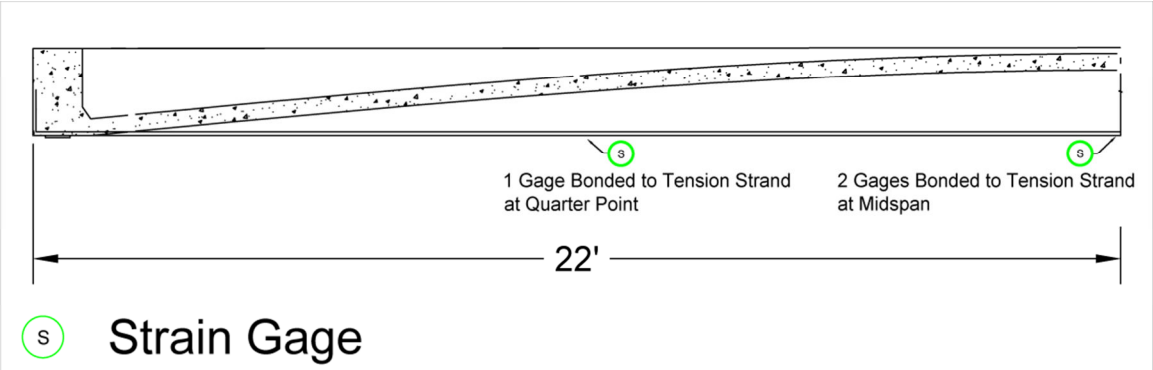

Figure 3-9 Elevation View of Tension Strand Instrumentation

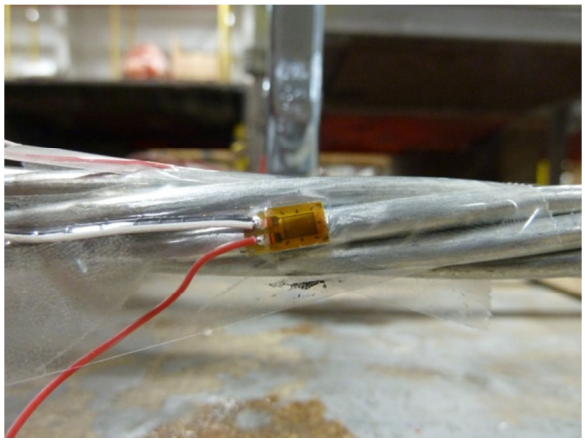

Figure 3-10 Strain Gage on Individual Wire on Tension Strand

Table 3-2 Strand Gage Labels

Location	HCB 1	HCB 2	HCB 3
Midspan Gage 1	TM-1	TM-3	TM-5
Midspan Gage 2	TM-2	TM-4	TM-6
North Quarter Point	TQ-1	TQ-2	TQ-3

3.2.2. Strain Gages on FRP Box

Adhesively-bonded, ¼ in. long, strain gages were attached to the fiber-reinforced polymer box of each beam (Figure 3-11 & Figure 3-12). For phase I testing, only HCB1 had gages attached to the FRP. Gages on HCB2 and HCB3 were placed after the data for phase I was analyzed. The gages were attached at eight locations at the midspan and at the north quarter point (Figure 3-13 & Figure 3-14). At the support, four strain gages were attached to the webs of the box (Figure 3-15). These strain gages were placed at various depths of the HCB to provide data for a strain profile. In addition, one strain gage was attached to the top and bottom of the flange at the midspan. This gage was used to help determine the contribution of the flange to the FRP box. The FRP strain gage locations are listed in Table 3-3.

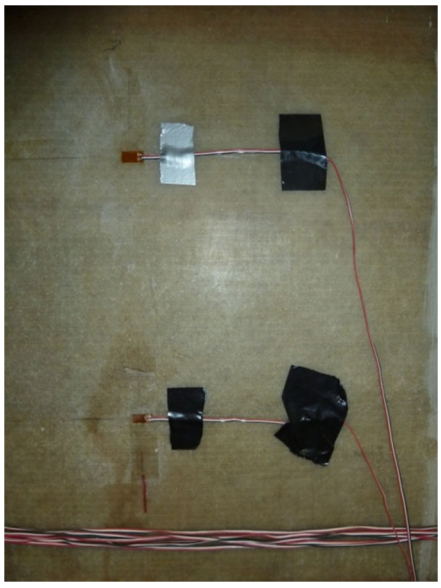

Figure 3-11 Strain Gage Installation on FRP

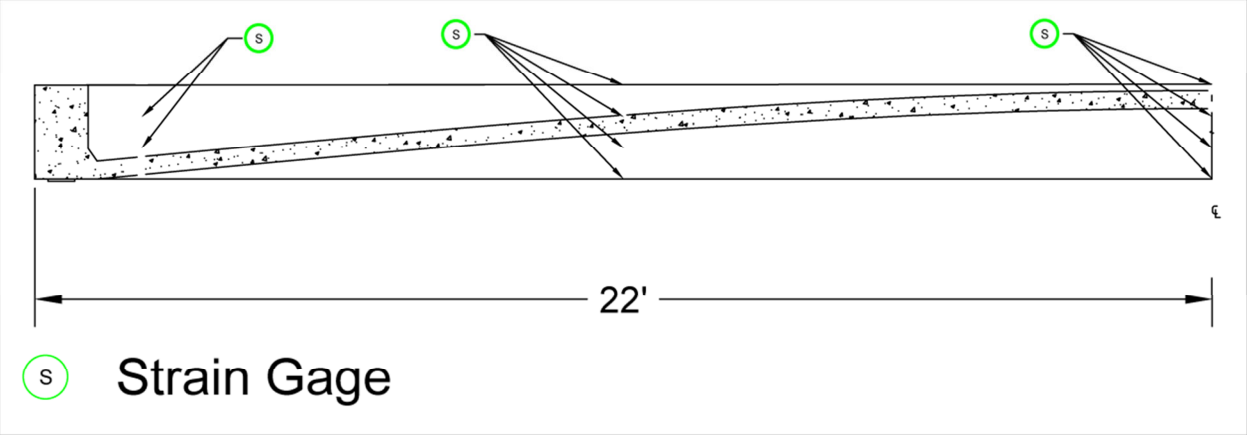

Figure 3-12 Elevation View of FRP Strain Gages

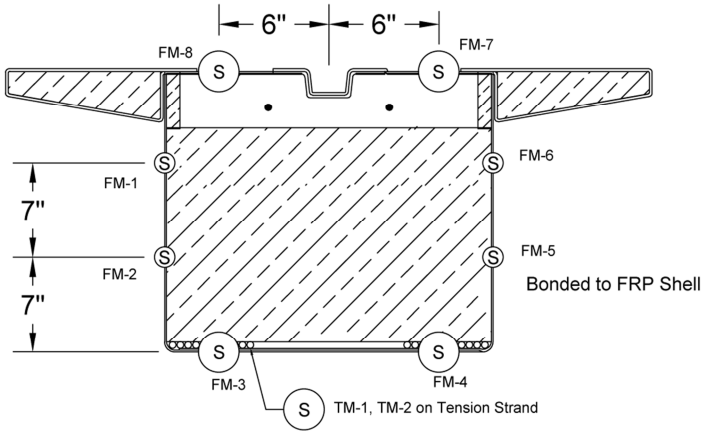

Figure 3-13 Section View of Strain Gages at Midspan

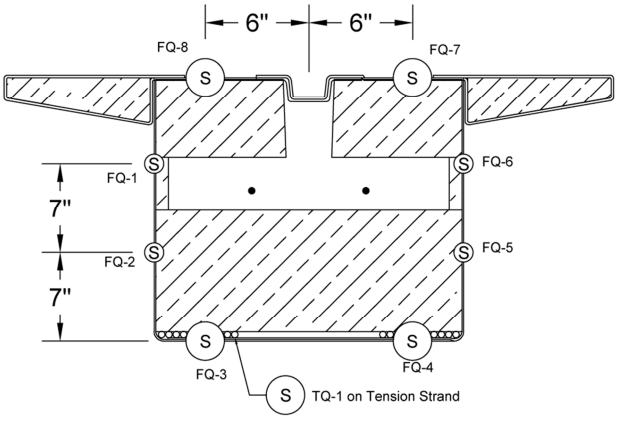

Figure 3-14 Section View of Strain Gages at Quarter Point

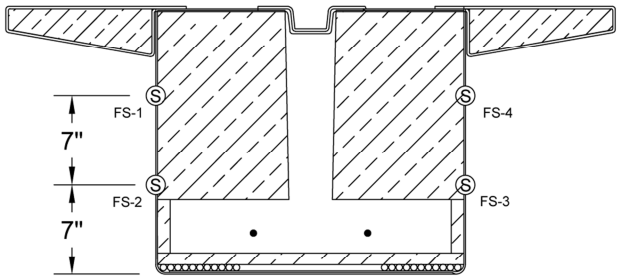

Figure 3-15 Section View of Strain Gages at Support

Table 3-3 FRP Strain Gage Labels

Transverse Location	Longitudinal Location								
	Midspan			Quarter Point			Support		
	HCB 1	HCB 2	HCB 3	HCB 1	HCB 2	HCB 3	HCB 1	HCB 2	HCB 3
Top Web on East Side	FM-1	FM-9	FM-17	FQ-1	FQ-9	FQ-17	FS-1	FS-5	FS-9
Bottom Web on East Side	FM-2	FM-10	FM-18	FQ-2	FQ-10	FQ-18	FS-2	FS-6	FS-10
Bottom Flange East Side	FM-3	FM-11	FM-19	FQ-3	FQ-11	FQ-19	-	-	-
Bottom Flange West Side	FM-4	FM-12	FM-20	FQ-4	FQ-12	FQ-20	-	-	-
Bottom of Web West Side	FM-5	FM-13	FM-21	FQ-5	FQ-13	FQ-21	FS-3	FS-7	FS-11
Top of Web West Side	FM-6	FM-14	FM-22	FQ-6	FQ-14	FQ-22	FS-4	FS-8	FS-12
Top Flange West Side	FM-7	FM-15	FM-23	FQ-7	FQ-15	FQ-23	-	-	-
Top Flange East Side	FM-8	FM-16	FM-24	FQ-8	FQ-16	FQ-24	-	-	-

3.2.3. Strain Gages on Deck Reinforcement

Adhesively-bonded, 1/8 in. long, strain gages were placed on longitudinal and transverse steel reinforcement in the deck. The placement of strain gages are shown in Figure 3-16. The labels for the gages and the naming convention are presented in Figure 3-17 and Figure 3-18 respectively. The longitudinal strain gage placements were chosen to supplement the gages on the respective HCB's to provide data for a composite section strain profile at the midspan and quarter point. Gages on the transverse reinforcement were placed in areas of expected maximum

positive and negative moments. Gages were also placed towards the north support of the setup to examine effects of the skew. As the transverse reinforcement layout called for alternating truss reinforcement with top and bottom mat straight reinforcement, gages were placed on both types of reinforcement. A protective coating was applied to all gages to decrease the possibility of damage during the deck concrete placement.

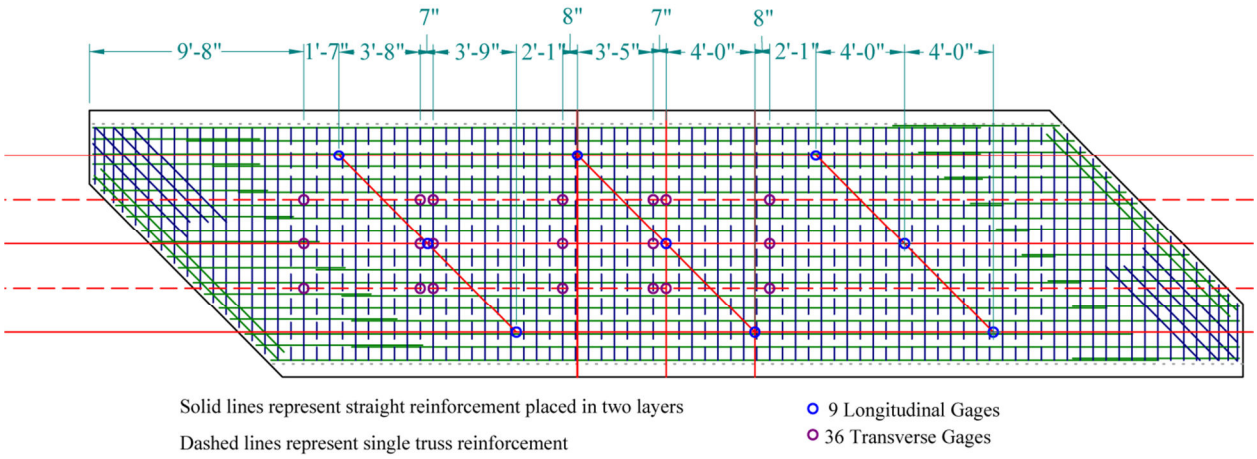

Figure 3-16 Deck Strain Gage Layout

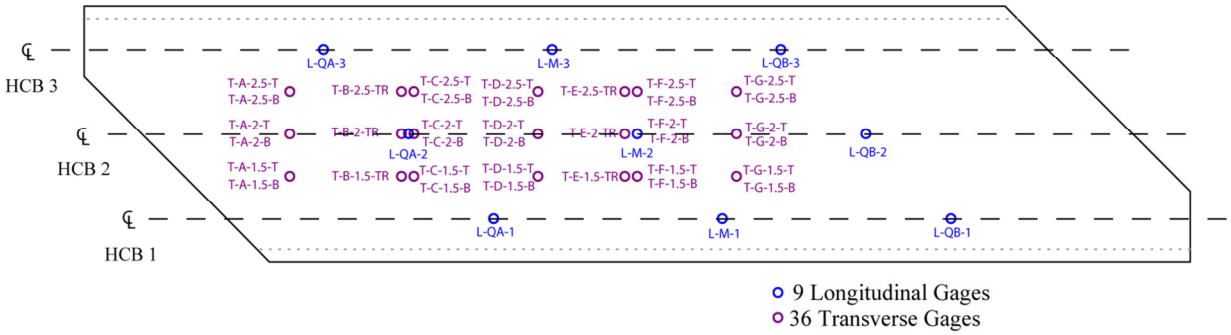

Figure 3-17 Deck Strain Gage Labels

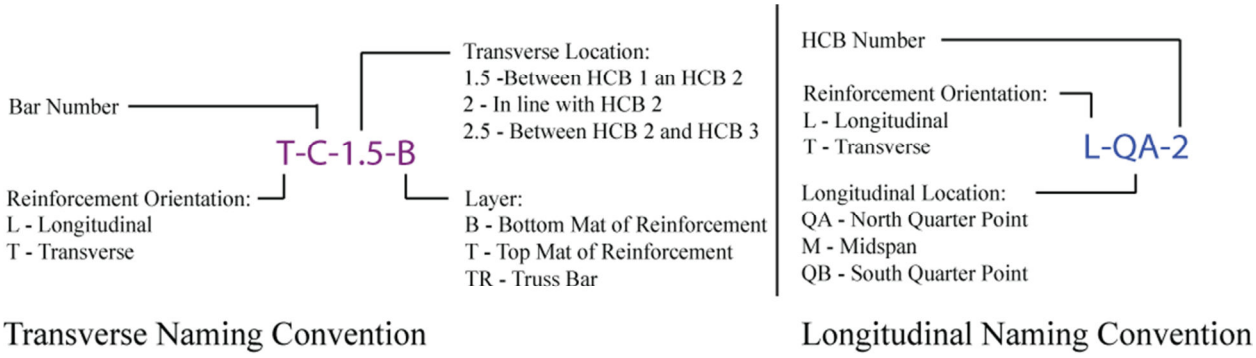

Figure 3-18 Deck Strain Gage Naming Convention

3.3. Concrete Vibrating Wire Gages

Vibrating wire strain gages were placed in the concrete arch. The vibrating wire gages consisted of a tube with two metal disks at each end (Figure 3-19). Inside of the tube is a steel wire that is attached to the metal disks. The tube fits into a housing that contains two coils. One coil is used to excite the steel wire; the other coil is used to measure the vibration in the wire. Also, within the housing is a thermistor for measuring temperature. The temperature affects the frequency of vibration of the wire thus needs to be recorded. A hose clamp was placed around the housing to hold the tube in place. A wire from the housing connects into either a readout box (Figure 3-20) or a data acquisition system.

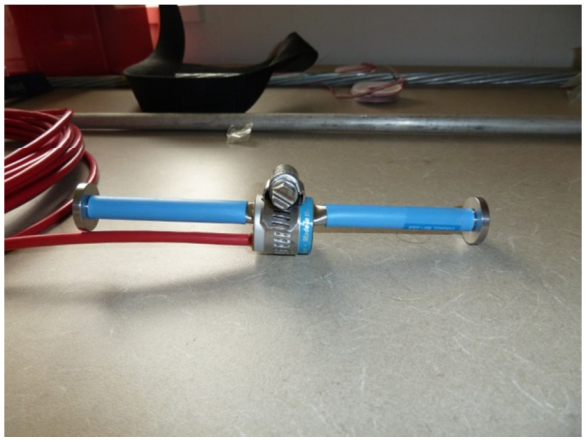

Figure 3-19 Geokon 4200 Vibrating Wire Gage

Figure 3-20 Geokon Readout Box

Though the vibrating wire gages were not in use for Phase I testing, they needed to be placed inside of the HCB prior to the FRP lids being attached. Six gages were placed in each HCB (Figure 3-21). Two gages were placed at the midspan, at the north quarter point, and at one and a half feet from the support. The naming convention for the gages is listed in Table 3-4.

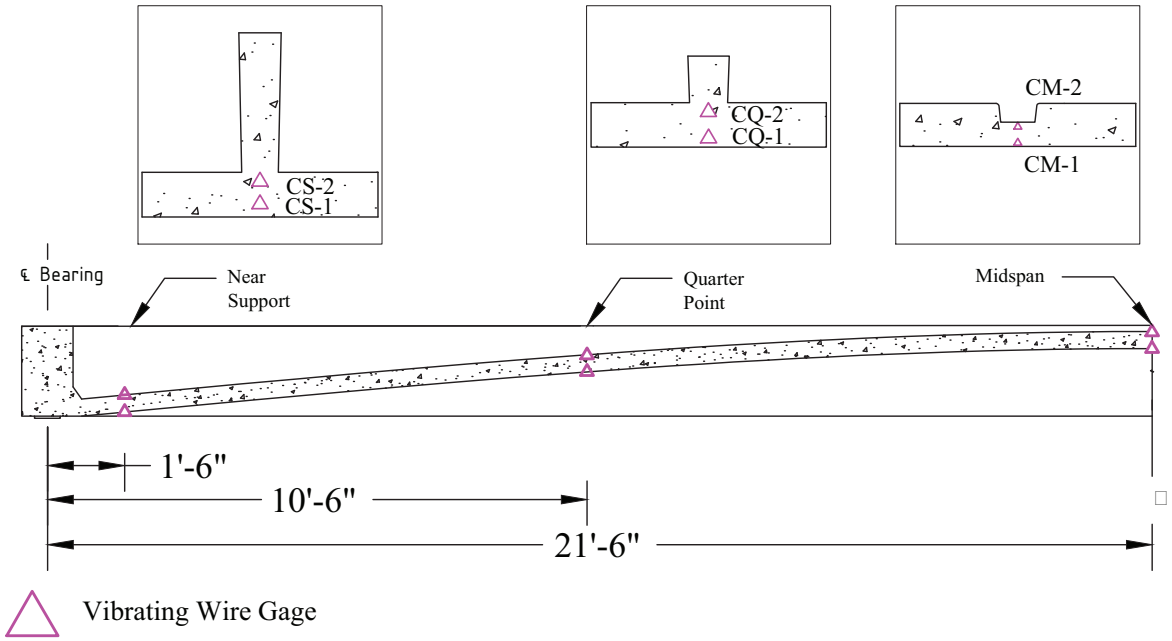

Figure 3-21 Elevation View of Concrete Arch Instrumentation

Table 3-4 Vibrating Wire Gage Labels

Location	HCB 1	HCB 2	HCB 3
Bottom of Arch at Midspan	CS-1	CS-3	CS-5
Top of Arch at Midspan	CS-2	CS-4	CS-6
Bottom of Arch at North Quarter Point	CQ-1	CQ-3	CQ-5
Top of Arch at North Quarter Point	CQ-2	CQ-4	CQ-6
Bottom of Arch at Support	CM-1	CM-3	CM-5
Top of Arch at Support	CM-2	CM-4	CM-6

All of the gages were placed within the arch profile. At each location, one gage was placed near the top of the arch and the other was placed near the bottom. Gages located near the bottom were attached to one of the loose tension strands that ran along the length of the arch. The gages were attached using tie wire as shown in Figure 3-22.

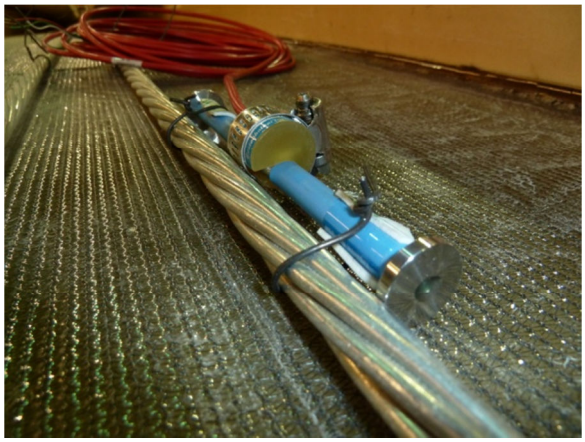

Figure 3-22 Installation of VWG on Bottom of Arch

Attachment to the strand provided insurance that the gage would not be knocked out of position during shear connector placement and concrete placement. When the shear connectors were placed, the bottom leg of the connectors bear against the bottom surface of the arch profile. The arch strand must be lifted to place it over the leg of the shear connector. The arrangement also ensured the gage remains fairly aligned with the length of the HCB. One disadvantage to the setup was that the strand was slightly off-center due to the placement of shear connectors between the two arch strands. The gages were a few inches away from the center; the effect was

assumed to be negligible. The cables attached to the gages were run to the outside of the beam using the nearest vent hole in the FRP lid.

For the support and quarter point, cages were constructed using tie wire to hold the gage at the top of the arch (Figure 3-23). The cages were attached to the foam by bending the end of the tie wire into hooks.

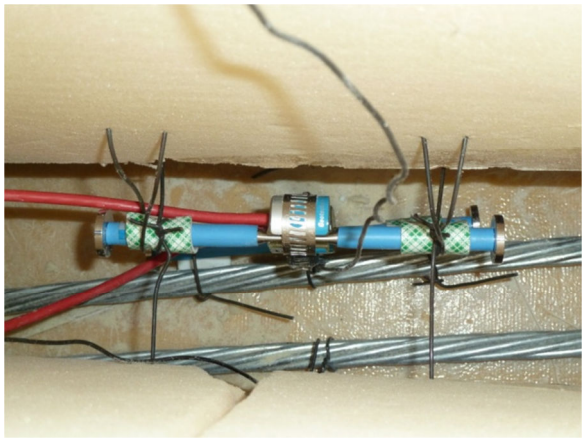

Figure 3-23 Installation of VWG at Top of Arch

For these gages, the alignment of the gage was not ensured during the placement of the shear connectors or the concrete. However, a larger cage could not be used because it would become an obstruction to the placement of the shear connectors. These cages held the gages slightly off-center to ensure the shear connectors could be placed properly. For the top of the arch at the midspan, the vibrating gage was tied to a chair (Figure 3-24). The gage was aligned with the length of the beam and held sturdily.

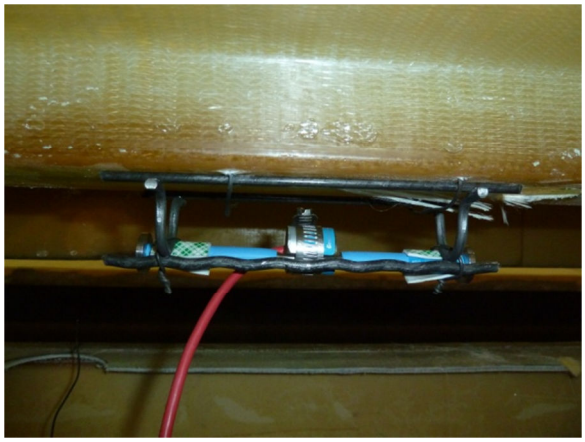

Figure 3-24 Installation of VWG at Top of Arch at Midspan

This gage was centered transversely in the arch because no shear connectors were placed within 1 ft of the midspan. However, the gage was embedded 1 in. into the arch due to the chair being attached to the bottom of the channel in the FRP lid.

3.4. Potentiometers

In addition to strain gages, potentiometers were used to measure deflections during testing. For the first two phases of testing, only three potentiometers were used as one beam was tested at a time. They were placed underneath the beam at the midspan and both quarter points. Nylon string was used to connect the potentiometers wires to the beam surface as the range of the potentiometers was around 8 in. and the height of the beams from the floor was 48 in. (Figure 3-26). Nine potentiometers were used in the third phase of testing. They were attached to each beam at the midspan and both quarter points (Figure 3-27). Potentiometers were calibrated with a height gage prior to each phase of testing. The accuracy of the potentiometers was to the nearest 0.005 in.

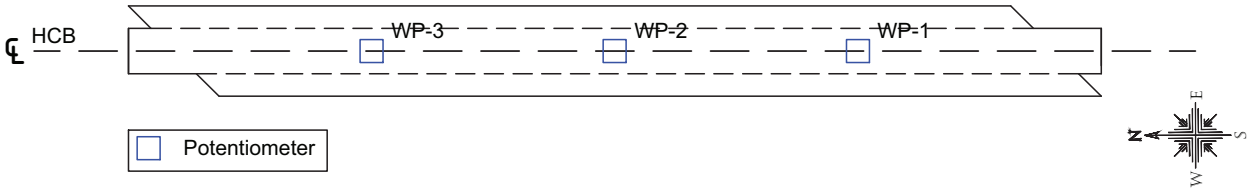

Figure 3-25 Potentiometer Layout for Phase I & II

Figure 3-26 Potentiometer Attached to HCB

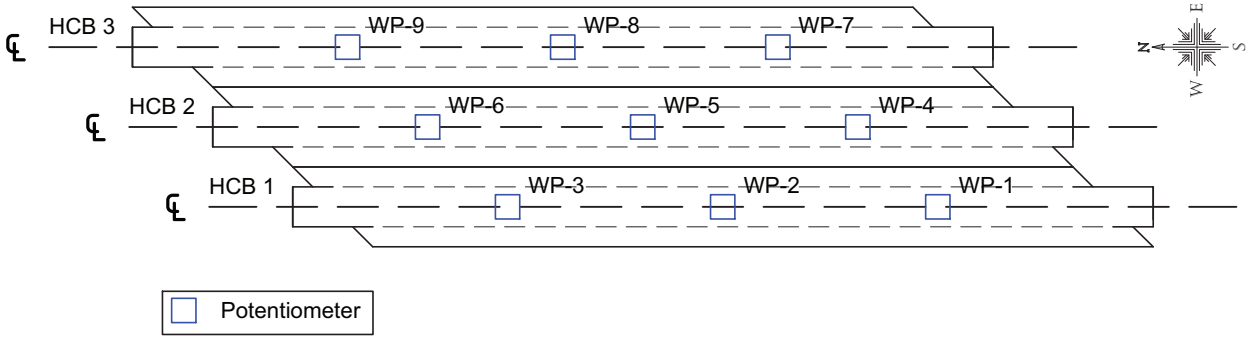

Figure 3-27 Potentiometer Layout for Phase III

3.5. Load Cells

Load cells were used to measure applied force and reactions. For the second and third phase, a load cell was placed between the actuator and the load frame to measure the applied force. A 50 kip load cell was used for the second phase (Figure 3-28), and a 300 kip load cell was used for the third phase (Figure 3-29). For the third phase of testing, six load cells were constructed and two cells placed underneath each beam at the northern end of the test setup (Figure 3-30). The load cells consisted of a solid steel 1.75 in. diameter cylinder cut to a length of 1 in. (Figure 3-31). A ½ in. hole was bored through ¾ in. into the cylinder. The hole was made to distribute stress towards the outer surface of the steel cylinder where the strain gages would be attached. Four 0°-90° ¼ in. adhesively bonded strain gage rosettes were placed around the outer circumference of the steel cylinders. Each rosette contained two strain gages; one was oriented to measure longitudinal strain and the other to measure the transverse Poisson strain. The strain gages were placed at each 90° quadrant around the circumference and were oriented to measure strain primarily along the length of the cylinder. The strain gages were connected in two parallel Wheatstone bridges. The Wheatstone bridge was able to account for varying strains due to eccentricity from loading. A protective coating was placed around each load cell to protect the solder connections. Each load cell was calibrated with the primary data acquisition system in a concrete cylinder testing machine. At the maximum calibration load of 28,000 lb, an error of approximately 1,000 lb was observed resulting in 3.6% error for the load cells at the supports.

Figure 3-28 50 Kip Load Cell used for Phase II

Figure 3-29 300 Kip Load Cell used for Phase III

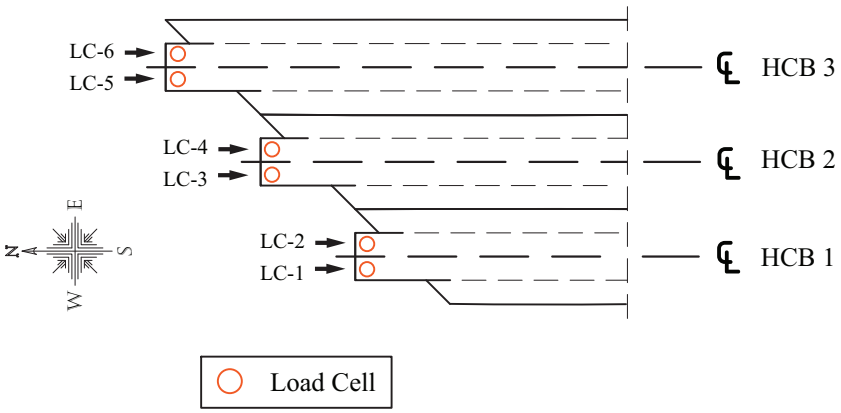

Figure 3-30 Support Load Cell Locations

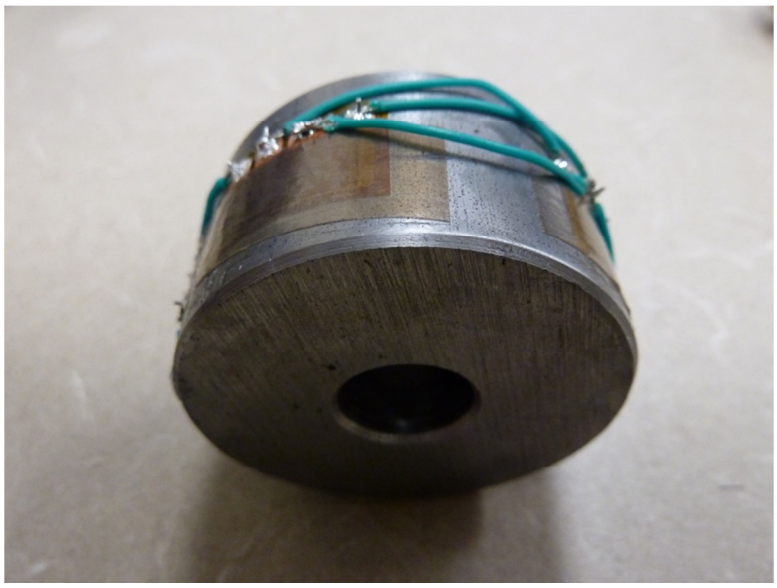

Figure 3-31 Support Load Cell Construction

3.6. Linear Variable Differential Transformers

Linear Variable Differential Transformers (LVDTs) were used to measure relative vertical movement between the concrete arch and the FRP box. The LVDTs were used on HCB1 only for phase II and III testing. The LVDT was mounted to a bracket that was attached to the FRP box using screws (Figure 5-31). Before the lid to the FRP box was attached, a hole was drilled through the foam and bottom flange at the midspan and the north quarter point at the

beam centerline. The hole extended from the bottom of the arch cavity to the bottom of the HCB. A string was threaded through the hole, and the top of the string was attached with a screw at the bottom of the arch cavity while the bottom end of the string was tied to the LVDT. Because the LVDT was not spring driven, a weight was placed on the LVDT to ensure the string remained taught. The results for these LVDT's for phase I and II were presented in *Out-of-Plane Web Deformation and Relative Arch Movement of Hybrid-Composite Beams Based on Photogrammetry* (Mascaro 2012).

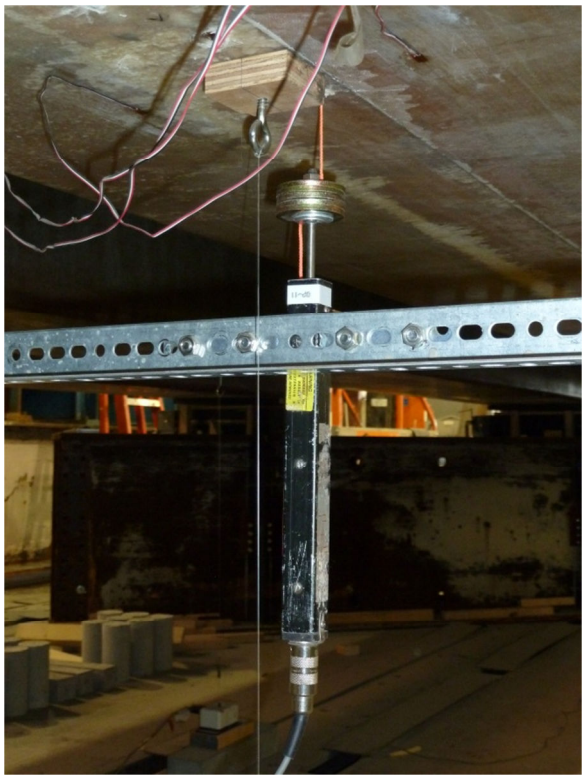

Figure 3-32 LVDT Mounted on HCB 1 at Midspan

For phase III testing, LVDT's were added to the north end of HCB 1 and to the south end of HCB 3. These LVDT's were mounted on the centerline of the end face of each beam (Figure 3-33). The purpose of these instruments was to measure any potential uplift that may have occurred at the acute supports. During phase III testing, additional LVDT's were added to

complement deflection measurements of the potentiometers. Spring driven LVDT's were attached to mobile stands to place perpendicular transversely to potentiometers of interest (Figure 3-34). For example, if HCB 1 was loaded for the maximum shear test, the LVDT's were placed perpendicular to WP-3 and so on.

Figure 3-33 LVDT Mounted at Acute Corner

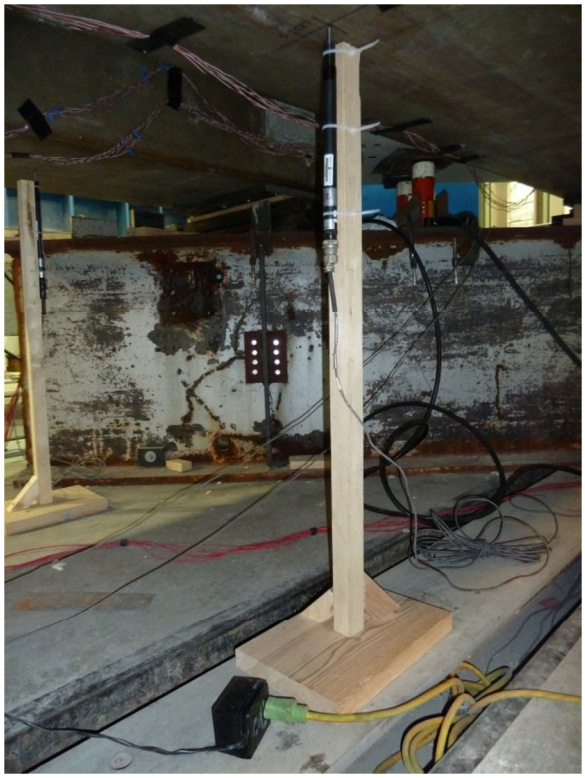

Figure 3-34 LVDT Mounted to Mobile Support

3.7. Dial Gages

Dial gages were used in phase II and phase III testing. For phase II, dial gages were placed on the face of the end of the beam to measure rotations at the pin support. For phase III, dial gages were placed horizontally against the exterior FRP web face at the midspan and both quarter points of HCB 1. At each location, a dial gage was placed 2.5 in. and 12 in. from the bottom face of the beam. The purpose of these gages was to measure out of plane deformations of the FRP web. Two additional dial gages were used in phase III to measure deflections transverse to the midspan of HCB 2. The gages were read at each load increment to supplement the data from the potentiometers.

3.8. Photogrammetry

Targets for photogrammetry analysis were attached to the west FRP web of HCB 1. For Phase I and II, the targets were attached along half of the span. For Phase III, targets were added to the other half of the beam. The targets were used to determine out of plane movement of the FRP web. Five targets were attached to the concrete arch to measure relative movement between the FRP web and the arch. Detailed descriptions of the photogrammetry configuration and results can be found in *Out-of-Plane Web Deformation and Relative Arch Movement of Hybrid-Composite Beams Based on Photogrammetry* (Mascaro 2012).

3.9. Data Acquisition Systems

Multi-channel data acquisition systems were used for each phase of testing. The primary data acquisition system was used for all three phases of testing. Potentiometers, LVDTs, load cells, and strain gages on the FRP were attached to the primary system. The primary system was set to record at an interval of 10 readings per second. Secondary systems were used in phase II and III testing due to compatibility issues with some instrumentation and the available channels in the primary system. One secondary system was used in phase II; this system was a proprietary system capable of reading vibrating wire gages at 50 readings per second. The data from this system was reduced to 10 readings per second to match the recording interval of the primary system. Unfortunately, the system was unavailable for the third phase of testing.

For phase III testing, two secondary systems were used to supplement the primary system. One secondary system was used to record data from the vibrating wire gages. The recording interval was limited by a relay switch that was used to read the eighteen gages. The relay read one gage approximately every 10 seconds. Thus, a set of readings was taken over a 3 minute interval at each load step. Because of the resulting large scan interval, data from loading

and unloading were not available for phase III. The other secondary system was similar to the primary system and was used to increase the number of channels by 32 so data from most of the strain gages in the deck could also be recorded. The scan interval for this system was set to 10 readings per second. The data was post-processed to synchronize the data from the three systems into one data file.

4 Methodology and Testing Procedures

Lab testing of the Hybrid Composite Beams (HCB) was performed to investigate the behavior of the beams for use in a skewed bridge and to assist with developing a design for the Tide Mill Bridge. Three main phases of testing were performed to understand distribution of forces between the different components of the HCB, understand the behavior of the individual HCB, and to understand the behavior of a three HCB system. The first phase of testing consisted of testing individual HCB's without the arch concrete in place. The second phase included testing of individual HCB's with the arch concrete in place. The third and final phase consisted of a skewed three-HCB system with a cast-in-place deck and end diaphragms. Additional testing occurred prior to phase I to understand the contribution of the FRP lid and wings to the stiffness of the FRP box.

Skewed simulated bridge abutments were fabricated to simulate the skewed bridge layout in the field. Each abutment was created by rigidly connecting two 17 ft W36x182 to the floor beams that are an integral part of the strong floor. The layout of the abutments with respect to the floor beams is shown in Figure 4-1. Floor beams ran along the length of the testing bays. There were three floor beams in the test setup; two on the outer edges of each bay, and one that is shared by both bays in the center of the setup.

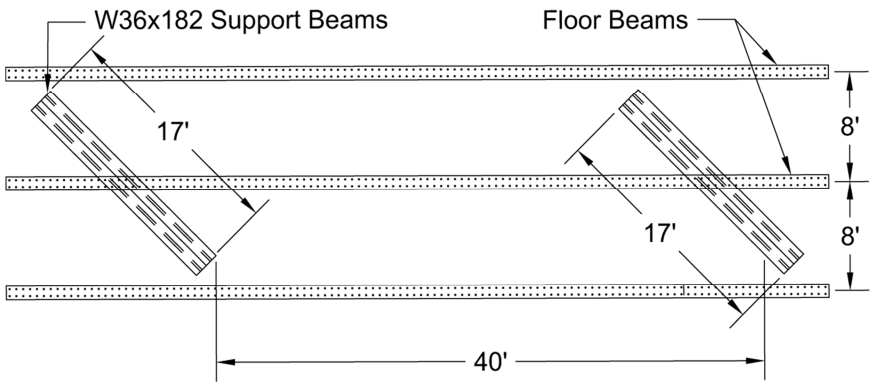

Figure 4-1 Floor Layout

4.1. Preparation for Phase I Testing

One departure from the standard HCB fabrication process was that the HCB was shipped to Virginia Tech without the FRP lid attached. This was done to facilitate instrumentation prior to testing. Before Phase I testing initiated, the bottom of the FRP box of HCB 1 (without the lid attached) was tested to determine how much the lid and wings contribute to the beam stiffness. The bottom of the HCB was loaded by using the lid as a dead weight. The lid was lifted off of the HCB using cranes in the lab. Two wood blocks were placed at the quarter points to distribute the weight from the lid to the bottom of the HCB. The instrumentation was then zeroed and set to record. Then lid was then lowered on to the wooden blocks while recording data.

In addition, data was recorded for HCB 1 when camber was introduced into the beam. Normally, the appropriate camber is introduced when the FRP box is fully assembled at the composites plant. Because the lids were not attached, the beams' stiffness was lower and the beams deflected more than anticipated when placed on their supports. Thus a 2 in. camber was introduced using screw jacks placed at the midspan before the FRP lid was glued on (Figure 4-2). The data system was zeroed, the system was set to record, and camber was introduced into the beam using the screw jack. The data for both the bottom component test and camber test

were to be used for development of a future model of the beam. After the camber was introduced and the beam interior was instrumented, the lid was attached with epoxy and screws.

Figure 4-2 Screwjack Introducing Camber into HCB

Figure 4-3 Epoxy used to Glue FRP Lid

4.2. Phase I Testing

To gain a better understanding of the behavior of the fiber reinforced polymer box, phase I testing was performed without the arch concrete in place. For HCB 1, foil strain gages were placed on the FRP box and steel strand. For HCB 2 and 3, strain gages were only placed on the tension strand. Based on the results from the first phase of testing, strain gages were attached to the FRP boxes of HCB 2 and 3 accordingly. Potentiometers were used for all tests on each beam and were placed at each quarter point and midspan. The beams were placed on pin and roller boundary conditions to be able to accurately calculate the induced moment from the loading (Figure 4-4). The pin and roller were each placed 6 in. from the beam end and perpendicular to the length of the beam. Shim plates were placed under the base of the pin and roller to account for differences in elevations between the two support beams. The resulting span length was 43 ft which is the span length of the Tide Mill Bridge.

Pin Support
(a)

Roller Support
(b)

Figure 4-4 Pin and Roller Boundary Conditions

Phase I testing consisted of loading individual FRP box beams with steel angles (each weighing 25 lb). For HCB1, they were evenly distributed along the length of the beam in one layer. For HCB 2 and HCB 3, the angles were placed at 17 points spaced 2.5 ft apart (Figure 4-5). The first angle was placed at midspan of the beam. The next two angles were placed simultaneously at each adjacent load point to the midspan. The next two angles were placed at the next adjacent points and so on until angles were placed at all load points. The deflections and strains were then recorded. This process was repeated four times with a new layer of angles so that each load point had five angles stacked when the beam was fully loaded. A total of 85 angles were placed on the beam equivalent to a weight of 2125 lb Photos of the beam were taken for a photogrammetry analysis when the beam was unloaded and when fully loaded.

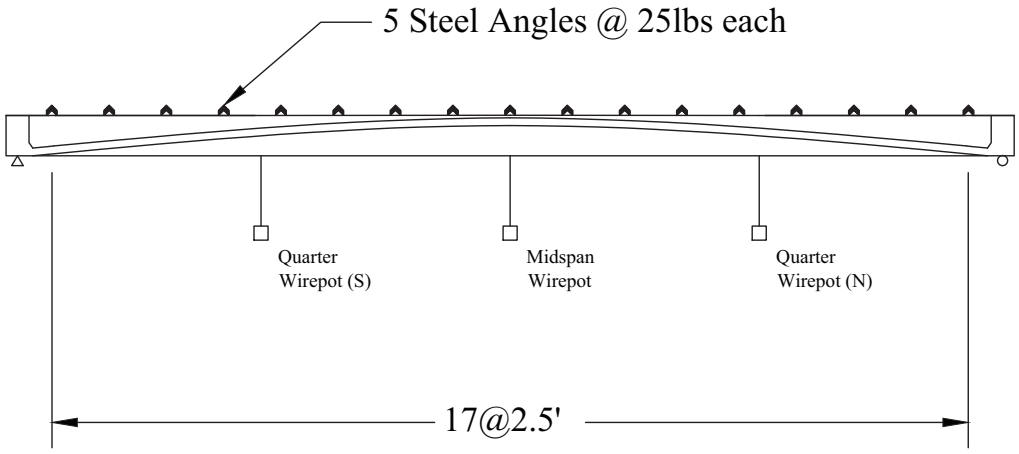

Figure 4-5 Placement of Steel Angles for Phase I Loading

The average distributed load applied was approximately 50 pounds per foot. For HCB 2 and 3 the tests were performed twice per beam. For HCB 1, the 85 angles were placed in one layer along the length of the beam. In addition to the uniformly distributed load tests, one point

load test was performed for each beam by stacking ten steel angles at midspan. The same instrumentation as the distributed load testing was used.

4.3. Preparation for Phase II

At the conclusion of Phase I, the shear reinforcement was placed in the beams. Along the length of the beam a total of 50 stirrups were placed at 45 degrees in pre-drilled holes (Figure 4-6).

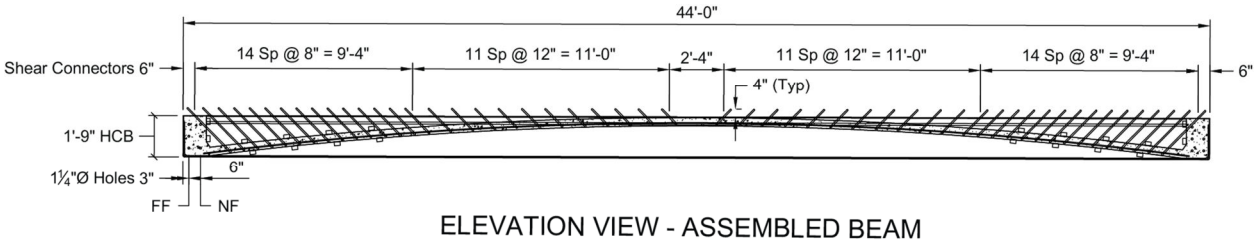

Figure 4-6 Elevation View of Shear Connectors

The projection of the stirrups above the top surface of the HCB was specified as 4 inches (Figure 4-6). In some cases, the shear connectors extended more than 4 in. due to obstructions from the FRP cross ties. To ensure the stirrups maintained this distance during the concrete pour, wooden blocks with reinforcement running in the longitudinal direction were placed underneath the shear connectors (Figure 4-7).

Figure 4-7 Reinforcement Tied to Shear Connectors

In addition to the placement of the shear connectors, plywood caps were installed at all holes on the FRP lids (Figure 4-8). The plywood caps prevented the concrete from overflowing through the holes (Figure 4-9). Drywall screws were screwed into one corner of the cap and into the FRP lid. A hole for another screw was predrilled at the opposite corner of the plywood piece, but the screw was not attached. The caps were rotated so that the holes were open. During the arch pour, when concrete reached the top of the lids, the cap was rotated so that the hole was completely blocked. The screw was then inserted and drilled in the pre-drilled hole in the cap and into the FRP lid. The wires from the concrete vibrating wire gages ran through the pour and vent holes at a number of locations. Finally, the reinforcement to tie the HCB's to the diaphragms was installed through predrilled holes at the beam ends (Figure 4-10). No. 4 bars with 90° bends were used.

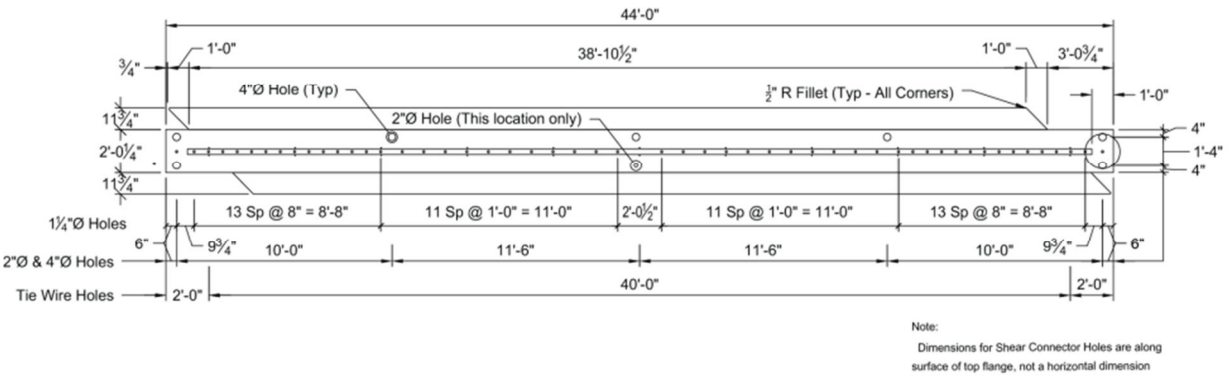

Figure 4-8 Hole Locations in Lid of FRP

Figure 4-9 Plywood Cap at End of HCB

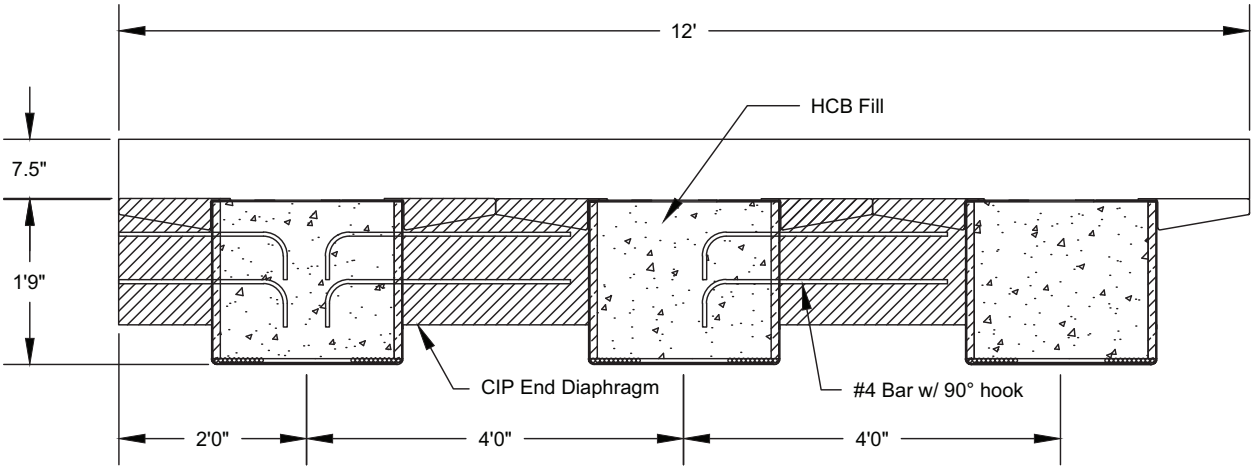

Figure 4-10 Cross Section of HCB System at North End

HCB 1 was place on a pin and roller, and HCB 2 and 3 were placed on bearing pads during the concrete placement. Data from strain gages attached to the FRP box and prestressing strand of HCB 1 was recorded during the arch pour. In addition, the concrete vibrating wire gages were connected to a data logger. This system was set to record strain and temperature in the concrete. For the arch pour, a concrete pump was used to pump the concrete into the HCB's (Figure 4-11).

Figure 4-11 Concrete Pump Used for Arch Pour

Each HCB had seven holes in the top flange that were used for filling. Concrete was first pumped into one of the quarter point holes (Figure 4-12). The concrete flowed down the arch channels to the voids at the ends of the arch. The concrete level at the end of the arch was observed through the vent holes. Once the concrete reached the top surface of the beam, the plywood caps were closed and screwed (Figure 4-13). Concrete pumping was continued for a short while to build up some pressure and force the concrete to go up the arch channel. The pump was stopped and the hose was moved to the quarter point on the opposite side of the beam. The process was repeated for the other half of the beam. The remaining holes were monitored; as soon as the concrete appeared to reach the surface of the FRP lid, the plywood caps were closed and screwed. Typically, the beams were "topped off" at the hole at the midspan. Once the concrete reached the surface of the lid, the plywood cap was closed and screwed. This process was repeated for the other HCB's. The HCB's were allowed to cure over a period of 28 days. Because the concrete was encased in the FRP box of the HCB's, they were not moist cured.

Figure 4-12 Concrete Pumped into Hole at Quarter Point

Figure 4-13 Plywood Caps Sealed at HCB End

4.4. Phase II Testing

Phase II testing occurred after the arch concrete was placed and had time to gain strength. The purpose of phase II was to investigate behavior of the individual HCB. The beams were placed on pin and roller boundary conditions as were used in phase I. Because, the FRP lid had a channel along the centerline of the beam, it was necessary to place plaster in the channel to provide a level surface for the load to bear on (Figure 4-14). A load frame was erected at the midspan of the beam. A 100-ton actuator was placed in the load frame so that it would bear on the centerline of the beam at the midspan. The actuator was connected to a hydraulic pump that was operated with a simple remote consisting of load and unload buttons.

Figure 4-14 Plaster Placed in Channel of HCB

For phase II testing, the same strain gage layout used on the FRP box for HCB 1 was used for HCB 2 and HCB 3. In addition to the instrumentation in phase I, concrete vibrating wire gages placed in the concrete arch were monitored. LVDT's were also place at the north quarter point and midspan of HCB 1 to measure the relative displacement of the arch to the FRP box. The concrete vibrating wire gages used a different data acquisition system than the other instrumentation for the test setup. Because of limitations of software, the secondary data system was set to record at 50 Hz while the primary system was set to record at 10 Hz. The data files were processed after testing to reduce the frequency to 5 Hz. A signal was necessary to synchronize the two data acquisition systems. This task was accomplished by using a clicker. The clicker consisted of a small specimen of aluminum that had two strain gages attached at the center of the specimen (Figure 4-15). One of the strain gages was hooked up to the primary system and the other was hooked up to the secondary system.

Figure 4-15 Clicker used to Synchronize Data Systems

When a test started, both systems were set to record, and the clicker was bent to create a spike in the data. After testing finished, a program was written to find the spike in the data files and use the corresponding index as the first entry in a new, processed data file. The data "spikes" were used to merge and synchronize the two data files.

Each beam was tested twice with a 15 kip point load at midspan and twice with two 12.5 kip point loads (25 kip total) at quarter points applied using a spreader beam (Figure 4-16). For the quarter point tests, small W shapes were used to set the spreader beam on top of the shear connectors. This was necessary because the shear connectors projected 4 in. from the top of the beam and would have interfered with the loading. The beams were loaded in 5 kip increments.

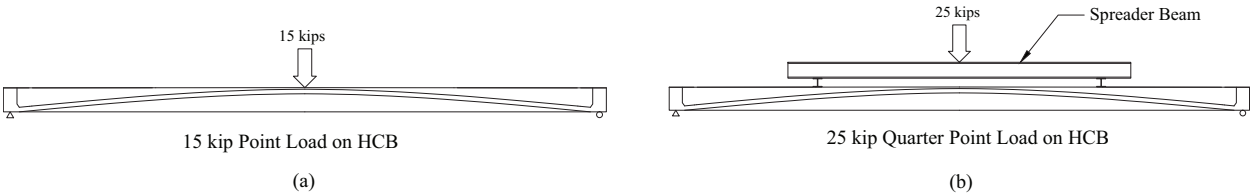

Figure 4-16 Phase II Loading Schemes

4.5. Preparation for Phase III Testing

At the conclusion of phase II testing, preparations began for phase III testing which consisted of the three-girder bridge system on a forty-five degree skew. Both the end diaphragms and the deck reinforcement layout imitated the actual reinforcement layout to be used in Tide Mill Bridge. End diaphragms were constructed before the deck. Both concrete placements consisted of the standard A4 mix used by VDOT in deck designs.

In preparation for the diaphragm concrete placement, all the HCB's were aligned with the strong floor and the simulated abutments and placed in their final positions on pins and rollers (identical to those used in previous phases of testing). 1 in. tall 1 in. diameter steel disks were placed between the bottom surface of the beam and the pin supports. These disks were used as place holders for load cells that were installed at a later time. The disks were also placed at the end of the beam with the rollers to keep the beams' elevation equal at each end. A 1 in. thick bearing plate was used between the disks and the bottom of the beams to prevent local bearing damage. The reinforcement extending out of the beam ends was bent at a forty-five degree angle to match the angle of the end diaphragm. Because of the large weight of the three-girder system, it could not be easily moved after the deck was cast. Thus, it was crucial the beams were as closely aligned as possible. The diaphragms were 16 in. deep whereas the beam height was 21 in. The bottom of the formwork was raised and supported from the support beams by approximately 1 ft. This distance accounts for the height of the pins or rollers, steel bearing plates, steel disks, and the 5 in. offset of the diaphragms. The diaphragm reinforcement was placed afterwards. The diaphragm shape varied for the south and north ends, but the reinforcement layout was similar (Figure 4-17 & Figure 4-18). The diaphragm reinforcement consisted of longitudinal bars that

were placed at the skew angle and transverse reinforcement that were hoops and hooks. The resulting reinforcement layout is show in Figure 4-19.

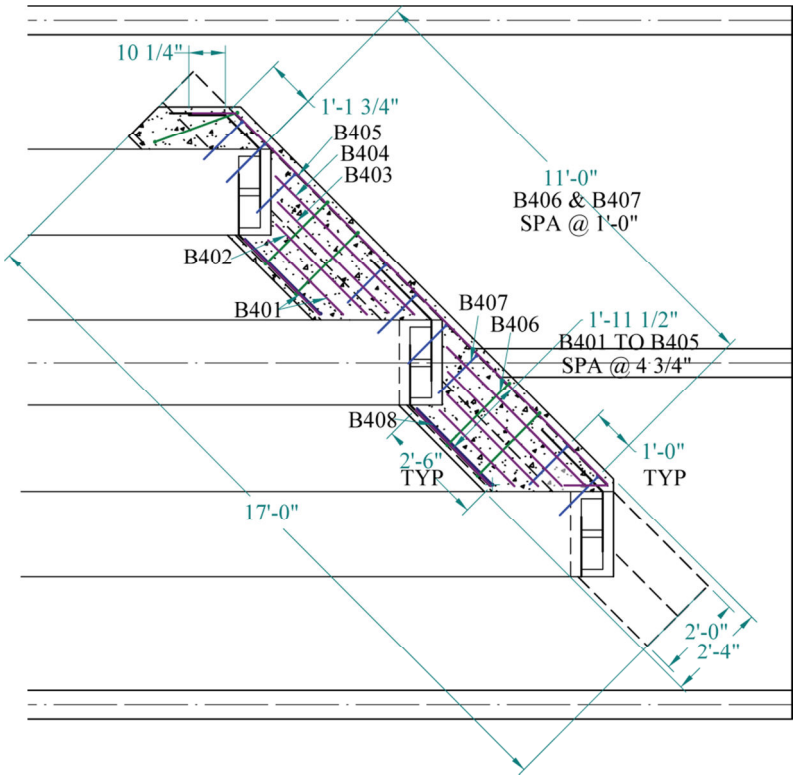

Figure 4-17 Plan View of Diaphragm at South End

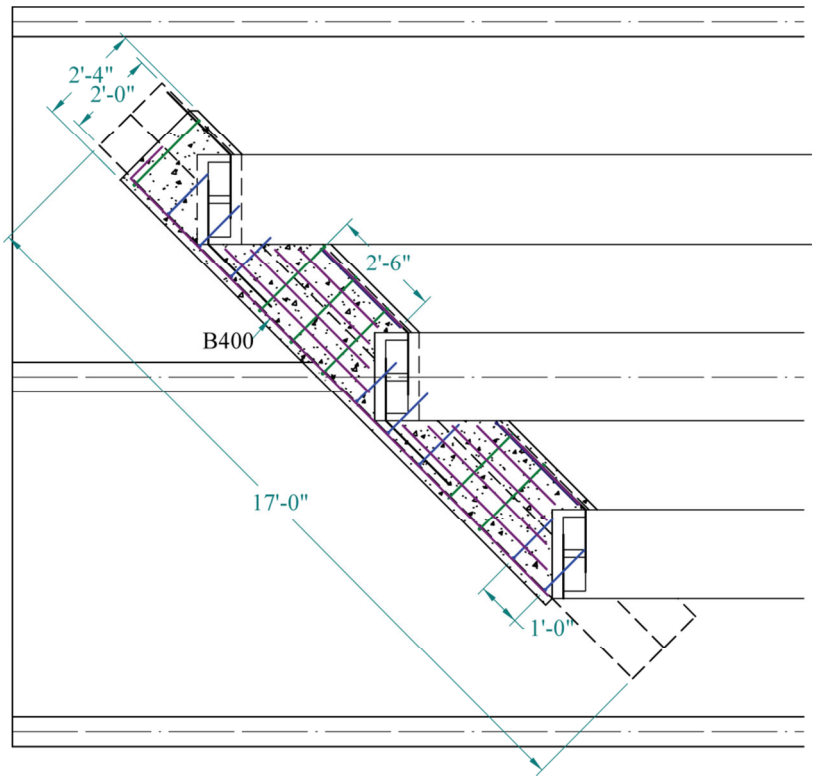

Figure 4-18 Plan View of Diaphragm at North End

Figure 4-19 Diaphragm Reinforcement

An A4 concrete mix (typically used by VDOT) was used for the diaphragms (Table 4-1, VDOT 2007), and vibrators were used to aid in the consolidation of the concrete. After concrete was placed at either side, a smooth finish was applied. Before the concrete set, a rake was used to

roughen the surface (Figure 4-20). This was done to improve the interface between the diaphragm and deck concrete. The diaphragms were moist-cured under burlap and plastic tarps for seven days. Erection of the deck formwork initiated after this seven day period.

Table 4-1 A4 Concrete Mix Design (VDOT 2007)

Class of Concrete	Design Minimum Laboratory Compressive Strength at 28 Days (f'c) (psi)	Aggregate Size No.	Nominal Max. Aggregate Size (in.)	Minimum Grade Aggregate	Minimum Cement Content (lb./yd³)	Maximum Water (lb. water/lb. cement)	Consistency (in. of slump)	Air Content (%)
A4 General	4,000	57	1	A	635	0.45	2-4	6 1/2 ± 1 1/2

Figure 4-20 Roughened Diaphragm Surface

The formwork for the diaphragms was kept on after the seven day moist cure so that the deck formwork could be extended off of the existing formwork. Before erection of the deck formwork commenced, tape was used to seal the longitudinal joints between the beams. The formwork walls were erected before the deck reinforcement was placed. Along the span of the beams, the deck was set back by 7 in. from the edge of the beam flange to allow space for formwork (Figure 4-21).

Figure 4-21 Deck Side Walls

The deck reinforcement design and layout followed standard design practices employed by VDOT. The HCB's were treated as very flexible beams, and a 7 in. spacing was used for the transverse reinforcement (Figure 4-22). In the corners of the skewed deck, top and bottom straight transverse reinforcement was used, and the reinforcement lengthened as the deck width gradually increased. For the full width portions of the deck, the transverse reinforcement consisted of alternating truss reinforcement and top and bottom reinforcement. Two mats of longitudinal reinforcement were used (Figure 4-23). The bottom mat consisted of seventeen forty foot No. 4 bars spaced according to Figure 4-23. For the acute angles of the skewed deck, additional reinforcement was placed in two layers at a forty five degree angle to match the angle of the skew. Fourteen longitudinal bars were used for the top mat.

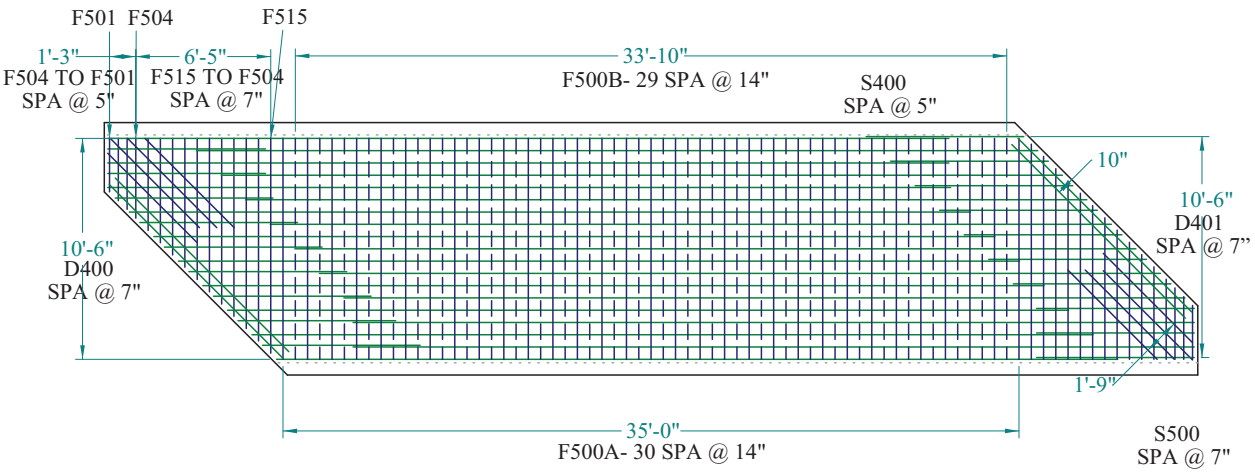

Figure 4-22 Deck Reinforcement Layout

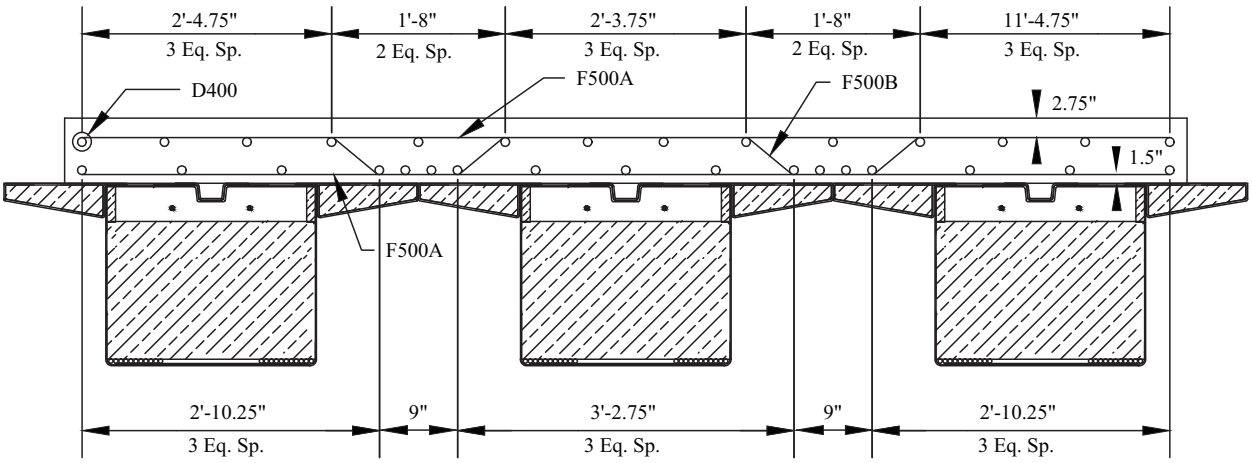

Figure 4-23 Deck Cross Section

An additional layer of steel was placed at one end of the deck to allow for the setup to be moved temporarily to place load cells in the place of steel disks. The steel was placed to account for negative moment that would be created by lifting the end of the setup upward. The reinforcement consisted of five No. 6 bars. To allow for the future removal of the entire deck and beam system, holes were drilled in the beam flanges to place PVC piping. Anchor rods are to be fed through the pipes and used in conjunction with HSS sections to lift the entire system.

Because the volume of concrete for the deck was large, two trucks were used for the concrete placement in the deck. As the last of the first truckload was placed, screeding

commenced at the midpoint of where the first truckload of concrete was placed; the screeding progressed towards the northern end (Figure 4-24). Locations where the PVC pipe extended out of the deck were left unscreeded and finished by hand (Figure 4-25). The surface was finished with a bull float and then lightly brushed.

Figure 4-24 Screeding of Deck

Figure 4-25 Finishing Done by Hand and Bullfloat

The second truckload arrived approximately 2 hours after the first truck arrived and half an hour after the last of the first truckload was placed. In order to reduce the influence of a cold joint where the two truckloads would meet, the concrete at the end of the first load was vibrated to reduce the amount of setting (Figure 4-26). The placement of concrete then shifted to the southern end of the setup and proceeded towards the midspan as was done with the first truckload. The surface was finished in the same manner as the northern end. Once all finished had been completed, wet burlap and a plastic tarp were laid over the deck. The burlap was remoistened every day for a 21 day period. During material testing of the second batch of concrete, the compressive strength was determined to be less than first batch. Thus moist curing was used for 21 days instead of the typical 7 days.

Figure 4-26 Edge of First Concrete Truckload

After the deck concrete reached strength, load cells were placed underneath the north end of the three HCB's. The north end of setup was jacked up using 11 in. actuators. Two actuators were placed between each of the beams (Figure 4-27). The actuators were to bear on the bottom diaphragm surface. A steel plate was placed between the actuator and the diaphragm surface to

increase the bearing area. The actuators were used to jack the north end of the test specimen up 1 in. The steel disks were removed and replaced with the six constructed load cells. In some locations shim plates were necessary to ensure the HCB's remained level. After the placement of the load cells, the test specimens were ready to test.

Figure 4-27 Actuators Placed under Diaphragm

4.6. Phase III Testing

After the deck achieved adequate strength, phase III testing commenced. Testing was configured to represent service loadings on Tide Mill Bridge. A total of 17 tests were performed using eight load configurations. Two tests for each loading configuration were run. The service loads for tests 1-12 represented the rear axles of a HL-93 truck bearing on four representative tire patches. 70-durometer neoprene bearing pads were arranged in a 9 in. x 18 in. patch at each load point on the concrete deck (Figure 4-28). Steel plates ½ in. thick were placed over the pads to ensure load distribution across the patch. The patches were spaced at 14 ft longitudinally and 6 ft transversely. The spreader beams were placed over the steel plates to load the patches evenly.

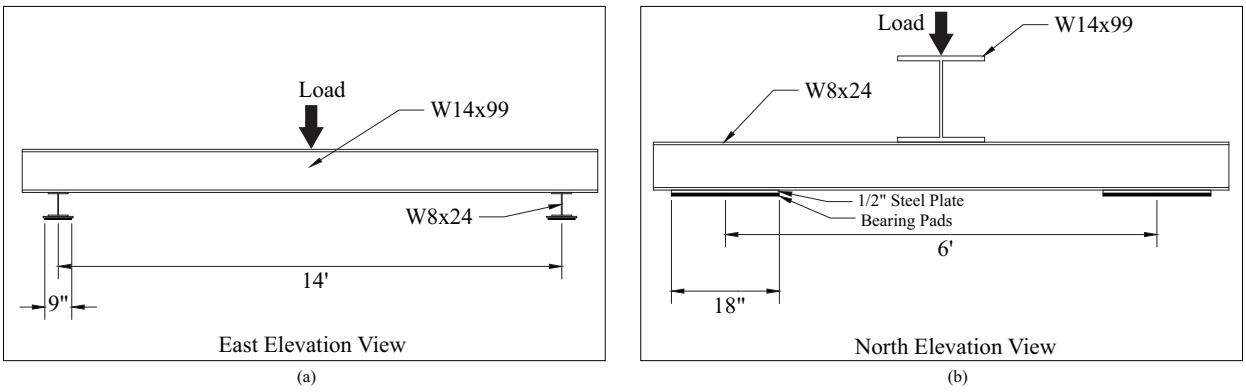

Figure 4-28 Loading Configuration

The loading magnitude was calculated by taking the weight of two rear axles of a HL-93 Truck (64 kips) and multiplying by the Dynamic Load Factor of 1.33. The resulting load was 85.12 kip which was spread equally among the four points. The loading locations were placed to generate high moment and shear (Figure 4-29). Detailed drawings of the location of the load patches can be found in Appendix D. For the first two tests, the load frame was centered longitudinally over the entire bridge setup. The spreader beams were placed so that the west wheel line was directly above the centerline of HCB 1. For the next two tests, the spreader beams were moved east 1 ft so that the two wheel lines straddled HCB 2. The next two tests had the east wheel line directly over the centerline of HCB 3. The next six tests were conducted to generate high shear in the test setup. The wheel lines were placed in the same transverse locations as the tests for high moments. The loads were placed so that the patches were as close to the supports as allowed by the lab layout.

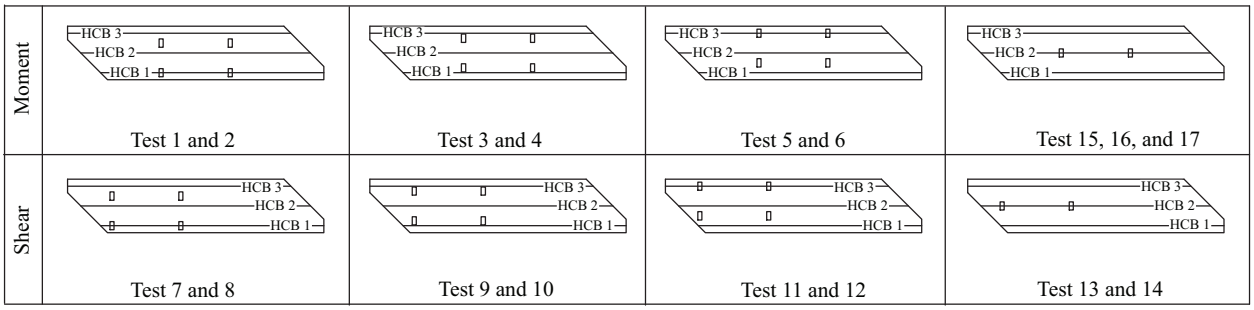

Figure 4-29 Phase III Loading Configurations

After the axle tests were concluded, four tests were conducted to represent one wheel line that was placed directly over the centerline of HCB 2. The shear tests were performed so that north patch of the wheel line was as close as allowed by the lab layout. Two moment tests were conducted with the wheel line centered over the midspan of HCB 2 and over the centerline of HCB 2.

After reviewing data for phase III testing, it was determined the moment distribution between the three girders was approximately equal (0.33). The model for Tide Mill Bridge used a distribution factor of 0.6 which was derived from the AASHTO Specifications for an exterior concrete box beam. After applying the experimentally determined distribution factor, it was determined the applied loading during phase III testing was approximately 50% of the service live load used for design calculations. Because the evaluation of the test system under full load was crucial prior to the construction of Tide Mill Bridge, an additional test was necessary to apply the higher moment. The test setup was nearly identical to the single wheel line tests discussed above (ST15 and ST16). A different spreader beam was used to be able to apply the higher loads. DEMEC points were adhesively bonded to the top surface of the deck as close to the midspan of HCB 2 as possible. Because of the presence of the spreader beam, the points were off-center from the beam centerline. The system was loaded in the following increments: 50 k, 100k, 120k, 140k, 150k, 160k, 170k, 180k, 190k, 195k, and 200k. The loading increments were

chosen so that the system could be carefully monitored during testing and permanent deformation in the system avoided.

5 Results and Discussion

The following chapter discusses results from the three phases of testing. The first phase consisted of testing the individual hybrid-composite beams without the arch concrete in place. The second phase involved testing of individual HCB's with the arch concrete in place. The third and final phase of testing consisted of testing three HCB's constructed in a skew bridge setup complete with end diaphragms and a cast-in-place deck. Results from material testing are also included.

5.1. Material Testing

Material testing was performed for each of the concrete components of the setup and a sample of strand used in the HCB. The concrete components consisted of the arch, diaphragms, and deck. Because the deck concrete placement consisted of two different concrete batches, a set of cylinders was made for each batch. Testing for the concrete components consisted of compressive strength, splitting tensile strength, and modulus tests performed on 4 in. by 8 in. cylinders. Testing for the strand consisted of determination of a calibration factor between strains on an individual wire to force in a 4 ft sample of prestressing strand.

5.1.1. Concrete Cylinder Testing

Concrete testing was performed based on established ASTM procedures. The compressive strength test followed ASTM C 39 - 05. Splitting tensile tests were performed based on ASTM C496 – 04, and modulus tests were based on ASTM C469 – 02. Cylinders were prepared from each respective component on the day of concrete placement. The arch concrete cylinders were cured within an environmental chamber where temperature and humidity were controlled. The diaphragm and deck cylinders were placed near the test setup to cure. These cylinders were expected to cure under similar conditions to the test specimens rather than conditions in the environmental chamber. Tensile tests were performed at 28 days and at the beginning of testing for each phase. Results from testing are presented in Table 5-1, Table 5-2, and

Table 5-3. Repetitions of testing are shown in parentheses. The presented results are averages for the cylinders tested. In general, the compressive strength of each component either reached or was close to specified strength of 5 ksi for the arch concrete and 4 ksi for the deck concrete. The strength of the arch concrete showed the greatest variation, and the cause is explained later in this section. Variation in the moduli of elasticity was observed. The collar used to read deformation in the cylinder may have given erroneous readings during some of the tests.

Table 5-1 Material Testing Results for Arch Concrete

	Experimental			AASHTO Design Values		
Day	Compressive Strength	Tensile Strength	Modulus of Elasticity	Compressive Strength	Tensile Strength	Modulus of Elasticity
7	5120 psi (3)	-	-	-	-	-
14	5360 psi (3)	-	-	-	-	-
28	6190 psi (3)	634 psi (2)	4480 ksi (2)	6000 psi	563 Psi	4458 ksi
45	5680 psi (3)	604 psi (2)	3900 ksi (2)	-	-	-
206	5910 psi (2)	518 psi (2)	3820 ksi (2)	-	-	-

Table 5-2 Material Testing Results for Diaphragm Concrete

	Experimental			AASHTO Design Values		
Day	Compressive Strength	Tensile Strength	Modulus of Elasticity	Compressive Strength	Tensile Strength	Modulus of Elasticity
7	4180 psi (2)	-	4480 psi (2)	-	-	-
14	4360 psi (3)	-	4680 psi (2)	-	-	-
28	4870 psi (2)	545 psi (2)	5250 psi (2)	4000 psi	460 Psi	3640 ksi
61	5730 psi (2)	460 psi (2)	4390 psi (2)	-	-	-

Table 5-3 Material Testing Results for Deck Concrete

		Experimental			AASHTO Design Values		
Day	Batch	Compressive Strength	Tensile Strength	Modulus of Elasticity	Compressive Strength	Tensile Strength	Modulus of Elasticity
7	Batch 1	3460 psi (2)	-	3890 psi (2)	-	-	-
	Batch 2	2690 psi (2)	-	3420 psi (2)	-	-	-

14	Batch 1	4400 psi (2)	-	4650 psi (2)	-	-	-
	Batch 2	3280 psi (2)	-	4000 psi (2)	-	-	-
21	Batch 1	4580 psi (2)	-	4620 psi (2)	-	-	-
	Batch 2	3440 psi (2)	-	4230 psi (2)	-	-	-
28	Batch 1	4480 psi (2)	525 psi (2)	4950 psi (2)	4000 psi	460 psi	3640 ksi
	Batch 2	3500 psi (2)	440 psi (3)	4390 psi (2)	4000 psi	460 psi	3640 ksi
40	Batch 1	4820 psi (2)	505 psi (2)	4700 psi (2)	-	-	-
	Batch 2	4060 psi (2)	430 psi (2)	6880 psi (2)	-	-	-

Segregation between the aggregate and cement was seen during placement of the arch concrete. Concrete directly from the truck was used to make the first cylinders. During the middle of the arch placement, another batch of concrete was taken from the truck to fill additional cylinders. Twenty four specimens were made for testing (Table 5-4). The concrete from the first batch appeared to segregate. The top layer of concrete appeared to have lower aggregate content and higher paste content (cement and fine aggregates) than lower layers. The degree of segregation varied for the cylinders made between the two extreme layers. The middle group of cylinders was made from bottom layer concrete from the first batch of the concrete. The last cylinders were made using the second batch which appeared to have a higher aggregate to paste ratio. The cylinders with low aggregate content typically performed worse than those with high aggregate content (Table 5-5). For each day of testing, cylinders were taken from the first and second batch to average the strengths and moduli. Day 45 represented the age of arch concrete at the start of phase II testing, and day 206 represented the start of phase III testing. Though the degree of segregation in each HCB's respective arch was not visible during placement, the concrete for the arch in HCB 3 was most likely to have the greatest degree of segregation because it was placed first.

Table 5-4 Specimen Mixture of Concrete Cylinders

Specimen Number	Specimen Mixture	Age (days)
#1	High Paste/Low Aggregate	7
#13	Medium Paste/Med Aggregate	7
#24	Low Paste/High Aggregate	7
#2	High Paste/Low Aggregate	14
#12	Medium Paste/Med Aggregate	14
#23	Low Paste/High Aggregate	14
#3	High Paste/Low Aggregate	28
#12	Medium Paste/Med Aggregate	28
#22	Low Paste/High Aggregate	28
#5	High Paste/Low Aggregate	45
#20	Medium Paste/Med Aggregate	45
#7	High Paste/Low Aggregate	45
#9	Medium Paste/Med Aggregate	206
#18	Medium Paste/Med Aggregate	206

Table 5-5 Compressive Strength for Arch Concrete Cylinders

	High Paste Content		Medium Paste Content		Low Paste Content		
Day	Specimen Number	Compressive Strength (psi)	Specimen Number	Compressive Strength (psi)	Specimen Number	Compressive Strength (psi)	Average
7	#1	3780	#13	5450	#24	6130	5120
14	#2	4380	#12	5370	#23	6330	5360
28	#3	6450	#12	6170	#22	5970	6197
45	#5	4300	#20	6760	#7	5970	5677
206	#9	5690	#18	6130	-	-	5910

5.1.2. Prestressing Strand Calibration

In addition to the concrete cylinders, testing was performed on a tension strand to determine the relationship between wire strain and strand force. As mentioned in section 3.2.1, the strain gages were applied to individual wires on the seven wire strand. The wires were wound helically around a central wire. Thus, strain measured in the wire is different than the overall strain in the strand. The test method used was similar to that used by Arrellaga et al (1993).

The test specimen consisted of a 4 ft sample of ½ in. diameter galvanized strand typical of that used in the hybrid composite beams for Tide Mill Bridge (Figure 5-1). The specimen was cut from the coil of strand to be used for beam fabrication. Four 1/8 in. adhesively bonded strain gages were placed on the strand. Gage 1 and 2 were placed at the center of the strand on different wires. The two additional gages were used to determine if the galvanized coating effected strain measurements. A 2 in. area was stripped of the zinc coating using diluted hydro-sulfuric acid. Gage 3 and 4 were attached to the bare steel in this region.

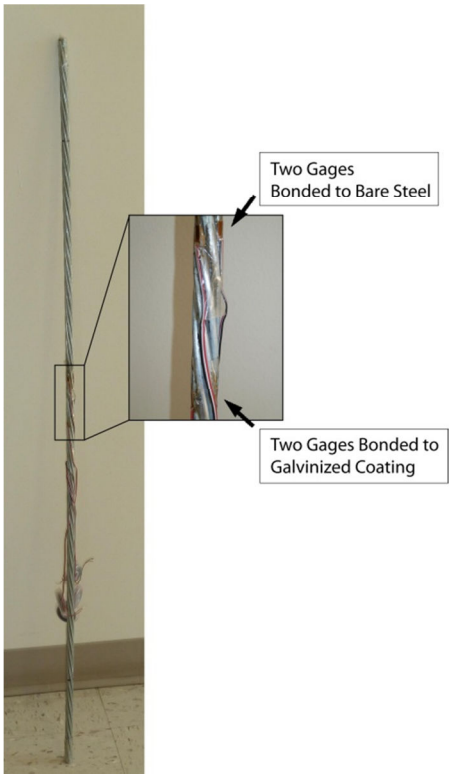

Figure 5-1 Strand Test Specimen

The test setup consisted of a universal test machine with a top and bottom crosshead (Figure 5-2). Load was read from the actuator load cell using a display on the pump control. The strain values were read manually using a readout box. Both the top and bottom crosshead had a through hole to place the strand (Figure 5-2). Prestressing anchors (commonly called chucks) were placed on either end of the strand. The length of strand between the anchors was 28 in. Half

of the yield load was used for the maximum applied load. This was to ensure the strand maintained linear-elastic behavior during testing. To eliminate effects of the curvature of the strand, a 4 kip force was applied to the strand before the gages and load cell were zeroed. The strand was loaded in increments of 2000 lb to provide data to form a load-strain relationship.

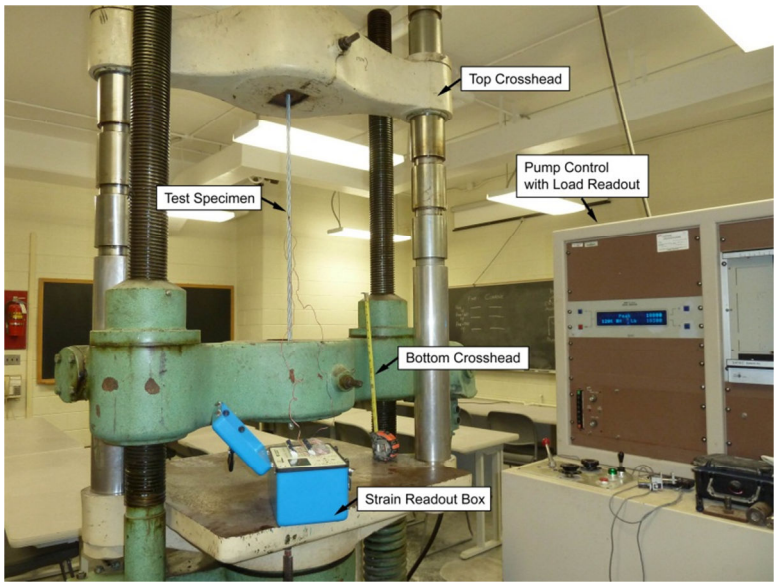

Figure 5-2 Strand Calibration Test Setup

Three tests were performed on the strand. The strand was slightly shifted after each test to determine if bearing conditions affected the strain measurements. Because of the helical nature of the strand, each wire may not be stressed equally; the anchors may have gripped some wires more than others. During the first test, gage 2 and 3 became debonded with the strand. Thus only data for gage 1 and 4 was used in the calculation of the conversion factor. The strain increased fairly linearly as the load was increased. Figure 5-3 represents the strain measurements from gage 1 and 4 for the three tests without strain and load measurements zeroed at 4 kips. The expected strains were calculated using the stress in the entire cross sectional area of the strand and using the modulus of elasticity of 28500 ksi. The slope of the load-strain relationship changed after the first load increment. Arrelaga et al noted this difference in slope in their testing

(1993). After the first increment, the slope appeared to stay the same. The strains for gage 1 and 4 were very close for tests 2 and 3 indicating the effects of the coating were minimal. Gage 1 and 4 were also attached to different wires, but showed similar strains (Figure 5-3). As Arrellaga et al noted, the strain values for the wires were expected to be slightly lower for the same load than the expected strand strain as was seen in Figure 5-3 (1993). With the exception of gage 1 for test 1, all of the results showed good agreement.

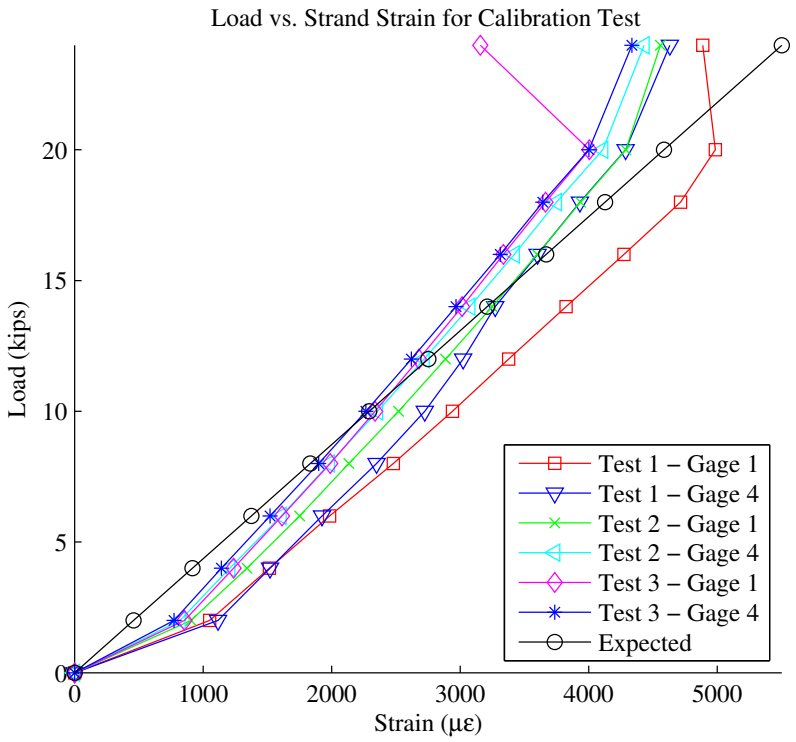

Figure 5-3 Load vs. Wire Strain for Test 2

Using the data from testing, a conversion factor was created to estimate strains in the overall strand. Table 5-6 presents average strains from the three tests and calculates an effective modulus for the stress and strain values at each load increment. The average modulus was calculated as 33600 ksi. The average modulus was markedly higher that the design value of 28500 ksi. The ratio of experimental modulus to design modulus was used to derive a conversion factor of 1.178. This factor was considerably higher than the average value of 1.05 seen in the

literature (Arrellaga et al 1933).The factor was used to multiply the measured strains for the wire to obtain strains for the strand.

Table 5-6 Experimental Modulus (with values zeroed)

Load (lbs.)	Stress (ksi)	Strain (με)	Modulus (ksi)
4000	0.0	0	-
6000	13.1	407	32200
8000	26.1	813	32100
10000	39.2	1220	32100
12000	52.3	1600	32700
14000	65.4	1960	33400
16000	78.4	2310	33900
18000	91.5	2670	34300
20000	105	3020	34800
22000	118	3360	35100
24000	131	3640	36000
Average Modulus			33660

However, it must be stated that there is inherent error in the calibration process. As Arrellaga et al discussed, the load-strain relationship is highly variable when the strand is subject to low stress (1993). This is due to the straightening of the strand as it becomes stressed. For the calibration tests, a 4 kip load was applied prior to zeroing the measurements. When the strands are placed in the HCB's, they are not prestressed, and any "straightening" effects are measured by the strain gages when the beams are loaded. Thus, conversions of the wire strains are only an approximation of the strand strains. Because the full extent of the "straightening" effects could not be determined, it was assumed that the self-weight of the beam removed these effects. The experimental values were multiplied by the conversion factor without any corrections to determine the overall strand strains.

5.1.3. Fiber-Reinforced Polymer Properties

Material properties provided by the manufacturer were used with Hillman's model (Table 5-7). The properties included modulus for both the 0° and 90° degree directions (0° was oriented along the span of the beam). Tensile and compressive ultimate stresses were also provided, though the compressive limit does not take buckling into account. Hillman believed the lateral ties would prevent buckling of the FRP webs and elastic buckling in the top flange was addressed by the inclusion of a small channel (Snape 2009). A limit for ultimate shear stress of 7.5 ksi was used rather than the value specified by the manufacturer. The limit was determined from experiments in previous studies (Hillman 2003).

Table 5-7 Material Properties for Fiber-Reinforced Polymer

Laminate Properties	
Resin Weight	0.54 lb/ft²
Fiber Weight	0.93 lb/ft²
Laminate Weight	1.47 lb/ft²
Volume Fraction	45% by Vol.
0° Modulus, Ex	3100 ksi
90° Modulus, Ey	2300 ksi
Shear Modulus	1010 ksi
0° Tensile Ultimate Stress	27.8 ksi
90° Tensile Ultimate Stress	20.6 ksi
Shear Ultimate Stress	19.1 ksi
0° Compressive Ultimate Stress	27.8 ksi
90° Compressive Ultimate Stress	20.6 ksi

5.2. Phase I Testing

After the individual HCB's were instrumented, the lids were glued on and the beams were ready for testing. At the time of Phase I testing, only the fiber-reinforced polymer box and the steel tension strand contributed to the stiffness of the beam; the concrete arch was not cast at

the time of testing. As mentioned previously, the loading for the first phase consisted of a uniform distributed load and a point load that were created using steel angles. For HCB 2 and HCB 3, each beam was tested twice with the distributed load and once with the point load. For these two beams, plateaus were clearly visible in the data for deflection and strain. This was due to the stacking of the steel angles in five layers at loading points. Values were recorded after each layer of angles was placed. For HCB1, one distributed load and one point load test were conducted. The load steps for HCB1 was not as discernible because the steel angles were placed in one layer across the length of the beam versus placing five angles at 17 load points used for HCB 2 and 3. Additional results for Phase I testing and arch placement data are presented in Appendix B.

5.2.1. Load-Deflection Behavior

In regards to the load deflection relationship, the HCB's were stiffer than the Hillman model predicted (Table 5-8). For the model, all concrete properties were set to zero. Thus the analysis only accounted for the stiffness of the FRP box and the steel strands. Moments at the tenth points were determined, and the corresponding values were used in the analysis. The calculated midspan deflection under a distributed loading was found to be approximately 0.41 in. From the test data, the average measured midspan deflection was 0.31 in. for the uniform loading (Table 5-8).

Table 5-8 Maximum Deflection for Phase I Testing

Test Number	HCB	Loading	Maximum Midspan Deflection (in.)	Predicted Midspan Deflection (in.)	Ratio
1	3	Distributed Load - 17 Load Pts.	0.33	0.41	0.80
2	3	Distributed Load - 17 Load Pts.	0.33	0.41	0.80
3	3	Point Load at Midspan	0.06	0.07	0.86
4	2	Distributed Load - 17 Load Pts.	0.29	0.41	0.71
5	2	Distributed Load - 17 Load Pts.	0.29	0.41	0.71
6	2	Point Load at Midspan	0.05	0.07	0.71
7	1	Distributed Load - One Layer	0.33	0.41	0.80
8	1	Point Load at Midspan	0.05	0.07	0.71

In the distributed load tests, the deflection was less than the predicted deflection. For HCB 2 and 3, the load versus deflection relationship was somewhat linear although the slope was not smooth. For example, for Test 4 of phase I, the load-deflection relationships at the north and south quarter points (WP -1 and WP-3 respectively) appeared to have slightly different slopes between each load plateau, but overall the relationship was close to linear (Figure 5-4). Additionally, the deflections at the north and south quarter points slightly differed; the deflections were predicted to be the same due to the symmetrically applied uniform loading.

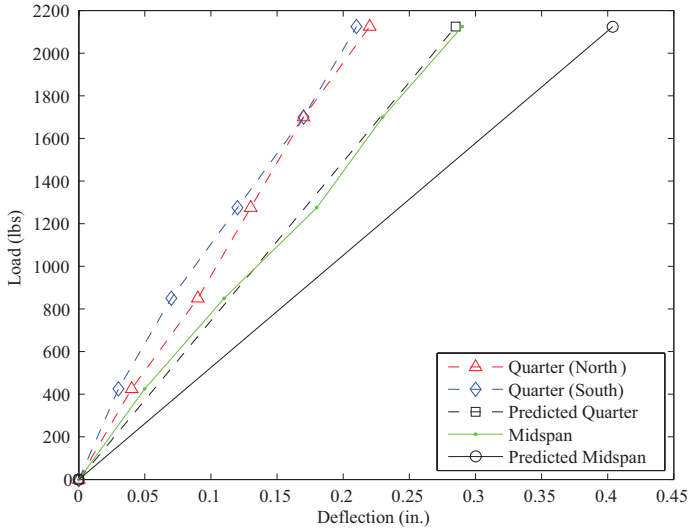

Figure 5-4 Load vs. Deflection for Test 4 (Uniform Load)

For the point load tests, deflections were also smaller than anticipated at both the midspan and quarter points. Test 6 was representative of the three point load tests conducted (Figure 5-5). There appeared to be a slight difference between deflections at the north and south quarter point; this may have been due to the accuracy of the potentiometers. Because only the maximum deflections were recorded for the point load tests, sufficient data was not available to determine if a linear load-displacement relationship was present for these tests.

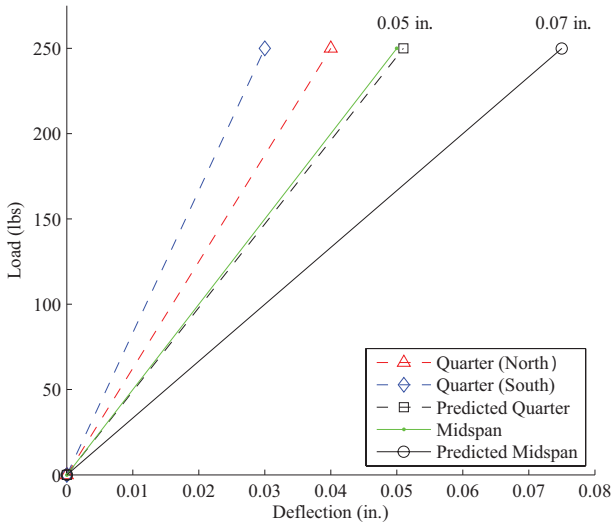

Figure 5-5 Point Load vs. Deflection for Test 6

In the above discussion, shear deformations were not included in the calculations of the predicted deflections. Hillman did not include shear deformations in his model, but his model was to be used for the HCB with the arch concrete in place or with both the arch concrete and deck concrete in place (Hillman 2011). Hillman only checked the stability of the FRP webs to ensure they did not buckle due to the pressure from the arch concrete placement. However, it is appropriate to include shear deformations in the expected value as the FRP is the main load carrying component for phase I and it has low shear stiffness. The inclusion of shear

deformations indicated that the Hillman model for Phase I would be even more conservative as the expected deflection would increase.

Shear deformations were accounted for by using the virtual work method typically used in structural analysis. Structural analysis using virtual work classically neglects shear deformation for steel and concrete structures and only uses flexural deformation. For the flexural term, the applied moment on the structure (M(x)) is used in conjunction with a virtual moment from a load applied at the location of interest ($M_v(x)$). Equations for the moments were determined in terms of x (the location along the span of the beam). Since midspan deflection was of interest, a virtual point load was applied at midspan. The two moment values are multiplied and then divided by the moment of inertia (I_b) and the modulus of elasticity (E). This term was then integrated over the length of the span (Eq. 4). To include the effects of shear deformation, an additional term was added to the flexural term. This term is similar to the flexural term. Instead of using applied moment and virtual moment, an applied shear (V(x)) and virtual shear ($V_v(x)$) are used. Equations for the shears were determined in terms of x (the location along the span of the beam). The two shear values are multiplied and divided by the shear area (A_v) and shear modulus (G). For the HCB, the shear area was taken as the area of the webs. This was in agreement with the area used for the shear limit state used by Hillman's model (Hillman 2011). The shear modulus was taken from the manufacturer's provided material properties. The equation was then integrated over the span of the beam (Eq. 5). The final equation consisted of the sum of the flexural term (Δ_f) and the shear term (Δ_v) to obtain the total deflection including shear deformation (Eq. 6).

$$\Delta_f := \int_0^{L_s} \frac{M(x) \cdot M_v(x)}{E \cdot I_b} \, dx \qquad \text{Eq. 4}$$

$$\Delta_v := \int_0^{L_s} \frac{V(x) \cdot V_v(x)}{G \cdot A_v} dx \qquad \text{Eq. 5}$$

$$\Delta := \int_0^{L_s} \frac{M(x) \cdot M_v(x)}{E \cdot I_b} dx + \int_0^{L_s} \frac{V(x) \cdot V_v(x)}{G \cdot A_v} dx \qquad \text{Eq. 6}$$

Including shear deformation in the deflection calculations showed that the observed deflections were smaller than predicted. Table 5-9 showed a noticeable increase in the deflection when shear deformations are included, but the ratio of observed values to the values calculated using virtual work was smaller than those observed when compared to Hillman's model. One explanation for the lower ratio was that the shear area taken for the HCB was conservative. Observations made by Waldron during review of literature were that the flanges may contribute to the shear area (2001). For the HCB, the flanges were expected to contribute to the flexural stiffness, and they may also be contributing significantly to the shear stiffness of the beams. Because the shear deformation and the flexural deformation of the HCB could not be uncoupled using the experimental data, the effects of shear deformation were unclear.

Table 5-9 Comparison to Deflections Including Shear Deformations

					Ratio	
Test Number	HCB	Maximum Midspan Deflection (in.)	Hillman Model (in.)	Virtual Work Calculation (in.)	Observed/ Hillman	Observed/ Virtual
1	3	0.33	0.41	0.44	0.80	0.75
2	3	0.33	0.41	0.44	0.80	0.75
3	3	0.06	0.07	0.09	0.86	0.67
4	2	0.29	0.41	0.44	0.71	0.66
5	2	0.29	0.41	0.44	0.71	0.66
6	2	0.05	0.07	0.09	0.71	0.56
7	1	0.33	0.41	0.44	0.80	0.75
8	1	0.05	0.07	0.09	0.71	0.56

The midspan deflections were used to calculate effective bending stiffness and moment of inertia and compared to calculated moment of inertia from the Hillman model. As mentioned previously the shear deformation cannot be differentiated from the flexural deformation, thus the shear deformation will be assumed to be negligible in the following calculations. An equivalent uniform load was calculated for the distributed load case with 17 point loads and used to calculate stiffness and moment of inertia at the midspan (Table 5-10). Because only the FRP and strand were contributing stiffness, the moment of inertia remained constant along the length of the beam and the use of the formulas was appropriate. These values were also calculated for the point load cases. The data showed differences in stiffness and moment of inertia between the three HCB's (Table 5-11). The measured moment of inertia was significantly higher than calculated from the Hillman model. In some cases the difference was as high as 53% and on average a difference of 36% was observed (Table 5-11). The measured values for the point load cases were found to be higher than those for the distributed load cases. The data suggests there may be additional components of the HCB shell that may be contributing stiffness. The Hillman model is shown to be very conservative in calculating the overall stiffness of the HCB shell.

Table 5-10 Stiffness Equations

	Bending Stiffness	Moment of Inertia
Distributed Load	$EI=\frac{5wL^4}{384\Delta}$	$I=\frac{5wL^4}{384\Delta E}$
Point Load	$EI=\frac{PL^3}{48\Delta}$	$I=\frac{PL^3}{48\Delta E}$

Table 5-11 Comparison of Measured and Calculated Stiffness at Midspan

Test Number	HCB	Measured Bending Stiffness (kip*in^2)	Measured Moment of Inertia (in^4)	Calculated Moment of Inertia (in^4)	Error
1	3	11500000	3720	3010	23%
2	3	11500000	3720	3010	23%
3	3	11900000	3850	3010	28%
4	2	13100000	4230	3010	40%
5	2	13100000	4230	3010	40%
6	2	14300000	4620	3010	53%
7	1	11500000	3720	3010	23%
8	1	14300000	4620	3010	53%
	Average	12600000	4090	3010	36%

The large differences between the predicted and observed values may be attributed to components of the HCB that were neglected when calculating the beam stiffness. In one such instance, the flanges of the HCB were completely neglected in calculation, though they may have contributed to the beam's moment of inertia. For phase I, they may have contributed significantly because the FRP and the steel strand are the only load-carrying components. Calculations were performed to include the flanges for section property calculations. The new moment of inertia was found to be 5080 in^4. The new section properties were much higher than both the predicted and experimental values. There may also be causes for reduction in the beams' stiffness which were unexplained. The channel in the top of the HCB may have also contributed to the moment of inertia. Additionally, the calculation sheet does not account for the stiffness of the foam that is used to form the conduit of the arch. Though the foam has a relatively low stiffness, it may have contributed to the beam stiffness during phase I testing.

The actual dimensions and makeup of the HCB may also affect the beam's stiffness due to difference between design and actual dimensions. One such difference may be due to the overlap of the glass fiber layers during the layup process. The overlaps were not continuous over the entire length of the beam. However, in the areas of overlap, the moment of inertia and the

modulus of elasticity may vary. Also unaccounted for was the buildup of resin during the infusion process. The tension strands near the bottom of the HCB were fully incased in resin, but this resin was not accounted for. The differences between the design dimensions and the as-built dimensions may have increased stiffness of the HCB's during phase I testing.

5.2.2. Behavior of Fiber-Reinforced Polymer

The behavior of the fiber-reinforced was expected to be linear elastic for phase I testing. Additionally, the FRP was expected to be the main load carrying component in the HCB because the arch concrete was not placed until phase II testing. Strains were only measured for HCB 1 because the FRP box of HCB 2 and 3 were not instrumented until the end of phase I testing. Also because a load cell was not used for phase I and load plateaus were not discernible, the load-strain relationship was not examined. The strains versus time plots were observed to note any unusual gage behavior. The gages mounted near the support were found to behave erratically and was not used for analysis. The measured strains were compared to predicted strains calculated using the transformed area approach.

The strains measured for HCB 1 were on average much smaller than the predicted strains (Table 5-12). Only the bottom flange gages showed strains close to or above the predicted strains. The magnitude of strains was small as was predicted due to the low loading. The data for the quarter point also showed measured strains to be smaller than predicted (Table 5-13).For some of the gage locations, a difference was shown between the east and west face of the beam. There was no clear pattern to the variation in strain measurement. For gage FQ-3 located on the bottom flange at the quarter point, a negative strain was observed. The strain was predicted to be positive indicating tension because of the location of the gage beneath the neutral axis. Closer examination of the strain gage data showed the following gages had irregular strain readings

during testing: FM-1, FM-2, FM-7, FQ-2, FQ-3, and FQ-5. These gages showed large spikes in strain reading or did not show a gradual increase in strain over time. The cause for the unusual behavior was unexplained.

Table 5-12 Comparison of Midspan Strains for Test 7

Location	Gage	Strain (με)		Ratio
		Measured	Predicted	
Top Flange - E.	FM-8	-136	-243	0.56
Top Flange - W.	FM-7	-89	-243	0.36
Top Web (14 in.) - E.	FM-1	-40	-139	0.29
Top Web (14 in.) - W.	FM-6	-81	-139	0.59
Bottom Web (7in.) - E.	FM-2	0	-34	0.01
Bottom Web (7in.) - W.	FM-5	-5	-34	0.15
Bottom Flange - E.	FM-3	81	70	1.16
Bottom Flange - W.	FM-4	71	70	1.02

Table 5-13 Comparison of Quarter Point Strains for Test 7

Location	Gage	Strain (με)		Ratio
		Measured	Predicted	
Top Flange - E.	FQ-8	-146	-179	0.81
Top Flange - W.	FQ-7	-116	-179	0.65
Top Web (14 in.) - E.	FQ-1	-77	-102	0.75
Top Web (14 in.) - W.	FQ-6	-91	-102	0.89
Bottom Web (7in.) - E.	FQ-2	23	-25	0.91
Bottom Web (7in.) - W.	FQ-5	11	-25	0.43
Bottom Flange - E.	FQ-3	-26	52	0.50
Bottom Flange - W.	FQ-4	36	52	0.69

Overall, the strains measured in the FRP box were observed to be less than the predicted strains in most cases. The transformed area approach appeared to conservatively predict the behavior of the FRP box. The behavior of the gages was discussed further in section 5.2.4 when discussing the strain profile.

5.2.3. Behavior of Prestressing Strand

Measured strains were found to be larger than predicted strain values from the transformed section approach used in Hillman's model. For phase I, one midspan strain gage for each beam was damaged. The damage may have occurred during the infusion process or shipment from the fabricator. All quarter point gages were operational as well as the additional gages at midspan. Predicted values were calculated using the transformed section approach and assuming strain compatibility between components in the HCB. The average measured strain in the tension strand at midspan was 60 με under uniform loading (Table 5-14) whereas the predicted strain was 45 με. In all cases, the measured strain was higher. The measured strains were on average 27% higher than the Hillman model.

Table 5-14 Maximum Prestressing Strand Strain for Phase I Testing

Test Number	HCB	Loading	Maximum Tension Strand Strain (με)	Predicted Tension Strand Strain (με)	Ratio
1	3	Distributed Load - 17 Load Pts.	61	45	1.36
2	3	Distributed Load - 17 Load Pts.	60	45	1.33
3	3	Point Load at Midspan	13	11	1.22
4	2	Distributed Load - 17 Load Pts.	59	45	1.30
5	2	Distributed Load - 17 Load Pts.	59	45	1.30
6	2	Point Load at Midspan	12	11	1.11
7	1	Distributed Load - One Layer	60*	45	1.33
8	1	Point Load at Midspan	13	11	1.22

*Corrected Data

In general, the predicted values were higher than measured strains. Test 4 was representative of all the distributed load tests conducted. The strains were greater than the predicted values, and the load-strain relationship remained fairly linear (Figure 5-6). Test 6 was representative of the point load tests and showed measured values were close to predicted values (Figure 5-7). Because only maximum strain was recorded, sufficient data was not available to analyze the load-strain relationship for the point load tests. One explanation for the higher

observed strains could be the higher location of the neutral axis compared to that used in Hillman's model. The neutral axis location will be discussed in the following section.

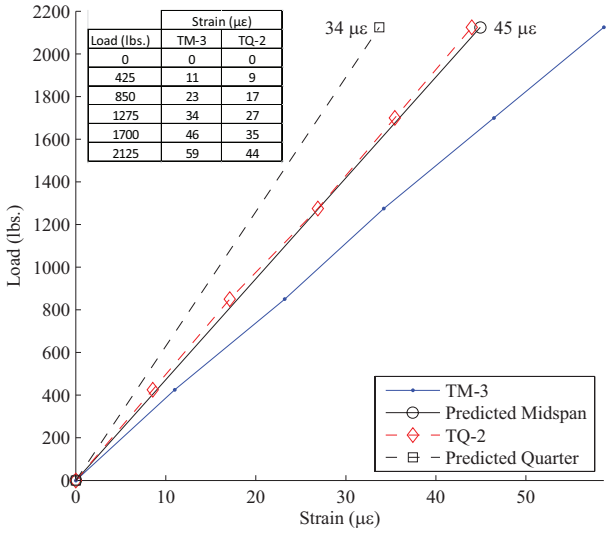

Figure 5-6 Load vs. Tension Strand Strain for Test 4 (Uniform Load)

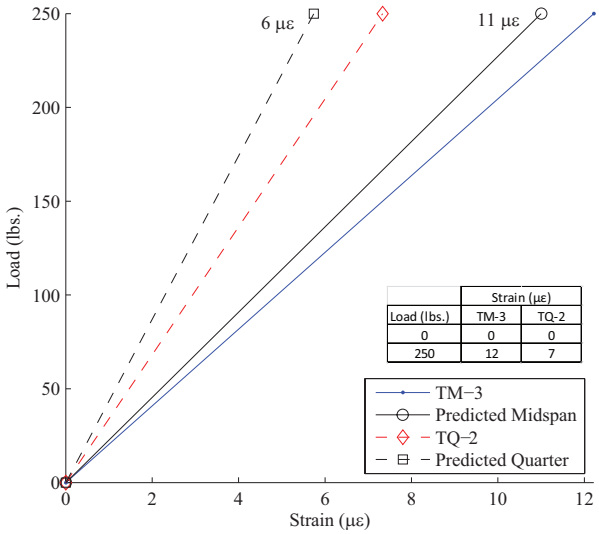

Figure 5-7 Point Load vs. Tension Strand Strain for Test 6

For each of the tests, the strain at the midspan was greater than at the quarter point. The calculated values supported this behavior because of the varying moment at each section. This approach assumed strain compatibility between the components. The test data suggests there is a

bond between the tension strands and the FRP shell. The bond may have been created during the infusion process in which the resin is drawn around the tension strands and the fiber layers. Phase I testing consisted of relatively small loads compared to service level loads, and the bond between these two components may have remained intact. Under higher loads, the bond between the two components may not remain intact.

5.2.4. Strain Profiles

For phase I, the FRP of HCB 1 was fully instrumented. Strain gages were placed at the midspan, quarter point, and near the support. Because the gages were placed at different depths at each longitudinal location, a strain profile could be generated from the data (Figure 5-8). Figure 5-8 shows the strain profile at the midspan under the full distributed load (2125 lbs.). The strain profiles for the east and west side of HCB 1 appear fairly linear although the profiles do not have a smooth slope. For each profile, the neutral axis appears to be located at a height of 7 in. from the bottom of the beam. This is markedly different from the location of the neutral axis at 4.69 in. found using the calculation sheets. As mentioned before, the flanges and the channel located in the top surface of the beam may have contributed significantly to the moment of inertia of the beam and thus shifted the location of the neutral axis upward. The neutral axis location including the added stiffness of the flanges was calculated to be 8.73 in. There may be unexplained causes for the reduction of section properties that may lead to a calculated location closer to the observed location. The upward shift could also have explained the higher measured strains in the strand than was predicted. Other than the location of the neutral axis there are a few other concerns from the strain gage data.

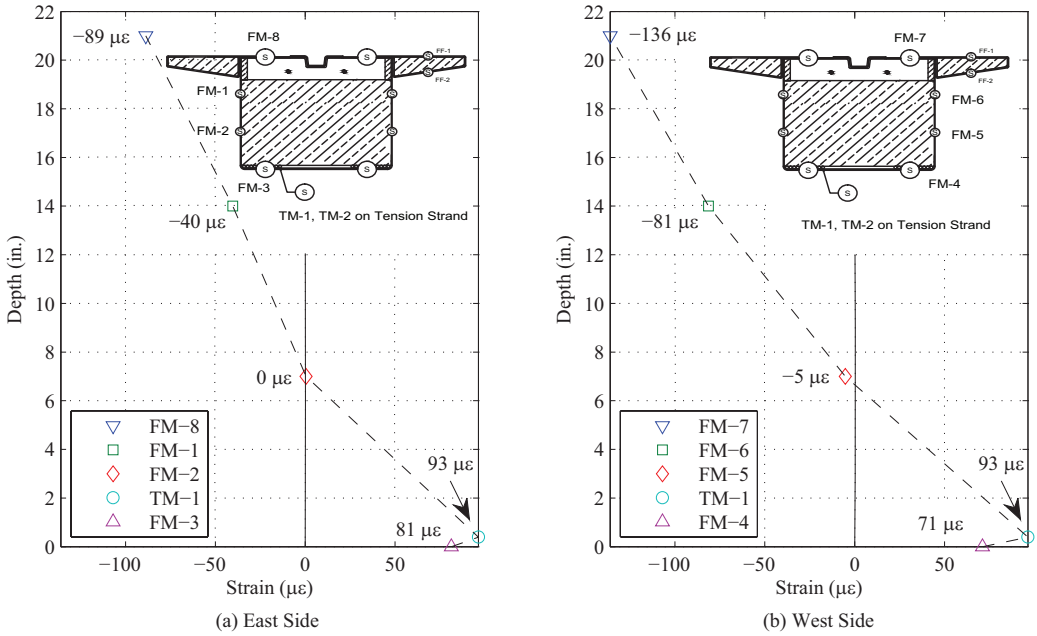

Figure 5-8 Strain Profiles for Test 7 at Midspan

Observing the plot of the strain profiles, a number of differences can be noticed between the east and west side of the beam. First, the magnitude of strain at the top surface of the beam varied. The registered strain in gage FM-7 was -136 με (Figure 5-8 (b)) compared to the strain of -89 με read by gage FM-8 (Figure 5-8 (a)). These two gages are placed symmetrically with respect to the cross section of the HCB and they are located at the same height. The difference suggests the beam is undergoing torsion under the loading. However, during Phase I testing, the angles were centered over the beam centerline as much as possible. The loading should have induced almost equal stress in both the east and west face. A number of factors may be responsible for the difference. The difference in the readings may have been due to imprecise placement of the steel angles. A poor bond in one of these two gages may also be an explanation for the difference. Additionally, the strain reading from TM-1 (a strain gage bonded to the tension reinforcement) creates a discrepancy between the gages bonded to the FRP on the bottom flange. The strain reading for TM-1 is 96 με compared to 71 με for FM-4 though FM-4 is located

slightly below TM-1 on the strain profile (Figure 5-8 (b)). The same behavior is seen for gage FM-3. Again, this may be related to poor bonding between gage and the component of interest. However, if poor bonding is not the reason for the discrepancy, the data suggests there is not a perfect bond between the tension strand and the FRP. The data from the quarter point can be used to observe if these occurrences are common or are local.

Observing the plots for strain profiles at the quarter points, there appear to be similar problems with the strain gages on the FRP (Figure 5-9). Unlike the gages at midspan, the profiles at the quarter point do not appear completely linear. The slope of the strain profile changes sporadically along the depth of the beam. There is no clear explanation for this behavior. Furthermore, the location of the strain profile has shifted upward to around 8 in. This shift may support the theory that the foam is contributing stiffness. At the midspan, the conduit for the arch is located at near the top of the beam. However, for the quarter point, the conduit is shifted down due to the parabolic nature of the arch. Thus, there is more foam towards the top of the beam which would increase the height of the neutral axis.

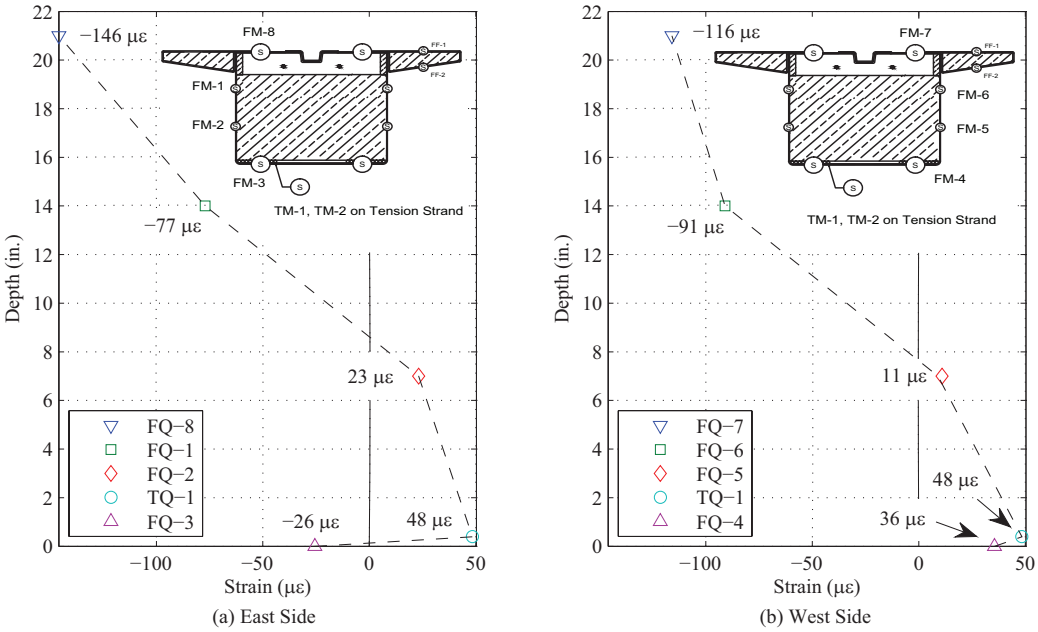

Figure 5-9 Strain Profiles for Test 7 at Quarter Point

As with the midspan location, strains from corresponding gages on the east and west side of the beam differed by a noticeable amount. Both the midspan and quarter point had higher measured strains on the west side of the HCB. Again, this behavior is suggesting unintended torsion induced in the beam, even though the loading was designed to cause only moment and shear into the beam. Though there is a difference in magnitude between the two profiles, the shape for each profile is similar with exception to the gages on the bottom of the beam. The strain reading from FQ-3 is negative (Figure 5-9 (a)) while the reading from FQ-4 was close to an expected positive value (Figure 5-9 (b)). The causes for the anomalies in the test data were unexplained.

Strain profiles for test 8, a point load at midspan, showed fairly linear behavior. The strain profiles for the east and west face at midspan have similar magnitudes of strain (Figure 5-10). Only the readings for gages FM-7 and FM-8 have a notable difference. At both the midspan and the quarter point the neutral axis location was observed to be close to 6 in. from the

bottom of the HCB. This was still greater than the predicted location of 4.69 in. The strain for the tension strand appeared to shift the slope of the strain profile. The strain profile for the east and west face at the quarter point appear to differ slightly in magnitude (Figure 5-11). As with test 7, the magnitude of strain appeared to be greater for the west face of the beam suggesting some form of torsion was induced in the beam. The profiles were linear for both midspan and quarter point. The strand in the strain was in good agreement with the strain in the bottom flange of the FRP. There appeared to be a small shift downward in the location of the neutral axis at the quarter point compared to the midspan. This behavior contradicted the observations made of test 7 in which the neutral axis was shifted upward at the quarter point.

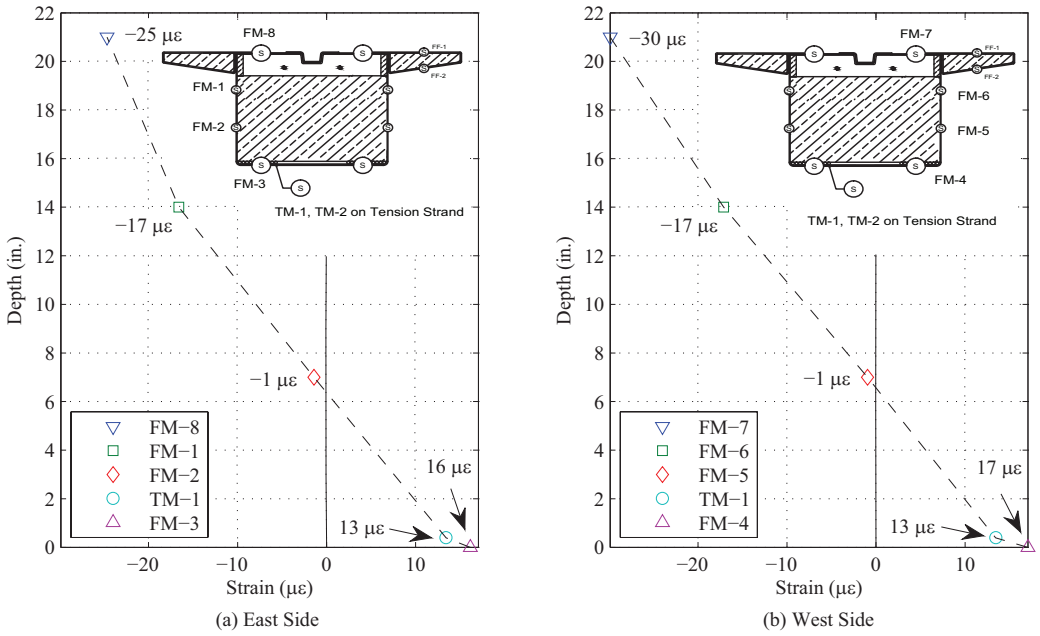

Figure 5-10 Strain Profile for Test 8 at Midspan

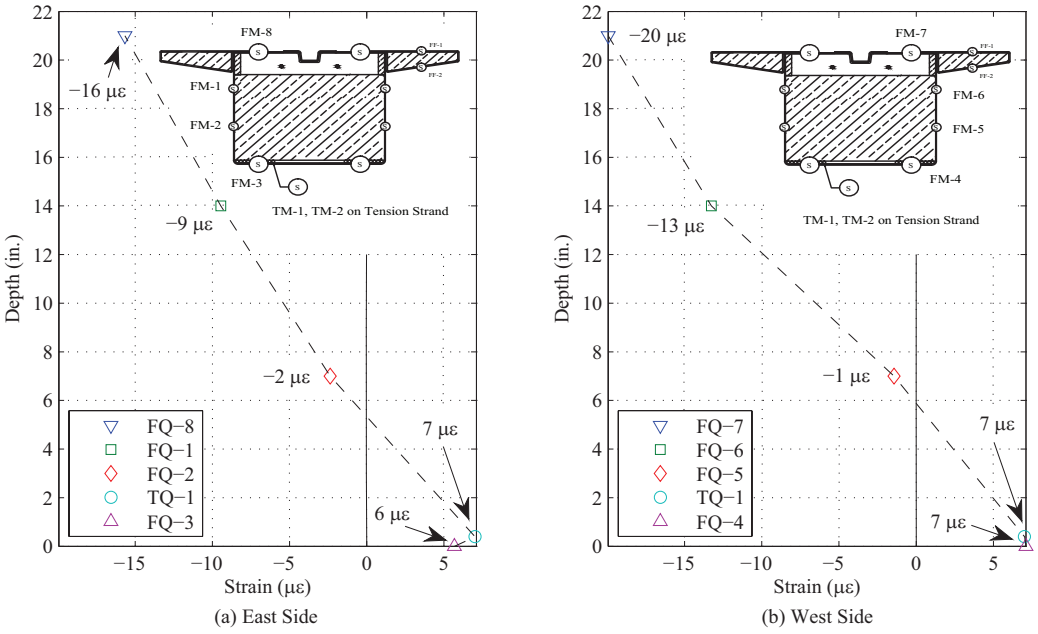

Figure 5-11 Strain Profile for Test 8 at Quarter Point

5.2.5. Summary of Phase I Results

Behavior of the FRP showed the transformed area approach was conservative in predicting strains except for the bottom flange in which the measured values were slightly above predicted values. The measured strand strain was higher than predicted. The strain profiles appeared to have a linear shape in most cases, but the measured neutral axis was higher than predicted. This may be a cause for the higher than expected strains for the FRP bottom flange and tension strand. Tension strand strain and FRP bottom flange strain were similar in most cases indicating strain compatibility existed between the two components.

5.3. Phase II Testing

After the concrete arches were cast and allowed to reach strength, phase II testing commenced on the three hybrid-composite beams. Two loading schemes were used for phase II: a point load applied at the midspan; and quarter point loads applied simultaneously at the north

and south quarter points. The magnitude of loading was determined using Hillman's model and setting the compressive stress limit in the concrete arch to $0.45f'_c$. This was to ensure the concrete remained within the linear-elastic range during testing. The planned test matrix consisted of two midspan point load and two quarter point load tests performed on each beam totaling twelve tests. Three additional tests were performed because data from the vibrating gages was not collected correctly. The data for all other instrumentation in these three tests were still usable. The test matrix is shown below in Table 5-15. Tests in which the vibrating wire gage data was not available are marked with dashes. Additional test results and estimated deck placement data are presented in Appendix C.

Table 5-15 Updated Test Matrix for Phase II Testing

Test Number	HCB	Loading	Location	Magnitude (kips)
-	1	Point Load	Midspan	15
1	1	Point Load	Midspan	15
2	1	Point Load	Midspan	15
-	1	Simultaneous Point Loads	North and South Quarter Points	12.5 each (25 total)
3	1	Simultaneous Point Loads	North and South Quarter Points	12.5 each (25 total)
4	1	Simultaneous Point Loads	North and South Quarter Points	12.5 each (25 total)
5	2	Point Load	Midspan	15
6	2	Point Load	Midspan	15
7	2	Simultaneous Point Loads	North and South Quarter Points	12.5 each (25 total)
8	2	Simultaneous Point Loads	North and South Quarter Points	12.5 each (25 total)
9	3	Point Load	Midspan	15
10	3	Point Load	Midspan	15
-	3	Simultaneous Point Loads	North and South Quarter Points	12.5 each (25 total)
11	3	Simultaneous Point Loads	North and South Quarter Points	12.5 each (25 total)
12	3	Simultaneous Point Loads	North and South Quarter Points	12.5 each (25 total)

5.3.1. Load-Deflection Behavior

The maximum midspan deflection values from phase II testing are presented in Table 5-16. Measured values fell within a relatively small range though differences were discernible.

For the point load tests, the deflections for test 2 (1.65 in.) and 9 (1.70 in.) were higher than the average measured midspan deflection of 1.59 in (Table 5-16). The difference was not large but there was no clear explanation for the discrepancy. The data for the quarter point load tests also showed good repeatability (Table 5-17). As predicted, the measured deflections for the quarter point load tests were higher than for the point load tests. The average measured deflection was found to be 1.77 in.; and all of the values fell between the range of 1.71 to 1.82 in. On average, the deflections for HCB 3 were higher than the other two beams suggesting a lower stiffness. For both loading types, the measured deflections were well below predicted values. The average difference between the two values was 0.52 in. resulting in an average ratio of 0.77 for measured to predicted deflection. Though the beams deflected less than predicted, the similar maximum midspan deflections suggested the behavior of the hybrid-composite beam is replicable.

Table 5-16 Maximum Midspan Deflection for Point Load Tests

Test Number	HCB	Loading	Maximum Midspan Deflection (in.)	Predicted Midspan Deflection (in.)	Ratio
-	1	15k Point Load at Midspan	1.56	2.11	0.74
1	1	15k Point Load at Midspan	1.54	2.11	0.73
2	1	15k Point Load at Midspan	1.65	2.11	0.78
5	2	15k Point Load at Midspan	1.59	2.11	0.75
6	2	15k Point Load at Midspan	1.53	2.11	0.73
9	3	15k Point Load at Midspan	1.70	2.11	0.81
10	3	15k Point Load at Midspan	1.57	2.11	0.74
		Average for HCB 1	1.58	2.11	0.75
		Average for HCB 2	1.56	2.11	0.74
		Average for HCB 3	1.64	2.11	0.77
		Average for All Beams	1.59	2.11	0.75

Table 5-17 Maximum Midspan Deflection for Quarter Point Load Tests

Test Number	HCB	Loading	Maximum Midspan Deflection (in.)	Predicted Midspan Deflection (in.)	Ratio
-	1	12.5k Point Load at Quarter Points	1.77	2.29	0.77
3	1	12.5k Point Load at Quarter Points	1.71	2.29	0.75
4	1	12.5k Point Load at Quarter Points	1.78	2.29	0.78
7	2	12.5k Point Load at Quarter Points	1.78	2.29	0.78
8	2	12.5k Point Load at Quarter Points	1.74	2.29	0.76
-	3	12.5k Point Load at Quarter Points	1.82	2.29	0.79
11	3	12.5k Point Load at Quarter Points	1.79	2.29	0.78
12	3	12.5k Point Load at Quarter Points	1.80	2.29	0.79
		Average for HCB 1	1.75	2.29	0.77
		Average for HCB 2	1.76	2.29	0.77
		Average for HCB 3	1.80	2.29	0.79
		Average for All Beams	1.77	2.29	0.77

Observing test data, the load-deflection relationship is shown to be linear in the majority of tests. Linear behavior was expected, as the magnitude of loading was chosen to keep the materials in the linear-elastic range and to prevent damage to the HCB's prior to phase III testing. Test 1 was typical of the load deflection relationship for point loading at midspan (Figure 5-12). The load-deflection relationship was linear while the unloading portion of the plot appears to be curved. This curvature in the relationship was likely due to the rapid return of the actuator head. The rate of loading was difficult to keep constant as the actuator loading was controlled manually rather than by a computer. As stated previously, the observed deflection for both the midspan and quarter points were well below the predicted values. The data showed that deflection of HCB1 returned to zero or very close to zero indicating no permanent deformations were induced.

Figure 5-13 shows the load relationship for Test 2 which had a relatively high midspan displacement compared to other tests as shown in Table 5-16. Overall, the deflections for Test 2 appear to be higher than those observed for Test 1. The average difference between maximum

displacements of the two tests was approximately 6%. This difference may have been due to a misalignment in the test setup. Test 2 was performed after the original twelve tests were completed. Thus the potentiometers and actuator had to again be placed in the appropriate locations. Slight differences in the location of these two components may have attributed to the different measurements observed. Otherwise, the same trends were observed for Test 2 as was seen in Test 1. The discontinuity in the unloading phase of the plot may have been due to the rapid unloading rate of the actuator as discussed previously.

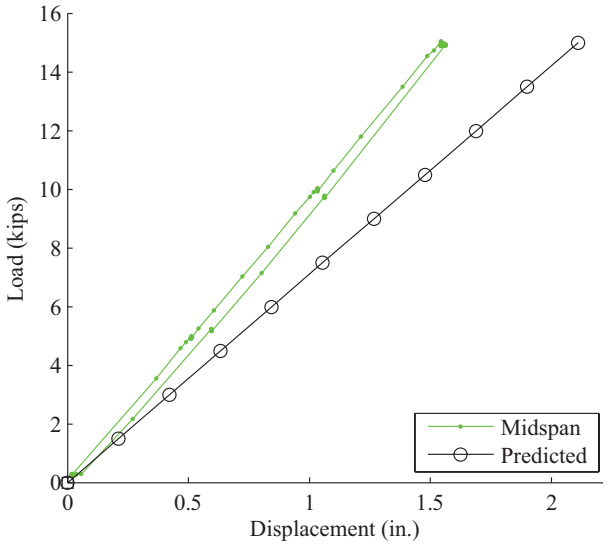

Figure 5-12 Load vs. Deflection Plot for Test 1

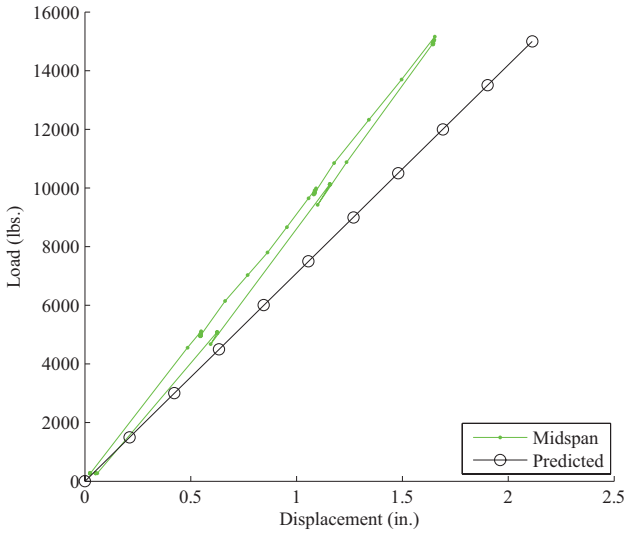

Figure 5-13 Load vs. Deflection for Test 2

Similar to the point loading, the load-deflection plot for the quarter point loading appeared to be linear and well below the predicted deflection for most tests. Test 3 was typical of quarter point load tests (Figure 5-14). Again the data showed a return to zero deflection once the HCB was fully unloaded indicating no permanent deformation. One test that was markedly different was Test 9 performed on HCB 3 (Figure 5-15). The load deflection relationship appeared to follow the predicted relationship closely up to a load of around 5 kips. The beam stiffness appeared to be lower than observed for other tests within this interval. For loads higher than 5 kips, the slope of the relationship increased for both the midspan and quarter points. The relationship represented an increase in stiffness at higher loads; the stiffness appeared to be the same as observed in other tests. This behavior was observed in both the loading and unloading phase of the plot. However, in the plot for the following test on the same beam (Test 10), the change in stiffness was not present (Figure 5-16). A slight change in slope was observed around a load of 8 kips, but the change was not as discernible as in Test 9. A possible reason for this shift may have been improper alignment of the actuator or spacer components between the

actuator head and the beam surface. At a slightly higher load, the alignment may have straightened which may have shifted the direction of loading.

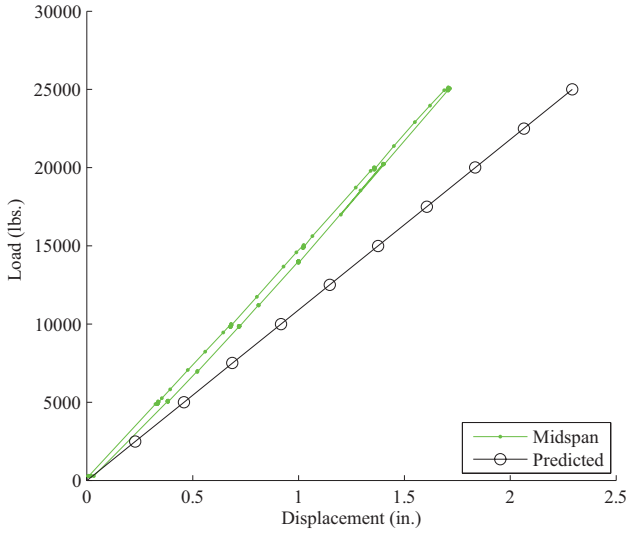

Figure 5-14 Load Deflection Plot for Test 3

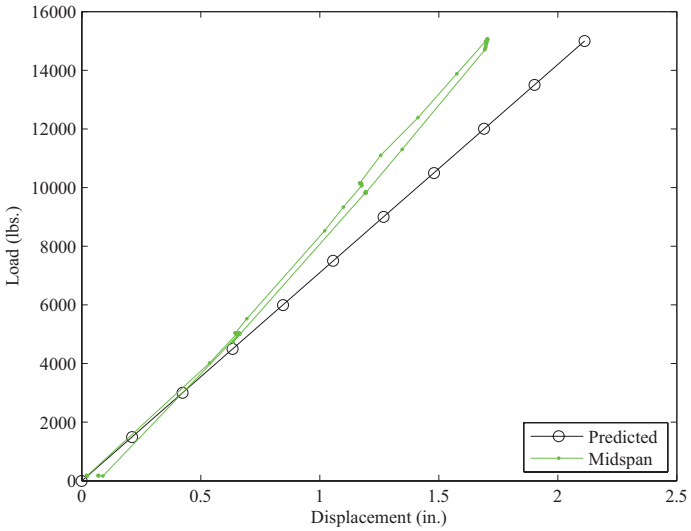

Figure 5-15 Load Deflection Plot for Test 9

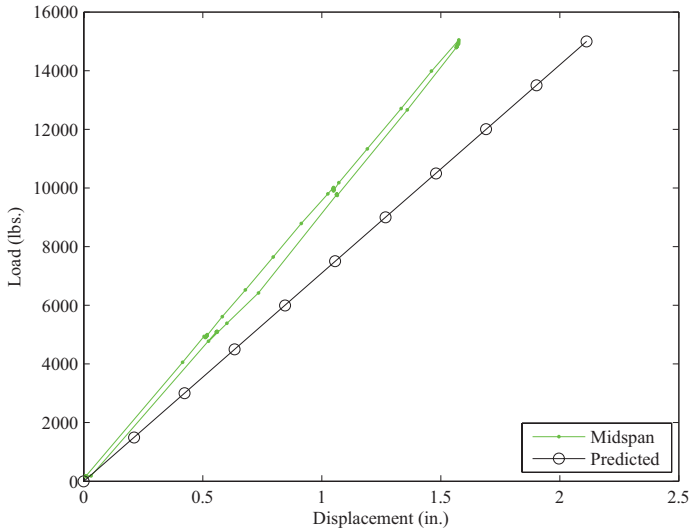

Figure 5-16 Load Deflection Plot for Test 10

Overall, the deflections from phase II testing were found to be smaller than predicted values in all cases. The design approach is conservative in calculating the stiffness of the HCB. As noted in the discussion of Phase I results, components of the HCB which are neglected may be contributing stiffness. One such component was the concrete fin that extends from the top surface of the arch to the top FRP flange. The fin does not exist at midspan because the arch profile rises to the bottom surface of the FRP top flange. The fin was at its greatest height near the supports. As the shape of the fin varied along the span of the beam, the effect on deflection was not easily discernible. However, since the fin increases the moment of inertia gradually from the midspan to the ends of the beam, the deflection was predicted to decrease.

5.3.2. Behavior of Fiber-Reinforced Polymer

Behavior of the Fiber-Reinforced Polymer (FRP) was expected to be linear-elastic during phase II testing. In general, composite materials are linear-elastic up to failure. During testing, audible cracking noise was observed from the composite material. The noise was due to straightening of fibers within the composite and did not represent physical damage to the FRP.

Because of the large number of strain gages applied to the FRP in phase II, only select plots will be presented.

Table 5-18 presents the average midspan strains for the point load tests. Any evident outliers were excluded from the calculation of average strain. These outliers were identified by their large magnitudes; usually they were on the order of 200% greater than values observed in other gages. Predicted strains were calculated using the transformed area approach and section properties from Hillman's model. The average ratio of measured to predicted strain was 0.88, but most of the gages showed a ratio of around 0.68 (Table 5-18). Both top flange gages and the top web west face gages were higher than expected. The cause for the top web strain on the west face to be higher was unknown because the gage on the east face at the same location registered lower strain. Though the ratio for this gage is greater than 1, the difference amounted to 31 με which was relatively small. The top flange gages appeared to have some problems associated with them which will be discussed later.

Table 5-18 Average Midspan Strains for Point Load Tests

Midspan Gages for Point Load Tests		Strain (με)		Ratio
Location	Gages	Average	Predicted	
Top Flange - E.	FM-8, FM-24	-518	-425	1.22
Top Flange - W.	FM-7, FM-15, FM-23	-541	-425	1.27
Top of Web (14 in.) - E.	FM-1, FM-9, FM-17	82	124	0.66
Top of Web (14 in.) - W.	FM-6, FM-14, FM-22	155	124	1.25
Bottom of Web (7 in.) - E.	FM-2, FM-10, FM-18	406	673	0.60
Bottom of Web (7 in.) - W.	FM-5, FM-13, FM-21	466	673	0.69
Bottom Flange - E.	FM-3, FM-11, FM-19	793	1222	0.65
Bottom Flange - W.	FM-4, FM-12, FM-20	830	1222	0.68
			Average	0.88

The highest compressive strains in the FRP were expected to occur in the top flange at quarter point for the quarter point load tests (Table 5-19). This was due to the constant moment region in combination with the lower neutral axis than was calculated for midspan. Predicted

strains were calculated in the same manner as for the point load tests. The average ratio of measured to predicted strains was 0.79 (Table 5-19). With exception of the top flange gage towards the west face of the beam; all measured strains were less than predicted. In general, gages on the east and west face of the beam were in agreement. The top flange gages showed the largest difference. The reason for the variation may be due to one of the potential causes discussed later.

Table 5-19 Average Quarter Point Strains for Quarter Point Loading

Quarter Point Gages for Quarter Point Load Tests		Strain (με)		Ratio
Location	Gages	Average	Predicted	
Top Flange - E.	FQ-7	-686	-720	0.95
Top Flange - W.	FQ-8, FQ-16, FQ-24	-830	-720	1.15
Top of Web (14 in.) - E.	FQ-1, FQ-9, FQ-17	-130	-147	0.88
Top of Web (14 in.) - W.	FQ-6, FQ-14, FQ-22	-80	-147	0.55
Bottom of Web (7 in.) - E.	FQ-2, FQ-10, FQ-18	309	427	0.72
Bottom of Web (7 in.) - W.	FQ-5, FQ-13, FQ-21	307	427	0.72
Bottom Flange - E.	FQ-3, FQ-11, FQ-19	659	1000	0.66
Bottom Flange - W.	FQ-4, FQ-12, FQ-20	694	1000	0.69
			Average	0.79

The majority of gages showed linear elastic behavior for the loading and unloading phases of testing. Test 1 was typical of the FRP strain gage behavior. Figure 5-17 showed the load-strain relationship for the gages attached to the bottom flange of the FRP box at midspan and at quarter point. All gages registered considerably lower than predicted strain. Both gages at midspan registered an identical strain. The gages at the quarter point showed a slight difference but were similar. Also, all gages returned to a zero strain reading after testing.

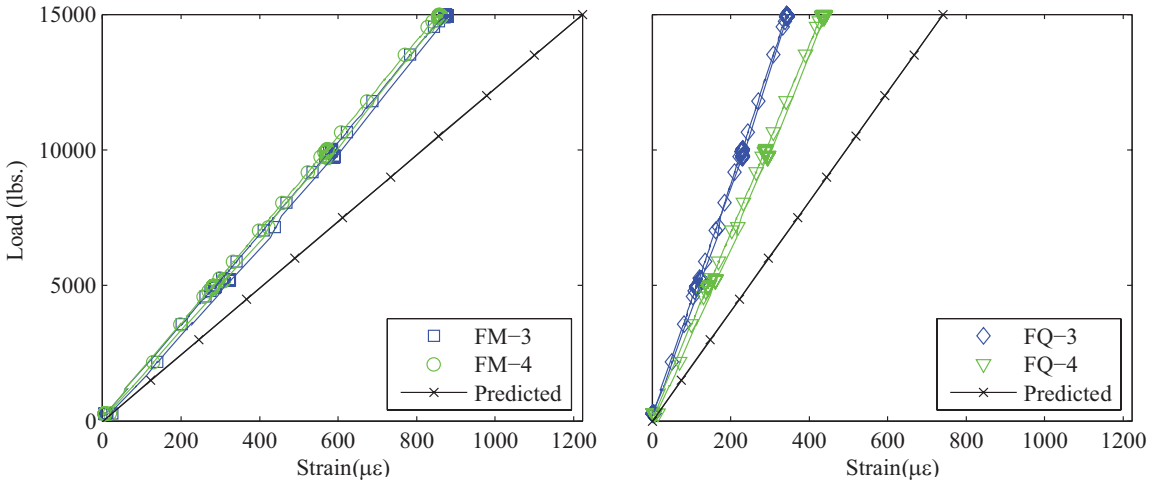

(a) Midspan (b) Quarter Point

Figure 5-17 Load vs. Strain for Bottom Flange for Test 1

Though linear behavior was observed in most gages, unusual nonlinear behavior was observed in a number of gages. The load-strain behavior for gages FQ-15 and FQ-16 is shown in Figure 5-18 for test 8. As the load increased, the change in measured strain in FQ-15 sharply decreased. The cause for the nonlinear behavior is unknown as the FRP box should have linear-elastic behavior up to failure. Furthermore, typical nonlinear behavior in materials represents a decrease in stiffness under increasing load. However, the opposite behavior was seen as the stiffness seemed to increase due to increased loading. Additionally, gage FQ-16 which was also mounted on the top flange showed fairly linear behavior and followed the predicted strain closely. The explanation for the nonlinear behavior was not clear, and the behavior was seen in a number of gages for all beams.

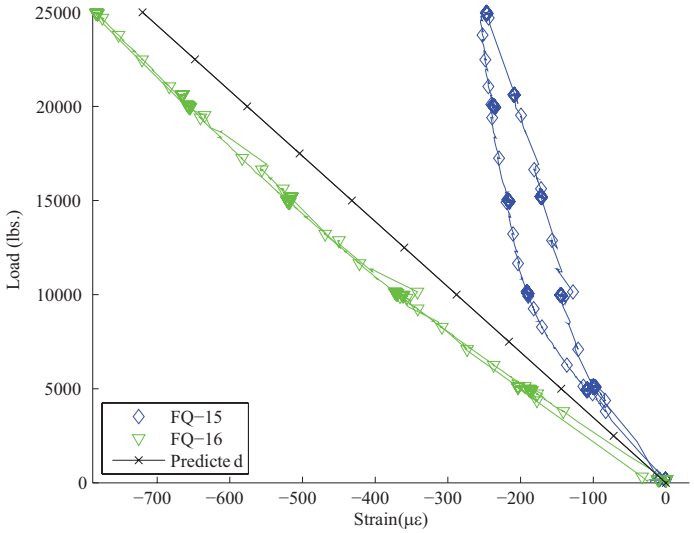

Figure 5-18 Load vs. Strain for Top Flange at Quarter Point for Test 8

A noticeable trend in the data was that strain measurements varied for each beam. Two apparently identical point load tests and two apparently identical quarter point tests were performed on each beam. Strain measurements were in agreement for each pair of tests. However, when comparing the data between beams, the strain values differed. Table 5-20 presents midspan strain measurements taken when the beam was subjected to a 15 kip point load. Evident outliers are highlighted. One case can be seen for the strain for the bottom flange near the east face in HCB 3. The average strain for the bottom flange was 811 με, but strains measured for test 9 and 10 averaged 618 με. Examination of the load-strain plot for test 9 showed the gage behaved linearly and that the lower measurement was not due to erratic behavior of the gage (Figure 5-19). The plot for test 10 was similar to test 9.

Table 5-20 Midspan FRP Gages for Point Load Tests

Midspan Gages for Point Load Tests		Test 1	Test 2	Test 5	Test 6	Test 9	Test 10
Location	Gages	HCB 1	HCB 1	HCB 2	HCB 2	HCB 3	HCB 3
Top Flange - E.	FM-8, FM-16, FM-24	-449	-547	-1061	-1455	-589	-488
Top Flange - W.	FM-7, FM-15, FM-23	1194	-543	-526	-732	-536	-365
Top of Web (14 in.) - E.	FM-1, FM-9, FM-17	84	84	58	55	108	101
Top of Web (14 in.) - W.	FM-6, FM-14, FM-22	167	187	139	125	163	150
Bottom of Web (7 in.) - E.	FM-2, FM-10, FM-18	414	423	389	374	433	403
Bottom of Web (7 in.) - W.	FM-5, FM-13, FM-21	486	501	434	413	498	464
Bottom Flange - E.	FM-3, FM-11, FM-19	874	889	898	861	639	598
Bottom Flange - W.	FM-4, FM-12, FM-20	859	870	864	810	815	763

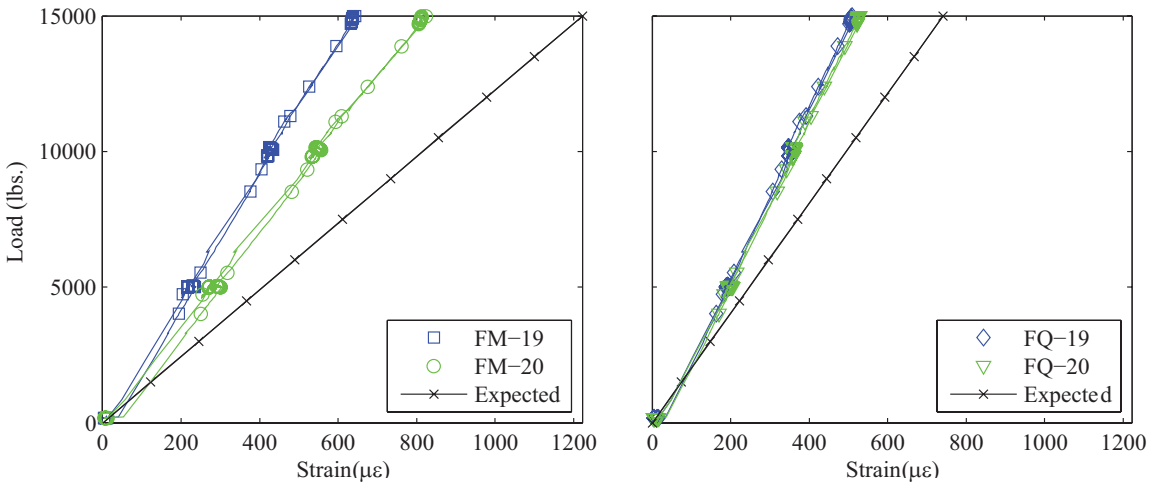

(a) Midspan (b) Quarter Point

Figure 5-19 Load vs. Strain for Bottom Flange for Test 9

A number of potential explanations could be the cause of the variation in strain measurements seen during phase II testing. One cause may have been poor bond with the FRP. Difficulty existed with instrumenting the FRP boxes, and a number of gages failed to adhere immediately following the application process. Another explanation for the variation could be the inherent anisotropic nature of composite materials picked up by the strain gages. A gage length of ¼ in. was used rather than ½ in. for the FRP gages due to limited availability by the supplier. The smaller gage length may have made the strain readings more susceptible to local

behavior of the FRP. The FRP was assumed to be quasi-isotropic in design. However, because the gage is mounted to the outer surface, the reading may be affected by the fiber orientation of the outer layer. Furthermore, if alignment of the fiber layers varied during the fabrication process, a difference in strain may be caused by relative alignment of the strain gage to the fiber direction.

A cause for the difference observed for the top flange gages may be due to local effects. The top flange appeared to have the largest variation of all the FRP strain gage locations. Because the top flange gages were very close to the applied load locations, they may have been more susceptible to effects from local behavior of the FRP. The load was expected to be transferred into the beam through the plaster placed prior to phase II testing (Figure 4-14). However, because the loading area was larger than the area filled with plaster, some of the load may have been transferred into the beam through the top flange of the FRP box. Also, any relative movement of the arch and concrete fin may have caused transverse bending in the FRP which could also be a reason for the erratic gage behavior.

Data from the usable gages showed that measured strains were consistently below strains calculated using Hillman's model. Excluding the top flange gages, the east and west strain measurements appeared to be in good agreement. Additionally, when the HCB's were unloaded the strain returned to zero indicating no permanent deformation occurred. Overall, the transformed section approach appeared to be appropriate in providing an estimate of measured FRP strains.

5.3.3. Behavior of Prestressing Strand

Linear behavior for the strand was observed during phase I testing. As the loads for phase II were also expected to be relatively small with respect to the HCB capacity, typical beam

behavior was expected. The strains in the strands were expected to increase significantly due to the upward shift of the neutral axis due to the contribution of the concrete arch. At the time of phase II testing, some gages attached to the tension strand were nonresponsive and were determined to have been damaged during the arch concrete placement. The remainder of the gages was used for analysis.

A range of values was observed between tests for the strain in the tension strand at midspan. Table 5-21 presents maximum measured strain for gages on the strands at midspan for each of the tests. As all midspan gages on HCB 3 were damaged, data from those gages were not presented. The table provides an overall comparison between predicted and observed behavior in the strand. The measured strain was found to be less than predicted values from Hillman's model. The strain values for the point load tests indicated a range of about 60 με and appeared to have a good level of repeatability (Table 5-21). The average ratio of measured to predicted strain was 0.62 for the point load tests. Observing the available data for the quarter point tests showed a range of approximately 32 με (Table 5-22). The average ratio for the quarter point tests was 0.74. The difference in ratio suggests the model predicted the strand strain for the quarter point tests more effectively. The average ratio for all tests was found to be 0.67. In general, the transformed area approach appears to be conservative in calculation of strand strains.

Table 5-21 Maximum Midspan Strain in Strand for Point Load Tests

Test Number	HCB	Loading	Maximum Midspan Strain (με)	Expected Midspan Strain (με)	Ratio
-	1	15k Point Load at Midspan	726	1191	0.61
1	1	15k Point Load at Midspan	749	1191	0.63
2	1	15k Point Load at Midspan	769	1191	0.65
5	2	15k Point Load at Midspan	746	1191	0.63
6	2	15k Point Load at Midspan	709	1191	0.60
		Average for HCB 1	748	1191	0.63
		Average for HCB 2	727	1191	0.61
		Average for HCB 1 and HCB 2	740	1191	0.62

Table 5-22 Maximum Midspan Strain in Strand for Quarter Point Load Tests

Test Number	HCB	Loading	Maximum Midspan Strain (με)	Expected Midspan Strain (με)	Ratio
-	1	12.5k Point Load at Quarter Points	673	893	0.75
3	1	12.5k Point Load at Quarter Points	655	893	0.73
4	1	12.5k Point Load at Quarter Points	674	893	0.75
7	2	12.5k Point Load at Quarter Points	655	893	0.73
8	2	12.5k Point Load at Quarter Points	642	893	0.72
		Average for HCB 1	667	893	0.75
		Average for HCB 2	648	893	0.73
		Average for HCB 1 and HCB 2	660	893	0.74

As shown in Figure 5-20, the strand strain linearly increased as the applied load increased. Figure 5-20 was typical of the behavior observed in the other midspan point load tests. As the data suggested in Table 5-21, the observed strains were much smaller than predicted strain from Hillman's model. The strand strain varied from midspan to the quarter point. This suggested the force in the strand was not constant along the span of the beam. The data supports the assumptions made by Hillman that the HCB follows beam behavior. Because the neutral axis at the quarter point was lower, a smaller strain was expected than observed at midspan.

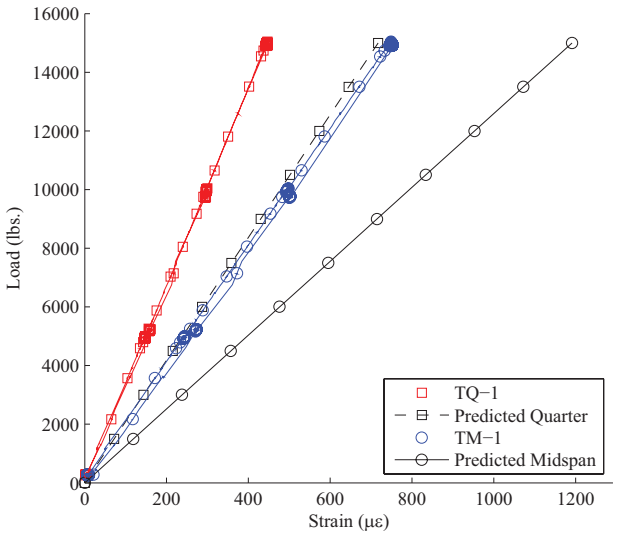

Figure 5-20 Load vs. Strand Strain for Test 1

For the quarter point tests, the strain values at the midspan and quarter point were also found to be less than predicted (Figure 5-21). From Hillman's model, the strain at the midspan was predicted to be slightly less than strain at the quarter points. This was due to a constant moment region that spanned between the quarter points and the variation in the moment of inertia. The measured strain at midspan and quarter point was nearly identical for Test 3 (Figure 5-21). The quarter point strain appeared to be slightly less. Both locations showed a linear increase in strain. When the beam was unloaded, the strand strains returned to zero. Different behavior was observed in HCB 2 during the quarter point loading in test 7 (Figure 5-22). The quarter point strain was slightly higher than observed for test 3. The quarter point was also greater than the strain at midspan which matched Hillman's prediction. The difference between measured strains at midspan and quarter point closely matched the expected difference (Figure 5-22). The quarter point test showed strains that were consistently less than expected.

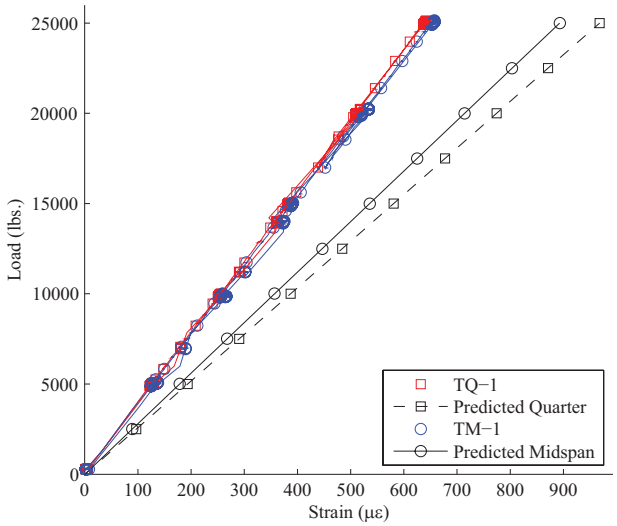

Figure 5-21 Load vs. Strand Strain for Test 3

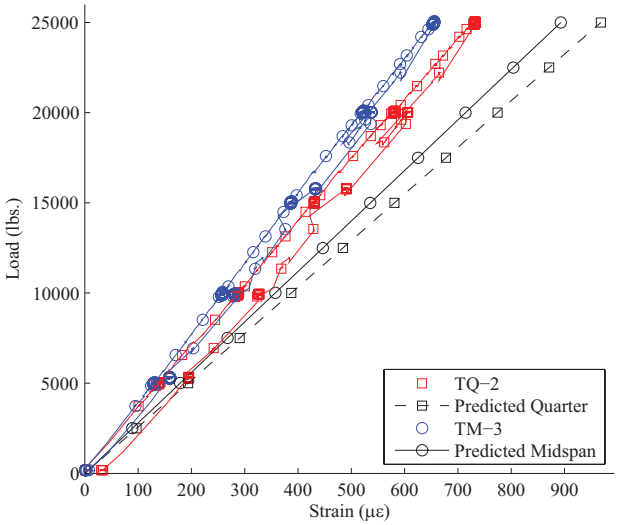

Figure 5-22 Load vs. Strand Strain for Test 7

Overall, the behavior observed during testing showed the transformed section approach consistently overestimated strains in the strand. Linear behavior was observed in all gages. The strand appeared to follow behavior predicted by the transformed area approach though magnitudes of strain were slightly less. For the point load tests, a difference was seen between the midspan and quarter point gages as was predicted by the model. For the quarter point load

tests, the model predicted the quarter point and midspan strains would be similar as was demonstrated from the experimental data. The transformed section approach was able to conservatively predict the behavior of the prestressing strand, but the measured strains were less than predicted.

5.3.4. Behavior of Concrete Arch

The data from the vibrating wire gages were used to observe behavior of the concrete arch during phase II loading. According to Hillman's observations, the HCB's were expected to undergo beam behavior rather than tied arch behavior for the low loadings used in phase II (Hillman 2003). Based on Hillman's model, the maximum strain in the concrete arch was expected to occur at the top of the arch at the midspan of the HCB. Table 5-23 presents the maximum measured strain at this midspan under the maximum applied point load, and Table 5-24 presents maximum measured strain for the quarter point tests. For the midspan and quarter points, the measured strains were much smaller than predicted strains. This indicated the compressive stress in the arch was less than was calculated using Hillman's model. For the support locations, measured strains were either found to be close to or much higher than predicted values. In most cases a difference was observed between the gage located in the top of the arch and the gage in the bottom of the arch indicating some bending occurred in the arch.

Table 5-23 Maximum Midspan Strain in Arch Top for Point Load Tests

Test	HCB	Loading	Maximum Midspan Strain in Arch Top (με)	Predicted Midspan Strain in Arch Top (με)	Ratio
1	1	15k PT	-168	-268	0.63
2	1	15k PT	-129	-268	0.48
5	2	15k PT	-187	-268	0.70
6	2	15k PT	-185	-268	0.69
9	3	15k PT	-160	-268	0.60
10	3	15k PT	-152	-268	0.57
	Average for HCB 1		-149	-268	0.55
	Average for HCB 2		-186	-268	0.69
	Average for HCB 3		-156	-268	0.58
	Average for All Beams		-164	-268	0.61

Table 5-24 Maximum Midspan Strain in Arch top for Quarter Point Load Tests

Test	HCB	Loading	Maximum Midspan Strain in Arch Top (με)	Predicted Midspan Strain in Arch Top (με)	Ratio
3	1	12.5k QPT	-136	-200	0.68
4	1	12.5k QPT	-136	-200	0.68
7	2	12.5k QPT	N/A	-200	N/A
8	2	12.5k QPT	-172	-200	0.86
11	3	12.5k QPT	-146	-200	0.73
12	3	12.5k QPT	-142	-200	0.71
	Average for HCB 1		-136	-200	0.68
	Average for HCB 2		-172	-200	0.86
	Average for HCB 3		-144	-200	0.72
	Average for All Beams		-146	-200	0.73

A number of trends were observed for the midspan arch behavior. The measured strains varied for each HCB as was seen in Table 5-23 and Table 5-24 despite identical loading. For HCB 1, the strain differed between the first and second point load tests by 39 με. The average midspan strain observed for HCB 1 was -149 με but the average strain for HCB 2 was found to be -186 με (Table 5-23). For HCB 3, an average strain of -156 με was observed. A similar trend was observed for the quarter point tests. The strain readings for HCB 1 and HCB 3 averaged -140 με and were within 8 με indicating good precision (Table 5-24). However, the strain for

HCB 2 test 8 was measured to be -172 με which was noticeably higher. Data was not available from test 7 due to an error with the data logger. The average ratio between measured and predicted strain values for the midspan was found to be 0.61 for the point load and 0.73 for the quarter point loads. Hillman's prediction for the arch strains were conservative in regards to the midspan.

Unusual behavior was observed in a number of vibrating wire gage readings. As mentioned in previous sections, alignments during setup may have been a cause for differences between tests performed on the same beam with the same load. The majority of gages showed linear behavior under loading, but a few gages showed some non-linearity. Others appeared to be malfunctioning as strain readings were sporadic as loading increased. Some gages did not return to zero strain when the beam was unloaded. Negative strain readings (indicating compression) were commonly observed; however, in a few cases, positive strain measurements were observed.

Examination of data from test 1 for the concrete arch showed measured strains was much smaller than predicted strains in most cases. The strains measured at the top of the arch at midspan (CM-2) and at the north quarter point (CQ-2) were similar (Figure 5-23). At both midspan and quarter point a notable difference was observed between the measured strain at the top and bottom of the arch implying the arch was undergoing bending. The difference is much greater at the quarter point. The measured strain for the support gages was much smaller than at the quarter point and midspan, but was greater than expected (Figure 5-23). From Hillman's model, the strains were predicted to be small near the supports due to the location of the neutral axis near the bottom of the HCB. The measured strain for the top of the arch at the support (CS-2) was found to be higher than the predicted value. Gage CS-1 was malfunctioning during testing and did not return usable strain measurements.

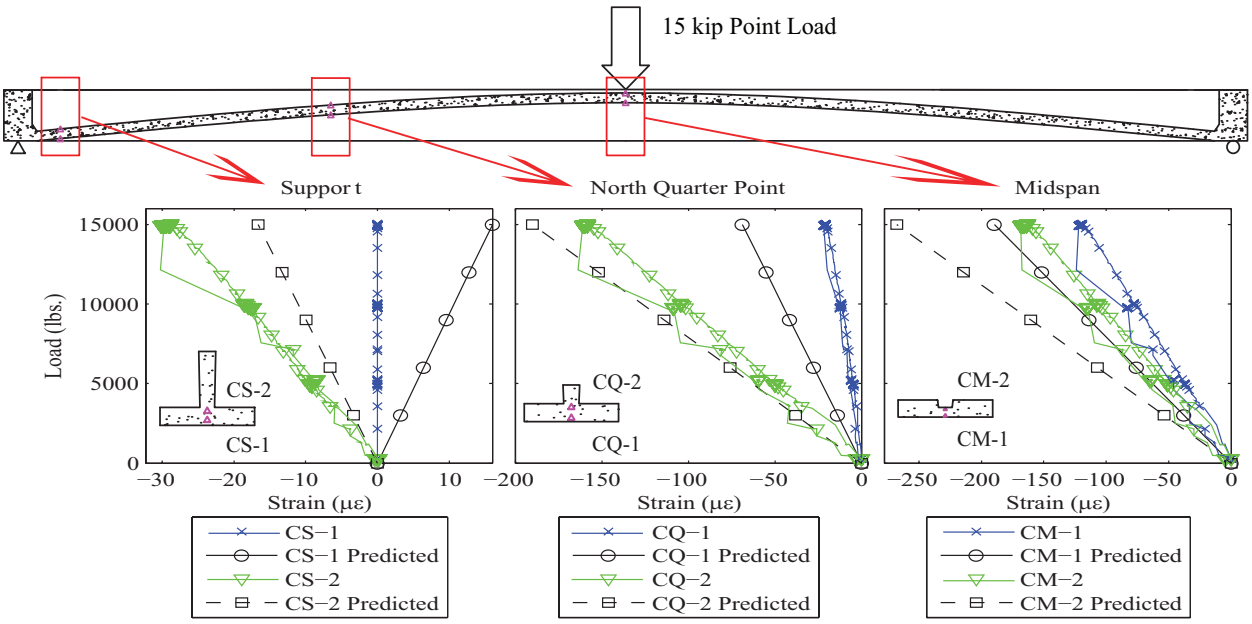

Figure 5-23 Load vs. Concrete Strain for Test 1

Different trends were observed for the concrete strains in test 2. Test 1 and test 2 consisted of identical loadings, but the observed strains were notably different in test 2 (Figure 5-24). One cause for the difference may have been due to alignment as test 2 was conducted after the original tests. An unusual difference was observed for the gages at the quarter point. Whereas all other gages in test 1 and 2 displayed linear behavior, the gages at the quarter point appeared non-linear. Also, the magnitude of strains was much larger than both the strains for test 1 and predicted values. Though non-linear behavior was observed, the measured strains returned to zero when the beam was unloaded. There was no clear explanation for the cause of the non-linear behavior. The midspan and support strains for test 2 were smaller than for test 1.

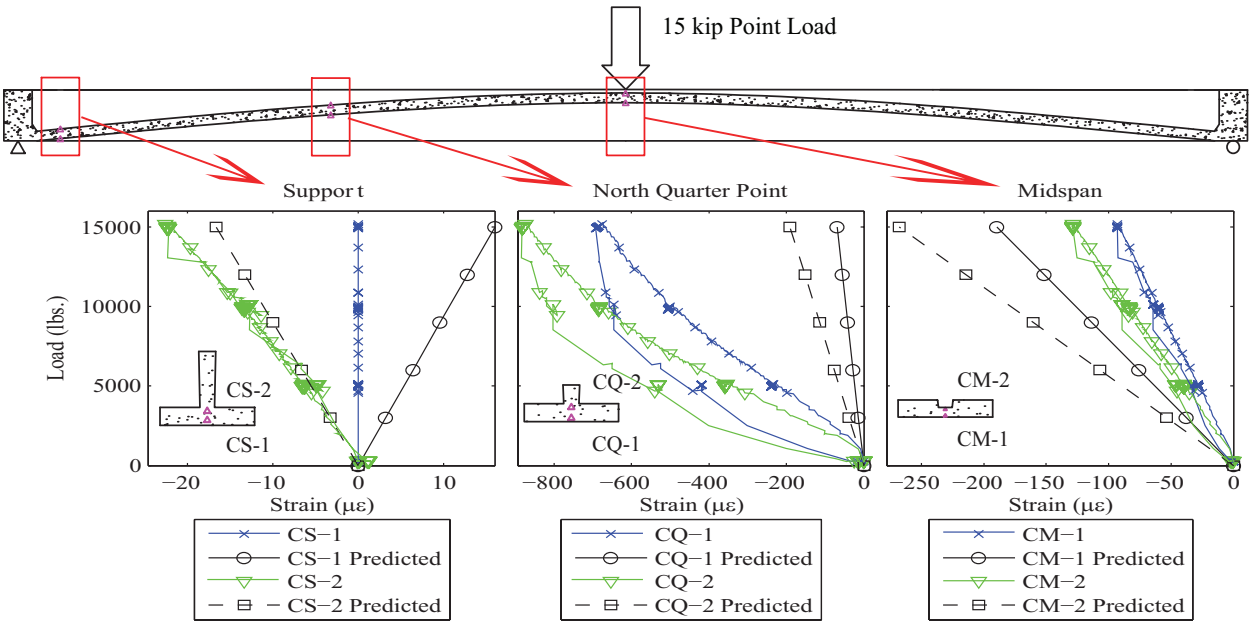

Figure 5-24 Load vs. Concrete Strain for Test 2

The plot for test 5, performed on HCB 2, showed smaller strains than observed for the gages in HCB 1 (Figure 5-25). Linear behavior was observed for midspan and quarter point gages, but the support gages showed slight non-linearity. For all strain gages, measured strains were smaller than predicted values using Hillman's model. Unlike tests 1 and 2, the strain for the top of the arch near the support was very close to the predicted strain (Figure 5-25). The strain for the bottom of the arch was expected to be positive indicating tension. This was due to the predicted location of the neutral axis near the bottom of the beam at the support. However, measured strains were negative for gage CS-3 indicating compression. Hillman noted in previous studies that the HCB may behave more as a tied arch near the support rather than a typical beam. Thus, the arch would be expected to be undergoing compression forces throughout the height. To support this idea further, the strains measured in CS-3 and CS-4 were very similar indicating bending was not present as was noted at the midspan and quarter point.

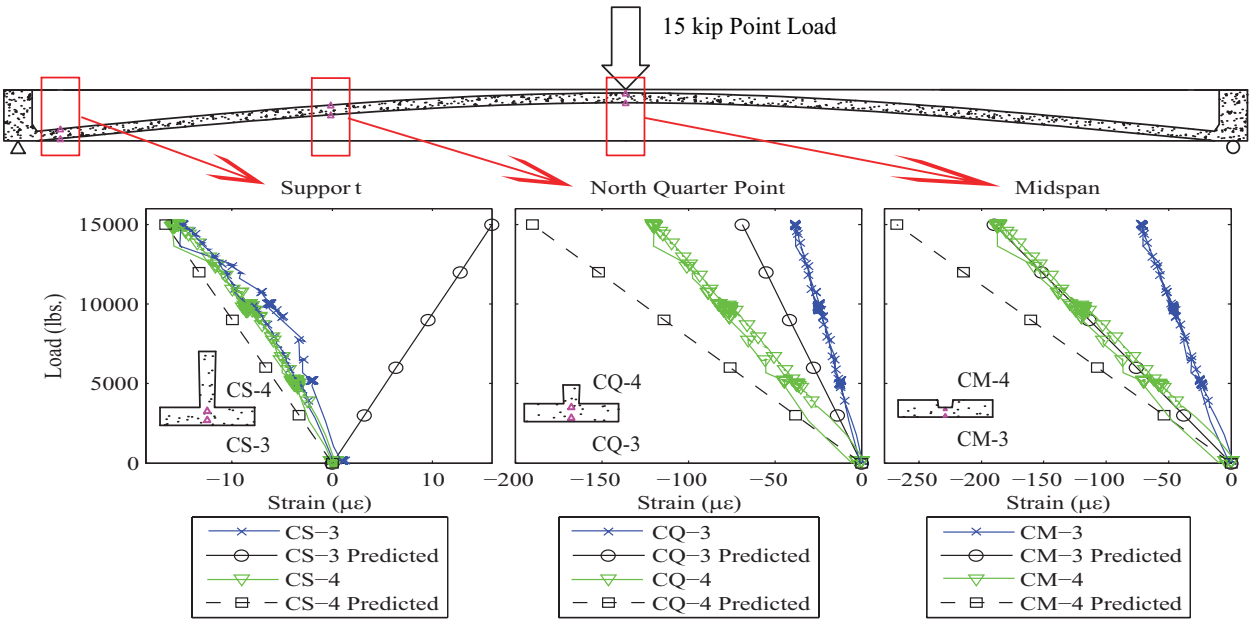

Figure 5-25 Load vs. Concrete Strain for Test 5

The arch behavior for the quarter point load tests displayed discernible differences with the behavior of the point load tests. Examining the strain measurements for test 3 on HCB 1, the midspan strains were very similar indicating minimal bending was occurring (Figure 5-26). The reading for CM-1 was close to but still less than the predicted strain. A prominent feature at the quarter point was the large difference between strain measured at the top and bottom. Gage CQ-1 on the bottom of the arch had a positive strain reading indicating tension. The readings during the unloading phase appear to indicate deformation occurred in the beam after the beam was unloaded. The recorded strains for Gage CQ-2 were almost twice the expected value (Figure 5-26). The increase in strain for CQ-2 appeared to be non-linear to a small degree. The strain for CS-2 was also much greater than the expected strain and that observed for the point load tests. The other gages showed linear behavior and returned to a zero strain reading when the beam was unloaded.

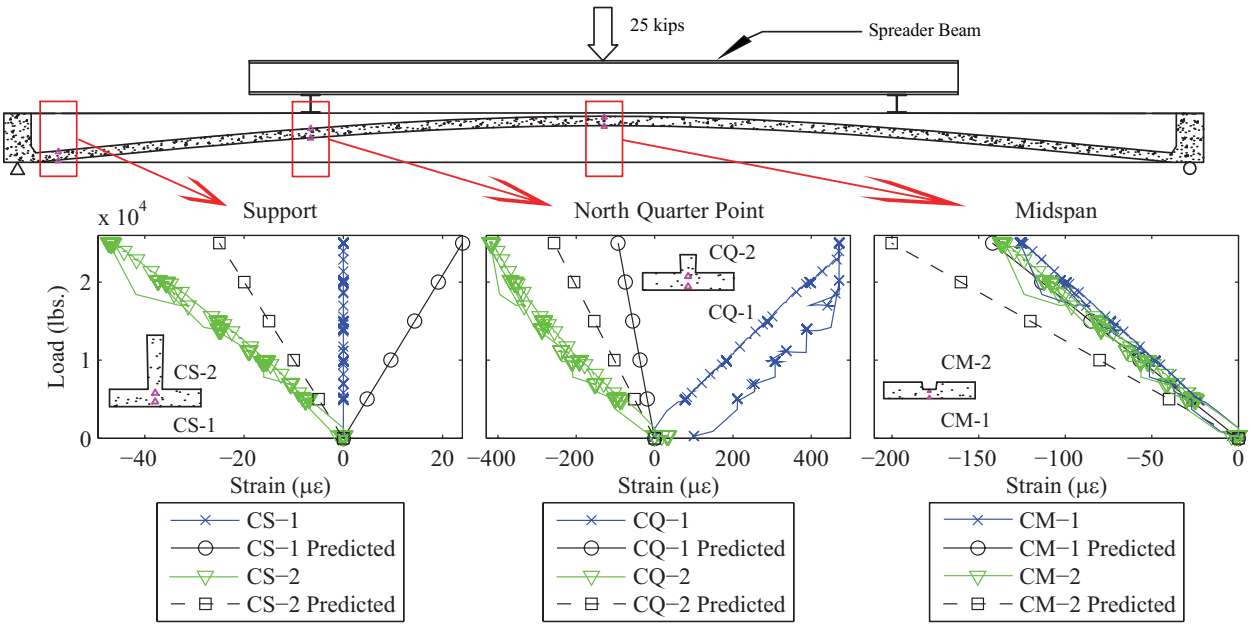

Figure 5-26 Load vs. Concrete Strain for Test 3

The data for test 4 showed identical behavior for the gages at the supports and midspan (Figure 5-27). The gages appeared linear and returned to zero strain when unloaded. The maximum strain measured by CQ-2 in the top of the arch increased significantly from around -400 με in test 3 to -650 με for test 4. Non-linear behavior was seen in the increase in strain. Though the strains were relatively high, the resulting stress was 2.47 ksi which was still less than the elastic limit of the concrete of $0.45f'_c$ (2.7 ksi). As was observed in test 3, the strain for CQ-2 returned to zero when the beam was unloaded indicating permanent deformation did not take place. An error appeared to have occurred with gage CQ-1. The gage registered positive strain at the beginning of the test and read a constant positive strain for the duration of the test.

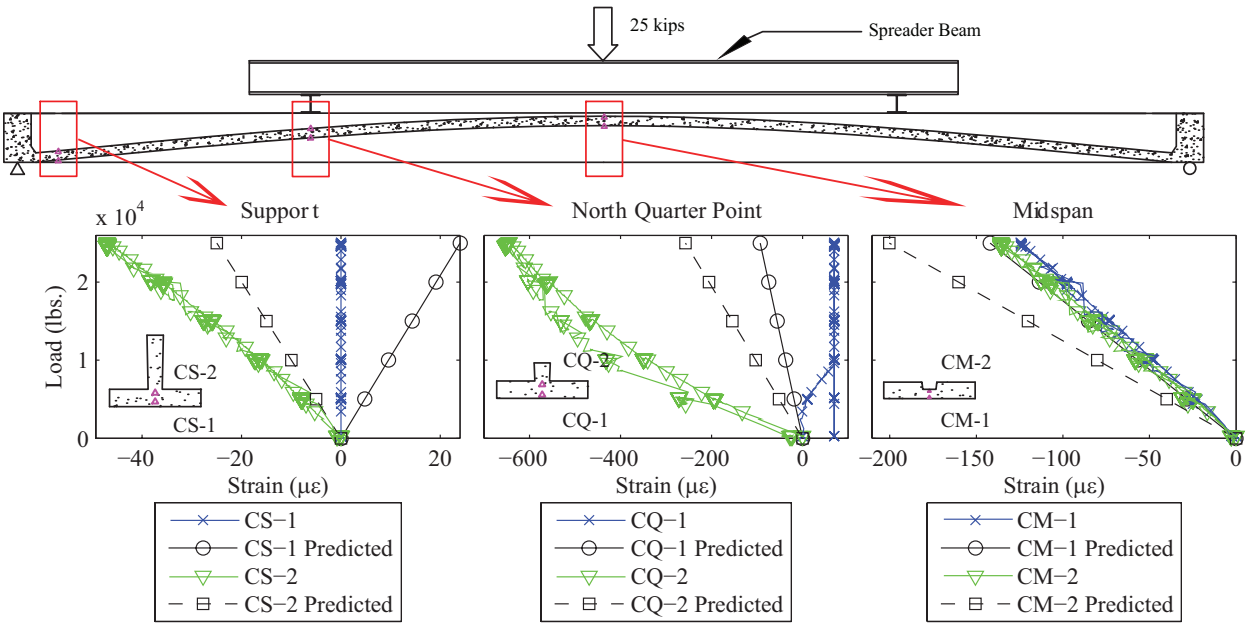

Figure 5-27 Load vs. Concrete Strain for Test 4

The strain plots for HCB 3 showed some similar trends though differences were noticeable. For gages at the midspan and quarter point, linear behavior was observed for test 11 (Figure 5-28). Slight non-linearity appeared in the plot for the support gages. All gages showed a zero strain reading when the beam was unloaded. One noticeable difference was the behavior of the quarter point gages. Unlike tests 3 and 4, the strain increased linearly for the top and bottom of the arch (Figure 5-28). The magnitude of strains was also much smaller. For gage CQ-6, the strain was smaller than the expected strain. A strain of -650 με was observed in test 3 and -150 με in test 11. Gage CQ-5 recorded tension strain as was seen in tests 3 and 4. The maximum strain recorded by the gage was 471 με for test 3 and 130 με for test 11. The behavior of the gages at the quarter point had unusual behavior which did not correspond to Hillman's model.

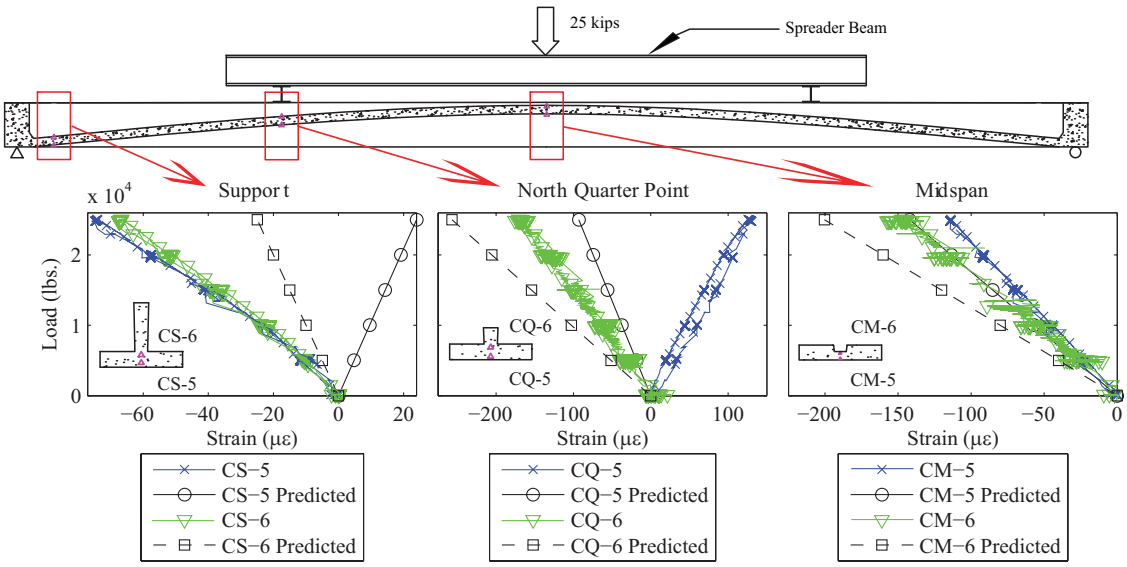

Figure 5-28 Load vs. Concrete Strain for Test 11

A number of explanations can be offered for the variation in arch concrete strains. As mentioned in section 5.1.1, segregation in the concrete mix occurred during the arch placement. The modulus of elasticity for the concrete cylinders was observed to vary. A variation in segregation may have caused the modulus of one beam's arch to vary from another. This may be the cause for the different average strain value listed in Table 5-23 and Table 5-24. During the arch placement, voids in the arch profile in the beams were observed near the midspan. The voids appeared to be caused by small pockets of air that were not pushed out by the flow of the concrete. The geometry of the arch may have varied from the values used for design. This may be the cause for some arch strain to be greater than predicted.

One explanation for the varying strain measurements seen between HCB's was that the vibrating wire gages may have been misaligned. Though effort was made during the instrumentation of the beams to keep the length of the gages aligned with the longitudinal direction of the beam, preparation for or placement of the arch concrete may have caused the gages to shift. Thus, the strain readings may not be for the longitudinal direction. Because the

concrete arch was encased by the FRP, observation of the gages during concrete placement was not possible.

The beams were subject to local effects. When the load was placed at midspan, the degree of bending at the midspan appeared to increase. When the load was placed at the quarter point, large tensile strains were measured in the bottom of the arch while compressive strains were measured in the top. The high degree of bending seen in the quarter point tests may have been due to the large FRP sheet placed at the midspan of the beam (Figure 5-29). The sheet was placed in the beam to add stability to the FRP webs prior and during to the arch concrete placement. It was neglected in all strength and deflection calculations. However, the FRP sheet may be restraining movement of the concrete arch thus acting as a very stiff spring at the midspan. Furthermore, a number of FRP ties placed near the support may restrain the arch as well (Figure 5-29). The arch segment between the midspan and the support would thus behave as a beam and deflect under the applied quarter point load (Figure 5-30). The added stiffness at the midspan due to the FRP sheet could also explain the lower degree of bending observed at midspan in the point load tests compared to the quarter point tests. The effective spring would support the segment of the arch at midspan thus making the arch more susceptible to local bending at the quarter point. The deflected shape could also explain the small amount of negative bending observed by the support gages for test 11 (Figure 5-28). The experimental data suggests the arch is sensitive to local bending from concentrated loading.

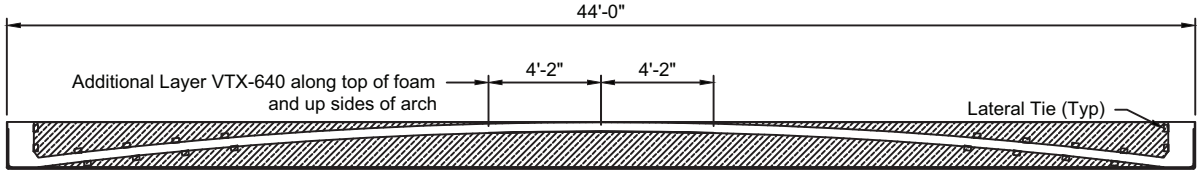

Figure 5-29 Elevation View of FRP Sheet and Ties (VDOT 2011)

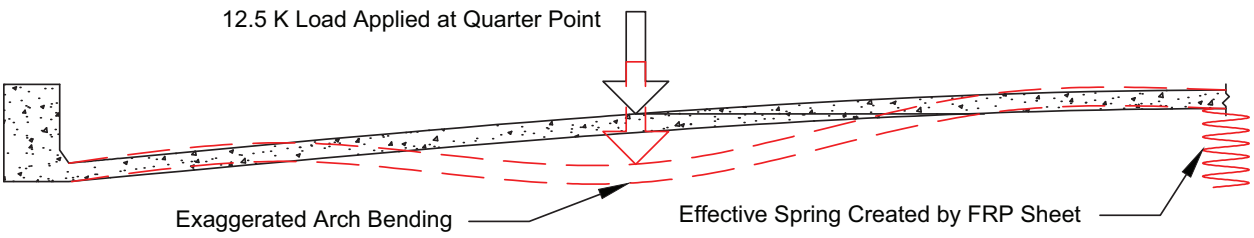

Figure 5-30 Midspan Spring Concept

Further support for this concept comes from observations made by Mascaro during analysis of the photogrammetry and LVDT data for Phase II (2012). Mascaro concluded the concrete arch had relative movement to the FRP box when observing quarter point instrumentation for the quarter point load tests. Furthermore, from the photogrammetry targets embedded within the arch, the maximum relative movement was observed at the target location nearest the applied load. The target indicated the arch moved downward relative to the FRP box. Other embedded targets showed minimal movement with the exception of the target located nearest the support. For this target, upward relative movement was observed. Though it was expected the FRP ties would provide some restrain, the ties were not as robust as the large FRP sheet placed at the midspan. Thus, they may not be completely restraining the arch near the support. In addition, the upward movement near the support follows the exaggerated arch bending shape seen in Figure 5-30.

From the material tests, the experimental modulus of rupture was found to be 604 psi, and the experimental modulus of elasticity was 3900 ksi. Using the experimental values, the maximum tensile strain of the concrete was calculated as 155 με before cracking occurred. The strains at the bottom of the arch at quarter point exceeded the cracking strain in some tests (Figure 5-26). This suggested the arch lost its ability to carry load. However, strains much larger than the cracking strain were observed in some tests. The explanation for this behavior may be due to the two loose prestressing strands that were placed in the bottom of the arch to anchor the

shear connectors. The strands may serve as a mechanism to carry tensile force in the arch though the concrete may have cracked. The current design method does not account for these strands, but they could be influence the arch behavior in regions of high local bending.

The transformed section approach appeared to predict sections of the arch behavior well, but failed to account for local effects. In most cases, strains for the arch were lower than the predicted strains from Hillman's model. Though the support strains were higher than predicted, the strains were relatively small. Hillman's model does not account for local effects from applied loads. The experimental data showed the quarter point of the arch is very susceptible to local bending that may be amplified by the presences of FRP ties that restrain movement. Though the local bending behavior was disconcerting, high concentrated loads are not expected to occur on the non-composite HCB. With the exception of local bending, Hillman's model provides a fair estimation of the arch behavior.

5.3.5. Strain Profiles

Strain profiles for phase II were constructed using strain gages on the FRP box, strain gages on the prestressing strand, and vibrating wire gages in the concrete arch. Because the materials were expected to be within their linear-elastic range and the load magnitudes were small, the HCB's were expected to have typical beam behavior. Strain compatibility was assumed and a linear strain profile was created using the transformed area approach in Hillman's model. Strain profiles were generated for tests in which the majority of the gages were functioning correctly. Using the strain profiles, the neutral axis locations for the respective beams were approximated and compared to Hillman's model.

The plots presented in the following discussion show the strains for both the east and west face of each respective HCB. Because the vibrating wire gages and prestressing strand

gages were placed near the centerline of the beam, they are used for both the east and west face plots. Additionally, the FRP strains are connected with a blue line while the vibrating wire gages are connected with a red line. The expected profile using the transformed area approach with section properties from Hillman's model is shown as the dashed black line.

The strain profile created using data from test 1, a point load applied at midspan of HCB 1, showed a somewhat linear profile created by the gages (Figure 5-31). Observing the profile created by only the FRP gages, a shape similar to the transformed section profile can be seen. The top flange of the HCB registered slightly higher strains than expected while the bottom flange measurements were noticeably smaller than predicted. Though the strains varied, the location of the neutral axis was in good agreement with that found using the Hillman model. The strain profile for the concrete arch also seemed to follow the general shape of the profile though the magnitude was slightly smaller (Figure 5-31). The strain for the prestressing strand was close to the bottom flange strain. With exception to the top flange, the FRP strain gages on the east and west face showed similar readings for each respective location indicating each side of the web was equally loaded.

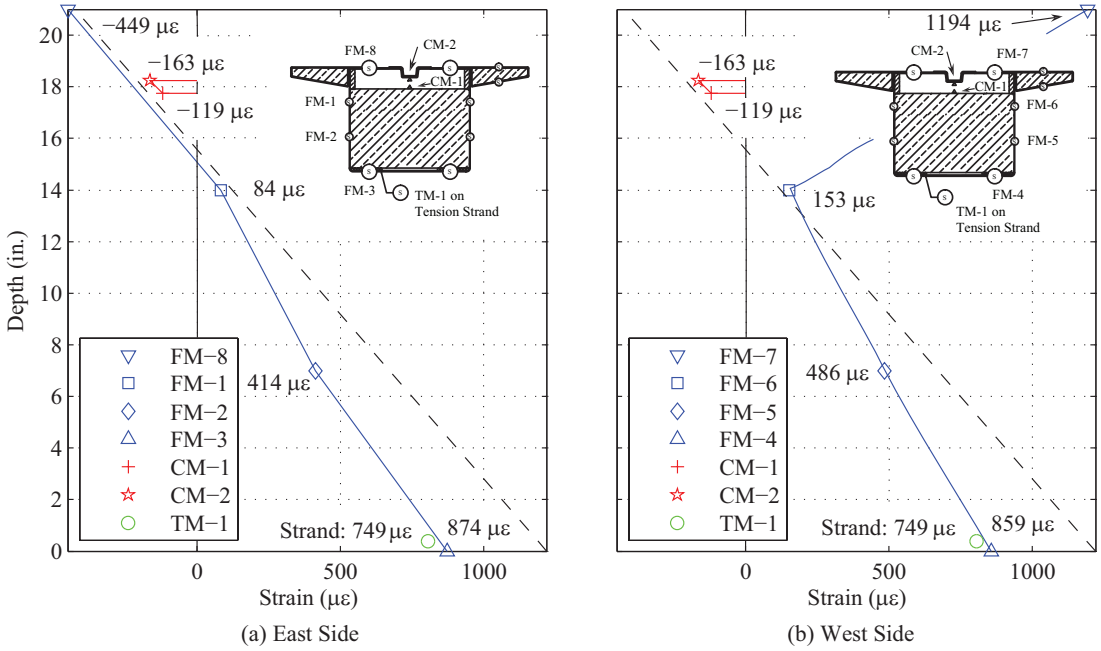

Figure 5-31 Midspan Strain Profile for Test 1

Observing the strain profile at the north quarter point of the same test, similar trends to the midspan were observed (Figure 5-32). The shape of the profile was somewhat linear, and gages for the east and west face had similar readings. The top flange gages appeared to have more variability than the other gages. The measured strains in the concrete also appeared to follow the profile well. Both the bottom flange gages and the tension strand gage were well below the expected strain value. The transformed area approach overestimated strains for the quarter point. The difference between observed and predicted neutral axis location may be the cause for the higher strains. Similar trends were observed for the point load tests for the other beams. The FRP strains appeared to vary slightly between beams, but a linear shape was observed. The strain distribution in the arch also appeared to vary as the interpolated slope between the top and bottom of the arch varied from the profile of the FRP gages. The point load tests generally showed linear strain profiles with respect to all gages.

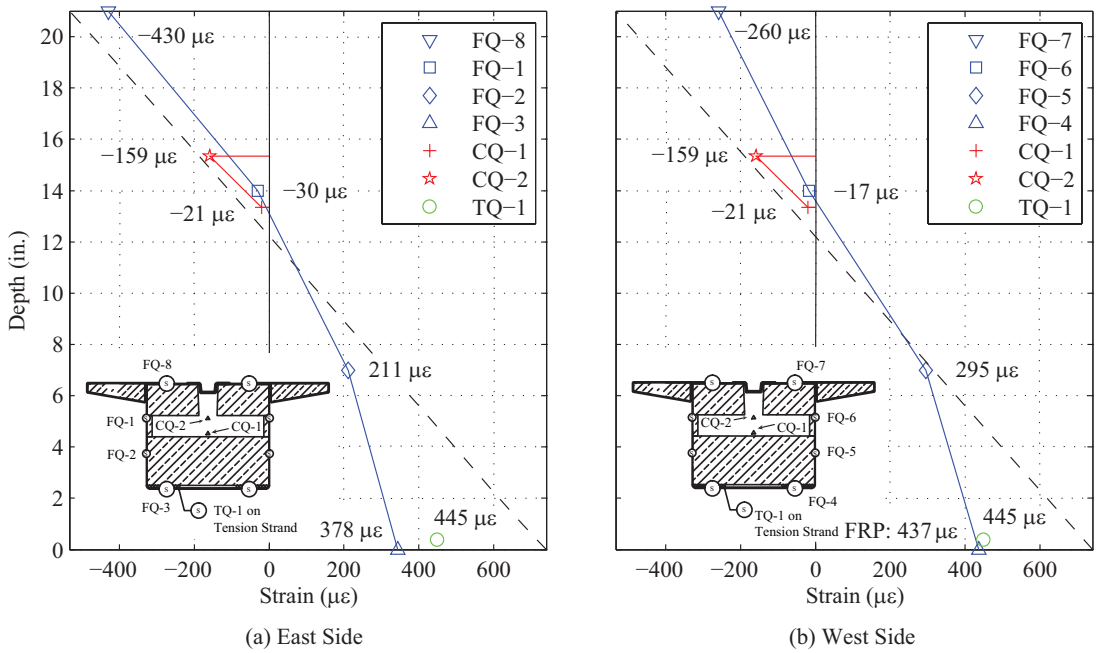

Figure 5-32 North Quarter Strain Profile for Test 1

The data for test 3, quarter point loads applied on HCB1, showed both similar and different trends than the point load test (Figure 5-32). Observing the midspan profile, the FRP strain profile appears to generally follow the predicted profile. The concrete strain values are also very close to the expected profile. The top flange gages (FM-7 and FM-8) showed a slight difference in strain, but the other FRP gage locations had similar readings. The cause for the difference may be due to its bond to the FRP but is otherwise unexplained. The location of the neutral axis measured by the gages was in good agreement with the transformed area approach. Hillman's model appeared to accurately predict midspan strains for the quarter point load test.

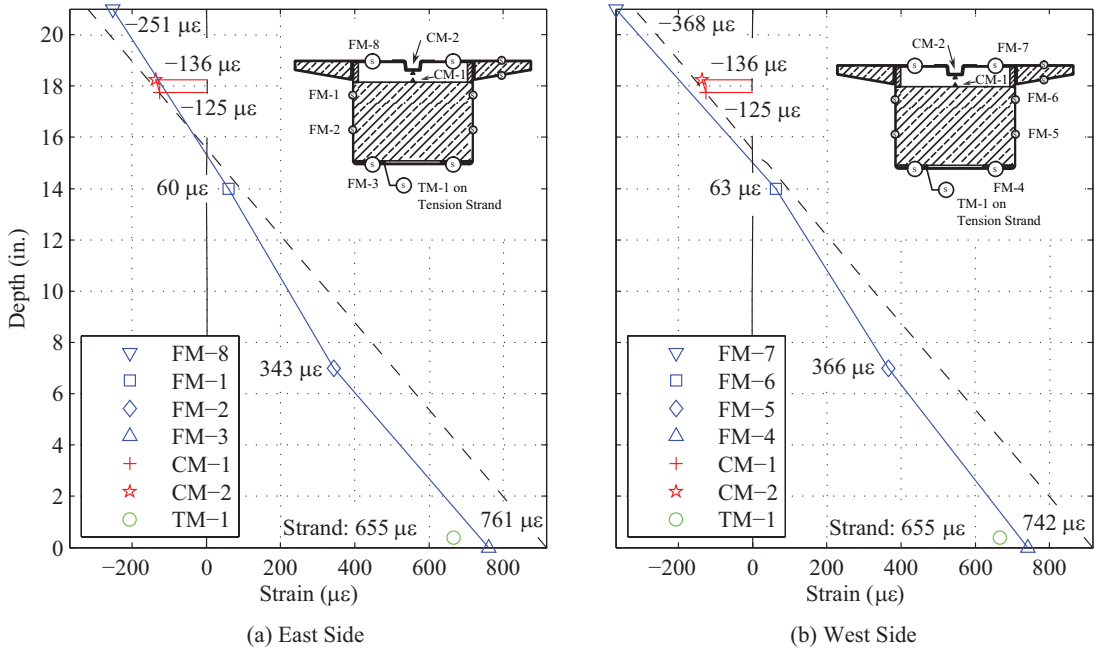

Figure 5-33 Midspan Strain Profile for Test 3

The strain profile for the quarter point of the same test showed unusual behavior for the concrete gages (Figure 5-34). Again, the FRP gages followed the general shape of the predicted profile and the neutral axis was in agreement with the predicted location. The strain for the bottom flange was noticeably smaller than the transformed area approach. Also worth noting was that the strand strain changed minimally between the midspan and quarter point. As noted in section above 5.3.4, the concrete gages indicated high local bending stresses occurring at the quarter point. Stresses measured at midspan and near the support showed a much smaller degree in variation between the top and bottom of the arch. As theorized earlier, the FRP sheet at midspan and ties near the support may be restraining the arch. However, since the arch is unrestrained at the location of applied load, it may be undergoing local bending. When comparing the arch strain profile to the overall beam strain profile, the extent of local bending is accentuated. The change in stress over the depth of the arch is significantly more than the change in stress over the depth of the FRP box.

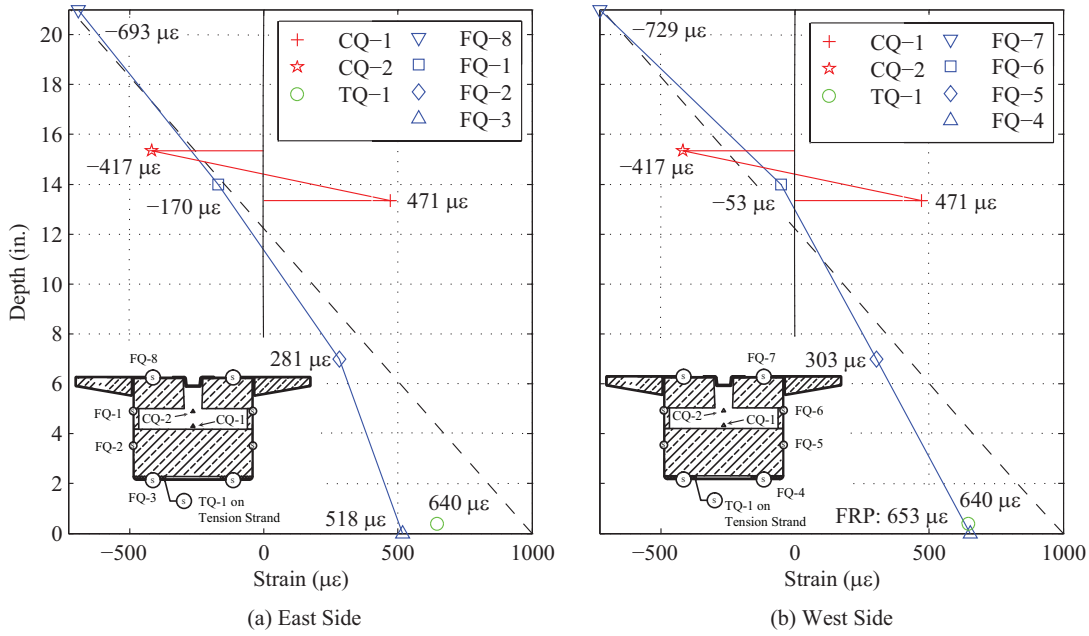

Figure 5-34 North Quarter Strain Profile for Test 3

Data for the quarter point tests showed similar behavior as test 3. Figure 5-35 and Figure 5-36 showed the behavior of HCB 3 under quarter point loads in test 11. The midspan profile indicated the bottom flange was subjected to less tensile strain than expected (Figure 5-35). The gages near the top of the HCB followed the slope of the expected profile more closely. The strains for the arch were also very close to the expected values. No data for the strand was available at midspan for HCB 3. High bending was observed in the arch at the quarter point which was in agreement with results seen in test (Figure 5-36). The tensile and compression region were more equally distributed along the depth of the arch in test 11 than seen in test 3. The top flange gages showed greatly different strain readings though other gage locations had similar readings. The neutral axis location also appeared to be in agreement with the calculated location using Hillman's model. Variations were observed in the top flange gages, but all other strain gages were similar for the three beams. The distribution of the strains profile through the arch also appeared to vary slightly. The magnitude of strain in the arch appeared to vary between

the beams though the loading was identical. Though there were some minor differences, the quarter point load tests showed a linear profile for the FRP and strand, but the arch appeared to be subject to higher bending at the quarter point.

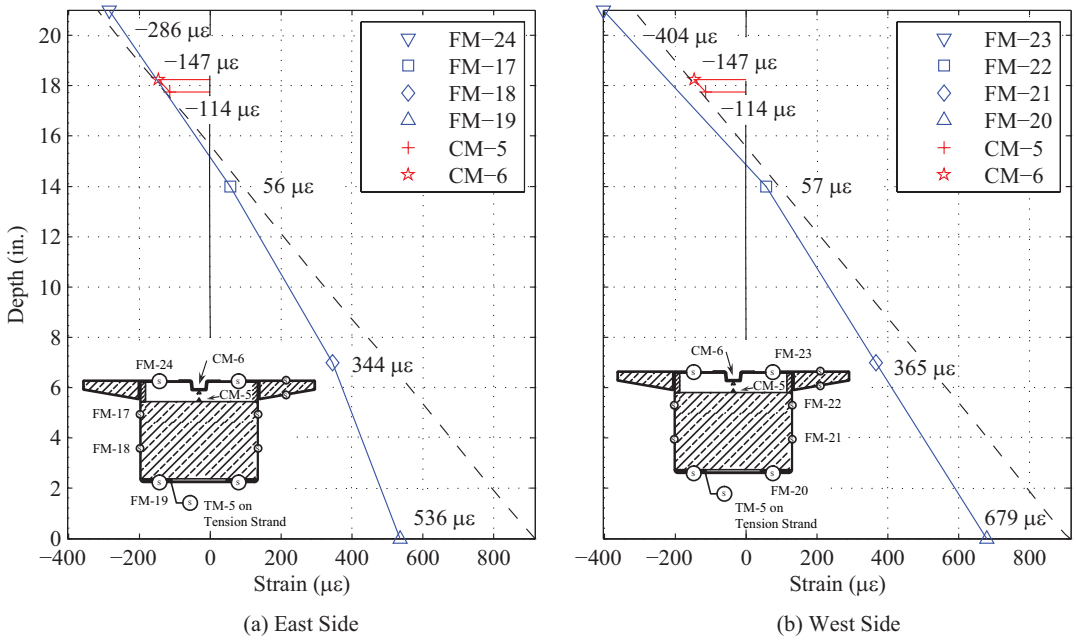

Figure 5-35 Midspan Strain Profile for Test 11

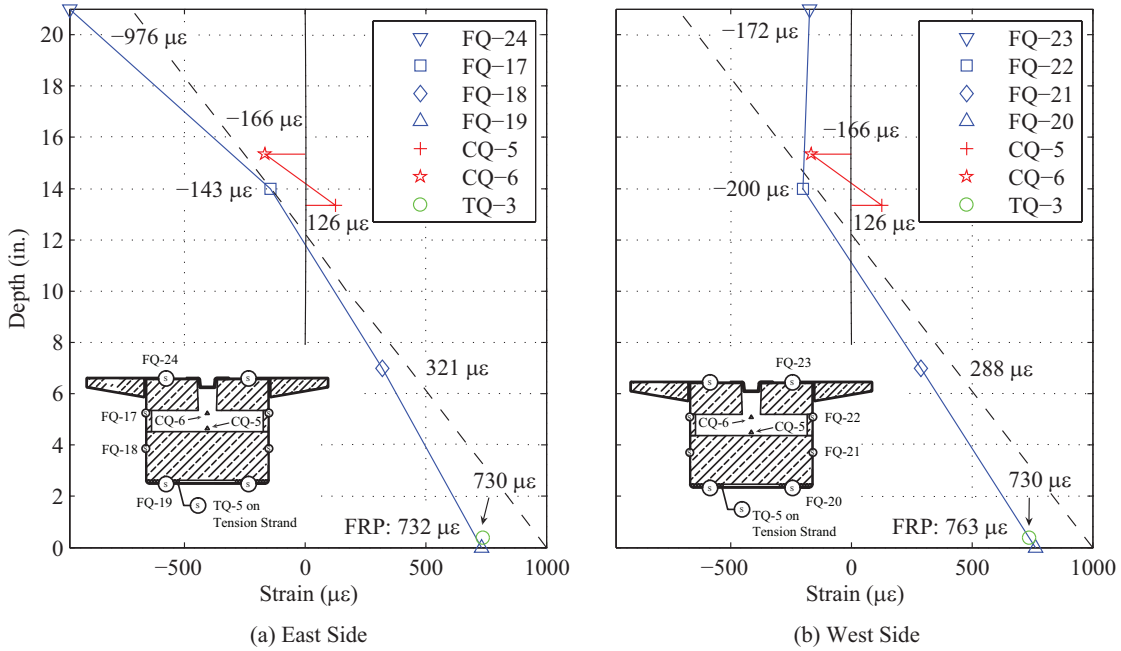

Figure 5-36 North Quarter Strain Profile for Test 11

A number of overall trends can be observed from the strain profiles generated for phase II tests. The shapes of the examined FRP profiles generally followed a linear shape. At midspan, the observed location of the neutral axis based on the FRP gages was in good agreement with the location calculated using the transformed section approach used in Hillman's model. On average, the quarter point neutral axis location appeared to be slightly higher than expected. In many cases, the concrete strain was close to or below the expected strains. The data suggested strain compatibility existed between the tension strand and the bottom flange of the FRP box. In many of the tests the strain values for the two components were very similar. The transformed area approach appeared to provide a conservative estimate for most of the FRP box gages and the tension strand gages.

The transformed section used in Hillman's model predicted maximum strains occurring at the bottom flange, but in many cases the maximum strain was observed in the top flange. The gages on the top flange of the FRP box indicated inherent error in the strain readings.

Differences between the top flange gages adhered towards the east and west side occasionally were on the order of 200%. The error did not appear to be due to torsion as gages mounted on other locations of the FRP box did not show such a large difference for the same tests. The different readings may be due to local effects caused by the proximity of the load points to the gages. However, in some cases the gages read different strains despite not being near the load location. Such large differences were not seen for gages mounted to the bottom of the FRP box. For the bottom flange gages, strains were consistently below expected strains from Hillman's model. With exception to the top flange gages, Hillman's model appeared to slightly overestimate strains in the FRP box.

For the quarter point tests, the strains in the concrete showed the arch was very susceptible to local bending between the midspan and the support. All quarter point load tests on all beams showed the bending occurring in the arch was uncoupled from the bending induced in the arch. Tensile strain was present in the bottom of the arch despite being located above the neutral axis indicated by the FRP gages. Hillman's model did not account for local bending occurring in the arch. The use of strain compatibility for the arch appeared impractical when the quarter point was subjected to high concentrated loads. However, prior to the placement of the cast-in-place deck, the HCB was not expected to experience concentrated loading as was used in phase II. Hillman's model approximates the strains in the FRP and strand well and often overestimated strains. However, the arch behavior between the supports and midspan appeared to be more difficult to model using the transformed area approach. The non-composite loads for the hybrid composite beam need to be carefully considered. Local bending should be considered during design if the beam is expected to undergo concentrated loading. Otherwise, the

transformed area approach appears to provide a fair estimate for the arch behavior for the midspan and supports.

5.3.6. Summary of Phase II Results

Linear elastic behavior was observed for the FRP and strand strains. Residual deformations were not observed for the FRP and strain. Most concrete gages showed linear strains in the arch though some unexplained non-linearity was present. Despite observed non-linear behavior, the majority of gages showed no permanent deformations. The strain profiles for the FRP and strand gages appeared to follow the profile predicted by the transformed area approach well. The measured FRP and strand strains were usually smaller than predicted. The midspan arch strains appeared to follow the predicted profile. Local effects appeared to cause unusual behavior at the quarter point. Large tensile strains were observed in the quarter point of the arch which was unaccounted for in Hillman's model. The strain distribution in the arch appeared to differ from the FRP and strand. The strain measured at the supports also appeared to differ from the predictions. Hillman's model approximated behavior of the FRP, strand, and midspan arch well. However, the behavior of the arch at the quarter point and supports suggested the model provide poor prediction of arch behavior.

5.4. Phase III Testing

Phase III testing commenced after the deck concrete reached the design compressive strength. The loading configurations presented in Section 4.6 are summarized in Figure 5-37 for convenience. Three different categories of tests were performed: service moment, service shear, and design moment. Additional test results are presented in Appendix D.

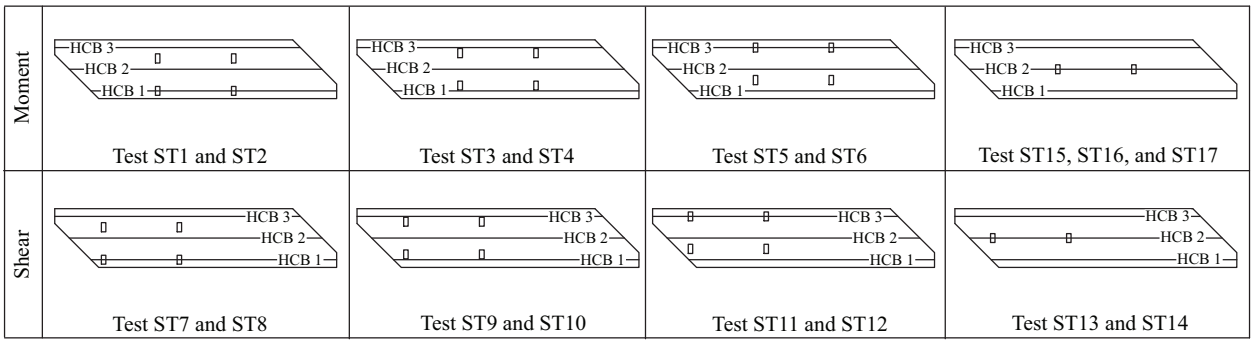

Figure 5-37 Loading Configurations for Phase III

5.4.1. Component Material Behavior

Each component of the HCB was investigated for linear-elastic behavior and permanent deformation after the system was unloaded.

5.4.1.1. Behavior of Fiber-Reinforced Polymer

The behavior of the fiber-reinforced polymer was expected to be linear elastic up to failure. Predicted strains from Hillman's model were not directly comparable because the tested transverse distribution differed from the design value used for Tide Mill Bridge. Hillman's model calculated the location of the neutral axis for the composite section at or near the top of the HCB's along the span length. Because they were the furthest from the neutral axis, the gages on the bottom flange of the beams were expected to register the highest strain in the FRP box. The maximum registered strains for these gages are listed in Table 5-25. The given values represent the highest strain reading among all beams observed at the either midspan or quarter point.

Table 5-25 Summary of Maximum Measured FRP Strain in Bottom Flange

Test Number	Strain (με)	Ultimate Strain (με)	Ratio	Beam Experiencing Max Strain (Gage)
ST1	623	8968	0.07	HCB 1 (FM-3)
ST2	620	8968	0.07	HCB 1 (FM-3)
ST3	580	8968	0.06	HCB 1 (FM-3)
ST4	576	8968	0.06	HCB 1 (FM-3)
ST5	559	8968	0.06	HCB 2 (FM-11)
ST6	555	8968	0.06	HCB 2 (FM-11)
ST7	388	8968	0.04	HCB 2 (FM-11)
ST8	386	8968	0.04	HCB 2 (FM-11)
ST9	401	8968	0.04	HCB 2 (FM-11)
ST10	401	8968	0.04	HCB 2 (FM-11)
ST11	421	8968	0.05	HCB 1 (FQ-4)
ST12	545	8968	0.06	HCB 1 (FQ-4)
ST13	162	8968	0.02	HCB 2 (FM-11)
ST14	160	8968	0.02	HCB 2 (FM-11)
ST15	276	8968	0.03	HCB 1 (FM-3)
ST16	275	8968	0.03	HCB 1 (FM-3)

The location of the maximum strain in the bottom flange varied based on the loading location. For the moment tests using both wheel lines (ST1 to ST6), the maximum strain occurred most often in the bottom flange of HCB 1. For test ST5 and ST6, the maximum strain was seen in HCB 2. The maximum strain locations generally agreed with those seen for maximum beam deflection (Table 5-25). For the shear tests, maximum strains were seen in HCB 2 for tests ST7 to ST10 while HCB 1 had the highest strains for test ST11 and ST12. Unusual behavior was observed for test ST11 and ST12. The maximum stress was measured at the bottom flange of HCB 1 at the quarter point (FQ-4) despite the location of the loading closer to HCB 3. The maximum strain for test ST11 varied from that seen in test ST12 though the tests were apparently identical. The variation was not seen for the other tests. As mentioned previously, the reaction for HCB 1 at the north end was expected to be greatest due to its location at an obtuse corner. This may be the cause for the relatively high strains in FQ-4. The single wheel line tests

(ST13 to ST16) showed similar behavior to the two wheel line tests. The maximum strains for the high moment tests frequently occurred in HCB 1. For the shear tests, the highest strain was shown in HCB 2.

One possibility for unusual behavior observed during testing for the maximum strains, may be related to the location of the measurements. Unlike previous phases of testing, the location of maximum moments and shear in the system was not apparent due to the transverse load distribution and skewed geometry of the system. The bearing conditions may affect the load distribution. The measurements were taken at the north quarter point and midspan. However, the actual maximum stress may not be occurring at the measurement locations. Thus, the maximum measured strain may not indicate which beam had the absolute greatest strains in the bottom flange. Without obtaining the full moment diagram for all three beams, the locations of the absolute maximum strains cannot be accurately determined.

Observation of the load-strain relationships showed linear behavior in all functioning gages. Strains for HCB 1 at midspan appeared greater than observed for the other two beams. Some results for test ST1 are presented in Figure 5-38. For HCB 1, the difference between the gage on the east and west side of the flange was minimal (Figure 5-38). However, a slightly greater difference was observed between gages for HCB 3 (Figure 5-39). The behavior for gage FM-20 also appeared to have slight non-linearity though the strain returned to zero when the system was unloaded. The difference was observed for both moment and shear tests. The cause for the difference was unexplained. Higher strains were observed for HCB 1 than HCB 2 and 3. The cause for the difference may be due to the end fixity provided by the diaphragms. For HCB 1, the diaphragm did not fully enclose the beam unlike HCB 2 and 3 (Figure 4-17 and Figure

4-18). Thus, the restraint at the support may be less than for beam 2 and 3, and the moment would be higher at the midspan of HCB 1 because of the lower degree of end fixity.

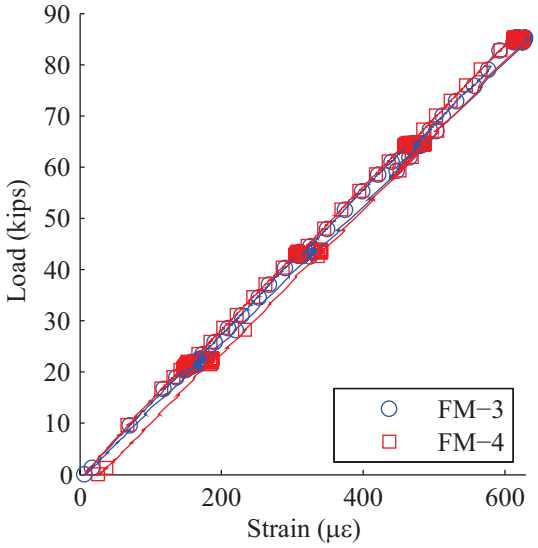

Figure 5-38 Load vs. Strain for Test ST1 for HCB 1

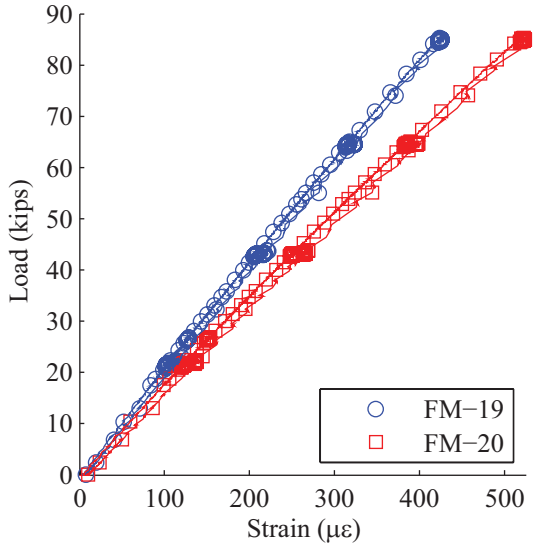

Figure 5-39 Load vs. Strain for Test ST5 for HCB 3

5.4.1.2. Behavior of Prestressing Strand

For phase III testing, the number of available channels limited the instrumentation that could be recorded at one time. Only the strand gages for the beam which was expected to have the most load were connected to the data system. The midspan gage for HCB 3 (TM-5) was not functional during testing. The strain in the strand was expected to be close to but a little less than the strain in the bottom flange gages. The maximum measured strand strains are presented in Table 5-26.

For the moment tests (ST1 to ST6), the quarter point strand strain in the beam of interest appeared to decrease as the load was moved transversely from HCB 1 to HCB 3. The trend also appeared in the strains for the midspan gages in HCB 1 and 2. The explanation in change may be due to the offsets between the midspan and quarter points between beams due to the skew. For the tests ST1 and ST2, the load points were placed closest to the north quarter point of HCB 1. As the load patches were moved towards the east side (HCB 3), they were placed farther from the north quarter point for the respective beam. In each pair of apparently identical tests, the strains appeared similar though there were a few cases where differences were observed. For instance, in test ST1 and ST2, the strain at midspan appeared to decrease by 65 με (Table 5-26). Also, the strain for the quarter point increased by 183 με between test ST11 and ST12. The cause for the difference was unexplained. A trend in the data showed the quarter point and midspan strain in the moment tests (ST2 to ST6) varied more than for the shear tests (ST7 to ST12). The quarter point strains were approximately 75% of the midspan strains for the moment tests. As was discussed for the previous phases, the bond between the strand and the FRP may have remained intact. Even for the higher loadings for Phase III, the strain in the strand appears to

vary along the length. For the shear tests, the strains at midspan and quarter point were much more similar.

Table 5-26 Summary of Maximum Phase III Strand Strains

Test Number	HCB	Strain (με)		Ultimate Strain (με)	Ratio	
		Quarter Point	Midspan		Quarter Point	Midspan
ST1	1	499	619	9474	0.05	0.07
ST2	1	475	554	9474	0.05	0.06
ST3	2	366	484	9474	0.04	0.05
ST4	2	359	485	9474	0.04	0.05
ST5	3	313	N/A	9474	0.03	N/A
ST6	3	321	N/A	9474	0.03	N/A
ST7	1	370	360	9474	0.04	0.04
ST8	1	368	375	9474	0.04	0.04
ST9	2	326	358	9474	0.03	0.04
ST10	2	318	356	9474	0.03	0.04
ST11	3	391	N/A	9474	0.04	N/A
ST12	3	574	N/A	9474	0.06	N/A
ST13	2	145	150	9474	0.02	0.02
ST14	2	134	144	9474	0.01	0.02
ST15	2	176	235	9474	0.02	0.02
ST16	2	177	233	9474	0.02	0.02

Inspection of the load-strain plots for the strand showed linear elastic behavior and no permanent deformation upon unloading of the system. Test 1 was indicative of the moment tests with the exception of the difference between midspan and quarter point strains as mentioned previously (Figure 5-40). The strains at both locations increased linearly with increasing load. In the majority of the tests, linear-elastic behavior was observed for the strands, and the data indicated no permanent damage took place as gages registered zero strain when the system was unloaded.

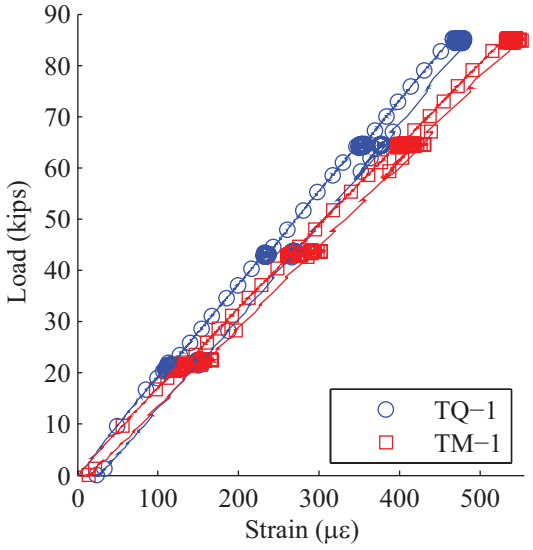

Figure 5-40 Load vs. Strand Strain for Test ST1

5.4.1.3. Behavior of Concrete Arch

For phase III, a different data acquisition system was used to record data from the vibrating wire gages. Because the new data system recorded data at a slower rate than the primary system, readings were taken at the following load increments: 21.5 k, 43 k, 64.5 k, and 85 k for the dual wheel line tests (ST1 to ST12); 10.5 k, 21 k, 31.5 k, and 43 k for the single wheel line tests (ST13 to ST16). Thus, the load-strain plots for the gages were made from a much smaller set of data than the other instrumentation. Additionally, a few gages were not operational prior to and during testing. Other gages that were operational before testing returned erroneous measurements when higher load increments were reached.

The data from phase III testing showed much of the arch was under tensile strains. Table 5-27 gives the maximum strains of the top and bottom gage at each location when the system was subject to the maximum applied load. Gages CQ-1 and CQ-3 were at the bottom of the arch at quarter point and were nonresponsive prior to testing. During loading, the system recorded off-scale readings from many other quarter point gages. As a result, much of the quarter point data

was not analyzed. From the available data at the quarter point, large tensile strains were observed. From the material tests, the experimental modulus of rupture was found to be 580 psi, and the experimental modulus of elasticity was 3820 ksi which corresponds to a strain at cracking of 152 με before cracking occurred. However, the measured strains at the quarter point were found to be much higher than the cracking strain. The strains at midspan were also found to be high though slightly smaller than the cracking strain. In contrast, compressive strains were seen at the support gages. The compressive strains were relatively small compared to the other gage locations.

Table 5-27 Summary of Maximum Arch Strains

Test Number	Midspan Strains (με)			Average	Quarter Point Strains (με)			Average	Support Strains (με)			Average
	HCB 1	HCB 2	HCB 3		HCB 1	HCB 2	HCB 3		HCB 1	HCB 2	HCB 3	
ST1	129	114	107	117	1578	N/A	403	**991**	-64	-28	-14	-35
ST2	129	113	106	116	N/A	N/A	402	**402**	-64	-28	-13	-35
ST3	114	110	109	111	N/A	N/A	469	**469**	-44	-23	-15	-27
ST4	112	107	106	108	N/A	N/A	429	**429**	-46	-30	-16	-31
ST5	103	108	110	107	N/A	N/A	446	**446**	0	-27	-21	-16
ST6	101	106	108	105	N/A	N/A	411	**411**	-29	-26	-20	-25
ST7	57	97	100	85	830	N/A	440	**635**	-20	-14	-13	-16
ST8	56	97	101	85	828	N/A	437	**633**	-20	-13	-13	-15
ST9	57	98	119	91	830	N/A	589	**710**	-12	-5	-19	-12
ST10	56	97	119	91	N/A	N/A	594	**594**	-12	-5	-18	-12
ST11	45	72	110	75	902	N/A	537	**720**	-12	5	-18	-8
ST12	44	71	110	75	819	N/A	523	**671**	-11	4	-18	-8
ST13	25	35	50	37	340	129	155	**208**	-6	6	-5	-2
ST14	24	35	48	36	333	128	152	**204**	-6	5	-4	-2
ST15	57	52	56	55	439	157	126	**241**	-16	-17	-7	-13
ST16	57	51	54	54	446	162	133	**247**	-17	-17	-6	-13

Bold values represent strains greater than cracking strain of 152 με

Variations between the same gage locations in each beam were observed in the strain readings (Table 5-27). Though variation in strain between beams was expected due to the load locations and the skewed geometry, the variation did not appear to follow any expected trends. The variation was most apparent in the available readings for the quarter point strain gages for HCB 1 and 3. For test ST7, the max strain at quarter point of HCB 1 was 830 με while at the same location for HCB 3 the strain was 440 με (Table 5-27). The higher strain in HCB 1 was expected as the applied loads were closest to the HCB 1. However, the loads for test ST10 were placed closest to HCB 3; the strains measured for HCB 1 remained higher than HCB 3. The strains at the quarter point for HCB 1 were consistently higher than HCB 3 for all tests. Comparing measured strains at each gage location for each beam to the average strain showed the degree of variation present for other gage locations (Table 5-27). Though the strains varied by beam, the strain readings for the same beam showed good agreement between the identical pairs of tests at each gage location (i.e. midspan of HCB 1 for ST1 and ST2).

The variation in strain readings may have been caused by a number of factors. As mentioned previously, the geometry of the system may affect the distribution of load to the arches of each respective beam. Because the system consisted of a skewed layout, the exact distribution of load was unknown. The boundary conditions may have affected the load distribution. The placement of the four loading patches could have also had a local effect on the readings. For phase II, local bending was observed in the arch when loads were applied at the quarter point. Similar local effects may be occurring due to the location of the four loading patches.

Though the magnitude of strains from Hillman's model cannot be quantitatively compared to results, a qualitative comparison can be made. Using the dead and applied loads for

both the non-composite and composite section, the arch was calculated to be in tension throughout its depth at the quarter point. At the midspan, the bottom of the arch was calculated to be in tension and the top was expected to be in compression. The predicted stress at the bottom of the arch was approximately 1.94 ksi which was much greater than the tested tensile strength seen during cylinder testing. The stress in the bottom of the arch (as determined from measured strain) was 1.67 ksi which was also above the tensile strength of the concrete. Though the model showed tension in the arch under both non-composite (HCB only) and composite loads (HCB and deck), maximum expected tensile stresses were not checked against the tensile strength of the concrete. The strain readings for the quarter point suggested no stiffness is provided by the arch because it was past the cracking strain. Though the concrete in the arch may have cracked, the arch should continue to carry through the two strands placed in the arch to anchor the stirrups. These strands are not accounted for in calculations, but they are placed in the bottom of the arch and should serve as a means to carry tensile force.

The load-strain plots for the arch concrete showed both linear and non-linear behavior in the tests conducted. For the tests ST1 to ST6 for high moment, linear behavior was mostly observed at the midspan and supports. The strain returned to zero when the system was unloaded. From the available data at the quarter point, the behavior of the arch was different than found at the midspan and supports. The strains varied from the loading and unloading phases of the test. Test ST1 was representative of that found in tests ST1 to ST6 (Figure 5-41). The slope of the strain increase appeared to be slightly non-linear. However, when the system was completely unloaded the gage did not show any residual strain. At the support, the strain at the bottom of the arch showed slightly greater compressive strains than the top indicating a small amount of negative bending. In contrast, a small amount of positive bending was seen at

midspan. Both gages at the top and bottom of the arch registered tensile strains at midspan (Figure 5-41). During unloading, the slope of the line appeared linear and showed no residual strain. The quarter point showed a much greater tensile strain than the midspan. As discussed previously, gage CQ-1 was not operational and gage CQ-2 recorded erroneous readings during some of the higher load increments. Though the arch experienced high tensile strains, the strains returned to zero for the unloaded system. For tests ST3 to ST6, the load-strain relationship was similar to test ST1, but the magnitudes of strains decreased at all gage locations.

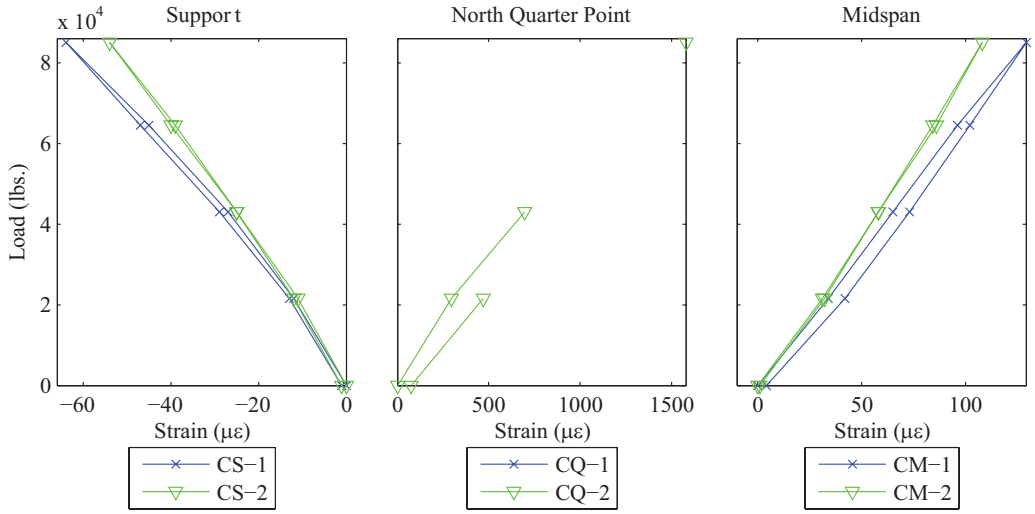

Figure 5-41 HCB 1 Arch Strains for Test ST1

For tests ST7 to ST12, higher shear and lower moment were expected due to the location of the loading. The magnitudes of strains observed at the supports and midspan decreased from those observed in tests ST1 to ST6. The strains at the supports appeared to have a non-linear increase in strain though the magnitudes of strain were small. For tests ST7 and ST8, the strains in the top and bottom of the arch near the support were very similar and indicated a small amount of positive bending (Figure 5-42). For test ST7, the strains at the top and bottom at midspan were nearly identical. However, for tests ST9-ST12, the strains varied for the top and bottom gage (Figure 5-43). The midspan gages all indicated tension and a small degree of positive bending

and the support gages indicated negative bending. As the load location moved from test ST7 to ST12, the magnitude of strain at midspan increased. This was due to the location of the four tire patches being located farther away from the support of the beam of interest.

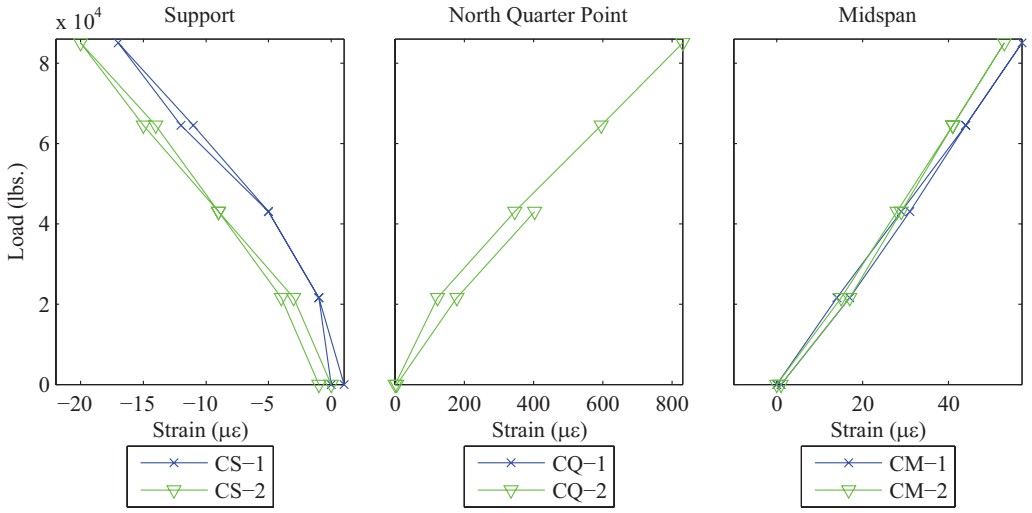

Figure 5-42 HCB 1 Arch Strains for Test ST7

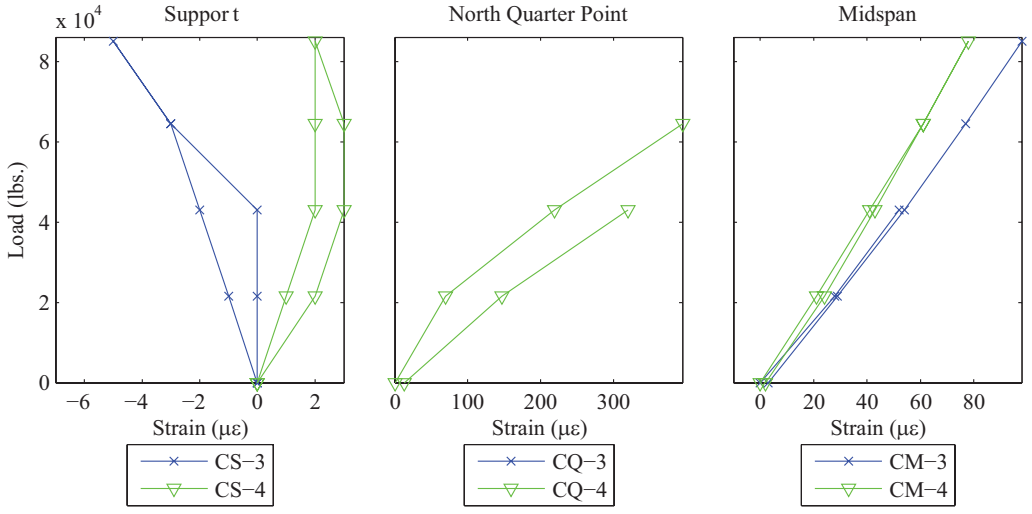

Figure 5-43 HCB 2 Arch Strains for Test ST9

Most of the gages at the midspan and supports showed linear behavior. The arch was consistently shown to be in tension at the midspan and quarter point. Compressive strains were observed near the support. With exception to the quarter point gages, linear-elastic behavior was noted in the majority of the gages. Non-linear behavior was present in a number of gages, but the

strains appeared to return to zero when the system was unloaded indicating no residual deformation. Typically, non-linear behavior results in residual response when the structure is unloaded. However, the unloading phase of the tests showed non-linear behavior as well and a return to zero strain. Also unexplained was the cause for the non-linear behavior in select support gages. The strains in the support gages were very low and well within the linear-elastic range of the arch concrete. One cause for the slight non-linearity seen for some gages may be due to the long recording interval for the vibrating wire gages. After the secondary data acquisition was set to record, a period of two to three minutes was necessary to individually scan all of the gages. During the recording interval, the load may have fluctuated slightly due to relaxation in the pump. The load was held as steady as possible, but keeping load constant was difficult to maintain during the entire duration of the interval.

For phase III testing, the gages in the bottom of the arch for HCB 1 and 2 were not functioning. Thus the complete behavior of the arch could only be obtained from HCB 3. Observing both gages at the quarter point of HCB 3 for test ST5 and ST6, revealed the bottom gage was registering very small tensile strains while the top of the arch was registering high tensile strains. This difference would suggest a large negative bending. However, because the system is a simple span, the development of high negative moments at the quarter points does not seem likely. Similar behavior was observed for test ST11 and ST12. Gage CQ-5 (bottom of arch) may not have been completely functional though it returned strain values. Otherwise, the small strains in the bottom of the arch are unexplained.

For phase II testing, local effects from the load configuration were determined to have been a cause for large local bending at the quarter point. Though load was not always placed directly over the quarter point, large tensile strains were observed. Observing Hillman's model,

the arch at the quarter point was below the neutral axis of the composite section and thus would be expected to experience positive strains. Though the distribution of load was expected to differ in Tide Mill Bridge from the test setup, the model provided an estimate for the behavior of the arch. Hillman's model calculated a strain of 436 με in the bottom of the arch and 15 με in the top. Almost the opposite behavior was seen from the experimental data seen for HCB 3. The strain at the top of the arch was approximately 400 με while the bottom was 9 με. The cause for the reversal of the strain profile was unknown. The use of Hillman's model for the arch appeared to be inappropriate as large differences in magnitude and sign of strains were observed.

5.4.1.4. Summary of Component Material Behavior

For the tests ST1 to ST16, linear-elastic behavior was observed in the strand and the FRP. As expected, strains for the moment tests (ST1 to ST 6) were higher than the shear tests (ST7 to ST 12). The unloaded system showed no residual strains in the FRP and strand. The concrete arch behavior was different than the FRP and strand. The quarter point gages showed strains above the tensile strain limit of the concrete. Concrete strains at some locations showed non-linear behavior though the strain magnitude was small. Strains returned to zero when the system was unloaded. No damage was observed in any of the components during the service load tests.

5.4.2. System Behavior

The system behavior of the three-HCB test specimen was examined to provide a basis for predicting behavior of Tide Mill Bridge. Strain profiles were constructed from strain data from each component of the composite section. The load versus deflection behavior of the system was investigated for the various loading configurations. Load distribution factors were experimentally determined for moment and shear using deflection, strains, and load

measurements. A final test was performed to load the system with the design service live load and observe resulting behavior.

5.4.2.1. Strain Profiles

Strain profiles for the composite section (HCB and CIP deck) were created by using the strain gages on the FRP box, strain gages on the prestressing strand, vibrating wire gages, and strain gage on the longitudinal reinforcement in the deck. Because data from all gages was not available, complete strain profiles were limited to a few locations. Hillman's model provided a calculated location for the neutral axis. However, since the transverse load distribution was different from Tide Mill Bridge, the model results were not compared to measured values. Neutral axis locations were calculated from the data at the midspan (Table 5-28). The average of the east and west FRP gages combined with the strand and arch gages were used to establish a linear trend line. The values were compared to the predicted location of 21.8 in. The average ratio of experimental to predicted neutral axis locations in the tests was slightly lower than 1. The lower ratio may be due to a higher than predicted beam stiffness as was seen in previous phases of testing. In general, the experimental data agreed well with the predicted location.

Table 5-28 Comparison of Midspan Neutral Axis Location

Test	Beam	Experimental	Predicted	Ratio
ST1	HCB1	22.0	21.8	1.01
ST2	HCB1	21.4	21.8	0.98
ST3	HCB2	21.1	21.8	0.97
ST4	HCB2	21.1	21.8	0.97
ST5	HCB3	22.3	21.8	1.02
ST6	HCB3	22.2	21.8	1.02
ST7	HCB1	20.3	21.8	0.93
ST8	HCB1	20.8	21.8	0.95
ST9	HCB2	20.8	21.8	0.95
ST10	HCB2	20.8	21.8	0.95
ST11	HCB3	22.1	21.8	1.01
ST12	HCB3	20.1	21.8	0.92
ST13	HCB2	20.8	21.8	0.95
ST14	HCB2	20.8	21.8	0.96
ST15	HCB2	20.4	21.8	0.94
ST16	HCB2	20.4	21.8	0.93
Average for HCB 1		21.1	21.8	0.97
Average for HCB 2		20.8	21.8	0.95
Average for HCB 3		21.7	21.8	0.99
Overall Average		21.1	21.8	0.97

The complete strain profile at midspan could only be created for HCB 2 because the longitudinal deck gages at this location for HCB 1 and 3 were damaged. Figure 5-44 shows the strain distribution through the depth of the composite section for test ST3. Overall, the strain profile was approximately to be linear and the gages on the east and west face of the beam were in good agreement. Strain measurements in the arch and in the strand were close to the interpolated strain profile of the FRP gages suggesting strain compatibility was maintained at the midspan (Figure 5-44). Similar results were seen in test ST4.

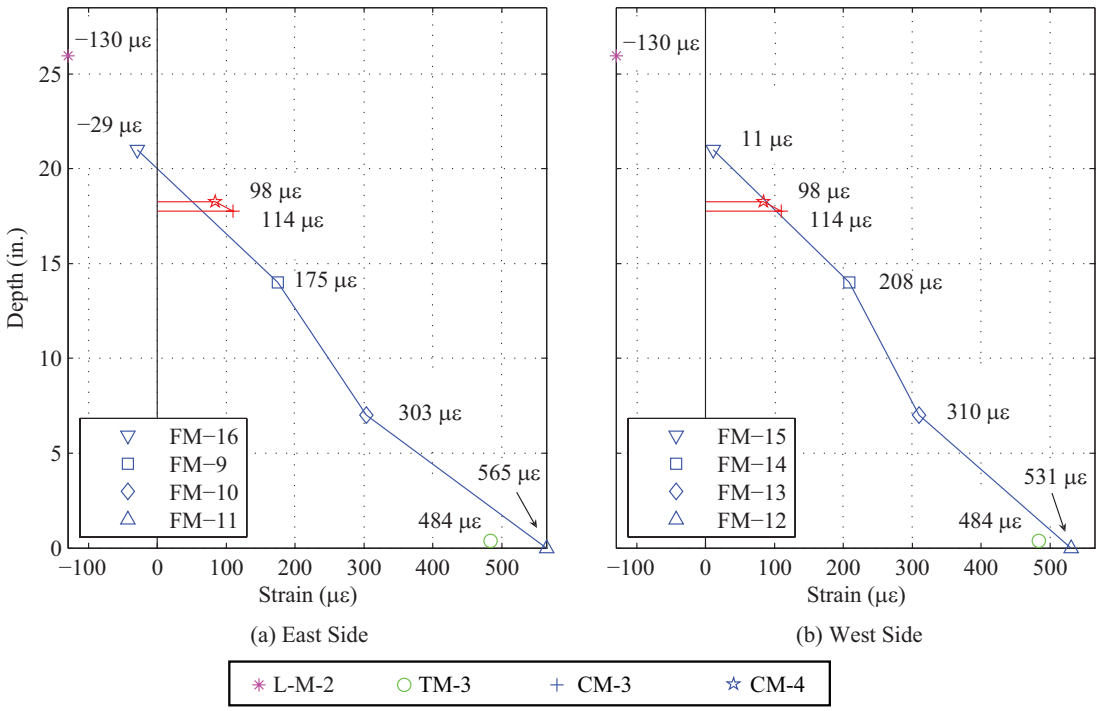

Figure 5-44 HCB 2 Midspan Strain Profile for Test ST3

At the quarter point for test ST3, similar features to the midspan were observed. The strain profile created by the gages on the east face was approximately linear (Figure 5-45). Though the profile for the west face did not appear to have a linear profile, review of the test data showed gage FQ-12 consistently registered less strain than FQ-11. The magnitudes of strain were smaller compared to the midspan profile. The concrete strain readings were not available when the beam was subjected to maximum load. The strand strain was similar to the strain for the bottom flange of the FRP. The observed neutral axis location appeared to agree with the predicted location.

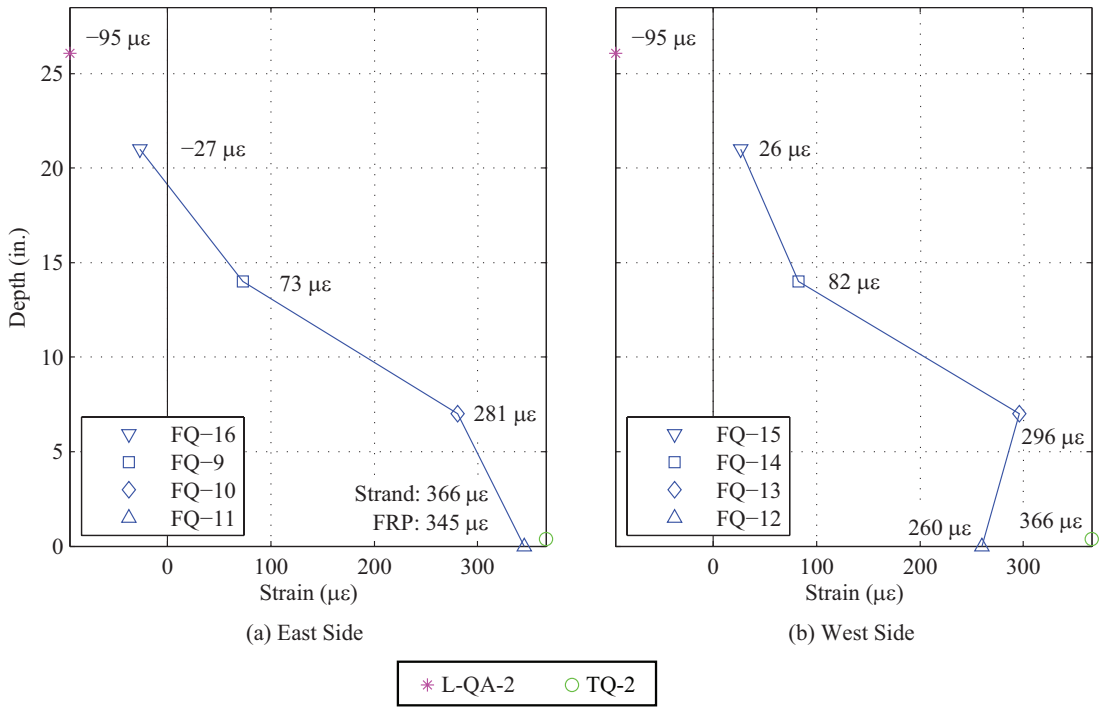

Figure 5-45 HCB 2 Quarter Point Strain Profile for Test ST3

For the shear tests performed on HCB 2, fairly linear profiles were observed. For the midspan, the profile follows a linear path from the bottom flange to the upper portion of the web (Figure 5-46). The concrete strains and the top flange strains showed a slightly steeper slope than the other strain gages. The behavior was observed on both the east and west face of the beam. The magnitude of strain decreased from the moment tests (ST1 to ST6) as was expected. The deck gages followed the linear profile created by the strand and lower FRP gages. The magnitudes of strain were lower than observed in test ST3.

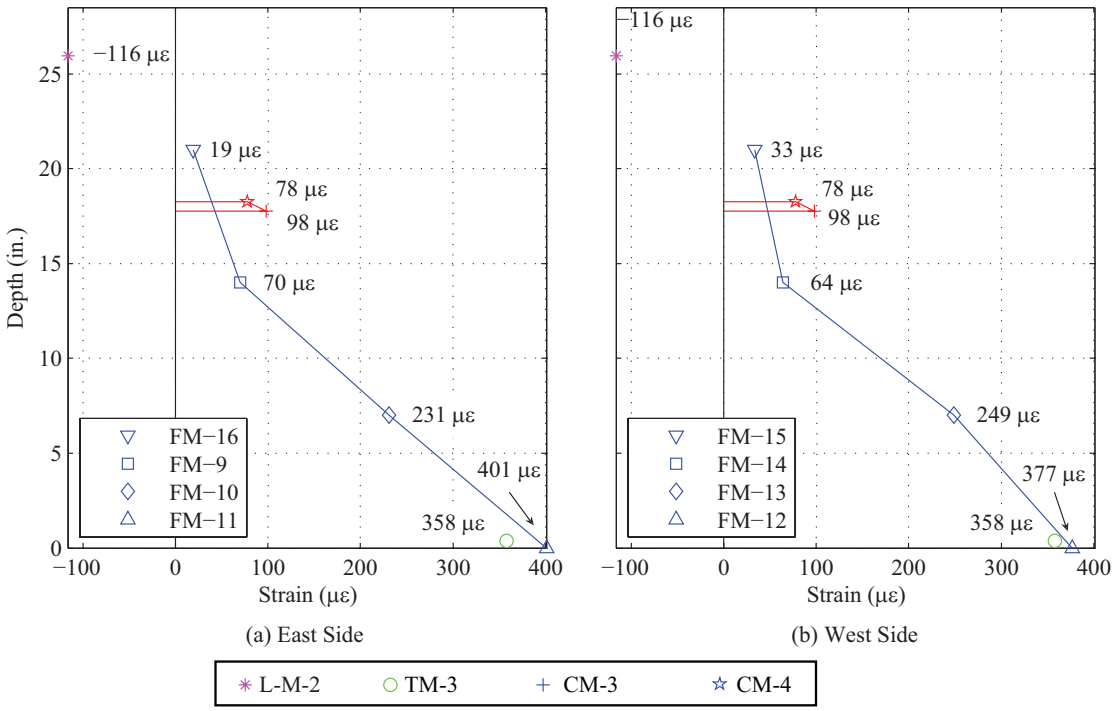

Figure 5-46 HCB 2 Midspan Strain Profiles for Test ST9

The strain profiles for the quarter point for test ST9 were also examined (Figure 5-47). As expected, the strain magnitude decreased from those observed at midspan. The strand strain appeared to remain relatively high compared to the bottom flange FRP gages. The shape of the profile also appeared to differ from that observed at midspan. The top flange and deck gage indicated a shallower slope for that profile than seen for the other FRP gages. The location of the neutral axis appeared to agree with the predicted location from the model.

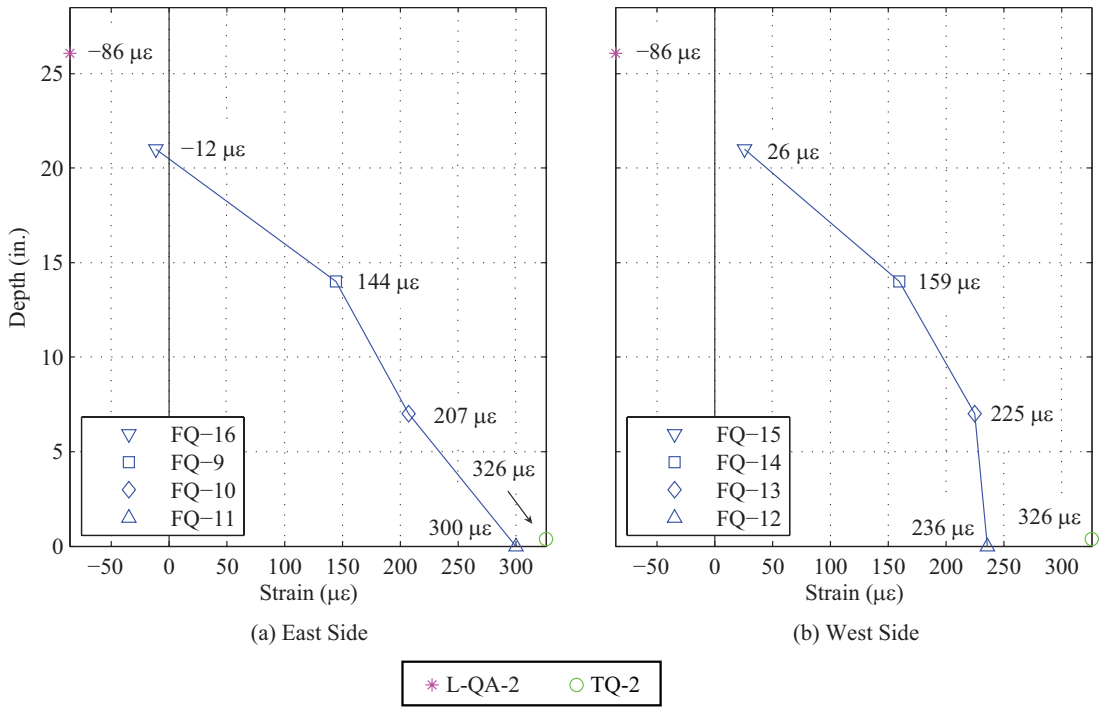

Figure 5-47 HCB 2 Quarter Point Strain Profiles for Test ST9

Tests ST15 and ST16 consisted of one wheel line placed directly over the midspan and centerline of HCB 2. The shape of the profile for the midspan appeared to be the same as observed in test 3 except the arch showed greater tensile strains than would be expected from the profile of the FRP gages (Figure 5-48). The quarter point arch strain does not follow the profile of the FRP strain. The magnitudes of strain in the FRP, strand, and deck gages were also smaller than test ST3 despite the load being centered over HCB 2 indicating load was distributed to the other girders. With exception of the arch strains, the strand and deck appear to maintain strain compatibility with the FRP box. The neutral axis location was also in agreement with Hillman's model. For the quarter point, the strain profile had slight curvature (Figure 5-49). The strains for the bottom flange and the bottom portion of the web were similar; this was seen for both faces of the beam. The tensile strain for the arch was larger than expected from the FRP profile.

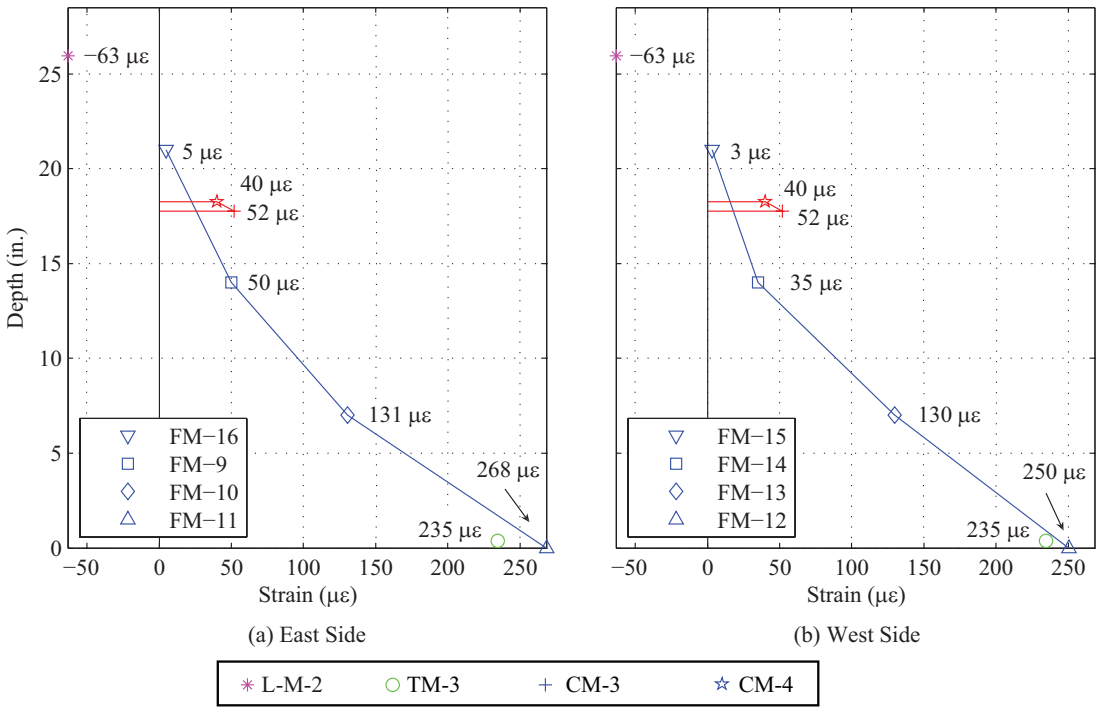

Figure 5-48 HCB 2 Midspan Strain Profiles for Test ST15

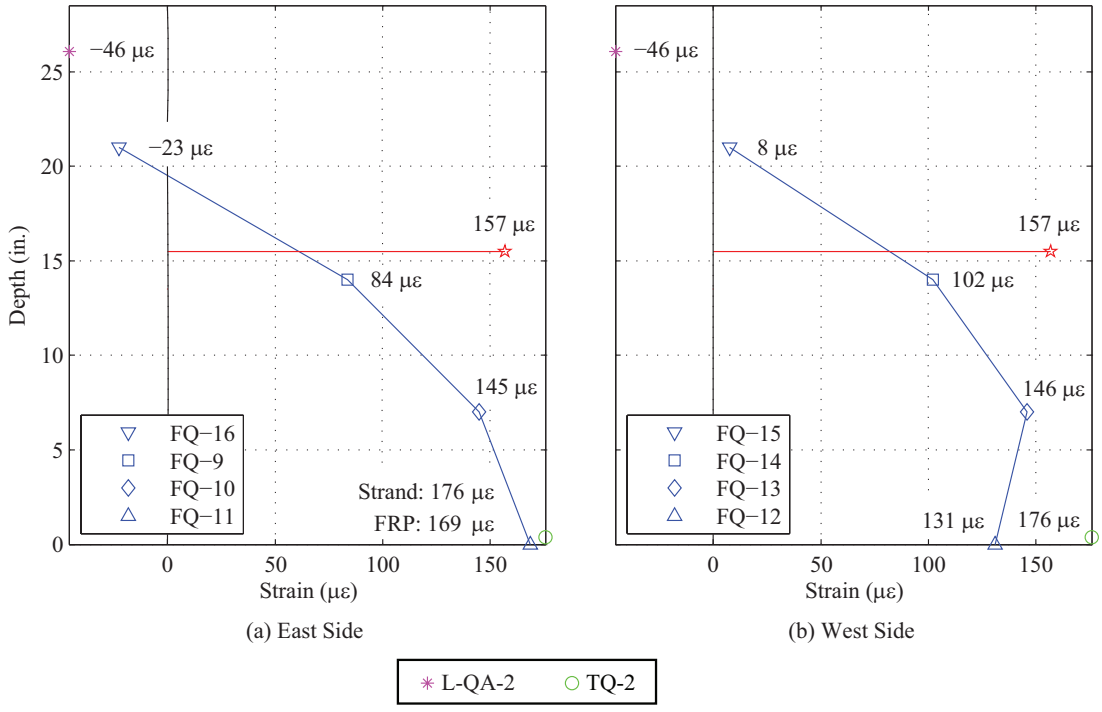

Figure 5-49 HCB 2 Quarter Point Strain Profiles for Test ST15

Overall, the strain profiles of the beams appeared linear with respect to the FRP gages, strand gage, and deck gages. The interpolated neutral axis location using experimental data was in agreement with the predicted location from Hillman's model. In some tests, the arch appeared to follow the strain profile at midspan. In others, the midspan strains were greater than the FRP strain profile. The quarter point arch strains were much larger than the FRP strain profile. Strain compatibility for the strand and deck appeared to apply as the strain measurements were close to the strain profile of the FRP. The transformed area approach appeared to be valid for the FRP, strand, and deck concrete for service loads; but the approach did not predict arch strains well.

5.4.2.2. Load-Deflection Behavior

For phase III testing, linear behavior was observed in the load-deflection behavior of the beams. The deflections returned to near zero indicating permanent deformation did not occur. Table 5-29 presents the maximum measured deflections for each test. The location of the potentiometers is given in Figure 3-27. From the results, the deflection of the exterior girders was shown to be greater than the interior girder.

Table 5-29 Summary of Maximum Measured Deflections

Test Number	Load Pattern	Load Magnitude (kips)	Deflection (in.)										Beam with Max Deflection (Potentiometer)
			HCB1			HCB 2			HCB 3			Max	
			N. Qtr.	Mid	S. Qtr.	N. Qtr.	Mid	S. Qtr.	N. Qtr.	Mid	S. Qtr.		
ST1	SL	85	0.42	**0.79**	0.61	0.48	0.71	0.47	0.51	0.67	0.44	0.79	HCB 1 (WP-2)
ST2	SL	85	0.41	**0.77**	0.58	0.47	0.69	0.44	0.50	0.65	0.43	0.77	HCB 1 (WP-2)
ST3	SL	85	0.36	0.69	0.51	0.44	0.67	0.43	0.53	**0.70**	0.46	0.70	HCB 3 (WP-8)
ST4	SL	85	0.35	**0.66**	0.47	0.45	0.63	0.48	0.48	0.65	0.40	0.66	HCB 1 (WP-2)
ST5	SL	85	0.32	0.60	0.43	0.42	0.63	0.36	0.52	**0.70**	0.43	0.70	HCB 3 (WP-8)
ST6	SL	85	0.33	0.61	0.44	0.42	0.63	0.36	0.52	**0.70**	0.43	0.70	HCB 3 (WP-8)
ST7	SL	85	0.22	0.45	0.36	0.26	0.44	0.25	0.32	**0.45**	0.30	0.45	HCB 1 (WP-2)
ST8	SL	85	0.21	0.42	0.33	0.24	0.41	0.23	0.30	**0.43**	0.29	0.43	HCB 3 (WP-8)
ST9	SL	85	0.23	0.45	0.36	0.29	0.48	0.29	0.35	**0.54**	0.38	0.54	HCB 3 (WP-8)
ST10	SL	85	0.20	0.40	0.33	0.25	0.44	0.26	0.33	**0.50**	0.35	0.50	HCB 3 (WP-8)
ST11	SL	85	0.18	0.35	0.30	0.24	0.42	0.28	0.34	**0.54**	0.38	0.54	HCB 3 (WP-8)
ST12	SL	85	0.17	0.33	0.27	0.22	0.39	0.24	0.31	**0.50**	0.35	0.50	HCB 3 (WP-8)
ST13	WL	43	0.17	0.17	0.13	0.11	0.19	0.08	0.16	**0.21**	0.15	0.21	HCB 3 (WP-8)
ST14	WL	43	0.06	0.14	0.10	0.08	0.16	0.04	0.13	**0.18**	0.12	0.18	HCB 3 (WP-8)
ST15	WL	43	0.19	0.29	0.21	0.19	0.28	0.13	0.23	**0.31**	0.17	0.31	HCB 3 (WP-8)
ST16	WL	43	0.15	0.29	0.19	0.19	0.28	0.18	0.23	**0.29**	0.17	0.29	HCB 3 (WP-8)

Load Patterns:

SL – Service Loading with two truck axles

WL – Service Loading with one wheel line

A number of explanations can be offered for the higher deflections observed in the exterior girders (Table 5-29). When the deck was constructed, the edge of the deck was set back from the edge of the exterior beam flanges by 7 in. to construct formwork. Thus the effective width of the deck for the exterior girder was 41 in. compared to 48 in. for the interior girder. The maximum deflection for all tests was found to occur in HCB 1, when the west wheel line was directly over the beam's centerline. For tests ST9 and ST10, the east wheel line was centered over HCB 3, but the deflection was notably smaller (Figure 5-28). The diaphragm may have affected the stiffness when the wheel line was placed directly over the beam. HCB 1 was not fully encased in the diaphragm as HCB 2 and 3 were and may have had a lower end fixity that would have allowed it to deflect more. When the load is not placed directly over the beam, the effect of the lower fixity does not appear to cause HCB 1 to deflect more. The cause for the frequency of the maximum deflection to occur in HCB 3 at WP-8 may have been to lower stiffness compared to HCB 1 and 2. As was seen in section 5.3.1, the deflections for HCB 3 were slightly greater than the other beams during phase II testing suggesting the stiffness was lower (Table 5-16 and Table 5-17). The difference in stiffness may be possible because variability may have been introduced during the beam fabrication or during the arch placement. Another possibility was that the absolute maximum deflection was not captured by the potentiometers. The location of the potentiometers was based on the previous two phases of testing. Because of the unsymmetrical nature of the system and the unknown load distribution, the exact location of the maximum displacement was unknown.

The load-deflection plots for the tests showed that the beams were behaving linear-elastically (Figure 5-50). As observed in Table 5-29, the maximum displacement occurred at midspan (WP-2). The difference in deflections seen at the two quarter points (WP-1 and WP-3)

was due to the unsymmetrical loading and construction of the system. A small residual displacement was observed after the system was completely unloaded though non-linear behavior did not occur. The residual displacement was small relative to the maximum observed deflection.

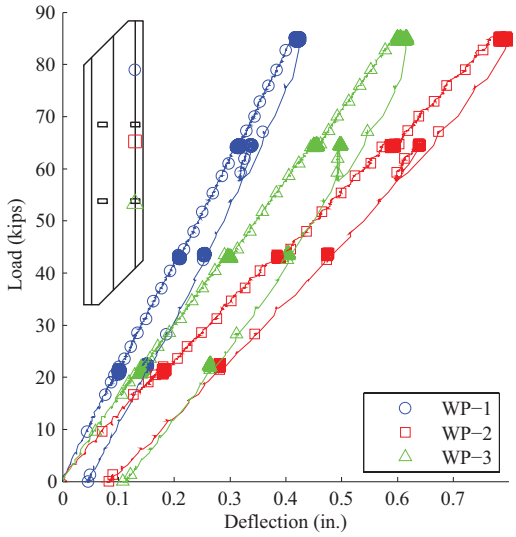

Figure 5-50 Load vs. Deflection for Test ST1

Deflections for test 1 and 2 were noticeably greater than for tests 3 through 6 (Figure 5-51). The interior girder has a higher stiffness because of the greater effective width of the deck, and the deflection was expected to be lower as the load was moved towards the center of the system. For tests 3 and 4, the system was symmetrically loaded. Deflections at the north and south quarter point were identical (Figure 5-51). The deflections returned to zero when the system was unloaded. Though the deflected shape of the system changed based on loading, the variation in deflection remained relatively small.

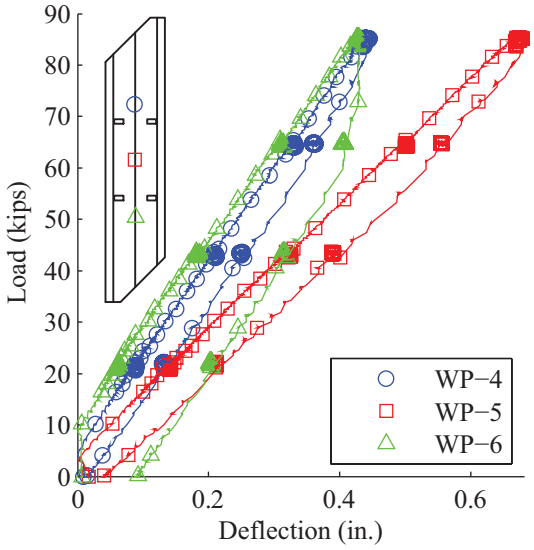

Figure 5-51 Load vs. Deflection for Test ST3

Similar behavior was observed for the high shear tests. Deflections were expected to be much smaller due to proximity of the loads to the north supports of the beams. Linear behavior was also observed in all beams for the tests. For test 7, deflections near the north quarter point were higher than the south quarter point as was expected. The deflections returned to zero indicating no permanent deformation took place. Because of the skewed shape of the deck, the shear loading locations for HCB 2 and 3 were further away from the supports than for HCB 1. Thus, the deflections at the north and south quarter points were more similar for HCB 2 and HCB 3. A problem with the potentiometer at the north quarter point (WP-6) was observed during the later tests (Figure 5-53). The potentiometer failed to record deflection during the lower load increment. This error was also shown for the unloading phase from 85 kips to 64.5 kips. The cause for the problem was unknown. Due to the error in the north quarter point measurement, the maximum deflections for both quarter points appeared identical. However, a higher deflection was more apparent at the north quarter point if the data is corrected. The deflections were corrected for the calculation of distribution factors.

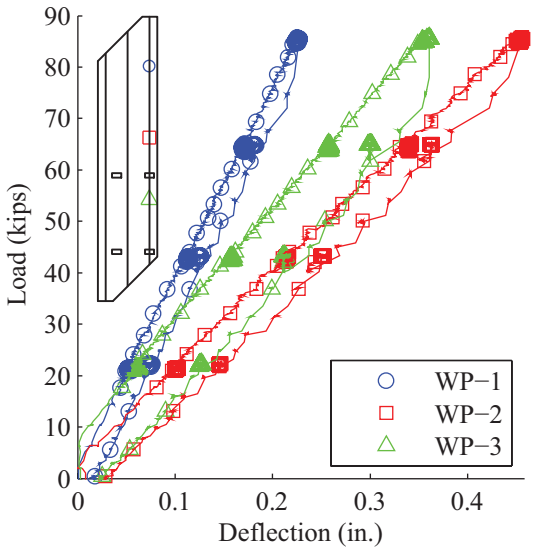

Figure 5-52 Load vs. Deflection for Test ST7

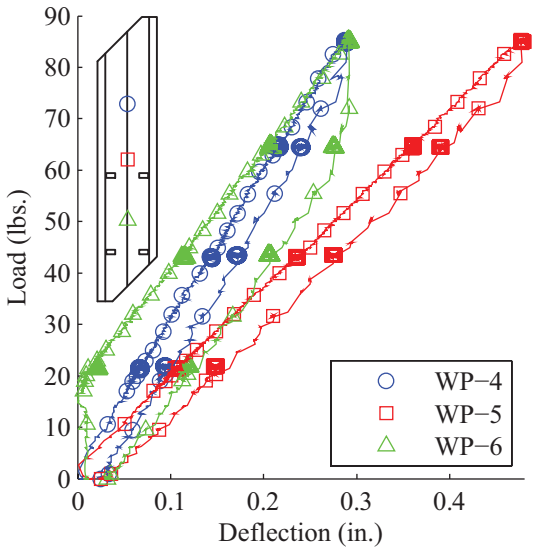

Figure 5-53 Load vs. Deflection for Test ST9

Overall, the load versus deflection behavior for the system showed consistent behavior during the moment and shear tests. Linear-elastic behavior was observed with minimal residual deflections from service loading. Maximum measured deflections appeared to occur at the exterior girders. This may be due to the smaller effective width of the deck for the composite section properties. The unsymmetrical load cases had expected trends in locations of higher and

lower deflections. The potentiometer data will be discussed further in discussion of distribution factors.

5.4.2.3. Load Distribution Factors

A simple method presented by Restrepo was used to calculate load distribution for the three-HCB system (2002). However, for the experimental test setup, the effective deck width for the exterior girders was less than for the interior girders. Thus, section modulus for each girder was considered in the distribution calculation. The formula used by Restrepo was a simplified form of an equation first derived by Stallings and Yoo for use in calculating distribution factors in steel bridges (1993). This formula takes into account differing section moduli by introducing a weighting variable that is a ratio of the *i*th girder section modulus to the typical interior girder section modulus.

Though the difference in section moduli were important to include in the calculation of the distribution factors, the difference led to a ratio of 0.979 and 0.977 for the exterior to interior girder section properties at midspan and quarter point, respectively. With section moduli included in calculations, the influence was relatively small. Another factor for the applicability of the formula is the effect of the skew. Equation 3 was developed for no skew bridges. For the test system, gages were placed on the midspan and north quarter point of each beam and the corresponding section properties were used. Because of the forty-five degree skew, the midspans and quarter points of the beams did not line up transversely; they were offset longitudinally from each adjacent beam by 4 ft (Figure 5-54). Dial gages and LVDT's were placed at select locations and provided deflection data at transverse sections for particular tests (Figure 5-54). Another assumption for the use of the formula was that plane sections remain plane after bending. Kassner assumed the formula maintained its validity because effects of shear deformation would

be included in the denominator and numerator of the ratio and thus cancel each other (2004). The strain profiles at midspan appeared to remain linear indicating plane sections remained plane after bending. Some non-linearity was observed at the quarter points which may indicate some shear deformations took place.

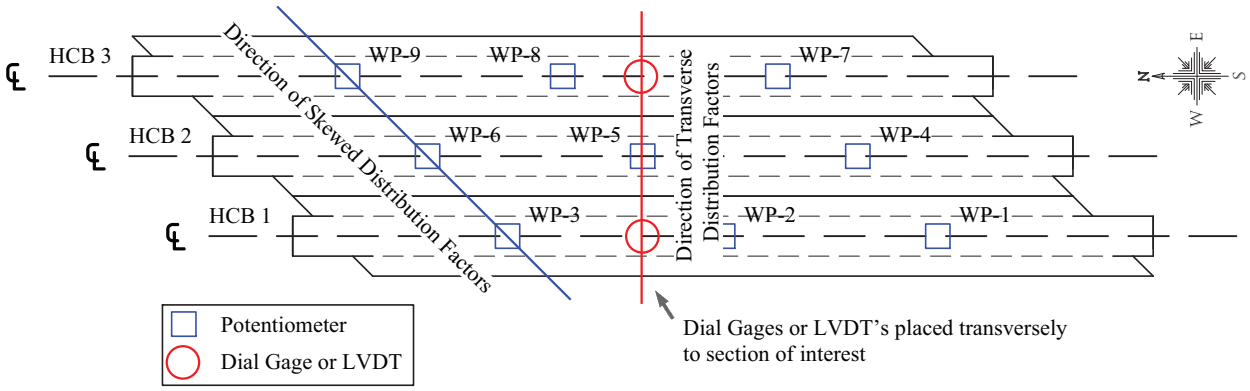

Figure 5-54 Direction of Distribution Factors

Phase III testing consisted of load points that simulated tire patches of a HL-93 truck. A two axle pattern and one wheel line pattern were used. The longitudinal spacing between the axles was 14 ft. and the transverse spacing between the wheel lines was 6 ft. Tests 1-6 were designed to create high moments in the system by placing the representative axles as close to the midspan of the beams as the test layout allowed. Because the width of the test system was approximately 10.5 ft., the ability to move the load configuration transversely was limited. This also limited testing to one lane loaded for the system. For test ST1 and ST2, the west wheel line was placed over the centerline of HCB 1 (Figure 5-56). The east wheel line was located approximately 2 ft. east from the centerline of HCB 2. The AASHTO guidelines specify using the lever rule to determine the distribution factors for exterior girders (2008). The wheel line is to be placed two feet inward from the face of the barrier on the exterior girder (Figure 5-55). For the Tide Mill Bridge, the wheel line for determination of the exterior girder distribution factor was located 3.25 ft. inward from the edge of the deck and 1.25 ft. inward from the centerline of

the exterior girder. Thus, the distance from the assumed hinge at the interior girder to the wheel line was 2.75 ft. Using the specified AASHTO location, the exterior girder distribution factor is 0.41 compared to 0.60 which was found using the actual load location used in test 1 and 2. The axles were placed at 11 ft. and 25 ft. along the span of HCB 1 from the beam end. Load locations for the other tests and calculations of distribution factors are presented in Appendix D. Another difference between the test setup and Tide Mill Bridge was the bearing conditions. Pin-roller bearing conditions were used for each of the beams whereas bearing pads were to be used for Tide Mill Bridge. The bearing pads provide some rotational stiffness which may affect bending in the beams. The differences between the experimental setup and Tide Mill Bridge may lead to differences in transverse load distribution.

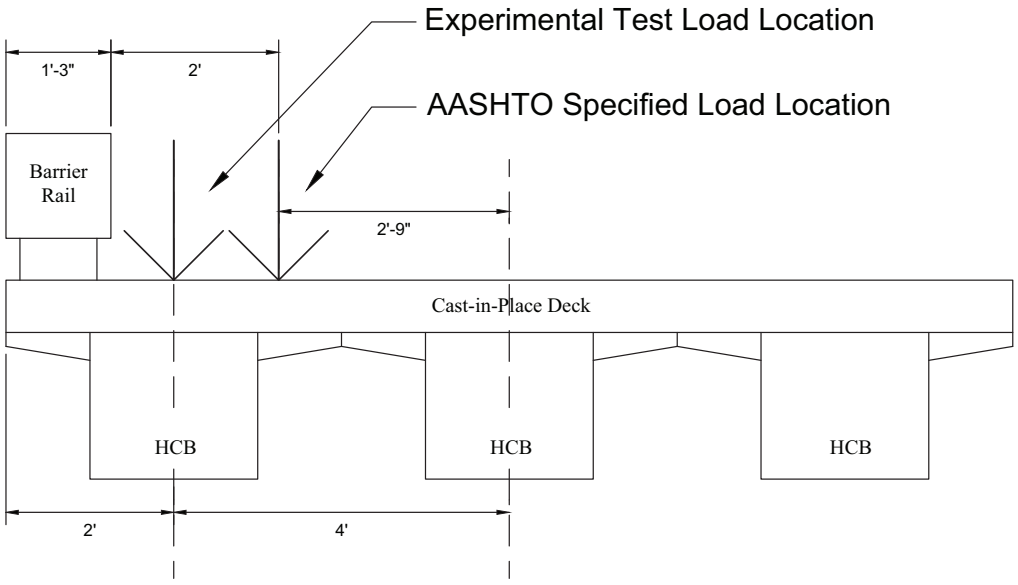

Figure 5-55 AASHTO vs. Experimental Exterior Wheel Line Placement

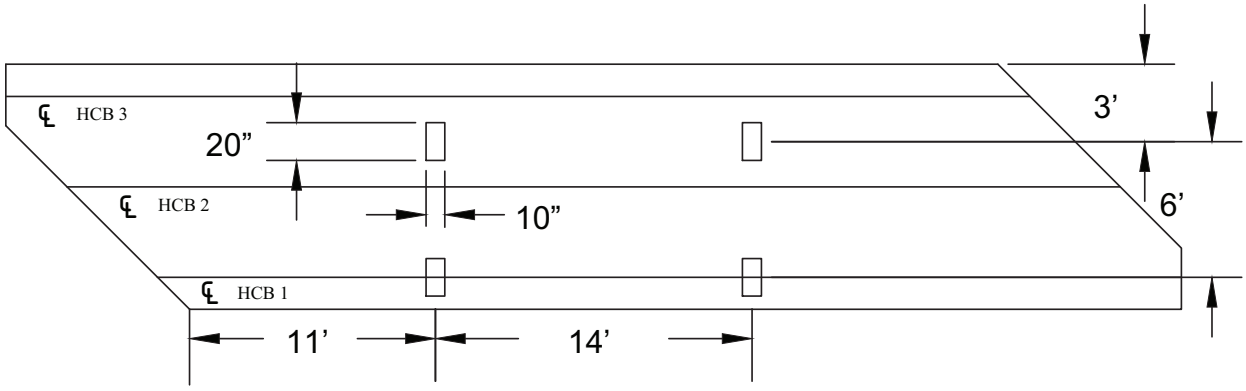

Figure 5-56 Loading Configuration for Test ST1

Equation 3 was used with deflection and strain values recorded from the system under the maximum load. Because two gages were on the bottom flange of each beam, the average strain value was taken. If strain gages did not appear to be functioning, they were excluded from calculations. In the middle of phase III testing, potentiometer WP-6, located at the north quarter point of HCB 2, malfunctioned. During low load increments, the potentiometer did not register a change in deflection. When 10-20 kips were applied, the potentiometer started to record deflections starting at zero. However, any deflection that occurred at prior loading was unaccounted for in the measurements. The slope for the remainder of the test appeared to be linear and followed expected behavior. Correction was applied to the data for WP-6 to include the unmeasured deflection. The recorded change in deflection for this potentiometer was used to derive a linear function that related load to deflection. Because no readings were taken for the low load increments, a y-intercept was included in this function. The y-intercept was removed from the formula and the formula was used to calculate corrected deflection measurements. Because linear-elastic behavior was observed in tests ST1-ST16, the corrected data should provide accurate behavior at the north quarter point of HCB 2.

5.4.2.3.1. Moment Distribution Factors

The deflection-based distribution factors for all tests were averaged and presented in Table 5-30. The deflection-based experimental factors agreed with the concept that the largest responses were expected at an exterior girder. The average distribution factor for the north quarter point of HCB 1 was larger than the other beams for the same location (north quarter point). HCB 3 had a larger average distribution factor for the south quarter point than the other two beams for the same location. Both of these locations were expected to have higher response due to their proximity to the obtuse corners (north end of HCB 1 and south end of HCB 3). The deflection-based distribution at midspan for all beams was equal. Observing the average location for all locations, the distribution factors were found to be equal. The averaged values for the strain-based DF's showed that HCB 1 had the largest factor (Table 5-31). This was consistently seen in each of the moment tests despite the location of the load. The strain-based factor was also consistently lower for HCB 3 for all of the moment tests. Though the factor for HCB 1 was higher, the distribution remained relatively equal.

Table 5-30 Deflection-Based Moment Distribution Factors

	Test	ST1	ST2	ST3	ST4	ST5	ST6	ST15	ST16	Average
HCB 1	North Quarter	**0.40**	**0.40**	0.36	0.35	0.32	0.35	0.34	0.35	0.36
	Midspan	**0.36**	**0.36**	0.33	0.34	0.31	0.31	0.33	0.33	0.33
	South Quarter	0.30	0.29	0.27	0.27	0.25	0.25	0.31	0.26	0.28
	Average	0.35	0.35	0.32	0.32	0.29	0.31	0.33	0.31	**0.32**
HCB 2	North Quarter	0.31	0.31	0.31	0.36	0.36	0.30	0.38	0.34	0.33
	Midspan	0.33	0.33	0.33	0.33	0.33	0.33	0.32	0.33	0.33
	South Quarter	0.35	0.35	0.34	0.36	0.34	0.34	0.32	0.34	0.34
	Average	0.33	0.33	0.33	0.35	0.34	0.32	0.34	0.34	**0.33**
HCB 3	North Quarter	0.29	0.30	0.32	0.29	0.32	0.35	0.28	0.31	0.31
	Midspan	0.31	0.31	0.34	0.33	**0.36**	**0.36**	0.35	0.34	0.34
	South Quarter	0.36	0.36	0.39	0.37	**0.41**	**0.41**	0.37	0.39	0.38
	Average	0.32	0.32	0.35	0.33	0.36	0.38	0.33	0.35	**0.34**

Table 5-31 Strain-Based Moment Distribution Factors

	Test	ST1	ST2	ST3	ST4	ST5	ST6	ST15	ST16	Average
HCB 1	North Quarter	0.39	**0.44**	0.40	0.39	0.37	0.37	0.35	0.38	0.39
	Midspan	**0.39**	**0.39**	0.37	0.37	0.34	0.34	0.37	0.37	0.37
	Average	0.39	**0.42**	0.38	0.38	0.36	0.36	0.36	0.37	**0.38**
HCB 2	North Quarter	0.32	0.29	0.30	0.31	0.32	0.32	0.34	0.32	0.31
	Midspan	0.35	0.35	0.36	0.35	0.36	0.36	0.36	0.36	0.36
	Average	0.33	0.32	0.33	0.33	0.34	0.34	0.35	0.34	**0.34**
HCB 3	North Quarter	0.29	0.27	0.30	0.30	0.31	0.31	0.31	0.31	0.30
	Midspan	0.26	0.25	0.27	0.28	0.30	0.31	0.27	0.27	0.28
	Average	0.28	0.26	0.29	0.29	0.31	0.31	0.29	0.29	**0.29**

A cause for the overall higher strain based factors at midspan for HCB 1 may be the concrete end diaphragms cast at each end. The diaphragms may have added a degree of fixity to the beam end. The ends of HCB 2 and HCB 3 were completely encased in the diaphragm, but HCB 1 was only partially encased. Thus the degree of fixity may have an influence on the amount of strain in the beam. The unsymmetrical nature of the setup may also be causing twisting throughout the cross section of the bridge. The twisting effects may be slightly increased by the presence of the two dissimilar diaphragms, and the gages may be registering a portion of this effect.

5.4.2.3.2. Transverse Moment Distribution Factors

In addition to the distribution factors created from the potentiometers, additional factors were calculated by using instrumentation placed in the transverse direction to WP-5 on HCB 1 and HCB 3, respectively (Table 5-32). Because the section properties varied at the section transverse to the location of WP-5 different weighing variables were obtained from Hillman's model. The variables included the effects of the effective width and the arch profile at each respective section. Due to the lower profile of the arch away from midspan, the section moduli for the exterior girders were slightly greater than for the interior girder for the transverse section located at the midspan of HCB 2. A ratio of 1.01 was found for exterior to interior section moduli and was used for the weighting variable. The factors were then calculated using the same formulas as above. The dial gage readings for test ST1 was not available and was excluded from the data analysis.

Table 5-32 Transverse Moment Distribution Factors

	HCB 1	HCB 2	HCB 3
Test ST2	0.29	0.31	0.33
Test ST3	0.36	0.32	0.32
Test ST4	0.36	0.31	0.33
Test ST5	0.36	0.30	0.36
Test ST6	0.33	0.31	0.36
Test ST15	0.37	0.29	0.35
Test ST16	0.37	0.29	0.34
Average Tests ST2 to ST6	0.34	0.31	0.34
Average Tests ST15 and ST16	0.37	0.29	0.34
Average Skewed Factors	0.32	0.33	0.34

The average transverse distribution factors were found to be relatively equal. The transverse data showed that the interior girder had a lower factor than either of the exterior girders. The cause for this may be due to the weighing factors. The results showed greater distribution factors and response in the exterior girders which agreed with literature. The results for the single wheel line tests (ST1-ST6) showed different behavior than observed in the dual (ST13 and ST14) wheel line tests. The transverse factors showed greater distribution towards the outside while the skewed factors showed an equal distribution between the three HCB's (Figure 5-34). Despite some differences between the skewed and transverse factors, the average distribution factors remained relatively equal.

5.4.2.3.3. Shear Distribution Factors

The skewed factors shear factors were calculated in the same manner for the moment distribution factors except the results for tests ST7 to ST14 were used. These tests generated high shear within the test system. Detailed drawings of the load configurations are available in Appendix D.

The deflection and strain based distribution factors are presented in Table 5-33 and Table 5-34 respectively. The average deflection-based distribution factors showed higher distribution to HCB 3 and lower distribution to HCB 1. For HCB 1, lower distribution factors were observed at the midspan and south quarter point compared to the other beams. The deflection-based distribution factors for HCB 3 were higher for the midspan and the south quarter point. For the north quarter point the distribution factor for HCB 2 was the highest. HCB 1 was expected to have the highest distribution factor at the north quarter point due to its proximity to the obtuse corner. The strain-based factors showed more equal distribution. Small differences between the deflection-based and strain-based factors were observed, but the factors remained relatively equal.

Tests 7 and 8 were expected to be the critical case for shear as the load was placed near the obtuse corner of the system. HCB 1 was expected to have the largest distribution factor based on literature (Ebeido 1995). The test results showed the deflection-based factor for HCB 1 at the north quarter point was higher than the other two beams for test ST7 (Table 5-33). However, the factor for HCB 2 was highest for an apparently identical test (ST8). The strain-based factors agreed with literature, as the distribution for the north quarter point of HCB 1 was higher than the other two beams. Though ST7 and ST8 was expected to be the critical case, higher distribution factors for the north quarter point were observed in other tests for HCB 2 (Table 5-34).

Table 5-33 Deflection-Based Shear Distribution Factors

	Test	ST7	ST8	ST9	ST10	ST11	ST12	ST13	ST14	Average
HCB 1	North Quarter	0.36	0.34	0.33	0.31	0.28	0.28	0.28	0.26	0.31
	Midspan	0.34	0.33	0.31	0.30	0.27	0.27	0.29	0.29	0.30
	South Quarter	0.28	0.27	0.26	0.26	0.24	0.23	0.38	0.23	0.27
	Average	0.32	0.32	0.30	0.29	0.26	0.26	0.32	0.26	**0.29**
HCB 2	North Quarter	0.34	0.36	0.33	0.35	0.35	0.36	0.39	**0.41**	0.36
	Midspan	0.33	0.33	0.33	0.33	0.32	0.33	0.33	0.33	0.33
	South Quarter	0.33	0.33	0.33	0.32	0.32	0.32	0.25	0.29	0.31
	Average	0.33	0.34	0.33	0.33	0.33	0.34	0.32	0.35	**0.33**
HCB 3	North Quarter	0.30	0.30	0.34	0.34	0.36	0.35	0.32	0.32	0.33
	Midspan	0.33	0.34	0.36	0.37	**0.41**	0.40	0.37	0.38	0.37
	South Quarter	0.39	0.40	0.40	0.42	0.45	0.44	0.36	**0.47**	0.42
	Average	0.34	0.35	0.37	0.37	0.41	0.40	0.35	0.39	**0.37**

Table 5-34 Strain-Based Shear Distribution Factors

	Test	ST7	ST8	ST9	ST10	ST11	ST12	ST13	ST14	Average
HCB 1	North Quarter	0.40	0.40	0.15	0.36	0.38	0.42	0.21	0.38	0.34
	Midspan	0.34	0.34	0.31	0.32	0.29	0.29	0.32	0.33	0.32
	Average	0.37	0.37	0.23	0.34	0.34	0.35	0.26	0.35	**0.33**
HCB 2	North Quarter	0.29	0.29	0.40	0.30	0.28	0.27	0.36	0.29	0.31
	Midspan	**0.37**	**0.37**	**0.37**	0.36	0.35	0.36	**0.37**	**0.37**	0.37
	Average	0.33	0.33	0.38	0.33	0.32	0.31	0.36	0.33	**0.34**
HCB 3	North Quarter	0.31	0.31	**0.44**	0.33	0.33	0.31	0.43	0.33	0.35
	Midspan	0.29	0.29	0.32	0.32	0.36	0.35	0.30	0.30	0.32
	Average	0.30	0.30	0.38	0.33	0.35	0.33	0.37	0.32	**0.33**

The unexpected transverse load distribution observed in the system may be due to the formula used to derive the distribution factors. The ratio of deflections and strains for the three beams were used to determine the factors. However, the potentiometers and strain gages were placed to primarily observe the flexural behavior of the beam. Because the shear tests consisted of loading near the supports, the degree of bending is much less that the moment tests. Because of the skew geometry of the system, higher bending may be occurring on the east side of the system which may affect the distribution factors. A higher degree of bending does not directly translate to higher shear in the beam.

5.4.2.3.4. Transverse Shear Distribution Factors

The LVDT's which were placed in the transverse direction to the location of interest were used to calculate transverse deflection-based distribution factors (Figure 5-52). The table also shows which potentiometer the LVDT's were placed transversely to. The transverse factors appeared to correlate differently than the skew direction factors. HCB 1 was expected to have the highest shear, and the distribution factor calculated based on deflection was found to be the lowest for HCB 1. HCB 3 consistently had the highest distribution factor. The average factors for these two beams were lower and higher than the skewed deflection-based factors respectively. As the load pattern moved from the west edge of the deck to the east edge, the distribution factor for HCB 3 increased while the factor for HCB 1 decreased. The factor for HCB 2 appeared to remain relatively the same for all tests. Similar distribution was observed between the single wheel line tests (ST13 and ST14) and the dual wheel line tests centered over HCB 2 (ST 9 and ST10). On average, the distribution factor using deflections for HCB 3 was the greatest though the shear was expected to be highest for HCB 1. Because of the proximity of the measurement

locations to the supports, the factors using transverse deflection readings may not be an accurate indication for shear distribution.

Table 5-35 Transverse Shear Distribution Factors

	Beam Location			Transverse Location	
	HCB 1	HCB 2	HCB 3	LVDT 5	LVDT 6
Test ST7	0.27	0.35	0.37	WP-3	WP-3
Test ST8	0.26	0.36	0.38	WP-3	WP-3
Test ST9	0.25	0.31	0.43	WP-6	WP-6
Test ST10	0.25	0.31	0.43	WP-6	WP-6
Test ST11	0.16	0.34	0.49	WP-9	WP-9
Test ST12	0.16	0.35	0.47	WP-9	WP-9
Test ST13	0.25	0.34	0.41	WP-6	WP-6
Test ST14	0.25	0.31	0.43	WP-6	WP-6
Average for Tests ST7-ST12	0.22	0.34	0.43		
Average for Tests ST13 & ST14	0.25	0.32	0.42		
Average Skewed Factors	0.29	0.33	0.37		

5.4.2.3.5. Load-Based Distribution Factors

The load cell data was not used for analysis due to the low confidence in the accuracy of the readings. Because of damage to some load cells, equilibrium at the north support was not established. In addition, the uneven seating of the beams on the load cells may have greatly affected the load readings.

5.4.2.3.6. Summary of Distribution Factor Results

The critical distributions factors observed from testing are presented in Table 5-36. All deflection and strain data from the service moment tests were used to determine the critical moment distribution factor for each beam. Deflection and strain based factors from the shear tests were used for the shear distribution factors. Load factors for the shear tests were determined to be more critical rather than those from the moment tests because the magnitude of shear was

much lower for the moment tests. The controlling moment and shear factors corresponded to tests ST2 and ST7, respectively.

Table 5-36 Critical Distribution Factors from Phase III Testing

	HCB 1	HCB 2	HCB 3
Moment Distribution Factor	**0.44**	0.38	0.41
Shear Distribution Factor	0.40	0.41	**0.49**

The controlling experimental distribution factors multiplied by multiple presence (1.2) were compared to factors calculated using the lever rule with one lane loaded and with multiple presence and skew correction included (Table 5-37). Correction factors were calculated using formulas in the LRFD Specifications. The correction factor for moment was found to be 0.80 and the correction factor for shear was 1.36. The moment correction was applied to all girders, but the shear correction was only applied to girders at the obtuse corners (exterior girders). The load location for the lever rule were based on actual distances used in testing rather than the 2 ft. distance from the barrier specified by AASHTO.

Table 5-37 Comparison of Experimental to Lever Rule Distribution Factors

Moment	Experimental Results	Lever Rule	Ratio
Interior Girder	0.45	0.24	1.89
Exterior Girder	0.53	**0.48**	1.10
Shear	Experimental Results	Lever Rule	Ratio
Interior Girder	0.50	0.30	1.66
Exterior Girder	0.59	**0.82**	0.72

The highest experimental distribution factors given for HCB 2 in Table 5-36 were used for the interior girder. The largest moment factor for HCB 3 and the largest shear factor for HCB1 were used for the exterior girder. Ratios were calculated for experimental to lever rule distribution factors for moment and shear for the interior and exterior girders. The lever rule factors were shown to be unconservative for the moment and shear distribution factors for the

interior girder. For the moment in the interior girder, the ratio of 1.58 was found. The test data showed that the average experimental distribution factor (0.45) was consistently larger than the lever rule factor of 0.24. However, an explanation for the high measured distribution factor may be dependent on the three HCB's used in the test system. HCB 2 was the only interior girder. For many tests, almost equal distribution was seen among the three beams. The addition of more girders may increase the distribution of moment and thus reduce the measured distribution factor for the interior girder. The ratio for the distribution factor for moment in the exterior girder indicated the lever rule provided a good approximation though the moment factor for the exterior girder was slightly higher than the lever rule. The lever rule factor for shear distribution in the exterior girder was conservative. The higher observed factor for moment and shear in the interior girder is a cause for concern, but the addition of more girders may cause the distribution factor to decrease.

The experimental values were also compared to factors used in the Hillman model (Table 5-38). The controlling experimental factors from Table 5-36 were used. Hillman found the lever rule for the exterior girder to control and used this distribution factor for both the interior and exterior girders for moment and shear. Hillman's model placed the load location for the lever rule 2 ft. from the edge of the deck rather than the face of the barrier rail. If the loads were placed per AASHTO specifications, the distribution factors would be 0.41 and 0.34 for the exterior and interior girder, respectively. The resulting location was the same as used for the experimental tests system. Though Hillman calculated skew correction factors in his model, he did not use them to adjust the design moments and shears. This resulted in a conservative factor for moment and an unconservative shear distribution factor compared to the AASHTO Specifications. The comparison of the experimental factors to those used in the Hillman model confirmed the

expected difference (Table 5-38). Hillman's model was shown to be conservative for all distribution factors except for shear for the exterior girder in which the factor was almost equal to the lever rule. Though Hillman did not include correction for shear, the distribution factor from the lever rule was close to the experimentally determined value for the critical shear case: distribution at the obtuse corner of the skew (exterior girder). The shear factor for the interior girder was shown to be conservative. The Hillman model used conservative moment and shear distribution factors.

Table 5-38 Comparison of Experimental to Hillman Model

Moment	Experimental Results	Hillman Model	Ratio
Interior Girder	0.45	0.60	0.76
Exterior Girder	0.53		0.88
Shear	Experimental Results	Hillman Model	Ratio
Interior Girder	0.50	0.60	0.83
Exterior Girder	0.59		0.98

Data from phase III testing was used to experimentally obtain and compare load distribution factors in the three-HCB system to the design values used for Tide Mill Bridge. In FRP bridge tests using I-shaped girders, the Standard Specification formulas for steel girders with a timber deck were used. However, the use of the concrete box beam may be more appropriate because the HCB has a higher torsional stiffness due to the shape of the FRP box. For the deflection limit state, Hillman's model used a distribution factor of 0.25 (Hillman 2011). This distribution factor was calculated by taking two lanes and dividing by eight girders to be used in the bridge. As the average distribution factor showed equal distribution, the use of the factor appeared adequate. The experimental test system consisted of only three HCB's which led to a much higher aspect ratio. The load distribution in the three-girder test specimen was examined to provide a basis for transverse behavior that may be seen for Tide Mill Bridge.

From the investigation of experimental distribution factors, the AASHTO formulas resulted in unconservative values for the interior girder, and Hillman's model was determined to be conservative for moment and shear distribution. Controlling cases for the experimental factors were determined from both the moment and shear tests. Deflection and strain data were used for moment distribution factors and shear distribution factors. The lever rule equation controlled the AASHTO distribution factors for moment and shear after correction for skew was applied. The moment and shear distribution in the interior girder was found to be unconservative compared to AASHTO formulas. An increased aspect ratio may cause this factor to decrease. Hillman's model also used lever rule factors for distribution but neglected corrections for skew. The model was shown to be conservative. Factors calculated using the lever rule in the model appeared to overestimate the transverse distribution, but the factors should be validated with field tests.

5.4.2.4. Design Service Live Load Test

After the completion of the two axle and single axles tests on the system (tests ST1-ST16), an additional test (ST17) was conducted. From analysis of the previous data, the transverse load distribution was determined to be approximately equal between the three HCB's. In contrast, the design distribution factor was 0.60 which was very conservative. As a result the highest applied moment that was induced in any single beam was approximately half of the live load used for design. Because the HCB needed to be evaluated for use in Tide Mill Bridge, the design moment needed to be applied to observe behavior under the full design service load conditions. Because of the high load that needed to be applied, one wheel line was applied on the system using a larger spreader beam rather than two wheel lines. The wheel line was placed over the centerline of HCB 2. Assuming an equal distribution between girders, a calculated maximum load of 200 kips was required to apply the design moment in HCB 2.

Loading progressed in increments described in section 4.6. In the previous phase III tests, no audible sounds were heard from the FRP. However, when the higher load increments were reached for the final test, a crackling noise similar to that observed in phase II was heard starting at 100 kips. Additionally, louder popping noises were heard near the maximum load starting at approximately 150 kips. These popping sounds came from near the top of the beams rather than the bottom flange where maximum tensile strains were occurring. One source of the noise may be the epoxy that glued the top flange to the bottom component of the HCB box. Another source could have been the tension strand delaminating from the bottom flange of the HCB. Because a high degree of bending was induced in the beam and the strand was under tension, the bond between the FRP and strand could have been damaged due to relative movement of the components.

Deflections observed during testing appeared to be linear until the higher load increments. After approximately 150 kip was applied to the system, slight non-linear load-deflection behavior was observed. The midspan deflection for HCB 2 is presented in Figure 5-57. A maximum deflection of 2.07 in. was observed at the midspan of HCB 2. When the system was unloaded, a residual deformation of approximately 0.1 in. was observed at the midspan of all beams. The unloading phase of the plot appeared linear, and the slope was about the same as for the loading phase. Though a residual displacement (0.12 in.) was observed, it was relatively small compared to the maximum deflection of 2.07 in.

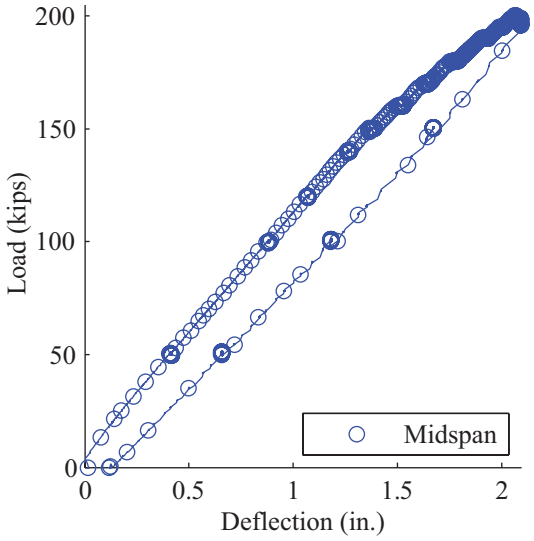

Figure 5-57 Load vs. Deflection for HCB 2 for Design Live Load Test

Similar non-linear behavior was observed for the strand strains. The unloading curve was linear and showed a small amount of residual deformation. The residual was smaller than seen for midspan deflection, and the deformation appeared to be a very small proportion of the maximum strain the strand experienced. In addition to load-strain behavior, the comparison between the total service level stress and the ultimate stress was of importance. The strand stress was calculated by applying the experimentally-derived conversion factor to the measured strains. The total strains consisted of strain induced from the arch concrete placement, deck concrete placement, and the full service live load test. Because strains were not recorded during the deck placement, these strains were estimated. Calculations are shown in Appendix C. Also, strains for the arch pour (Appendix B) were recorded for HCB 1 and were assumed to be the same for HCB 2. In the HCB design was controlled by the deflection limit of L/800 as per AASHTO Specifications. Thus, beam was expected to have reserve strength. The total strains for the strand are presented in Table 5-39. As expected, the ratio between the service level strain and the ultimate stress was small. The highest strains occurred during the full live load tests. The strains

during the arch pour were relatively small. Though non-linear behavior was observed in the load-strain relationship, the measured strain showed the strand was well below the yield stress limit of 243 ksi.

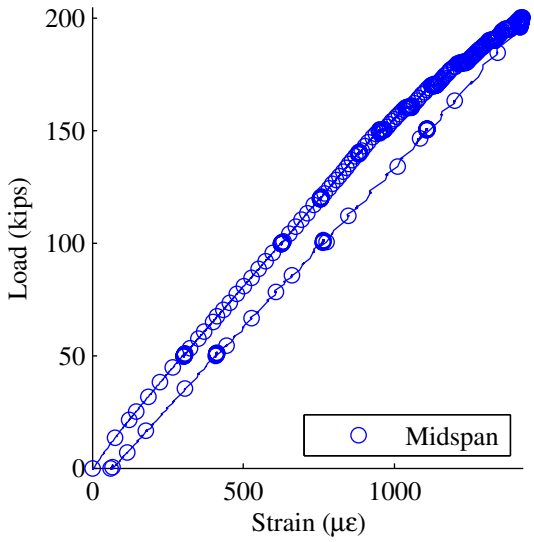

Figure 5-58 Load vs. Strand Strain for HCB 2 for Design Live Load Test

Table 5-39 Comparison of Measured to Ultimate Stresses in Strand

		Strains (με)				Stress (ksi)		
	Gage	Arch Pour	Deck Pour	Service Loading	Total Strain	Total Stress	Ultimate Stress	Stress Ratio
North Quarter Point	TQ-2	38	518	1099	1655	47.2	270	0.17
Midspan 1	TM-3	151	577	1422	2150	61.3	270	0.23

The strand stresses were also compared to the stresses predicted from Hillman's model (Table 5-40). The Hillman model approximated the measured stresses well.

Table 5-40 Comparison of Measured to Predicted Stresses in Strand

		Stress (ksi)		Stress Ratio
	Gage	Total Measured Stress	Predicted	
North Quarter Point	TQ-2	47.2	50.2	0.94
Midspan 1	TM-3	61.3	73.7	0.83

For the FRP strains, slight non-linearity was observed near the higher load increments. The FRP gages on the bottom flange and top flange were expected to have the highest strains due to their relatively large distance from the neutral axis. Along with the deflection and the strand strains, the FRP gages suggest the HCB's were behaving non-linearly near the design service load (Figure 5-59). When the system was unloaded, relatively small residual strains were observed. The strains for both bottom flange gages were similar. Though the FRP strains appeared high, the ratio of measured stresses to ultimate stresses was small (Table 5-41). The highest observed ratio was 0.26. The top flange gages all had small ratios of measured to ultimate stress. The small strains in the top flange are due to the shift in the neutral axis location towards the top of the beam as the arch and deck were placed. Gages that were in compression for the arch and deck placement were shown to be in tension under the design load.

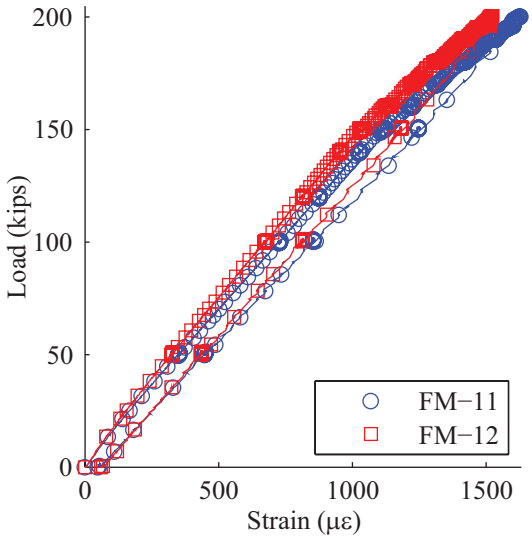

Figure 5-59 Load vs. Bottom Flange Strain for HCB 2 for Design Live Load Test

Table 5-41 Comparison of Measured to Ultimate Stresses in FRP

		Strains (με)				Stress (ksi)		
	Gage	Arch Pour	Deck Pour	Service Loading	Total Strain	Total Stress	Ultimate Stress	Stress Ratio
Bottom Flange	FQ-11	45	460	1078	1583	4.91	27.8	0.18
	FQ-12	77	460	950	1486	4.61	27.8	0.17
	FM-11	163	507	1624	2294	7.11	27.8	0.26
	FM-12	67	507	1520	2094	6.49	27.8	0.23
Top Flange	FQ-15	-662	-367	427	-602	-1.87	27.8	0.07
	FQ-16	-275	-367	533	-109	-0.34	27.8	0.01
	FM-15	-296	-212	104	-404	-1.25	27.8	0.05
	FM-16	N/A	-212	123	-89	-0.28	27.8	0.01

The measured values were compared to predicted stresses for the FRP flanges. In all cases, the measured stresses were smaller than those predicted by Hillman's model. The model was more effective in predicting the stresses on the bottom flange. For the top flange gages, the model largely overestimated the stresses in the FRP. Because the top flange gages were observed to be close to the neutral axis, the compression strains from service loads were not as large as predicted. Hillman's model provided a reasonable approximation for the behavior of the bottom flange of the HCB, but greatly overestimated stresses in the top flange.

Table 5-42 Comparison of Measured to Predicted Stresses in FRP

			Stress (ksi)		Stress Ratio
		Gage	Total Stress	Predicted	
FRP	Bottom Flange	FQ-11	4.91	5.82	0.83
		FQ-12	4.61	5.82	0.78
		FM-11	7.11	8.52	0.84
		FM-12	6.49	8.52	0.76
	Top Flange	FQ-15	-1.87	-3.2	0.57
		FQ-16	-0.34	-3.2	0.10
		FM-15	-1.25	-3.11	0.40
		FM-16	-0.28	-3.11	0.09

The arch of HCB 2 was examined under the full live load. For the previous service load tests, beam behavior was observed, and the arch was observed to be in tension at the quarter point midspan. Observation of the strains during testing showed similar traits to previous service level tests (Figure 5-60). Both midspan and quarter point gages registered tensile strains indicating the arch was part of the overall beam behavior of the HCB. The support gages registered higher compressive strains than observed in previous service load tests. Most of the gages appear to increase linearly for the lower load increments. For higher load increments, unusual curvature was observed in the load-strain relationship. The curvature did not represent typical non-linear behavior because the slope was not gradually decreasing. Rather, the slope of the line was both increasing and decreasing as the loading increased. The cause for the behavior was unknown. For the unloading phase of the plots, fairly linear behavior was observed and the unusual curvature seen during loading was not apparent. The strains also returned to zero despite the observed curvature indicating either no or low deformation in the arch.

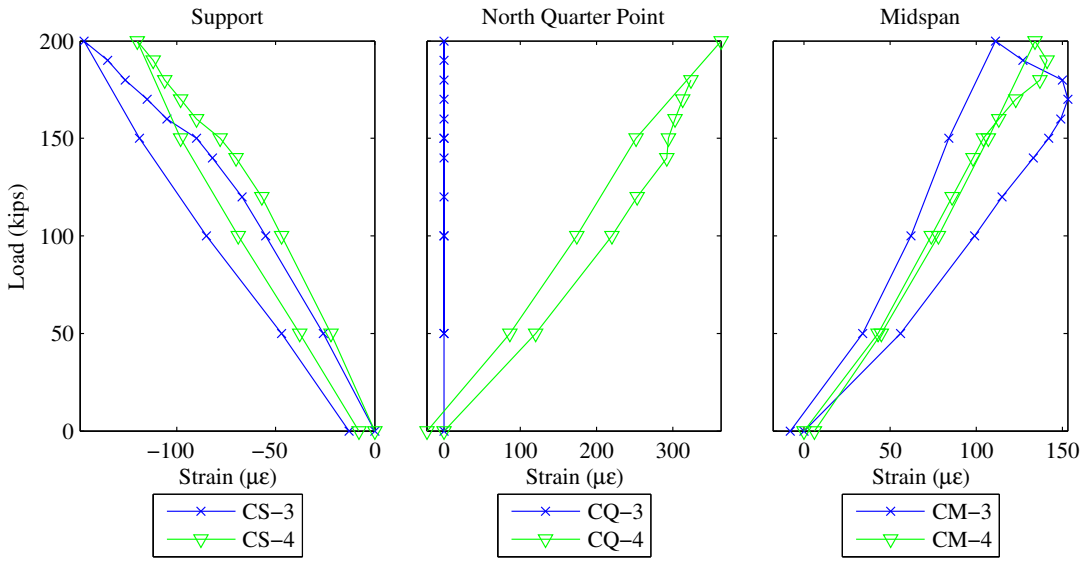

Figure 5-60 Load vs. Strain for HCB 2 Arch for Design Live Load Test

The total arch strains for HCB 2 were converted to stresses using the experimentally-derived modulus of elasticity (Table 5-43). Additionally, because the compressive and tensile values were recorded from the cylinder tests, experimentally-derived ultimate stresses were used. The resulting stress near the support was found to be much smaller than the compressive strength of the arch concrete. At the quarter point, readings for gage CQ-3 were not available. The deck placement strain was not available for gage CQ-4, and the strain read by gage CQ-6 was used instead. The tensile strain in the arch was much greater than the ultimate tensile stress. A ratio of measured to ultimate stress of 2.5 was found. As was discussed for phase II, the strands in the bottom of the arch may serve as a mechanism for the arch to continue to carry tensile force though it may have cracked. The arch appeared to be sensitive to local bending effects from loading as observed in previous phases.

Table 5-43 Comparison of Measured to Ultimate Stresses in Arch

		Strains (με)				Stress (ksi)		
	Gage	Arch Pour	Deck Pour	Service Loading	Total Strain	Total Stress	Ultimate Stress	Stress Ratio
Support	CS-3	-	-75	-147	-222	-0.85	-5.91	0.14
	CS-4	-	-80	-120	-200	-0.76	-5.91	0.13
Quarter Point	CQ-3	-	N/A	N/A	N/A	N/A	N/A	N/A
	CQ-4	-	(-21)	363	342	1.31	0.52	2.52
Midspan	CM-3	-	-21	111	90	0.34	0.52	0.66
	CM-4	-	-30	134	104	0.40	0.52	0.76

The arch strains were compared to predicted stresses from Hillman's model (Table 5-44). Hillman's model calculated the stresses for the top and bottom surface of the arch. Because the gages were located 1 in. from the top and bottom, linear interpolation was used between the top and bottom stresses to determine stresses at the gage locations. Hillman's model predicted much of the arch would be in tension. At the midspan, tensile stress was expected in the bottom of the arch but the top of the arch was expected to be in compression. From the test data, both gages

showed a tensile strain. The strain at the bottom of the arch (0.34 ksi) was considerably smaller than predicted (1.07 ksi). The top gage measured tensile strains (0.40 ksi) similar to the bottom of the arch which was significantly different from the predicted value of 0.08 ksi in compression. Because the arch falls farther away from the neutral axis towards the beam ends, tensile stresses were predicted throughout the arch depth for the quarter point and support locations. However, compressive stresses at the supports were observed from the data. The compressive stresses were also considerably larger than the tensile stresses predicted. Though the ratios of measured to predicted strain was high for the support gages, the compressive stresses were relatively small compared to the ultimate stress. For the quarter point, the arch stress was considerably higher than the predicted stress. For the top and bottom of the arch, the predicted stresses were calculated to be higher than the experimentally derived cracking stress. The relatively high stresses at the quarter point are one of the most critical observations made from the test data.

Table 5-44 Comparison of Measured to Predicted Stresses in Arch

			Stress (ksi)		Stress Ratio
		Gage	Total Stress	Predicted	
Concrete	Support	CS-3	-0.85	0.33	2.57
		CS-4	-0.76	0.19	4.03
	Quarter Point	CQ-3	N/A	N/A	N/A
		CQ-4	1.31	0.57	2.29
	Midspan	CM-3	0.34	1.07	0.32
		CM-4	0.40	-0.08	4.97

Strain profiles for HCB 2 were constructed in the same manner as previous tests. The shape of the strain profile was of interest under the design service load. The top flange gages (FM-15 & FM-16) behaved irregularly just before reaching the maximum load; the data was corrected approximate the measured strain at max load. The midspan profile showed fairly linear behavior and gages on the east and west faces were in close agreement (Figure 5-61). Strain

compatibility appeared to exist between the strand, FRP, and deck concrete. The arch appeared to differ from the profile seen for the other components. The magnitudes of strain in the arch were less than the interpolated FRP strains at the same height. For earlier tests, the arch strain were seen to follow the FRP profile well (Figure 5-44). Also in these tests, the top and bottom arch gage are in tension. Although both top and bottom gages were in tension in test ST17, the profile created by the arch was in negative bending. The degree of negative bending was small but now indicated that the midspan behavior of the arch may not follow the overall strain profile created by the other components. Previous testing showed that the quarter point behavior of the arch was decoupled from the overall beam behavior. The location of the neutral axis was higher for test ST17 compared to test ST3 (Figure 5-33). The neutral axis location was located approximately at 22 in. from the bottom flange (Figure 5-61). The observed location agreed with Hillman's predicted value of 21.8 in. A linear strain profile was observed for the strain, FRP, and deck concrete at midspan that appeared to follow predicted behavior. The midspan arch strain profile was not in agreement with the other components as was seen in previous tests and may indicate the loss of strain compatibility at this location.

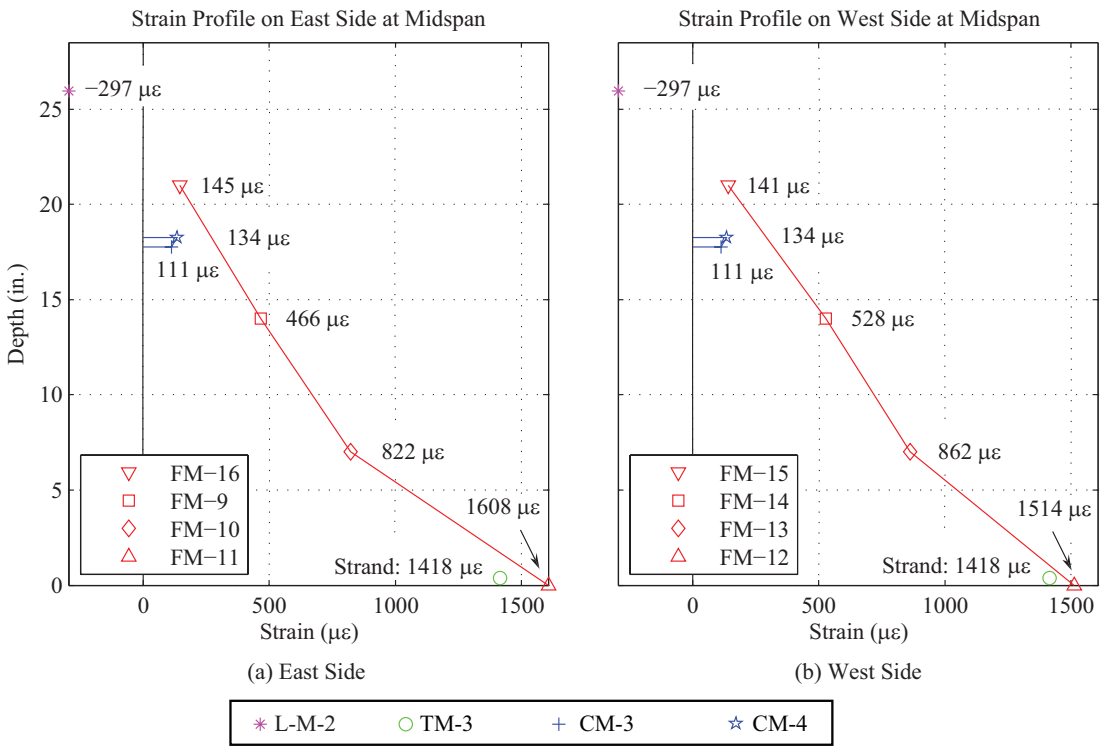

Figure 5-61 HCB2 Midspan Strain Profile for ST17

The profile at the quarter point is shown in Figure 5-62. The most notable feature in the plot was the behavior of the top flange gages. The gages appeared to be subject to local effects from the load point. The other gages showed a larger degree of variation between the east and west faces. With exception of the top flange gages, the components of the beam appear to show a linear profile. Readings for CQ-3 were not available for phase 3, and a strain profile for the arch profile could not be established. The strand (TQ-2) and the top of the arch (CQ-4) appeared to approximately follow the profile created by the FRP gages. The location of the neutral axis from experimental results was approximately 23 in. and was higher than the predicted location of 20.9 in (Figure 5-62). The deck and strand appeared to follow a linear profile created by the FRP gages. Because both the top and bottom gage readings were not available, the compatibility of the arch strains to the FRP strains could not be established.

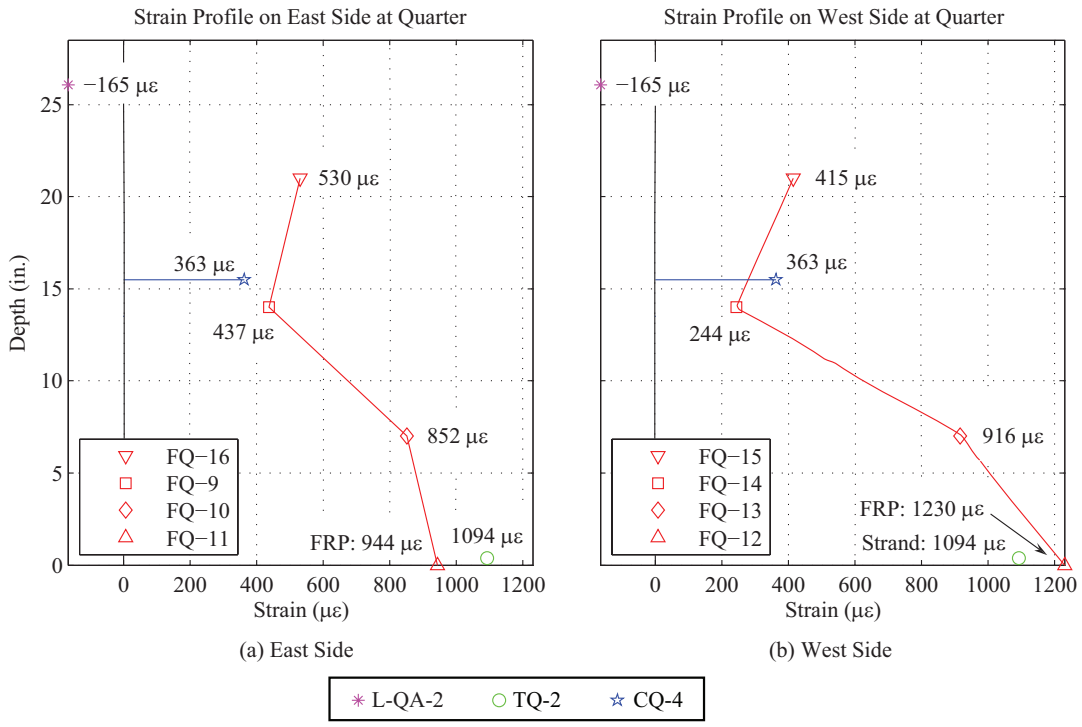

Figure 5-62 HCB2 Quarter Point Strain Profile for ST17

Distribution factors for the design live load test were examined. Because of the large deflections during tests, the range of the LVDT's and dial gages were exceeded and deflections under maximum loading were not available for the calculation of transverse factors. The skewed distribution factors showed results in agreement with previous tests (Table 5-45). The distribution was slightly higher in HCB 2 overall which was expected due to the placement of load over the beam's centerline.

Table 5-45 Distribution Factors for Test ST17

	Deflection-Based				Strain-Based			
Location	HCB 1	HCB 2	HCB 3	Total	HCB 1	HCB 2	HCB 3	Total
North Quarter	0.35	0.35	0.30	1.00	**0.36**	0.34	0.30	1.00
Midspan	0.33	0.35	0.32	1.00	0.35	**0.36**	0.29	1.00
South Quarter	0.28	**0.36**	**0.36**	1.00				
Average	0.32	0.35	0.33	1.00	0.36	0.35	0.30	1.00

The controlling factors for the exterior and interior girders were found to be the same at 0.36 (Table 5-45) which was then multiplied by the multiple presence factor. The results from the final test were compared to the lever rule factors and factors used in Hillman's model in Table 5-46 and Table 5-47, respectively. The interior girder factors were higher than the lever rule as was seen for previous tests. All experimental factors were less than those used in Hillman's model. Though the applied load was higher for the final test, it did not represent a critical case. Higher distribution factors were observed in previous tests.

Table 5-46 Comparison of Experimental Distribution Factors to Lever Rule Factors

Moment	Experimental Results	Lever Rule	Ratio
Interior Girder	0.44	0.24	1.82
Exterior Girder	0.43	**0.48**	0.90
Shear	Experimental Results	Lever Rule	Ratio
Interior Girder	0.44	0.30	1.45
Exterior Girder	0.44	**0.82**	0.53

Table 5-47 Comparison of Experimental Distribution Factors to Hillman Model Factors

Moment	Experimental Results	Hillman Model	Ratio
Interior Girder	0.44	0.60	0.73
Exterior Girder	0.44		0.73
Shear	Experimental Results	Hillman Model	Ratio
Interior Girder	0.44	0.60	0.73
Exterior Girder	0.43		0.72

Though Hillman's model appeared to provide a fair estimate for the FRP and strand components of the HCB under service loads, the predictions for the arch behavior were poor. Strains were often much different from those predicted using the model. In some cases, compressive strains were observed where tensile strains were predicted and vice versa. Observation of strain profiles at the midspan and quarter point showed a degree of strain compatibility existed between the FRP, strand, and deck concrete. The arch behavior at midspan

was close to the approximated strain profile of the FRP. Compared to previous tests the arch strain decreased from the interpolated FRP strains at the same depth, and negative bending was observed where positive bending was observe in all previous phase III tests. Though, the arch behavior appeared to follow the strain profile for lower loads in tests ST1-ST16, the behavior appeared to start to decouple from the beam behavior for higher loads. The Hillman method appears to approximate behavior of FRP, strand, and deck concrete well, but the model for the arch concrete needs refinement.

6 Conclusions and Recommendations

The Hybrid Composite Beam (HCB) invented by John Hillman was evaluated prior to use for Tide Mill Bridge. The test program consisted of three phases of testing to determine the individual HCB behavior and a skewed three-HCB system behavior. The current design methodology uses a transformed section approach to account for the different components of the HCB. This approach assumes aspects of typical beam behavior. Such aspects include plane sections before bending remaining plane after bending and strain compatibility between components. Because of the relative lack of available literature on HCB, a test program was warranted to evaluate the beam's performance. The linear-elastic behavior was studied by observing each individual component of the beam. The strain compatibility assumption was investigated by creating strain profiles from measurements taken through the depth of the non-composite and composite sections. In addition to individual behavior, the behavior of an HCB system was of interest. Because Tide Mill Bridge was to consist of a 45 degree skew, knowledge of transverse distribution was critical. Prior literature scarcely discussed transverse load distribution in HCB structures. Experimental distribution factors for moment and shear were examined by testing a skewed three-HCB system. A final load test was conducted to load the HCB's in the system to the full live load used for design. The total strains were converted to stresses and compared to ultimate stresses and Hillman's model.

6.1. Conclusions

- Overall, components of the HCB were shown to behave linear-elastically during service level tests. Minimal or no permanent deformation was induced in the HCB's after each

test was completed further confirming linear-elastic behavior. Only during the final test, non-linearity and small residual deflections and strains were observed.

- The transformed area approach was found to be valid for the FRP, strand, and deck concrete. Predicted strains were often slightly conservative compared to measured results because of unaccounted stiffness in the HCB. The neutral axis locations observed from testing were in general agreement with the predicted location. Strain profiles constructed using the measurements for each component showed linear behavior with exception of the arch concrete.
- The behavior of the arch was uncoupled from the overall HCB behavior. For phase II testing, the arch was shown to be highly susceptible to local effects from loading. Local bending at the quarter points was observed that led to strains well beyond the cracking limit of the concrete. The high tensile strains suggest the two loose strands in the bottom of the arch profile may continue to provide a mechanism for tensile force. The transformed section approach did not predict the arch behavior well.
- Distribution factors for the three-girder system were controlled by response of exterior girders for moment and shear. The exterior girder moment and shear factors were in agreement or lower than the AASHTO LRFD Specifications using the lever rule with correction for skew. The AASHTO interior girder factors were found to be unconservative compared to measured results. The three-girder system had a higher aspect ratio which may have caused the interior moment factor to be higher than would be experienced in Tide Mill Bridge. Hillman did not include correction for skew in his model. As a result, the moment factors were conservative and the shear factor for the exterior girder was close to experimental results.

- When stresses for the final service test, deck placement, and arch placement were totaled; they were typically found to be much lower than the ultimate stresses provided from manufacturer or experimentally derived data. Only the tensile strains in the arch at quarter point were greater than the ultimate stress. Comparisons to Hillman's model showed effective prediction of the strand and FRP material. The model provided a poor prediction for the arch. Tensile strains in the arch were commonly under predicted.

6.2. Recommendations

- After observation of the data, the HCB was shown to be adequate for use in Tide Mill Bridge for service loads. The final load tests showed mostly linear behavior with very small residual strains and displacements. Though the arch behavior was shown to greatly vary from Hillman's model, Hillman does not account for the arch in strength calculations of the composite section. Thus the arch behavior was assumed to be irrelevant to strength.
- The current design methodology should be used to predict behavior of the FRP, strand, and deck.
- Loads on the non-composite HCB section (with arch concrete but without deck concrete in place) should be carefully considered during design. Local bending was shown to occur in arch under concentrated loads.
- Consideration needs to be made for tensile strains in the arch for the composite section. The model predicted strains higher than cracking strains in the arch.
- An alternate method of analysis for the arch should be used. The model for the arch behavior should be refined.

6.3. Recommendations for Future Work

- A more appropriate design methodology for the arch in the HCB needs to be established. Large tensile strains and high ratios of measured to predicted strains were found during testing indicating the current model performed poorly. Though the arch was not used in strength calculations for the composite section, the behavior of the arch needs to be predictable. Without a valid model for the arch, the adoption of the HCB by more engineers may become difficult due to the perceived unpredictable behavior compared to traditional structural systems.
- The behavior of the system under the ultimate load should be investigated. Slight non-linear behavior was observed during the design service live load test. The strains for many of the materials for the HCB components were still within published linear-elastic range. The source of the non-linearity for this study was not evident. Also, Hillman's model neglected contribution of the arch to the composite girder moment capacity. The capacity needs to be experimentally validated and actual effects of the arch investigated under ultimate loading.
- After the experimental test program has concluded, an autopsy should be performed on at least one of the three tested beams. Both the condition of the arch and the locations of the vibrating wire gages could be observed to provide insight to observed arch behavior during phase II and III testing. The bond between the strand and the FRP and the relative movement of the arch to the FRP box could be investigated.
- Field testing for Tide Mill Bridge is necessary to validate the observations on transverse load distribution. Though full-scale HCB specimens were used for the three-girder system; modifications to the abutments and number of girders were made to

accommodate the available lab space. The difference between the test setup and Tide Mill Bridge may greatly affect transverse load distribution.

- Shear distribution factors need to be validated. Load cells at the north support of the setup were damaged and equilibrium could not be established and were not used for calculation of distribution factors. Instead, deflection and strain data were used to determine shear distribution factors. These values may not be adequate indicators of shear as, strains and deflections were measured near the supports and may be small. The distribution needs to be confirmed either by performing new tests on the experimental system or providing adequate instrumentation for the field test of Tide Mill Bridge
- This study focused primarily on flexural behavior of the HCB. However, shear behavior has been largely overlooked in the current design methodology and previous literature. Though testing has been provided to validate the current method for flexural design, no experimental data has been used to validate the shear design method. A research program focused on the shear behavior of the HCB is warranted.

References

American Association of State Highway and Transportation Officials (AASHTO) [2008]. LFRD Bridge Design Specifications: Fourth Edition. Washington D.C.

Arrellaga, J.A., C.L. Roberts, J.E. Breen, and M.E. Kreger. "Instrumentation Systems for Field Study of Segmental Box Girder Bridges." University of Texas at Austin, 1993. Web. <http://fsel.engr.utexas.edu/publications/detail.cfm?pubid=728104822>.

Barker, Richard, and Jay Puckett. *Design of Highway Bridges: An LRFD Approach*. Second. Hoboken, NJ: John Wiley & Sons, Inc., 2007. 309-318. Print.

Ebeido, Tarek, and John Kennedy. "Girder Moments in Simply Supported Skew Composite Bridges." *Canadian Journal of Civil Engineering*. 23.4 (1996): 904-916. Web. 28 July. 2011.

Ebeido, Tarek, and John Kennedy. "Shear Distribution in Simply Supported Skew Composite Bridges." *Canadian Journal of Civil Engineering*. 23.4 (1995): 1143-1154. Web. 26 July. 2011.

Hayes, Michael, John Lesko, and et. al. "Laboratory and Field Testing of Composite Bridge Superstructure." *Journal of Composites for Construction*. 3.4 (2000): 120-128. Web. 28 July. 2011.

Hillman, John. "HCB Design Spreadsheet." Microsoft Excel. 2011.

Hillman, John. *Investigation of a Hybrid-Composite Beam System.* Washington: Transportation Research Board, Aug. 2003. Web. 4 July 2011. <http://onlinepubs.trb.org/onlinepubs/IDEA/FinalReports/HighSpeedRail/HSR-23Final_report.pdf>

Hillman, John. *Product Application of a Hybrid-Composite Beam System.* Washington: Transportation Research Board, Mar. 2008. Web. 4 July 2011. < <http://onlinepubs.trb.org/onlinepubs/archive/studies/idea/finalreports/highspeedrail/hsr-43final_report.pdf>

Huo, Xiaoming, Edward Wasserman, and Pingsheng Zhu. "Simplified Method of Lateral Distribution of Live Load Moment." *Journal of Bridge Engineering*. 9.4 (2004): 382-390. Print.

Huo, Xiaoming, Edward Wasserman, and Rizwan Iqbal. "Simplified Method of Lateral Distribution of Live Load Shear." *Journal of Bridge Engineering*. 10.5 (2005): 544-554. Print.

Kassner, Bernard. "Long-Term In-Service Evaluation of Two Bridges Designed with Fiber-Reinforced Polymer Girders." MS thesis. Virginia Polytechnic Institute and State University, 2004. Web.

Khaloo, Ali, and H. Mirzabozorg. "Load Distribution Factors in Simply Supported Skew Bridges."*Journal of Bridge Engineering*. 8.4 (2003): 241-244. Web. 26 July. 2011. <http://ascelibrary.org/action/showAbstract?page=241&volume=8&issue=4&journalCode=jbenf2>.

Maine Department of Transportation (MDOT). "Knickerbocker Bridge Plans." 2009

Mascaro, Margaret. "Out-of-Plane Web Deformation and Relative Arch Movement of Hybrid-Composite Beams Based on Photogrammetry." Project and Report. Virginia Polytechnic Institute and State University, 2012. Print.

Precast/Prestressed Concrete Institute (PCI). (2001). PCI Bridge Design Manual, PCI Institute, Chicago, IL.

Restrepo, Edgar. "Determination of AASHTO Bridge Design Parameters through Field Evaluation of the Rt. 601 Bridge: A Bridge Utilizing Strongwell 36 in. Fiber-Reinforced Polymer Double Web Beams as the Main Load Carrying Members." MS thesis. Virginia Polytechnic Institute and State University, 2002. Web. <http://scholar.lib.vt.edu/theses/available/etd-12162002-113130/>.

Snape, Thomas and Robert Lindyberg. *Test Results: HC Beam for the Knickerbocker Bridge.* Orono: Advanced Structures & Composites Center, Sep. 2009. Web. 4 July 2011. < <http://onlinepubs.trb.org/onlinepubs/archive/studies/idea/finalreports/highspeedrail/hsr-43final_report.pdf>

Stallings, Michael, and C.H. Yoo. "Tests and Ratings of Short-span Steel Bridges." *Journal of Structural Engineering*. 119.7 (1993): 2150-2168. Web. 17 Aug. 2012. <http://ascelibrary.org/doi/abs/10.1061/(ASCE)0733-9445(1993)119:7(2150)>.

Virginia Department of Transportation (VDOT). 2007 Road and Bridge Specifications. pg. 188.

Virginia Department of Transportation (VDOT). "Tide Mill Interim Plans." 2011.

Waldron, Christopher. "Determination of the Design Parameters for the Route 601 Bridge: A Bridge Containing the Strongwell 36 in. Hybrid Composite Double Web Beam." MS thesis. Virginia Polytechnic Institute and State University, 2001. Web. <http://scholar.lib.vt.edu/theses/available/etd-08082001-152240/>.

Appendix A – Sample Calculations

Hybrid-Composite Beam Worksheet

NOTE: The sample calculations are for a point load applied at midspan to one non-composite Hybrid-Composite Beam. The below calculations are for demonstrative purposes of the HCB design methodology only. Actual design calculations were performed in a Microsoft Excel Sheet provided by HC Bridge.

Original Sheet by: R. Ericksson

Modifications by: Shainur Ahsan

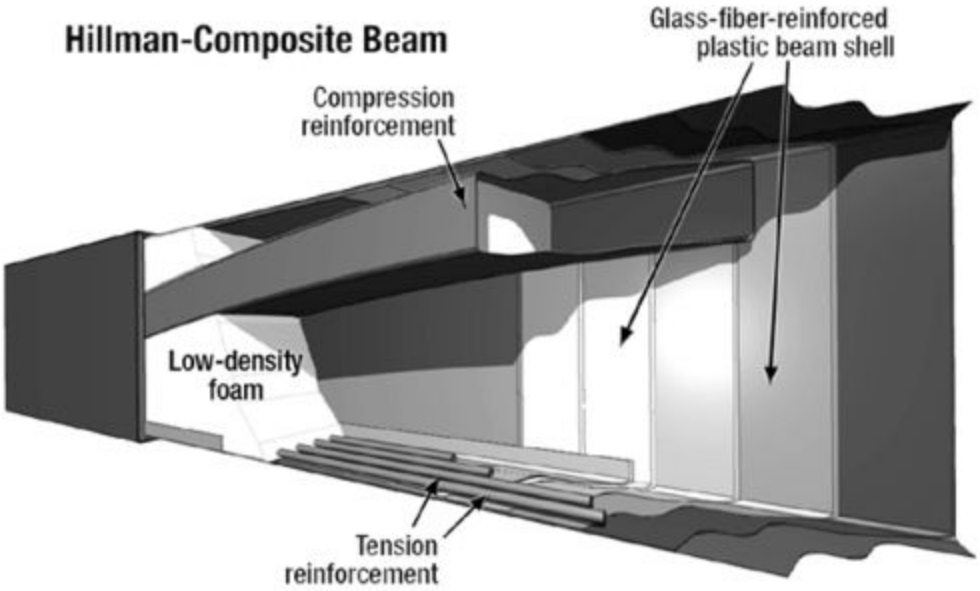

Table of Contents

1. Material Properties

2. Geometry

3. Loads

4. Load & Resistance Factors

5. Structural Analysis

   a. Deflection Check

   b. Flexural Strength Check

6. Bending Stress Check

1. Material Properties

Concrete:

Arch:

$f_c := 6ksi$ 28-Day compressive strength of arch concrete

$\gamma_c := 0.15kcf$ Density of arch concrete

Deck:

$f_{ct} := 0ksi$ 28-Day compressive strength of deck concrete

$\gamma_d := 0.15kcf$ Density of deck concrete

Steel:

Steel Strand:

$A_{strand} := 0.153in^2$ Area of one prestressing strand

$d_b := 0.5in$ Nominal diameter of prestressed strand

$f_{pu} := 270ksi$ Tensile strength of prestressing strand

$E_p := 27500ksi$ Modulus of elasticity of prestressing steel

FRP:

E-Glass Fiber:

$E_f := 10500ksi$

$\upsilon_f := 0.22$

Vinyl Ester Resin:

$E_m := 520ksi$

$\upsilon_m := 0.22$

Fiber Volume Ratio: $V_f := 0.53\%$

Glass Properties:

Webs:

$E_{w11} := 3100ksi$ $E_{w22} := 2300ksi$ $G_{w22} := 1010ksi$ $\upsilon_{w12} := 0.30$ $\tau_{allow} := 19ksi$

Flanges:

$E_{f11} := 3100ksi$ $E_{f22} := 2300ksi$ $G_{f22} := 1010ksi$ $\upsilon_{f12} := 0.3$ $\upsilon_{f21} := 0.26$

2. Geometry:

Beam:

$h := 21in$	Height of HCB
$b := 24in$	Width of HCB shell
$t_{glass\_lam} := 0.156in$	Glass laminate thickness
$N_{layers\_glass\_tf} := 1$	Number of glass layers in top flange
$N_{layers\_glass\_bf} := 1$	Number of glass layers in bottom flange
$N_{layers\_glass\_web} := 1$	Number of glass layers in web
$a_{arch} := 4in$	Thickness of arch concrete in HCB
$b_{fin} := 3.5in$	Width of "fin" that connects arch to HCB
$WP_{thrust\_line} := 2in$	Working point at thrust line
$N_{strands} := 22$	Number of unstressed prestressing strands per beam
$L_{ovr} := 44ft$	Overall length of precast section
$L_{des} := 43ft$	Design span of precast section

Slab:

$t_{slab} := 0in$	Thickness of CIP slab above HCB
$t_h := 0in$	Thickness of CIP haunch
$b_h := 60in$	Width of CIP haunch

Bridge:

$Spcg := 4ft$	Beam Spacing
$N_{beam} := 3$	Number of precast sections in bridge cross section
$N_{tracks} := 1$	Number of rail tracks
$Width_{overall} := 12ft$	Overall width of bridge
$Width_{ctc} := 13.5ft$	Curb to curb width of bridge

3. Loads:

Dead:

$w_{sw} := 0.182klf$ Beam self weight (per beam)

$w_{deck} := 0klf$ Weight of CIP deck (per beam)

$w_{barrier} := 0klf$ Weight of barrier or parapet (per beam)

Dead Weight

Place 20 kip point load at midspan

$$M_{DW} := \begin{pmatrix} 0 \\ 516 \\ 1032 \\ 1548 \\ 2064 \\ 2580 \\ 2064 \\ 1548 \\ 1032 \\ 516 \\ 0 \end{pmatrix} \cdot kip \cdot in \qquad V_{DW} := \begin{pmatrix} 20 \\ 20 \\ 20 \\ 20 \\ 20 \\ 0 \\ -20 \\ -20 \\ -20 \\ -20 \\ -20 \end{pmatrix} \cdot kip$$

Moments calculated using MASTAN2

Calculation Check

$$M_{max} = \frac{P \cdot L}{4}$$

$$M_{max} := \frac{20kip \cdot L_{des}}{4} = 2.58 \times 10^{3} \cdot kip \cdot in$$

5. Structural Analysis:

Beam Check Points

Check 10th points along half of the beam span

$i := 1..11$

$x_i := \left(\frac{i-1}{10}\right)\cdot L_{des}$

$x^T = (0 \;\; 4.3 \;\; 8.6 \;\; 12.9 \;\; 17.2 \;\; 21.5 \;\; 25.8 \;\; 30.1 \;\; 34.4 \;\; 38.7 \;\; 43)\,\text{ft}$

Shears & Moments

Non-composite loads:

Beam self-weight

$V_{sw_i} := w_{sw}\cdot\left(\frac{L_{des}}{2} - x_i\right)$ $\qquad M_{sw_i} := \frac{w_{sw}\cdot x_i}{2}\cdot\left(L_{des} - x_i\right)$

$V_{sw}^T = (3.913 \;\; 3.13 \;\; 2.348 \;\; 1.565 \;\; 0.783 \;\; 0 \;\; -0.783 \;\; -1.565 \;\; -2.348 \;\; -3.13 \;\; -3.913)\cdot\text{kip}$

$M_{sw}^T = (0 \;\; 15.143 \;\; 26.921 \;\; 35.334 \;\; 40.382 \;\; 42.065 \;\; 40.382 \;\; 35.334 \;\; 26.921 \;\; 15.143 \;\; 0)\cdot\text{kip}\cdot\text{ft}$

Deck weight

$V_{deck_i} := w_{deck}\cdot\left(\frac{L_{des}}{2} - x_i\right)$ $\qquad M_{deck_i} := \frac{w_{deck}\cdot x_i}{2}\cdot\left(L_{des} - x_i\right)$

$V_{deck}^T = (0 \;\; 0 \;\; 0 \;\; 0 \;\; 0 \;\; 0 \;\; 0 \;\; 0 \;\; 0 \;\; 0 \;\; 0)\cdot\text{kip}$

$M_{deck}^T = (0 \;\; 0 \;\; 0 \;\; 0 \;\; 0 \;\; 0 \;\; 0 \;\; 0 \;\; 0 \;\; 0 \;\; 0)\cdot\text{kip}\cdot\text{ft}$

Composite Loads:

$V_{barrier_i} := w_{barrier}\cdot\left(\frac{L_{des}}{2} - x_i\right)$ $\qquad M_{barrier_i} := \frac{w_{barrier}\cdot x_i}{2}\cdot\left(L_{des} - x_i\right)$

$V_{barrier}^T = (0 \;\; 0 \;\; 0 \;\; 0 \;\; 0 \;\; 0 \;\; 0 \;\; 0 \;\; 0 \;\; 0 \;\; 0)\cdot\text{kip}$

$M_{barrier}^T = (0 \;\; 0 \;\; 0 \;\; 0 \;\; 0 \;\; 0 \;\; 0 \;\; 0 \;\; 0 \;\; 0 \;\; 0)\cdot\text{kip}$

Impact Factor

$$\text{Impact} := \text{if}\left(L_{des} \le 14\text{ft}, 0.60, \text{if}\left(L_{des} \le 127\text{ft}, \frac{2.25}{\sqrt{\frac{L_{des}}{\text{ft}}}}, 0.2\right)\right) = 0.343$$

Determine k, distance from bottom of HCB to centroid of arch (compression reinforcement)

$$a_a := \frac{-4\cdot\left(h - N_{layers\_glass\_tf}\cdot t_{glass\_lam} - \frac{a_{arch}}{2} - WP_{thrust\_line}\right)}{L_{des}^{2}} = -2.53\times 10^{-4}\cdot in^{-1}$$

$$b_a := \frac{4\cdot\left(h - N_{layers\_glass\_tf}\cdot t_{glass\_lam} - \frac{a_{arch}}{2} - WP_{thrust\_line}\right)}{L_{des}} = 0.131$$

$$c_a := WP_{thrust\_line}$$

$$k_{a_i} := a_a\cdot\left(x_i\right)^2 + b_a\cdot x_i + c_a$$

$$k_a^{T} = (2 \quad 8.064 \quad 12.78 \quad 16.149 \quad 18.17 \quad 18.844 \quad 18.17 \quad 16.149 \quad 12.78 \quad 8.064 \quad 2)\cdot in$$

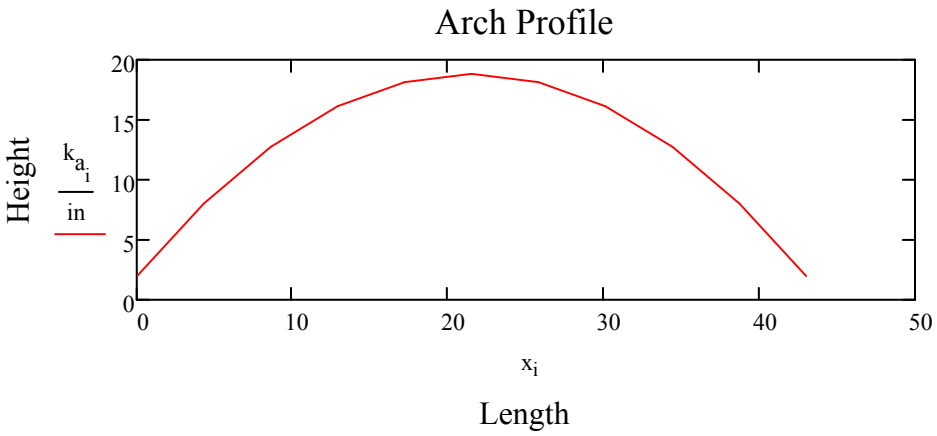

Total thicknesses of top & bottom flanges and webs of HCB:

$$t_{top} := N_{layers\_glass\_tf}\cdot t_{glass\_lam} = 0.156\cdot in$$

$$t_{bottom} := N_{layers\_glass\_bf}\cdot t_{glass\_lam} = 0.156\cdot in$$

$$t_{web} := N_{layers\_glass\_web}\cdot t_{glass\_lam} = 0.156\cdot in$$

Total area & height of tension reinforcement:

$$A_{str} := N_{strands}\cdot A_{strand} = 3.366\cdot in^2$$

$$z_s := t_{bottom} + 0.5\cdot d_b = 0.406\cdot in$$

HCB Properties (with compression reinforcement):

Top Flange:

$A_{tf} := b \cdot t_{top} = 3.744 \cdot in^2$ $y_{tf} := h - \frac{t_{top}}{2} = 20.922 \cdot in$

$I_{o\_t} := \frac{b \cdot t_{top}^3}{12} = 7.593 \times 10^{-3} \cdot in^4$

Bottom Flange:

$A_{bf} := b \cdot t_{bottom} = 3.744 \cdot in^2$ $y_{bf} := \frac{t_{bottom}}{2} = 0.078 \cdot in$

$I_{o\_b} := \frac{b \cdot t_{bottom}^3}{12} = 7.593 \times 10^{-3} \cdot in^4$

Webs (combined):

$A_{web} := 2 \cdot h \cdot t_{web} = 6.552 \cdot in^2$ $y_{web} := \frac{h}{2} = 10.5 \cdot in$

$I_{o\_w} := \frac{2 \cdot t_{web} \cdot h^3}{12} = 240.786 \cdot in^4$

Tension Reinforcement (unstressed strand):

$n_{str} := \frac{E_p}{E_{w11}} = 8.871$ $A_s := A_{str} \cdot n_{str} = 29.86 \cdot in^2$ $y_{strand} := z_s = 0.406 \cdot in$

$I_{o\_s} := 0in^4$ (neglect)

Arch Concrete:

$E_c := 57000 \cdot \sqrt{\frac{f_c}{1000ksi}} \cdot ksi = 4.415 \times 10^3 \cdot ksi$

$n_{conc} := \frac{E_c}{E_{w11}} = 1.424$

$A_c := a_{arch} \cdot b \cdot n_{conc} = 136.729 \cdot in^2$

$y_{c_i} := k_{a_i}$

$y_c^T = (2 \quad 8.064 \quad 12.78 \quad 16.149 \quad 18.17 \quad 18.844 \quad 18.17 \quad 16.149 \quad 12.78 \quad 8.064 \quad 2) \cdot in$

$I_{o\_a} := \frac{a_{arch}^3 \cdot b \cdot n_{conc}}{12} = 182.305 \cdot in^4$

Total area of HCB

$$A_{HCB} := A_{tf} + A_{bf} + A_{web} + A_s + A_c = 180.628 \cdot in^2$$

Centroid of HCB

$$y_{bar_i} := \frac{A_{tf} \cdot y_{tf} + A_{bf} \cdot y_{bf} + A_{web} \cdot y_{web} + A_s \cdot y_{strand} + A_c \cdot y_{c_i}}{A_{HCB}}$$

Moment of Inertia of HCB:

$$I_{HCBL1_i} := I_{o\_t} + A_{tf} \cdot \left(y_{tf} - y_{bar_i}\right)^2$$ Contribution of top flange

$$I_{HCBL2_i} := I_{o\_b} + A_{bf} \cdot \left(y_{bf} - y_{bar_i}\right)^2$$ Contribution of bottom flange

$$I_{HCBL3_i} := I_{o\_w} + A_{web} \cdot \left(y_{web} - y_{bar_i}\right)^2$$ Contribution of web

$$I_{HCBL4_i} := I_{o\_s} + A_s \cdot \left(y_{strand} - y_{bar_i}\right)^2$$ Contribution of strand

$$I_{HCBL5_i} := I_{o\_a} + A_c \cdot \left(y_{c_i} - y_{bar_i}\right)^2$$ Contribution of arch concrete

$$I_{HCB_i} := I_{HCBL1_i} + I_{HCBL2_i} + I_{HCBL3_i} + I_{HCBL4_i} + I_{HCBL5_i}$$

$$I_{HCB}^T = \left(2.298 \times 10^3 \quad 2.861 \times 10^3 \quad 4.989 \times 10^3 \quad 7.414 \times 10^3 \quad 9.231 \times 10^3 \quad 9.897 \times 10^3 \quad 9.231 \times\right.$$

Section Modulus:

Bottom of HCB:

$$S_{bb_i} := \frac{I_{HCB_i}}{y_{bar_i}}$$

$$S_{bb}^T = (958.707 \quad 409.525 \quad 472.569 \quad 565.627 \quad 630.633 \quad 653.366 \quad 630.633 \quad 565.627 \quad 472.569 \quad 4$$

$$S_{tb_i} := \frac{I_{HCB_i}}{\left(h - y_{bar_i}\right)}$$

$$S_{tb}^T = \left(123.541 \quad 204.205 \quad 477.76 \quad 939.35 \quad 1.451 \times 10^3 \quad 1.691 \times 10^3 \quad 1.451 \times 10^3 \quad 939.35 \quad 477\right.$$

5.a Deflection Check

Use conjugate beam method to compute live load deflections. For a simple-span beam, this is accomplished by loading a conjugate beam with the M/EI diagram. This beam is then analylzed using beam theory. Sheas represents rotations while moments represent deflections.

$M_{Design} := M_{sw} + M_{DW}$

$\text{Deflection}(M, E, I, x, L_{span}) :=$

SumAreaArm ← 0

$L_{seg} \leftarrow x_2 - x_1$

for $i \in 1 .. \text{last}(x) - 1$

$\text{Area} \leftarrow L_{seg} \cdot \frac{\frac{(M_i + M_{i+1})}{2}}{E \cdot I_i}$

$\text{Arm} \leftarrow L_{span} - (i - 0.5) \cdot L_{seg}$

$\text{SumAreaArm} \leftarrow \text{SumAreaArm} + \text{Area} \cdot \text{Arm}$

$R_L \leftarrow \frac{\text{SumAreaArm}}{L_{span}}$

$D_1 \leftarrow 0\text{in}$

for $i \in 1 .. \text{last}(x) - 1$

SumAreaArm ← 0

for $j \in 1 .. \text{last}(x) - 1$

break if $j > i$

$\text{Area} \leftarrow L_{seg} \cdot \frac{\frac{(M_j + M_{j+1})}{2}}{E \cdot I_j}$

$\text{Arm} \leftarrow [i - (j - 0.5)] \cdot L_{seg}$

$\text{SumAreaArm} \leftarrow \text{SumAreaArm} + \text{Area} \cdot \text{Arm}$

$\text{Arm} \leftarrow i \cdot L_{seg}$

$D_{i+1} \leftarrow R_L \cdot \text{Arm} - \text{SumAreaArm}$

return D

$\Delta_{LL} := \text{Deflection}(M_{DW}, E_{w11}, I_{HCB}, x, L_{des})$

$\Delta_{LL}^{T} = (0 \quad 0.873 \quad 1.582 \quad 2.063 \quad 2.329 \quad 2.382 \quad 2.226 \quad 1.886 \quad 1.386 \quad 0.746 \quad 0) \cdot \text{in}$

5.b Flexural Strength Check

Factored Moments:

Group I

$M_{ul_i} := M_{Design_i}$

$M_{ul}^T = (0 \quad 58.143 \quad 112.921 \quad 164.334 \quad 212.382 \quad 257.065 \quad 212.382 \quad 164.334 \quad 112.921 \quad 58.143 \quad 0$

Group IA

$M_{ulA_i} := M_{Design_i}$

$M_{ulA}^T = (0 \quad 58.143 \quad 112.921 \quad 164.334 \quad 212.382 \quad 257.065 \quad 212.382 \quad 164.334 \quad 112.921 \quad 58.143$

Adopted Moments

$$M_{u_i} := \begin{cases} M_{ul_i} & \text{if } \left(M_{ul_i} \geq M_{ulA_i}\right) \\ M_{ulA} & \text{otherwise} \end{cases}$$

$M_u^T = (0 \quad 58.143 \quad 112.921 \quad 164.334 \quad 212.382 \quad 257.065 \quad 212.382 \quad 164.334 \quad 112.921 \quad 58.143 \quad 0)$

Maximum usable compressive strain in concrete:

$\varepsilon_{cu} := 0.003$

Assumed height of neutral axis:

$y_u := 15.125in$

Compute strain, stress, force, and resulting moment in each element of the cross section:

Slab Concrete:

Strain:

$\varepsilon_{cs} := -\varepsilon_{cu} = -3 \times 10^{-3}$

Stress:

$$\beta_1 := \begin{cases} 0.85 & \text{if } f_{ct} \leq 4ksi \\ 0.65 & \text{if } f_{ct} \geq 8ksi \\ 0.85 - \left(\frac{f_{ct} - 4ksi}{ksi} \cdot 0.05\right) & \end{cases} \qquad \beta_1 = 1.05$$

$F_{CS} := -\beta_1 \cdot f_c \cdot Spcg \cdot t_{slab} = 0$

Height of Composite Section: $h_c := 28.5in$

$$arm_{CS} := \left(-h_c + y_u\right) + \frac{t_{slab}}{2} = -13.375 \cdot in$$

$$M_{CS} := F_{CS} \cdot arm_{CS} = 0 \cdot kip \cdot ft$$

Arch Concrete:

$$\varepsilon_c := -\varepsilon_{cu} = -3 \times 10^{-3}$$

$$F_C := -\beta_1 \cdot f_c \cdot b \cdot a_{arch} = -604.8 \cdot kip$$

$$arm_C := -\left(h - y_u - t_{top} - \frac{a_{arch}}{2}\right) = -3.719 \cdot in$$

$$M_C := F_C \cdot arm_C = 187.438 \cdot kip \cdot ft$$

HCB Top Flange:

$$\varepsilon_{TF} := \left(\frac{h - y_u}{h_c - y_u}\right) \cdot \varepsilon_{cs} = -1.318 \times 10^{-3}$$

$$F_{TF} := \varepsilon_{TF} \cdot E_{w11} \cdot b \cdot t_{top}$$

$$arm_{TF} := \left(-h + y_u\right) + \frac{t_{top}}{2} = -5.797 \cdot in$$

$$M_{TF} := F_{TF} \cdot arm_{TF} = 88.662 \cdot kip \cdot in$$

HCB Top Portion of Web (in compression):

$$\varepsilon_{WT} := \frac{\varepsilon_{TF}}{2} = -6.589 \times 10^{-4}$$

$$F_{WT} := 2 \cdot \varepsilon_{WT} \cdot E_{w11} \cdot \left(h - y_u\right) \cdot t_{web} = -3.744 \cdot kip$$

$$arm_{WT} := \frac{2 \cdot \left(-h + y_u\right)}{3} = -3.917 \cdot in$$

$$M_{WT} := F_{WT} \cdot arm_{WT} = 14.664 \cdot kip \cdot in$$

HCB Bottom Flange:

$$\varepsilon_{BF} := \left(\frac{-y_u}{h_c - y_u}\right) \cdot \varepsilon_{cs} = 3.393 \times 10^{-3}$$

$$F_{BF} := \varepsilon_{BF} \cdot E_{w11} \cdot b \cdot t_{bottom} = 39.375 \cdot kip$$

$$arm_{BF} := y_u - \frac{t_{bottom}}{2} = 15.047 \cdot in$$

$$M_{BF} := F_{BF} \cdot arm_{BF} = 592.475 \cdot kip \cdot in$$

HCB Bottom Portion of Web (in tension):

$$\varepsilon_{WB} := \frac{\varepsilon_{BF}}{2} = 1.696 \times 10^{-3}$$

$$F_{WB} := 2 \cdot \varepsilon_{WB} \cdot E_{w11} \cdot y_u \cdot t_{web} = 24.814 \cdot kip$$

$$arm_{WB} := \frac{2 \cdot y_u}{3} = 10.083 \cdot in$$

$$M_{WB} := F_{WB} \cdot arm_{WB} = 250.212 \cdot kip \cdot in$$

Strand:

$$\varepsilon_s := -\left(\frac{y_u - z_s}{h_c - y_u}\right) \cdot \varepsilon_{cs} = 3.301 \times 10^{-3}$$

$$f_s := \varepsilon_s \cdot \left[887 + \frac{27613}{\left[1 + \left(112.4 \cdot \varepsilon_s\right)^{7.36}\right]^{\frac{1}{7.36}}} \right]$$

Devalapura and Tadros, 1992

$$T_1 := \left(112.4 \cdot \varepsilon_s\right)^{7.36} = 6.781 \times 10^{-4}$$

$$T_2 := \left(1 + T_1\right)^{\frac{1}{7.36}} = 1$$

$$f_{so} := \varepsilon_s \cdot \left(887 + \frac{27613}{T_2} \right) \cdot ksi = 94.083 \cdot ksi$$

$$f_s := \begin{cases} f_{so} & \text{if } f_{so} \le 270ksi \\ 270ksi & \text{otherwise} \end{cases}$$

$$F_s := A_{str} \cdot f_s = 316.684 \cdot kip$$

$$arm_s := y_u - z_s = 14.719 \cdot in$$

$$M_s := F_s \cdot arm_s = 4.661 \times 10^3 \cdot kip \cdot in$$

Sum of Forces:

$\Sigma F := F_{CS} + F_C + F_{TF} + F_{WT} + F_{WB} + F_{BF} + F_s = -242.965 \cdot kip$

Flexural Strength

$M_n := M_{CS} + M_C + M_{TF} + M_{WT} + M_{BF} + M_{WB} + M_s = 7.857 \times 10^3 \cdot kip \cdot in$ $\phi_f := 0.9$

$\phi M_n := \phi_f \cdot M_n = 7.071 \times 10^3 \cdot kip \cdot in$

$\phi M_n = 589.24 \cdot kip \cdot ft$

$M_{u_6} = 257.065 \cdot kip \cdot ft$

$Flex\_Ck := \begin{cases} \text{"OK"} & \text{if } \phi M_n \geq M_{u_6} \\ \text{"NG"} & \text{otherwise} \end{cases} = \text{"OK"}$

6. Bending Stress Check

Service Moments:

Dead Load:

non-composite:

$M_{DL\_nc_i} := M_{sw_i} + M_{deck_i}$

$M_{DL\_nc}^{T} = (0 \quad 15.143 \quad 26.921 \quad 35.334 \quad 40.382 \quad 42.065 \quad 40.382 \quad 35.334 \quad 26.921 \quad 15.143 \quad 0)$

composite:

$M_{DL\_c_i} := M_{barrier_i}$

$M_{DL\_c}^{T} = (0 \quad 0 \quad 0 \quad 0 \quad 0 \quad 0 \quad 0 \quad 0 \quad 0 \quad 0 \quad 0)\cdot kip\cdot ft$

Service Stresses:

Dead Load:

non-composite:

top HCB:

$$f_{HCB\_top\_DL\_nc_i} := \frac{M_{DL\_nc_i}}{S_{tb_i}}$$

$f_{HCB\_top\_DL\_nc}^{T} = (0 \quad 0.89 \quad 0.676 \quad 0.451 \quad 0.334 \quad 0.299 \quad 0.334 \quad 0.451 \quad 0.676 \quad 0.89 \quad 0)\cdot k$

bottom HCB:

$$f_{HCB\_bot\_DL\_nc_i} := \frac{-M_{DL\_nc_i}}{S_{bb_i}}$$

$f_{HCB\_bot\_DL\_nc}^{T} = (0 \quad -0.444 \quad -0.684 \quad -0.75 \quad -0.768 \quad -0.773 \quad -0.768 \quad -0.75 \quad -0.684 \quad -$

Maximum Allowable Stress in Concrete Arch to Remain Elastic

$0.4f_c = 2.4 \cdot ksi$

Calculation of Stress in Concrete due to a 20 kip Point Load at Midspan

$$f_{HCB\_conc\_arch_i} := \frac{M_{u_i} \cdot \left(k_{a_i} + a_{arch} \cdot 0.5 - y_{c_i}\right) \cdot n_{conc}}{I_{HCB_i}}$$

Moment calculated at top of arch

$f_{HCB\_conc\_arch}^{T} = (0 \quad 0.695 \quad 0.774 \quad 0.758 \quad 0.786 \quad 0.888 \quad 0.786 \quad 0.758 \quad 0.774 \quad 0.695 \quad 0) \cdot$

$\max\left(f_{HCB\_conc\_arch}\right) = 0.888 \cdot ksi$

The max stress is less than allowable

Calculate the Maximum Point Load based on Stress at Top of Arch

$$M_{max\_P} := \frac{0.4 \cdot f_c \cdot I_{HCB_6}}{\left(k_{a_6} + a_{arch} \cdot 0.5 - y_{c_6}\right) \cdot n_{conc}} = 694.876 \cdot kip \cdot ft$$

$$P_{max} := \frac{M_{max\_P} \cdot 4}{L_{des}} = 64.64 \cdot kip$$

Calculation of Stress in Concrete Fin due to a 20 kip Point Load at Midspan

$$f_{HCB\_conc\_fin_i} := \frac{M_{u_i} \cdot \left[(h - 1.75in) - y_{c_i}\right] \cdot n_{conc}}{I_{HCB_i}}$$

Moment calculated at top of fin

$f_{HCB\_conc\_fin}^{T} = (0 \quad 3.885 \quad 2.503 \quad 1.175 \quad 0.425 \quad 0.18 \quad 0.425 \quad 1.175 \quad 2.503 \quad 3.885 \quad 0) \cdot ksi$

$\max\left(f_{HCB\_conc\_fin}\right) = 3.885 \cdot ksi$

Calculate the Maximum Point Load based on Stress at top of Concrete Fin

$$M_{max\_P2} := \frac{0.4 \cdot f_c \cdot I_{HCB_1}}{\left[(h - 1.75in) - y_{c_1}\right] \cdot n_{conc}} = 18.709 \cdot kip \cdot ft$$

$$P_{max2} := \frac{M_{max\_P2} \cdot 5 \cdot 4}{L_{des}} = 8.702 \cdot kip$$

Calculation of Stress in Concrete Fin due to local bearing of 20 kips

Assume load is spread over a square area. The fin is 4 inches at the top and tapers down to 3 inches at the arch surface near the support. Take an average of 3.5 in.

$a := 3.5in$

$\sigma_{bearing} := \frac{20kip}{a^2} = 1.633 \cdot ksi$

Calculate the Maximum Point Load based on Local Bearing

$P_{max3} := 0.4 \cdot f_c \cdot a^2 = 29.4 \cdot kip$

Maximum Point Load to be Applied to HCB

$Max\_P := \min\left(P_{max}, P_{max2}, P_{max3}\right) = 8.702 \cdot kip$

Calculation of Expected Strains

$$\varepsilon = \frac{M \cdot y}{I \cdot E}$$

Strain for Top of FRP

Midspan

$$y_{FRP\_top\_m} := 21in - y_{bar_6} = 5.853 \cdot in$$

$$\varepsilon_{FRP\_top\_m} := \frac{\left(-M_{DW}\right)_6 \cdot y_{FRP\_top\_m}}{I_{HCB_6} \cdot E_{w11}} = -4.922 \times 10^{-4}$$

Quarter Point

$$y_{FRP\_top\_q} := 21in - \frac{\left(y_{bar_3} + y_{bar_4}\right)}{2} = 9.168 \cdot in$$

$$M_{FRP\_top\_q} := \frac{M_{DW_3} + M_{DW_4}}{2} = 1.29 \times 10^3 \cdot kip \cdot in$$

$$I_{FRP\_top\_q} := \frac{I_{HCB_3} + I_{HCB_4}}{2} = 6.201 \times 10^3 \cdot in^4$$

$$\varepsilon_{FRP\_top\_q} := \frac{-M_{FRP\_top\_q} \cdot y_{FRP\_top\_q}}{I_{FRP\_top\_q} \cdot E_{w11}} = -6.152 \times 10^{-4}$$

Strain for Bottom of FRP

Midspan

$$y_{FRP\_bottom\_m} := y_{bar_6} = 15.147 \cdot in$$

$$\varepsilon_{FRP\_bottom\_m} := \frac{M_{DW_6} \cdot y_{FRP\_bottom\_m}}{I_{HCB_6} \cdot E_{w11}} = 1.274 \times 10^{-3}$$

Quarter Point

$$y_{FRP\_bottom\_q} := \frac{y_{bar_3} + y_{bar_4}}{2} = 11.832 \cdot in$$

$$M_{FRP\_bottom\_q} := \frac{M_{DW_3} + M_{DW_4}}{2} = 1.29 \times 10^3 \cdot kip \cdot in$$

$$I_{FRP\_bottom\_q} := \frac{I_{HCB_3} + I_{HCB_4}}{2} = 6.201 \times 10^3 \cdot in^4$$

$$\varepsilon_{FRP\_bottom\_q} := \frac{M_{FRP\_bottom\_q} \cdot y_{FRP\_bottom\_q}}{I_{FRP\_bottom\_q} \cdot E_{w11}} = 7.94 \times 10^{-4}$$

Strain for 7 inches from bottom of FRP

Midspan

$$y_{FRP\_7\_m} := y_{bar_6} - 7in = 8.147 \cdot in$$

$$\varepsilon_{FRP\_7\_m} := \frac{M_{DW_6} \cdot y_{FRP\_7\_m}}{I_{HCB_6} \cdot E_{w11}} = 6.851 \times 10^{-4}$$

Quarter Point

$$y_{FRP\_7\_q} := \frac{y_{bar_3} + y_{bar_4}}{2} - 7in = 4.832 \cdot in$$

$$M_{FRP\_7\_q} := \frac{M_{DW_3} + M_{DW_4}}{2} = 1.29 \times 10^{3} \cdot kip \cdot in$$

$$I_{FRP\_7\_q} := \frac{I_{HCB_3} + I_{HCB_4}}{2} = 6.201 \times 10^{3} \cdot in^4$$

$$\varepsilon_{FRP\_7\_q} := \frac{M_{FRP\_7\_q} \cdot y_{FRP\_7\_q}}{I_{FRP\_7\_q} \cdot E_{w11}} = 3.243 \times 10^{-4}$$

Strain for 14 inches from bottom of FRP

Midspan

$$y_{FRP\_14\_m} := y_{bar_6} - 14in = 1.147 \cdot in$$

$$\varepsilon_{FRP\_14\_m} := \frac{M_{DW_6} \cdot y_{FRP\_14\_m}}{I_{HCB_6} \cdot E_{w11}} = 9.649 \times 10^{-5}$$

Quarter Point

$$y_{FRP\_14\_q} := \frac{y_{bar_3} + y_{bar_4}}{2} - 14in = -2.168 \cdot in$$

$$M_{FRP\_14\_q} := \frac{M_{DW_3} + M_{DW_4}}{2} = 1.29 \times 10^{3} \cdot kip \cdot in$$

$$I_{FRP\_14\_q} := \frac{I_{HCB_3} + I_{HCB_4}}{2} = 6.201 \times 10^{3} \cdot in^4$$

$$\varepsilon_{FRP\_14\_q} := \frac{M_{FRP\_14\_q} \cdot y_{FRP\_14\_q}}{I_{FRP\_14\_q} \cdot E_{w11}} = -1.455 \times 10^{-4}$$

Strain for Tension Strand

Midspan

$$y_{strand\_m} := y_{bar_6} - z_s = 14.741 \cdot in$$

$$\varepsilon_{strand\_m} := \frac{M_{DW_6} \cdot y_{strand\_m}}{I_{HCB_6} \cdot E_{w11}} = 1.24 \times 10^{-3}$$

Quarter Point

$$y_{strand\_q} := \frac{y_{bar_3} + y_{bar_4}}{2} - z_s = 11.426 \cdot in$$

$$M_{strand\_q} := \frac{M_{DW_3} + M_{DW_4}}{2} = 1.29 \times 10^{3} \cdot kip \cdot in$$

$$I_{strand\_q} := \frac{I_{HCB_3} + I_{HCB_4}}{2} = 6.201 \times 10^{3} \cdot in^4$$

$$\varepsilon_{strand\_q} := \frac{M_{FRP\_14\_q} \cdot y_{strand\_q}}{I_{strand\_q} \cdot E_{w11}} = 7.667 \times 10^{-4}$$

Strain for Concrete

Midspan

Top

$$y_{concrete\_top\_m} := 1in + y_{c_6} - y_{bar_6} = 4.697 \cdot in$$

$$\varepsilon_{concrete\_top\_m} := \frac{\left(-M_{DW}\right)_6 \cdot y_{concrete\_top\_m}}{I_{HCB_6} \cdot E_{w11}} = -3.949 \times 10^{-4}$$

Bottom

$$y_{concrete\_bot\_m} := y_{c_6} - 1in - y_{bar_6} = 2.697 \cdot in$$

$$\varepsilon_{concrete\_bot\_m} := \frac{\left(-M_{DW}\right)_6 \cdot y_{concrete\_bot\_m}}{I_{HCB_6} \cdot E_{w11}} = -2.268 \times 10^{-4}$$

Quarter Point

Top

$$y_{concrete\_top\_q} := \frac{y_{bar_3} + y_{bar_4}}{2} - \frac{y_{c_3} + y_{c_4}}{2} + 1in = -1.632 \cdot in$$

$$M_{concrete\_top\_q} := \frac{M_{DW_3} + M_{DW_4}}{2} = 1.29 \times 10^3 \cdot kip \cdot in$$

$$I_{concrete\_top\_q} := \frac{I_{HCB_3} + I_{HCB_4}}{2} = 6.201 \times 10^3 \cdot in^4$$

$$\varepsilon_{concrete\_top\_q} := \frac{M_{concrete\_top\_q} \cdot y_{concrete\_top\_q}}{I_{concrete\_top\_q} \cdot E_{w11}} = -1.095 \times 10^{-4}$$

Bottom

$$y_{concrete\_bot\_q} := \frac{y_{bar_3} + y_{bar_4}}{2} - \frac{y_{c_3} + y_{c_4}}{2} - 1in = -3.632 \cdot in$$

$$M_{concrete\_bot\_q} := \frac{M_{DW_3} + M_{DW_4}}{2} = 1.29 \times 10^3 \cdot kip \cdot in$$

$$I_{concrete\_bot\_q} := \frac{I_{HCB_3} + I_{HCB_4}}{2} = 6.201 \times 10^3 \cdot in^4$$

$$\varepsilon_{concrete\_bot\_q} := \frac{M_{concrete\_bot\_q} \cdot y_{concrete\_bot\_q}}{I_{concrete\_bot\_q} \cdot E_{w11}} = -2.437 \times 10^{-4}$$

Strain for gage on bottom of wing

Midspan

$$y_{FRP\_wing\_m} := 21in - y_{bar_6} - 3in = 2.853 \cdot in$$

$$\varepsilon_{FRP\_wing\_m} := \frac{(-M_{DW})_6 \cdot y_{FRP\_wing\_m}}{I_{HCB_6} \cdot E_{w11}} = -2.399 \times 10^{-4}$$

Quarter Point

$$y_{FRP\_wing\_q} := 21in - \frac{(y_{bar_3} + y_{bar_4})}{2} - 3in = 6.168 \cdot in$$

$$M_{FRP\_wing\_q} := \frac{M_{DW_3} + M_{DW_4}}{2} = 1.29 \times 10^{3} \cdot kip \cdot in$$

$$I_{FRP\_wing\_q} := \frac{I_{HCB_3} + I_{HCB_4}}{2} = 6.201 \times 10^{3} \cdot in^{4}$$

$$\varepsilon_{FRP\_wing\_q} := \frac{-M_{FRP\_wing\_q} \cdot y_{FRP\_wing\_q}}{I_{FRP\_wing\_q} \cdot E_{w11}} = -4.139 \times 10^{-4}$$

Strain for gages at support

7 inches from bottom

$$y_{bars} := \frac{y_{bar_2} - y_{bar_1}}{x_2 - x_1} \cdot \left(1ft - x_1\right) + y_{bar_1} = 3.465 \cdot in$$

$$y_{FRP\_7\_s} := 7in - y_{bars}$$

$$M_{FRP\_7\_s} := \frac{M_{DW_2} - M_{DW_1}}{x_2 - x_1} \cdot \left(1ft - x_1\right) + M_{DW_{1b}} = 120 \cdot kip \cdot in$$

$$I_{FRP\_7\_s} := \frac{I_{HCB_2} - I_{HCB_1}}{x_2 - x_1} \cdot \left(1ft - x_1\right) + I_{HCB_1} = 2.429 \times 10^{3} \cdot in^{4}$$

$$\varepsilon_{FRP\_7\_s} := \frac{M_{FRP\_7\_s} \cdot y_{FRP\_7\_s}}{I_{FRP\_7\_s} \cdot E_{w11}} = 5.634 \times 10^{-5}$$

14 inches from bottom

$$y_{FRP\_14\_s} := 14in - y_{bars}$$

$$M_{FRP\_14\_s} := \frac{M_{DW_2} - M_{DW_1}}{x_2 - x_1} \cdot \left(1ft - x_1\right) + M_{DW_1} = 120 \cdot kip \cdot in$$

$$I_{FRP\_14\_s} := \frac{I_{HCB_2} - I_{HCB_1}}{x_2 - x_1} \cdot \left(1ft - x_1\right) + I_{HCB_1} = 2.429 \times 10^{3} \cdot in^{4}$$

$$\varepsilon_{FRP\_14\_s} := \frac{M_{FRP\_14\_s} \cdot y_{FRP\_14\_s}}{I_{FRP\_14\_s} \cdot E_{w11}} = 1.679 \times 10^{-4}$$

Strain for concrete gages at support

Top

$$y_{cs} := \frac{y_{c_2} - y_{c_1}}{x_2 - x_1} \cdot \left(1\,ft - x_1\right) + y_{c_1} = 3.41 \cdot in$$

$$y_{concrete\_top\_s} := 1\,in + y_{cs} - y_{bars}$$

$$M_{concrete\_top\_s} := \frac{M_{DW_2} - M_{DW_1}}{x_2 - x_1} \cdot \left(1\,ft - x_1\right) + M_{DW_1} = 120 \cdot kip \cdot in$$

$$I_{concrete\_top\_s} := \frac{I_{HCB_2} - I_{HCB_1}}{x_2 - x_1} \cdot \left(1\,ft - x_1\right) + I_{HCB_1} = 2.429 \times 10^{3} \cdot in^4$$

$$\varepsilon_{concrete\_top\_s} := \frac{M_{concrete\_top\_s} \cdot y_{concrete\_top\_s}}{I_{concrete\_top\_s} \cdot E_{w11}} = 1.507 \times 10^{-5}$$

Bottom

$$y_{concrete\_bot\_s} := y_{cs} - y_{bars} - 1\,in$$

$$M_{concrete\_bot\_s} := \frac{M_{DW_2} - M_{DW_1}}{x_2 - x_1} \cdot \left(1\,ft - x_1\right) + M_{DW_{1b}} = 120 \cdot kip \cdot in$$

$$I_{concrete\_bot\_s} := \frac{I_{HCB_2} - I_{HCB_1}}{x_2 - x_1} \cdot \left(1\,ft - x_1\right) + I_{HCB_1} = 2.429 \times 10^{3} \cdot in^4$$

$$\varepsilon_{concrete\_bot\_s} := \frac{M_{concrete\_bot\_s} \cdot y_{concrete\_bot\_s}}{I_{concrete\_bot\_s} \cdot E_{w11}} = -1.68 \times 10^{-5}$$

Appendix B – Supplemental Phase I Results

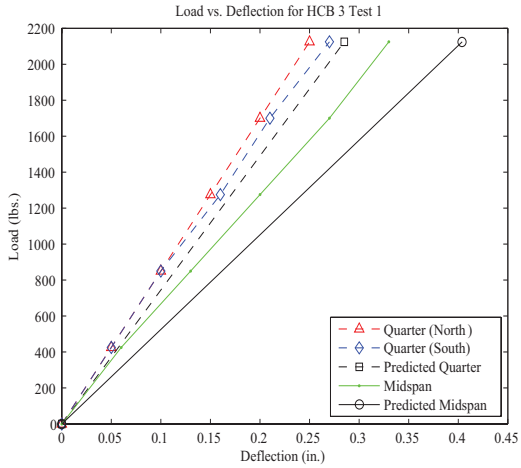
Load vs. Deflection for HCB 3 Test 1
Load (lbs.)
Deflection (in.)
Quarter (North)
Quarter (South)
Predicted Quarter
Midspan
Predicted Midspan

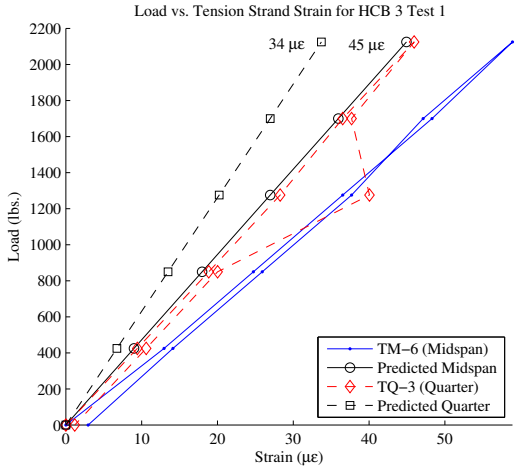
Load vs. Tension Strand Strain for HCB 3 Test 1
34 με
45 με
Load (lbs.)
Strain (με)
TM−6 (Midspan)
Predicted Midspan
TQ−3 (Quarter)
Predicted Quarter

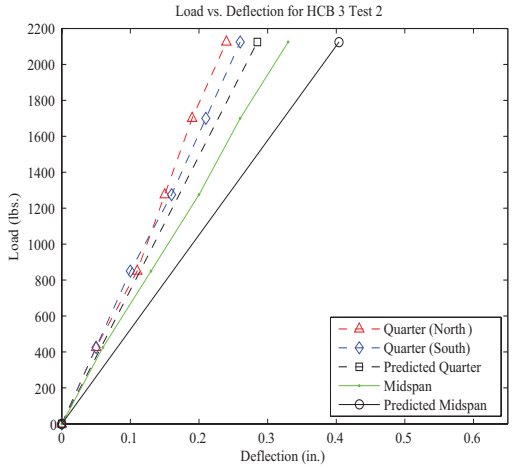
Load vs. Deflection for HCB 3 Test 2
Load (lbs.)
Deflection (in.)
Quarter (North)
Quarter (South)
Predicted Quarter
Midspan
Predicted Midspan

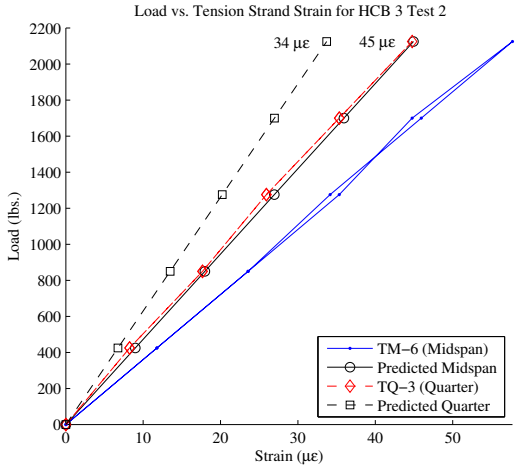
Load vs. Tension Strand Strain for HCB 3 Test 2
34 με
45 με
Load (lbs.)
Strain (με)
TM−6 (Midspan)
Predicted Midspan
TQ−3 (Quarter)
Predicted Quarter

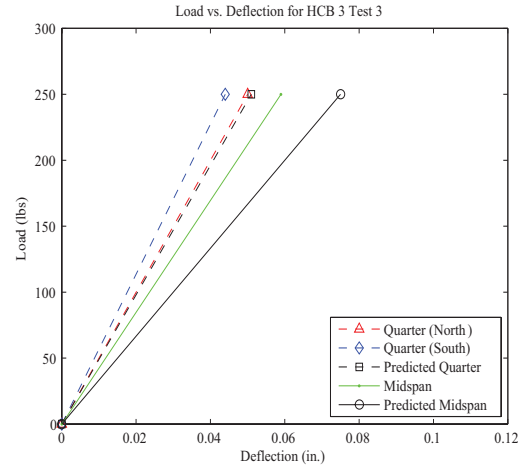
Load vs. Deflection for HCB 3 Test 3
Load (lbs)
Deflection (in.)
Quarter (North)
Quarter (South)
Predicted Quarter
Midspan
Predicted Midspan

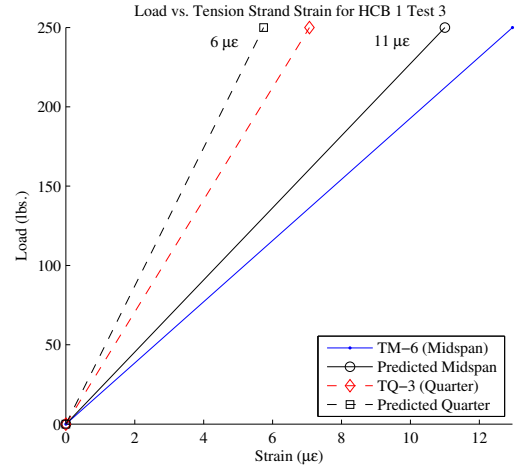
Load vs. Tension Strand Strain for HCB 1 Test 3
6 με
11 με
Load (lbs.)
Strain (με)
TM−6 (Midspan)
Predicted Midspan
TQ−3 (Quarter)
Predicted Quarter

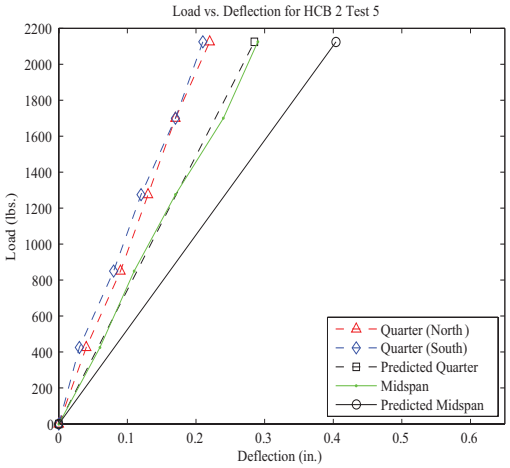
Load vs. Deflection for HCB 2 Test 5
Load (lbs.)
Deflection (in.)
Quarter (North)
Quarter (South)
Predicted Quarter
Midspan
Predicted Midspan

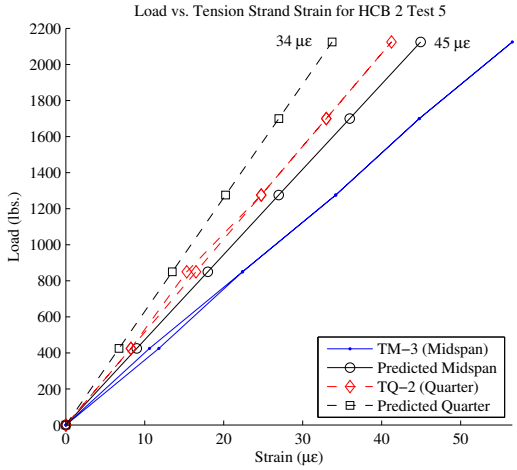
Load vs. Tension Strand Strain for HCB 2 Test 5
34 με
45 με
Load (lbs.)
Strain (με)
TM−3 (Midspan)
Predicted Midspan
TQ−2 (Quarter)
Predicted Quarter

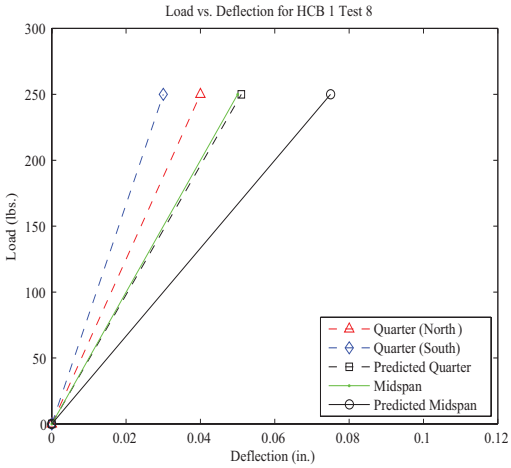
Load vs. Deflection for HCB 1 Test 8
Load (lbs.)
Deflection (in.)
Quarter (North)
Quarter (South)
Predicted Quarter
Midspan
Predicted Midspan

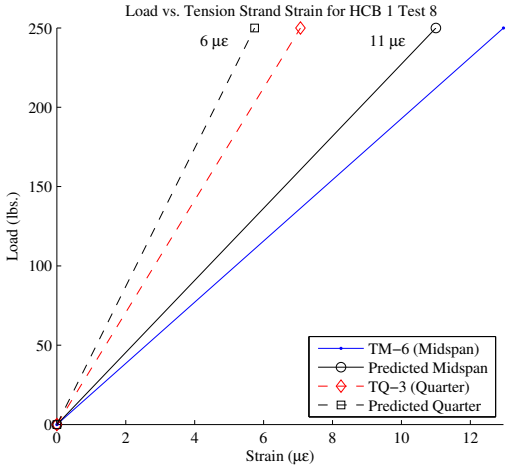
Load vs. Tension Strand Strain for HCB 1 Test 8
6 με
11 με
Load (lbs.)
Strain (με)
TM−6 (Midspan)
Predicted Midspan
TQ−3 (Quarter)
Predicted Quarter

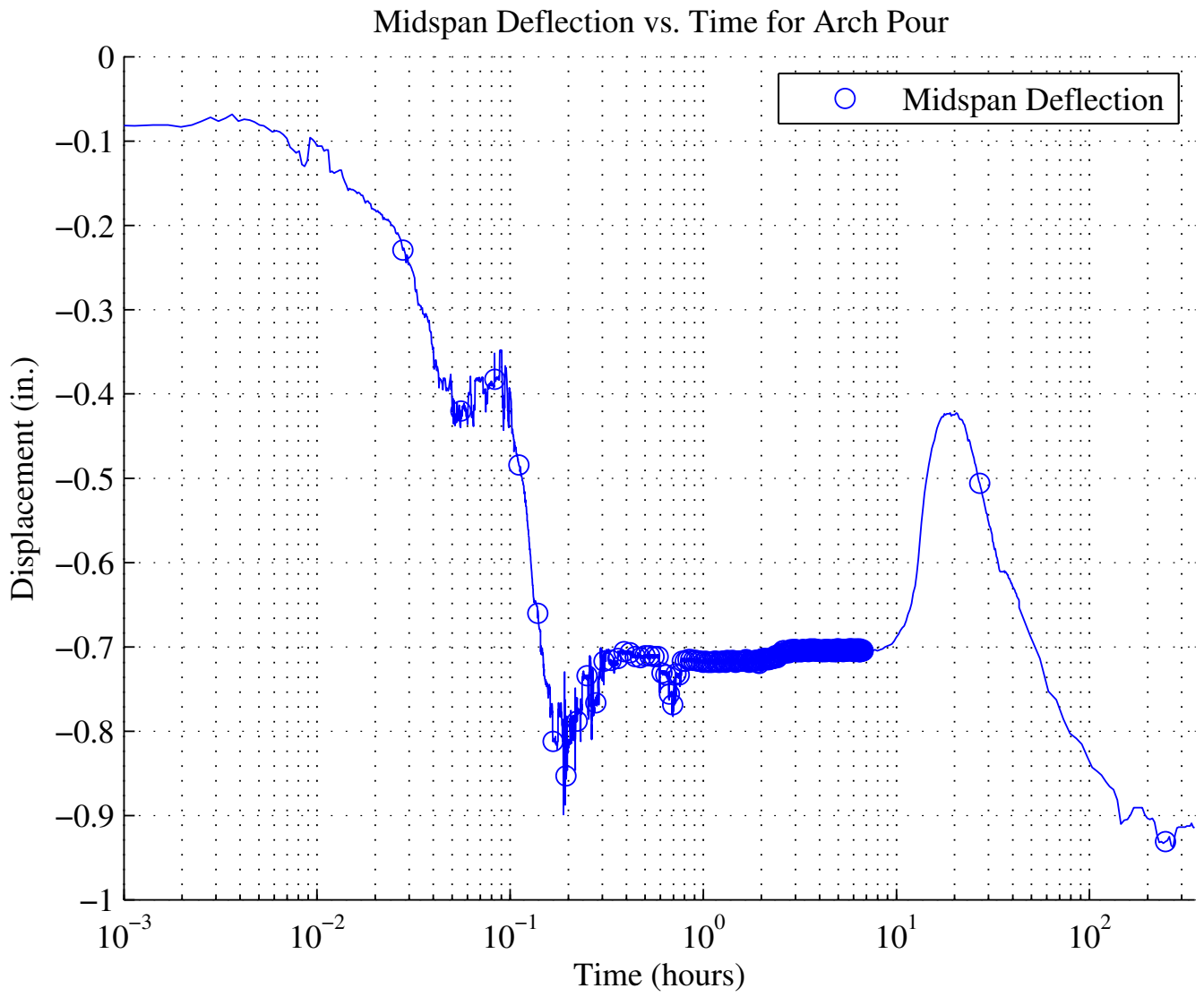
Midspan Deflection vs. Time for Arch Pour
Midspan Deflection
Displacement (in.)
Time (hours)
0
−0.1
−0.2
−0.3
−0.4
−0.5
−0.6
−0.7
−0.8
−0.9
−1
10^−3
10^−2
10^−1
10^0
10^1
10^2

Measured Deflection and Strains for Arch Pour (in., με)

Gage	WP-1	WP-2	WP-3	FS-1	FS-2	FS-3	FS-4	TQ-1	TM-1	TM-2
Max Values	-0.76	-0.94	-0.59	-175	-2587	-193	-141	148	133	1950
Last Value	-0.73	-0.91	-0.56	-172	-17	-193	-130	32	128	73
Gage	FQ-1	FQ-2	FQ-3	FQ-4	FQ-5	FQ-6	FQ-7	FQ-8		
Max Values	-377	-106	106	136	-231	-520	-438	-678		
Last Value	-371	-99	45	77	-230	-509	-275	-662		
Gage	FM-1	FM-2	FM-3	FM-4	FM-5	FM-6	FM-7			
Max Values	-206	-106	199	402	-68	-252	-307			
Last Value	-101	-101	163	67	-61	-244	-296			

Appendix C – Supplementary Phase II Results

Load vs. Deflection Plots

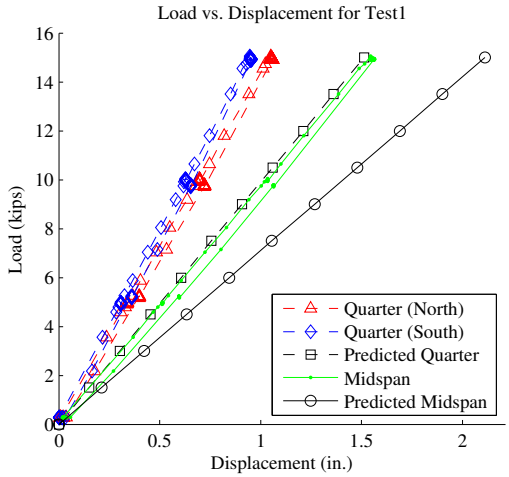

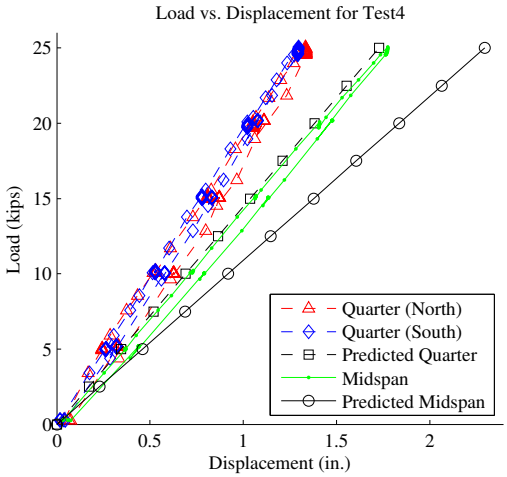

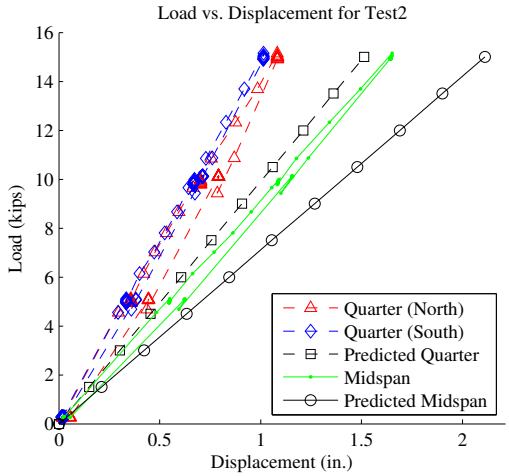

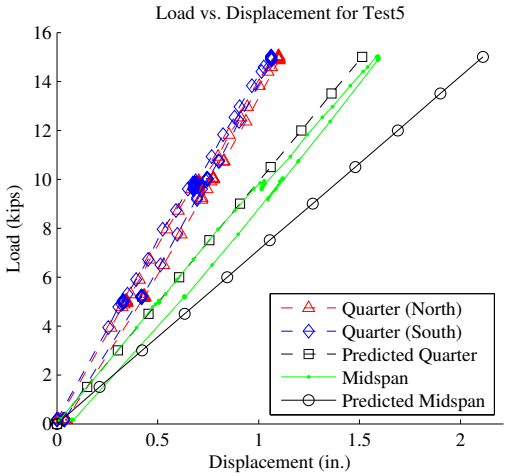

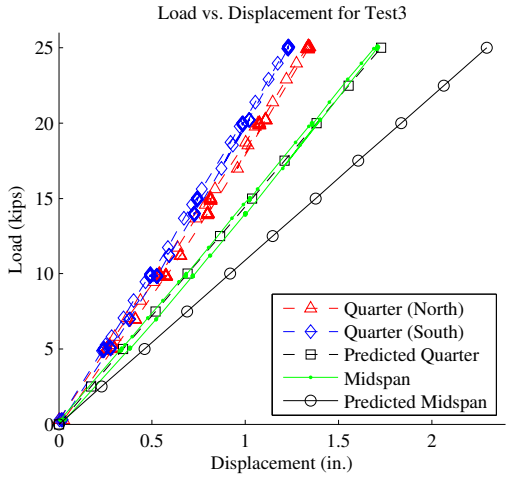

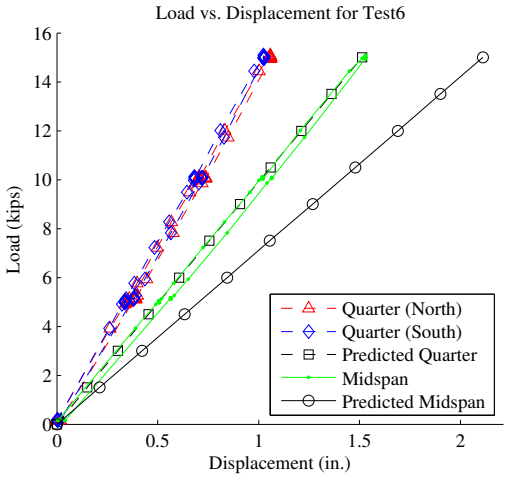

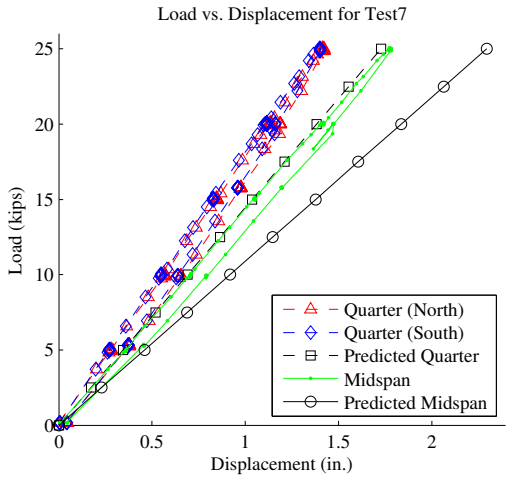
Load vs. Displacement for Test7
Load (kips)
Displacement (in.)
Quarter (North)
Quarter (South)
Predicted Quarter
Midspan
Predicted Midspan

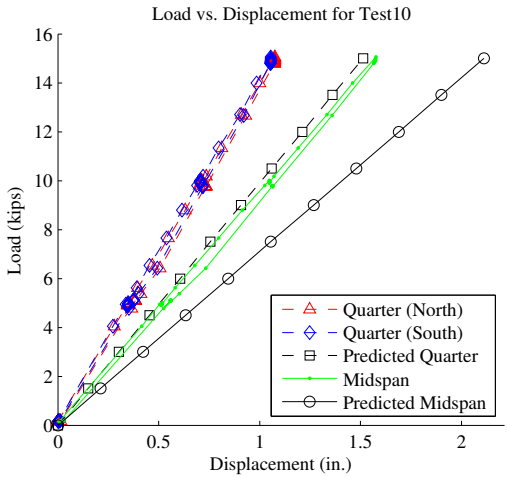
Load vs. Displacement for Test10
Load (kips)
Displacement (in.)
Quarter (North)
Quarter (South)
Predicted Quarter
Midspan
Predicted Midspan

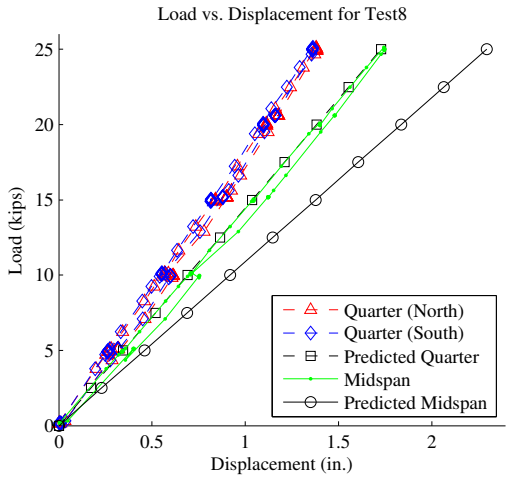
Load vs. Displacement for Test8
Load (kips)
Displacement (in.)
Quarter (North)
Quarter (South)
Predicted Quarter
Midspan
Predicted Midspan

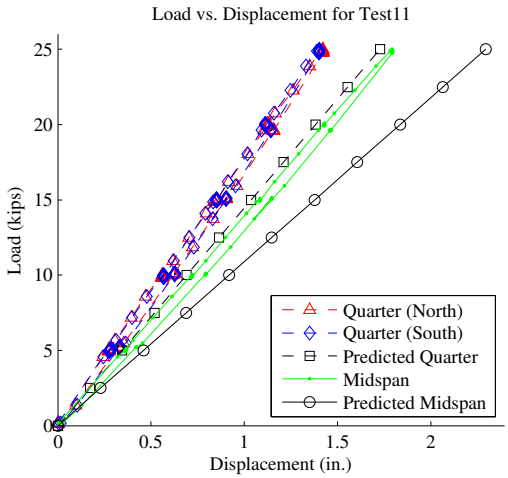
Load vs. Displacement for Test11
Load (kips)
Displacement (in.)
Quarter (North)
Quarter (South)
Predicted Quarter
Midspan
Predicted Midspan

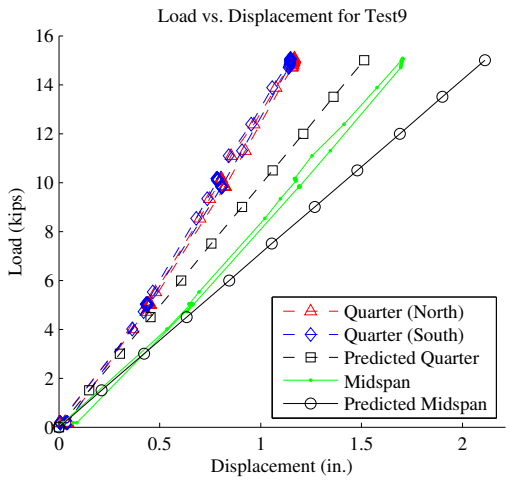
Load vs. Displacement for Test9
Load (kips)
Displacement (in.)
Quarter (North)
Quarter (South)
Predicted Quarter
Midspan
Predicted Midspan

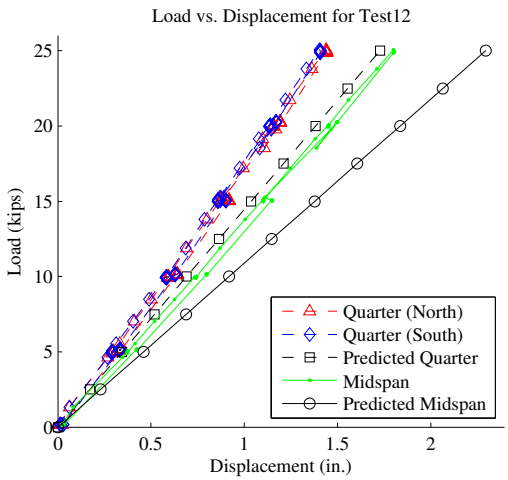
Load vs. Displacement for Test12
Load (kips)
Displacement (in.)
Quarter (North)
Quarter (South)
Predicted Quarter
Midspan
Predicted Midspan

Load vs. Strand Strain

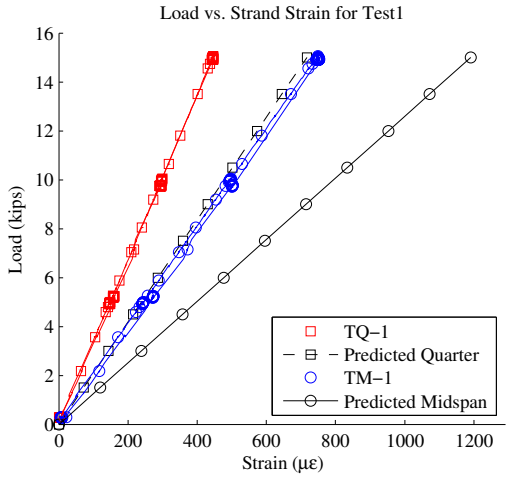

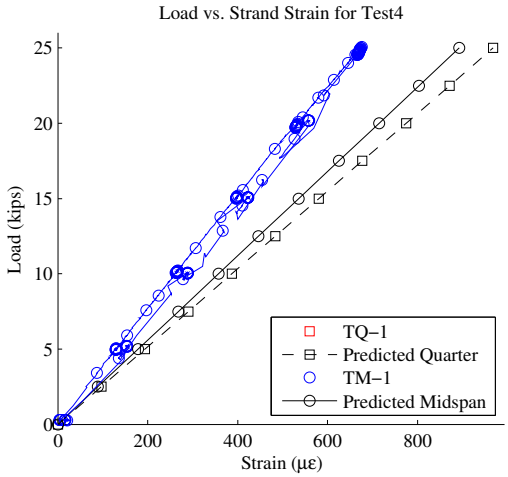

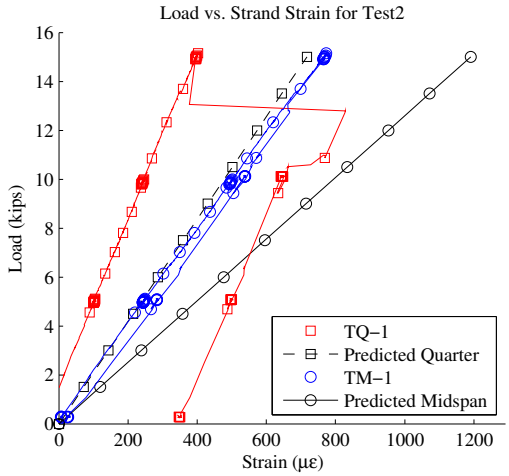

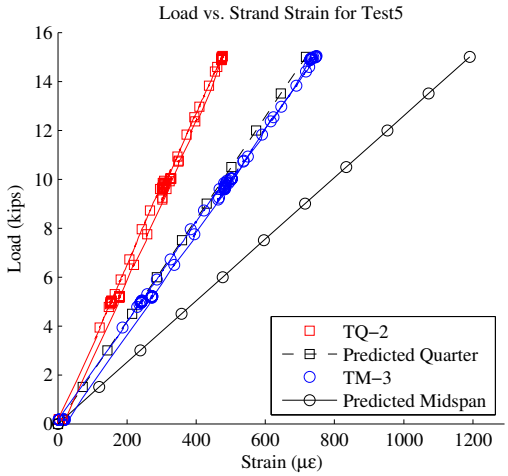

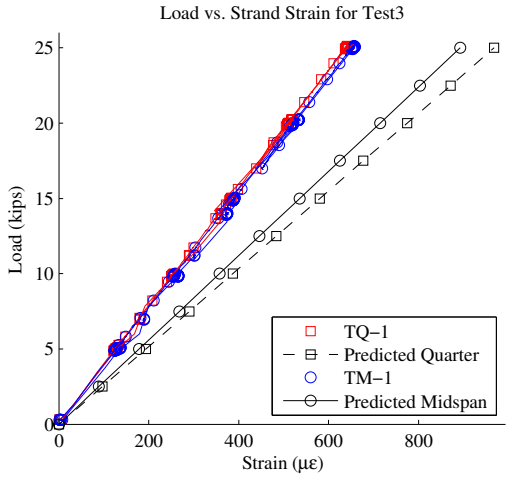

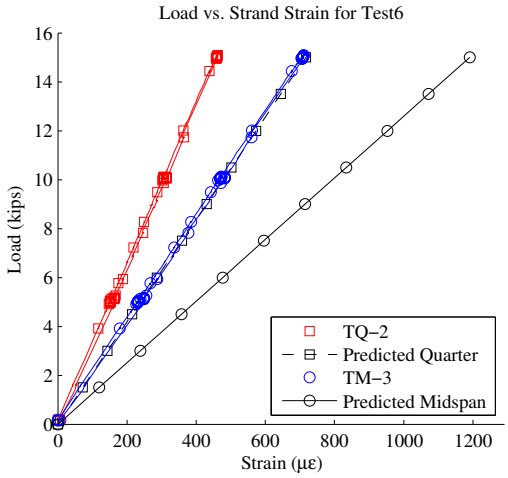

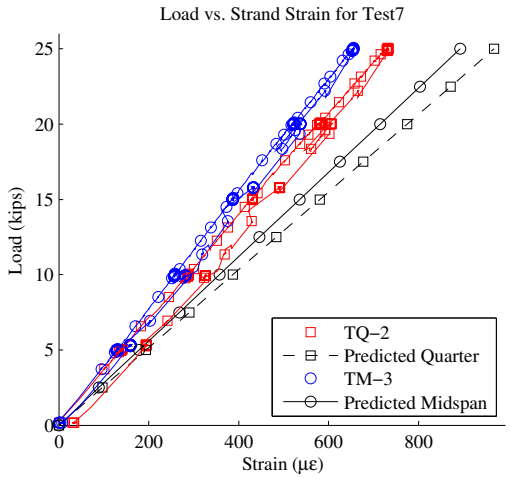
Load vs. Strand Strain for Test7
Load (kips)
Strain (με)
TQ–2
Predicted Quarter
TM–3
Predicted Midspan

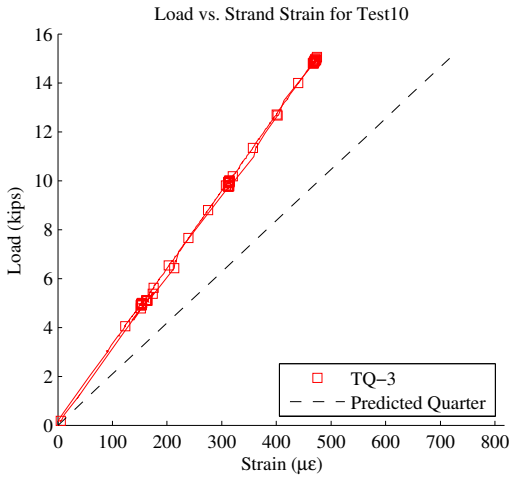
Load vs. Strand Strain for Test10
Load (kips)
Strain (με)
TQ–3
Predicted Quarter

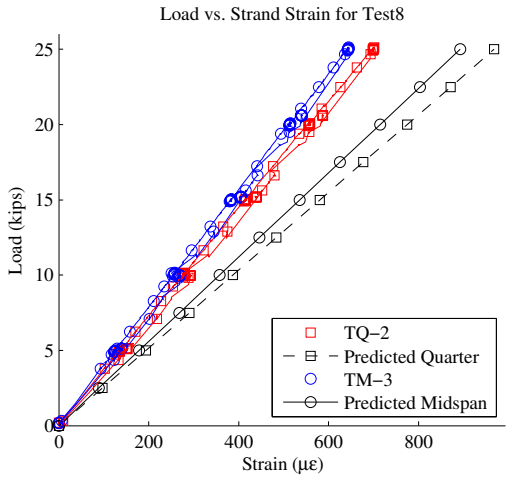
Load vs. Strand Strain for Test8
Load (kips)
Strain (με)
TQ–2
Predicted Quarter
TM–3
Predicted Midspan

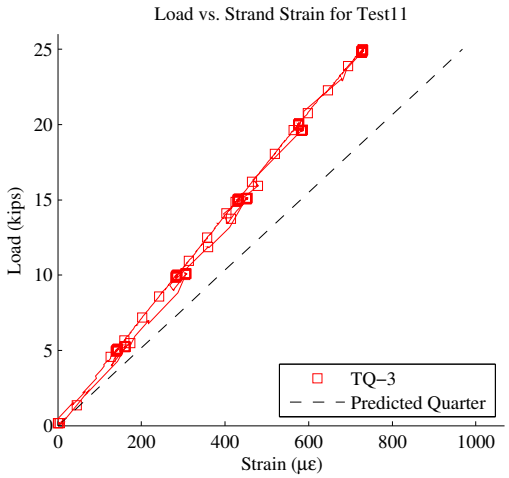
Load vs. Strand Strain for Test11
Load (kips)
Strain (με)
TQ–3
Predicted Quarter

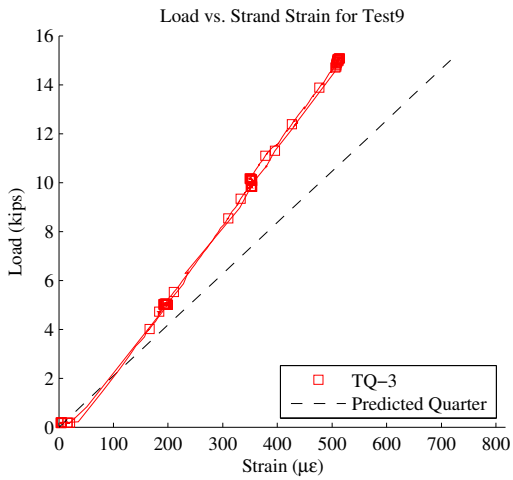
Load vs. Strand Strain for Test9
Load (kips)
Strain (με)
TQ–3
Predicted Quarter

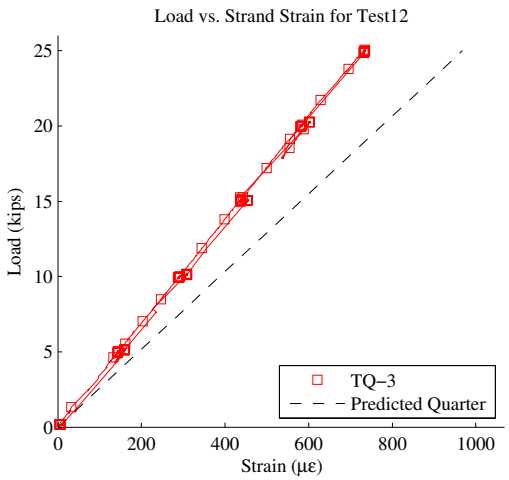
Load vs. Strand Strain for Test12
Load (kips)
Strain (με)
TQ–3
Predicted Quarter

Load vs. Bottom Flange Strain

Test 1

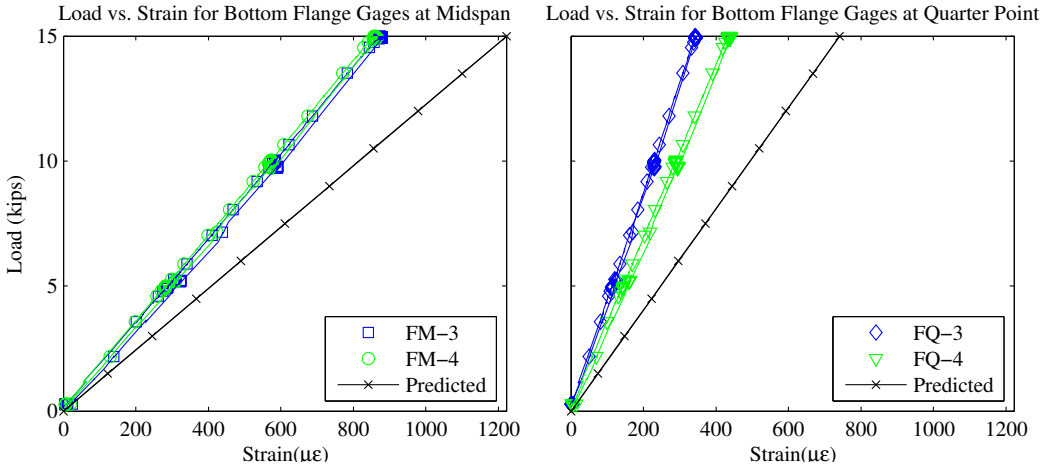

Test 2

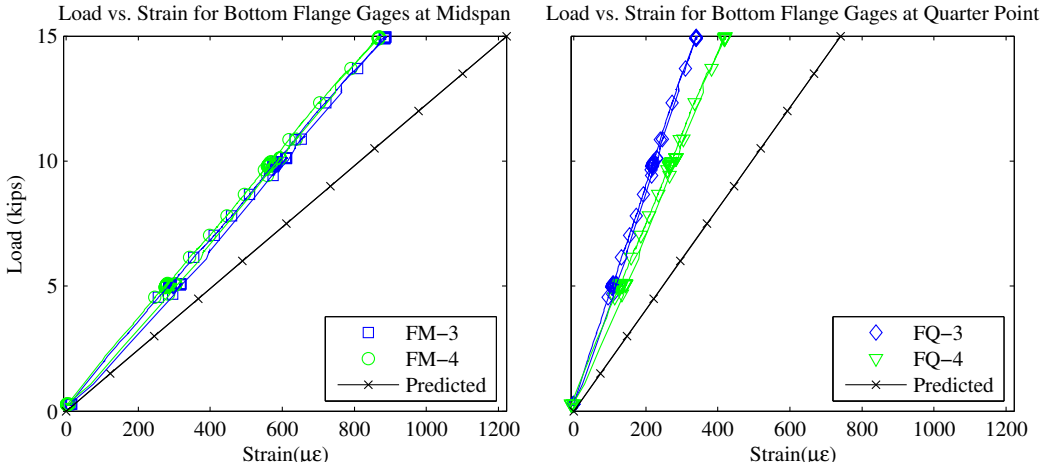

Test 3

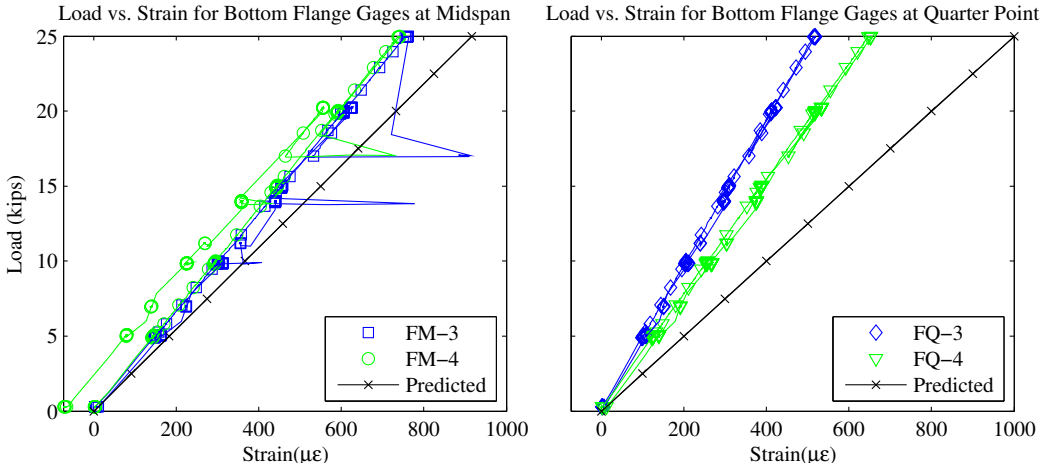

Test 4

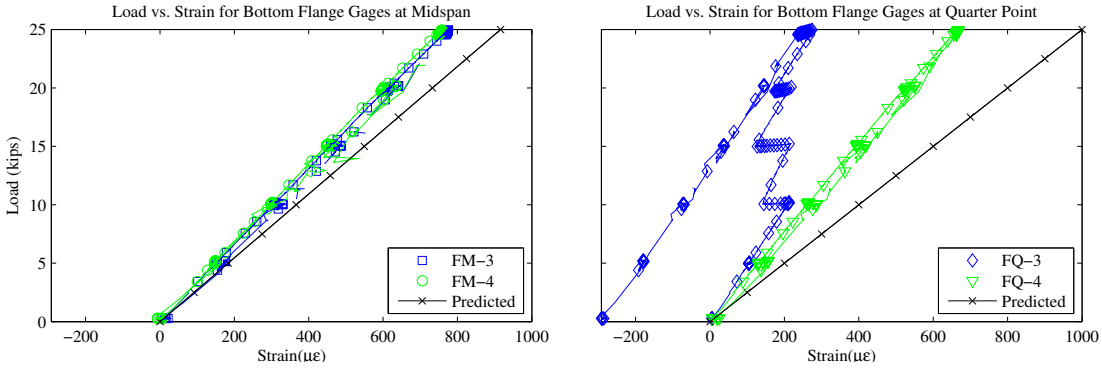

Test 5

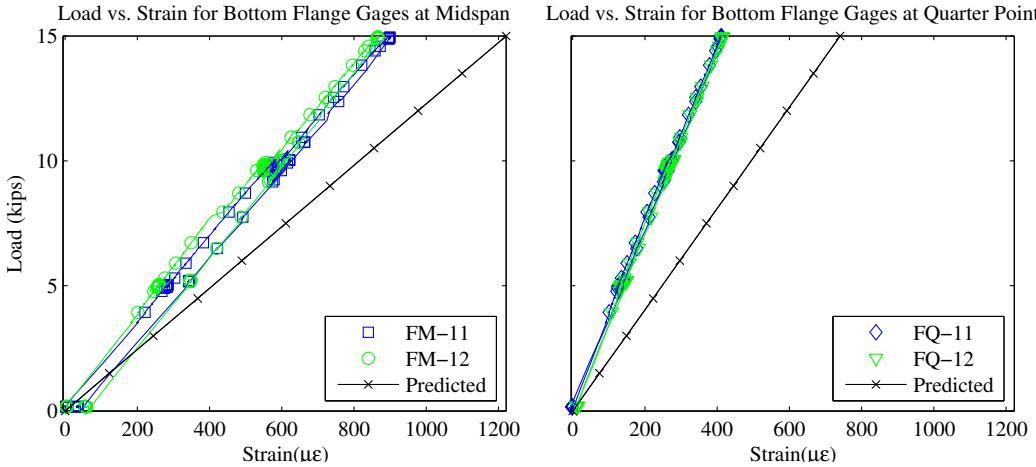

Test 6

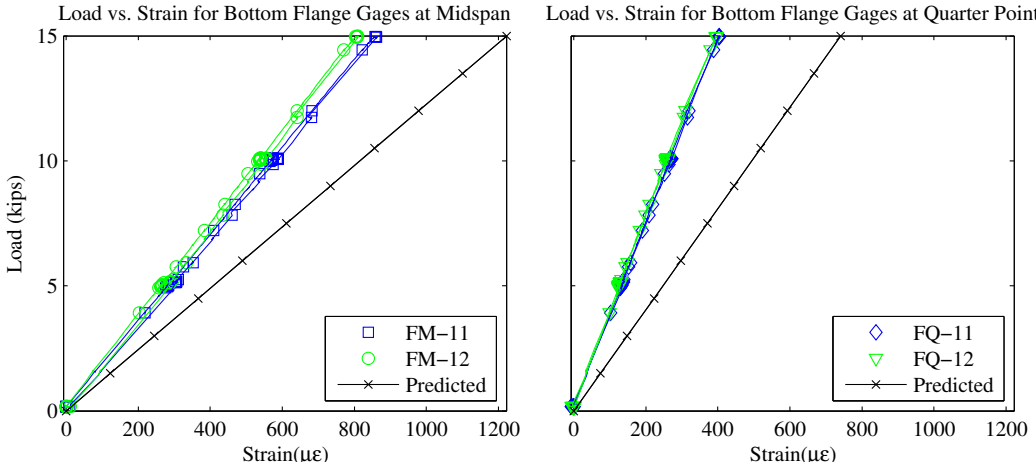

Test 7

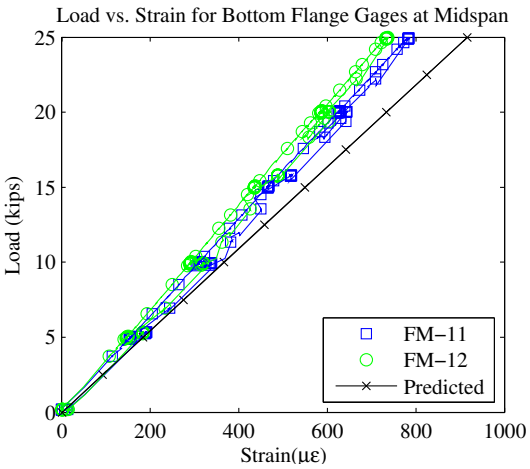

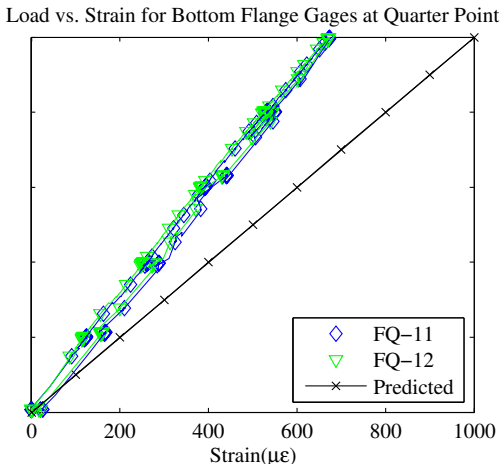

Test 8

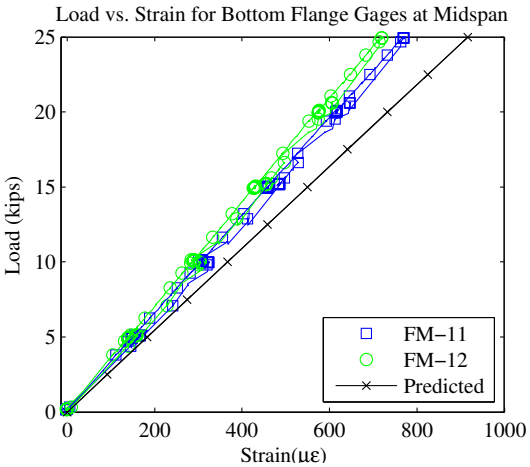

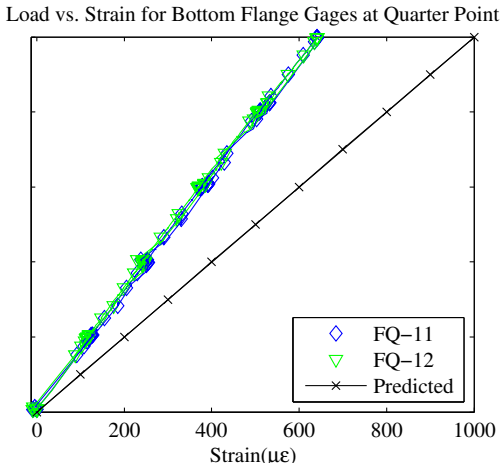

Test 9

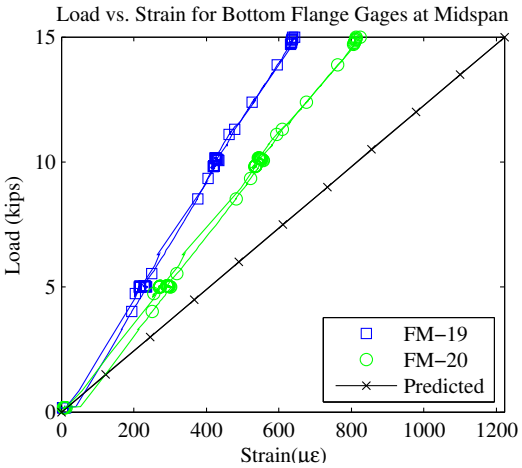

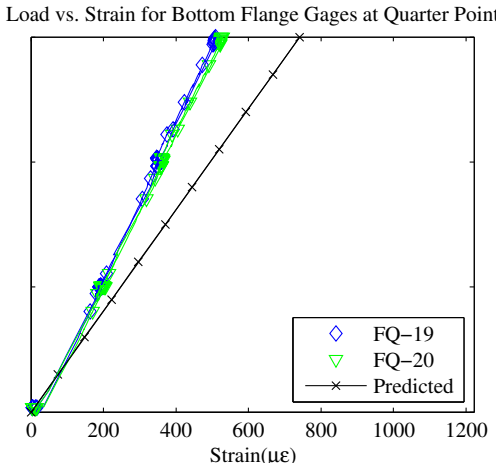

Test 10

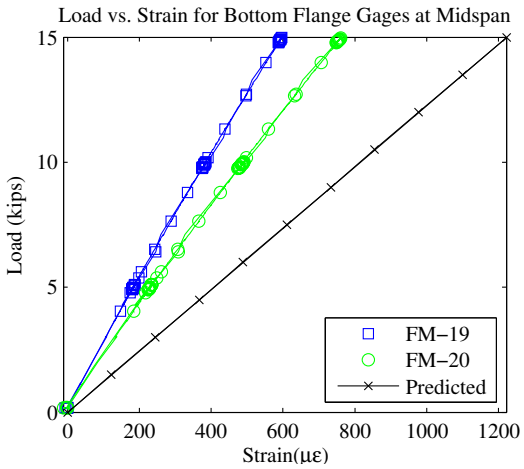

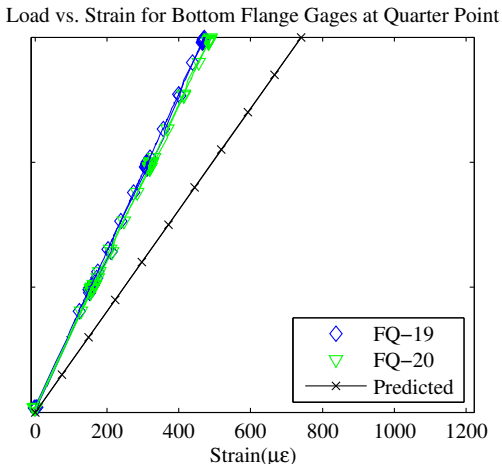

Test 11

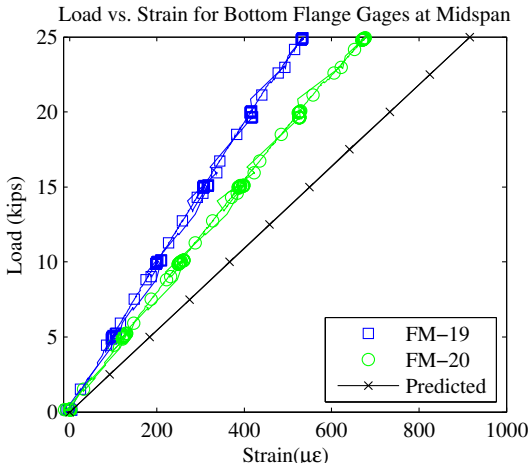

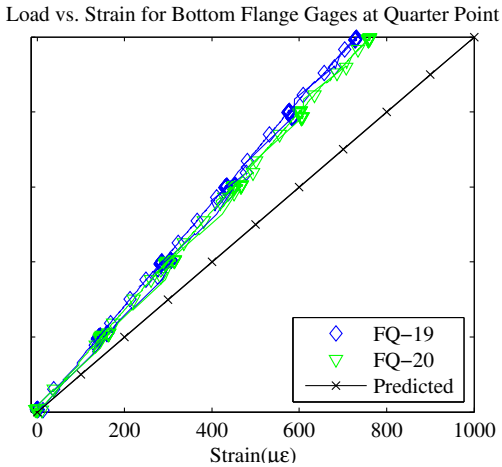

Test 12

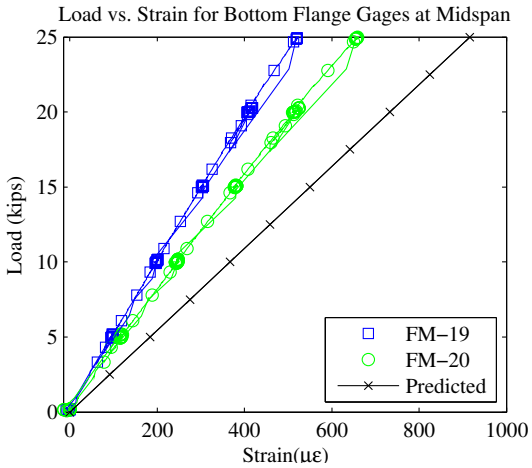

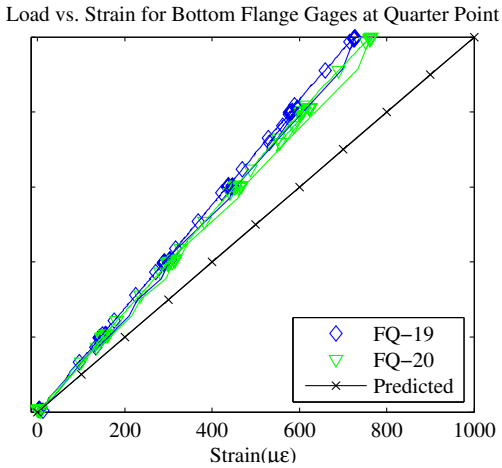

Load vs. Concrete Arch Strains

Load vs. Concrete Strains for Test 1

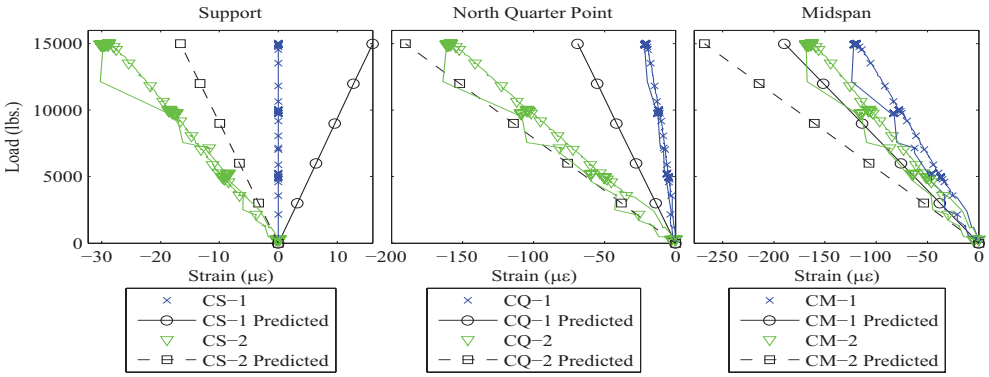

Load vs. Concrete Strains for Test 2

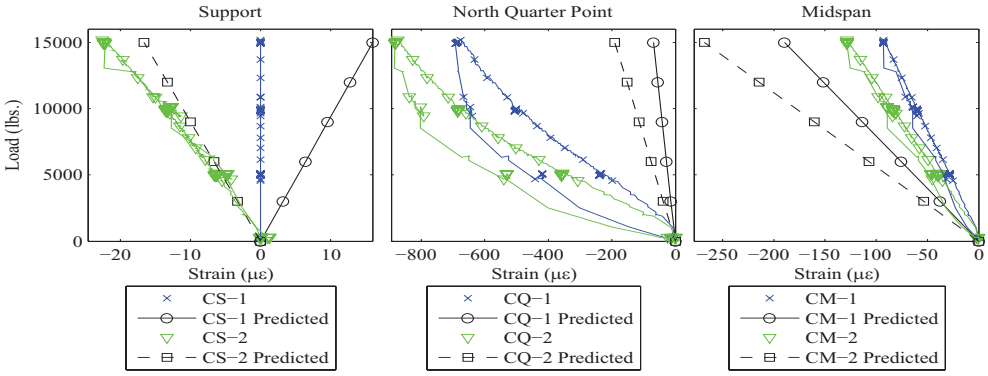

Load vs. Concrete Strains for Test 3

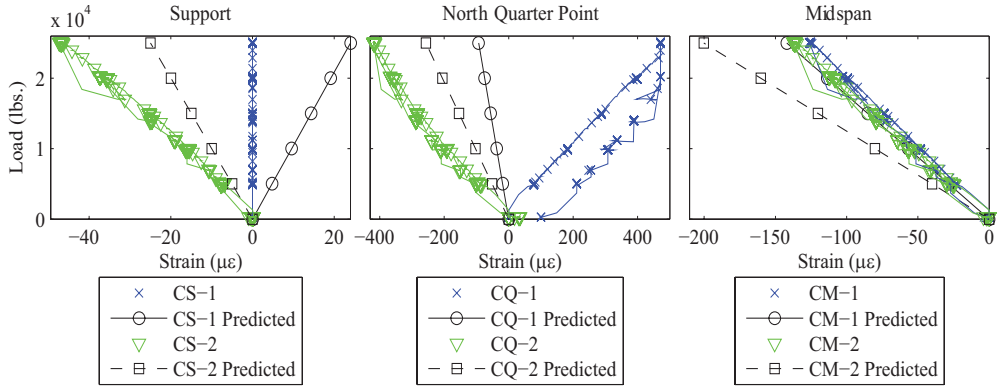

Load vs. Concrete Strains for Test 4

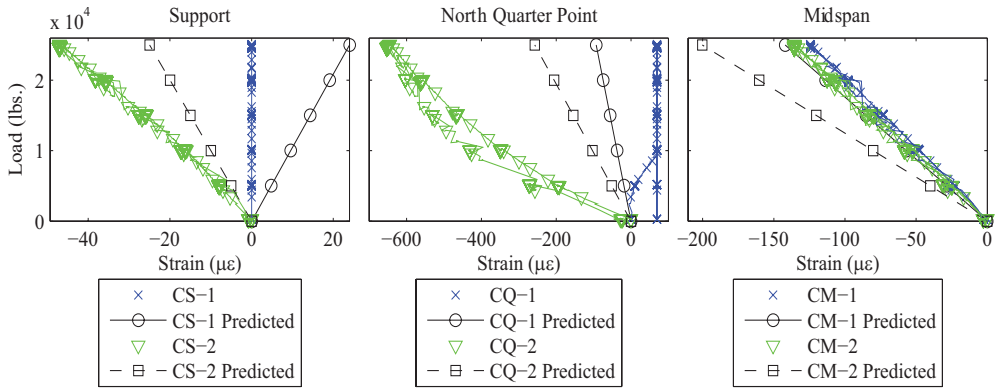

Load vs. Concrete Strains for Test 5

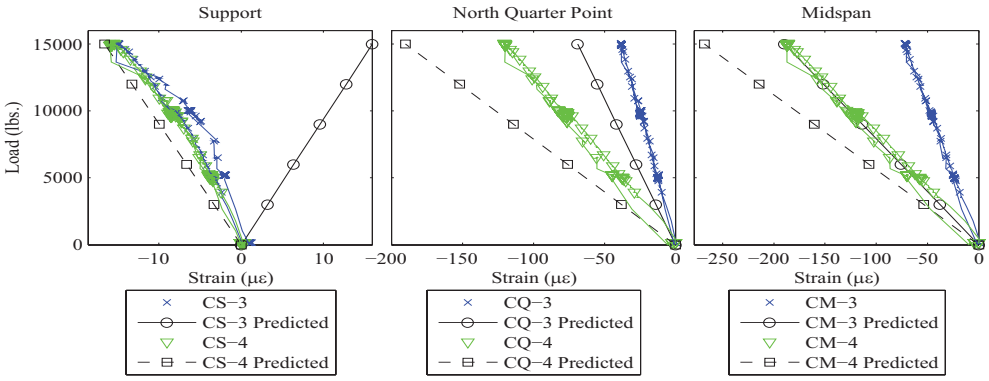

Load vs. Concrete Strains for Test 6

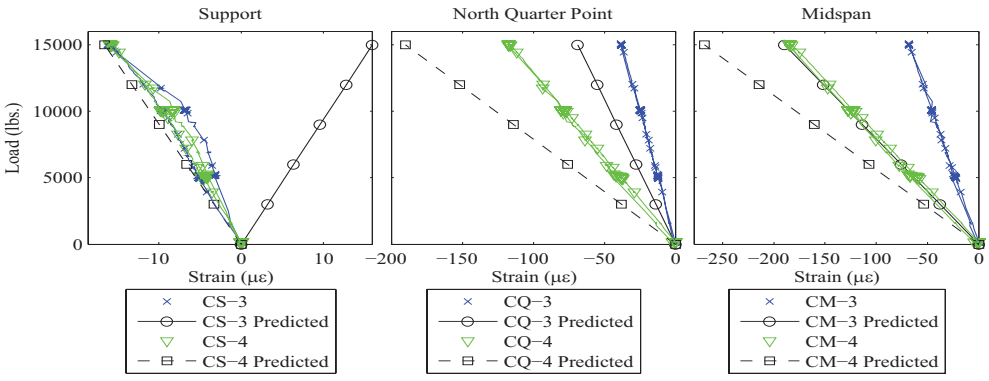

Load vs. Concrete Strains for Test 7

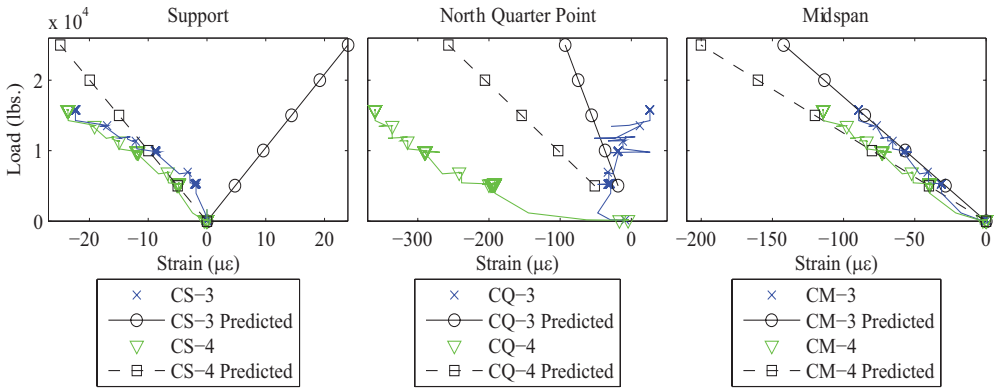

Load vs. Concrete Strains for Test 8

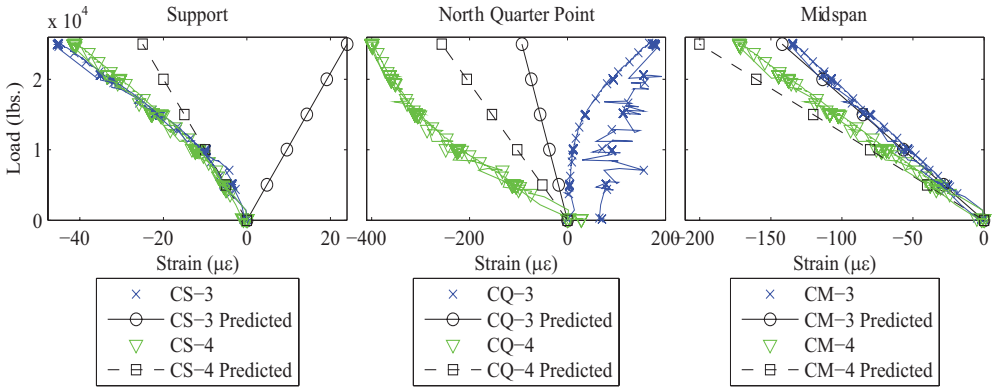

Load vs. Concrete Strains for Test 9

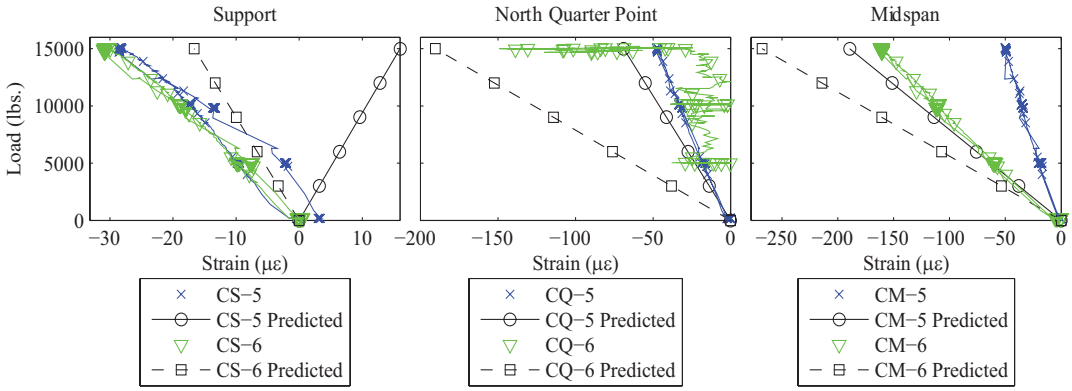

Load vs. Concrete Strains for Test 10

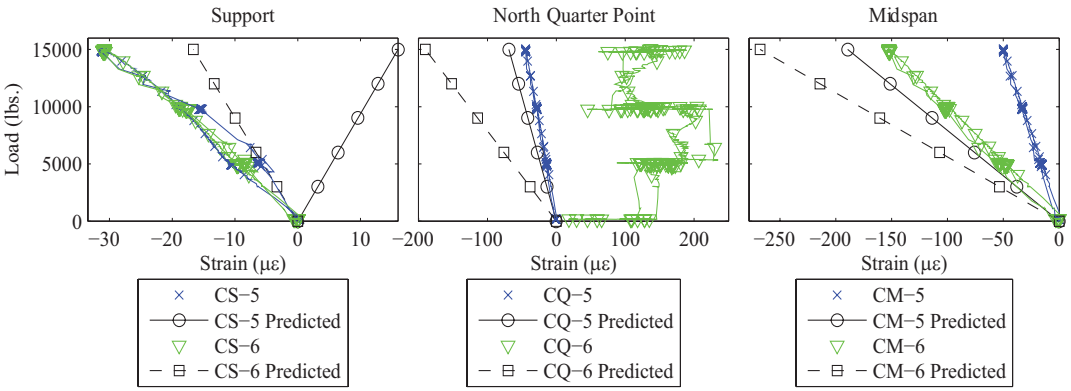

Load vs. Concrete Strains for Test 11

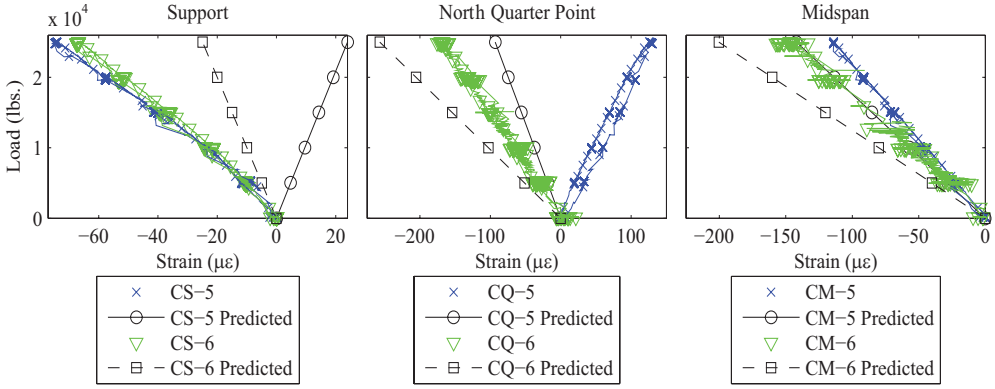

Load vs. Concrete Strains for Test 12

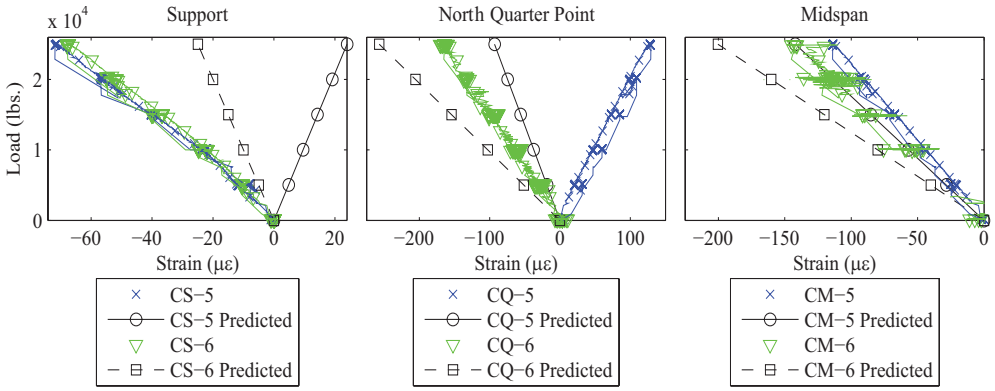

Strain Profiles

Test 1

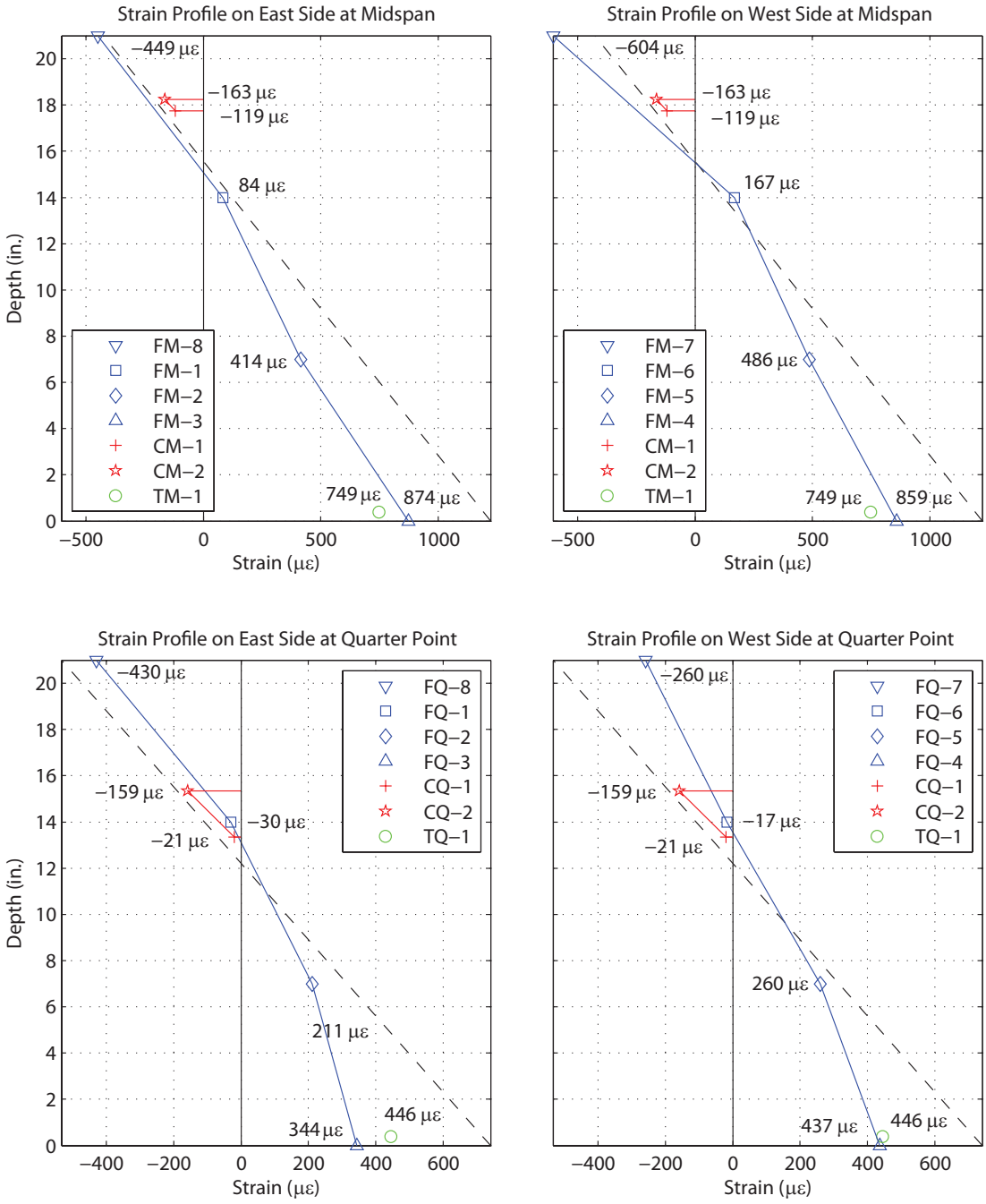

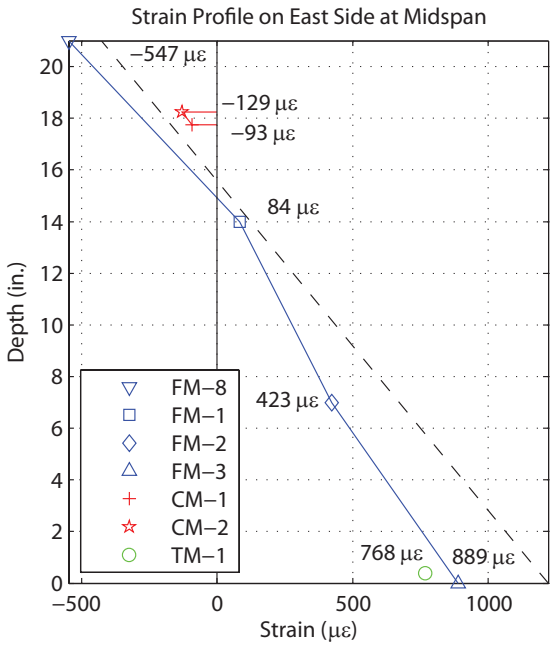
Strain Profile on East Side at Midspan
−547 με
−129 με
−93 με
84 με
423 με
768 με
889 με
FM−8
FM−1
FM−2
FM−3
CM−1
CM−2
TM−1
Depth (in.)
Strain (με)

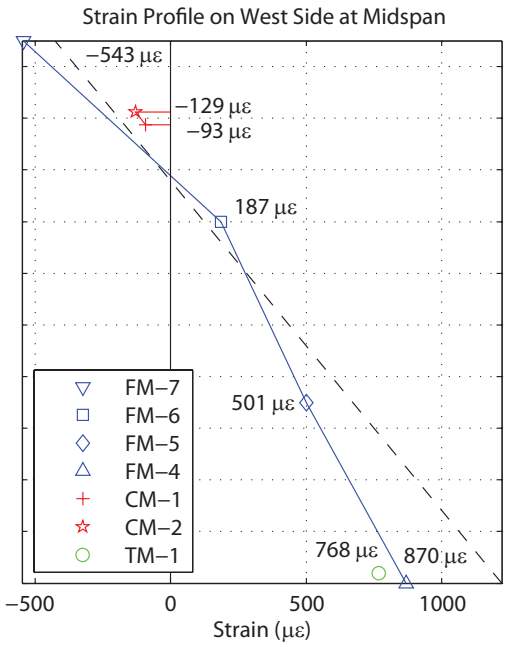
Strain Profile on West Side at Midspan
−543 με
−129 με
−93 με
187 με
501 με
768 με
870 με
FM−7
FM−6
FM−5
FM−4
CM−1
CM−2
TM−1
Strain (με)

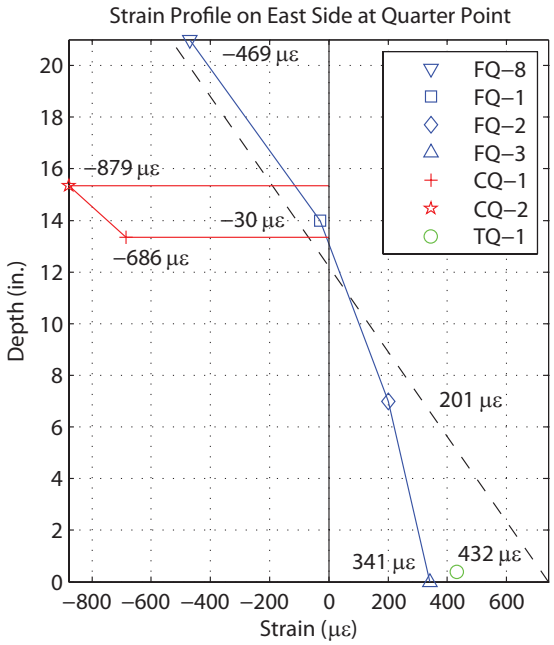
Strain Profile on East Side at Quarter Point
−469 με
−879 με
−30 με
−686 με
201 με
341 με
432 με
FQ−8
FQ−1
FQ−2
FQ−3
CQ−1
CQ−2
TQ−1
Depth (in.)
Strain (με)

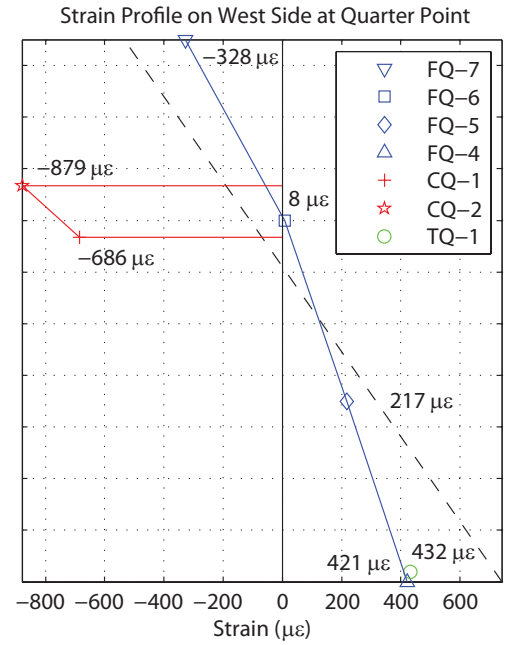
Strain Profile on West Side at Quarter Point
−328 με
−879 με
8 με
−686 με
217 με
421 με
432 με
FQ−7
FQ−6
FQ−5
FQ−4
CQ−1
CQ−2
TQ−1
Strain (με)

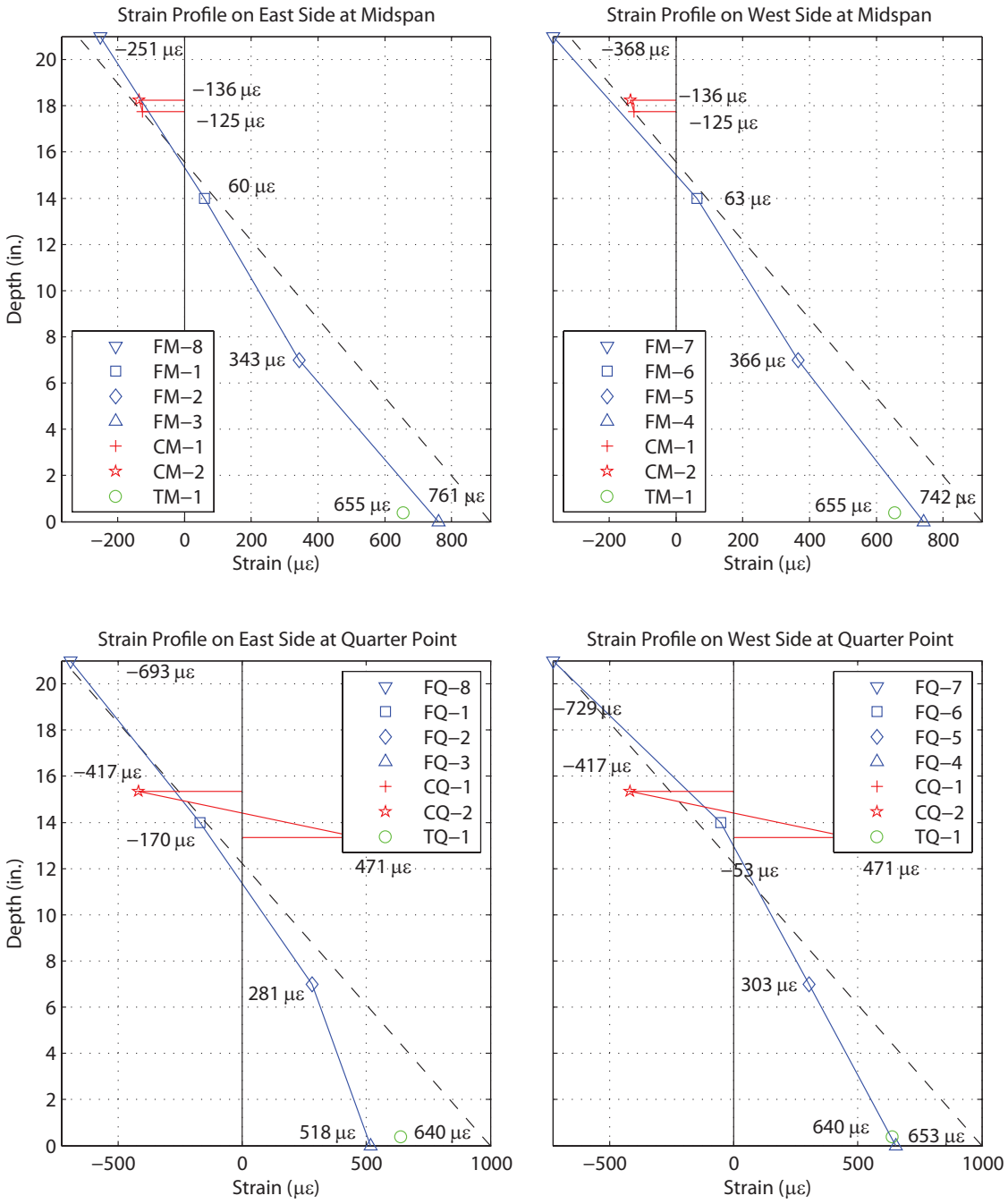
Strain Profile on East Side at Midspan
−251 με
−136 με
−125 με
60 με
343 με
655 με
761 με
FM−8
FM−1
FM−2
FM−3
CM−1
CM−2
TM−1
Depth (in.)
Strain (με)
Strain Profile on West Side at Midspan
−368 με
−136 με
−125 με
63 με
366 με
655 με
742 με
FM−7
FM−6
FM−5
FM−4
CM−1
CM−2
TM−1
Strain (με)
Strain Profile on East Side at Quarter Point
−693 με
−417 με
−170 με
471 με
281 με
518 με
640 με
FQ−8
FQ−1
FQ−2
FQ−3
CQ−1
CQ−2
TQ−1
Depth (in.)
Strain (με)
Strain Profile on West Side at Quarter Point
−729 με
−417 με
−53 με
471 με
303 με
640 με
653 με
FQ−7
FQ−6
FQ−5
FQ−4
CQ−1
CQ−2
TQ−1
Strain (με)

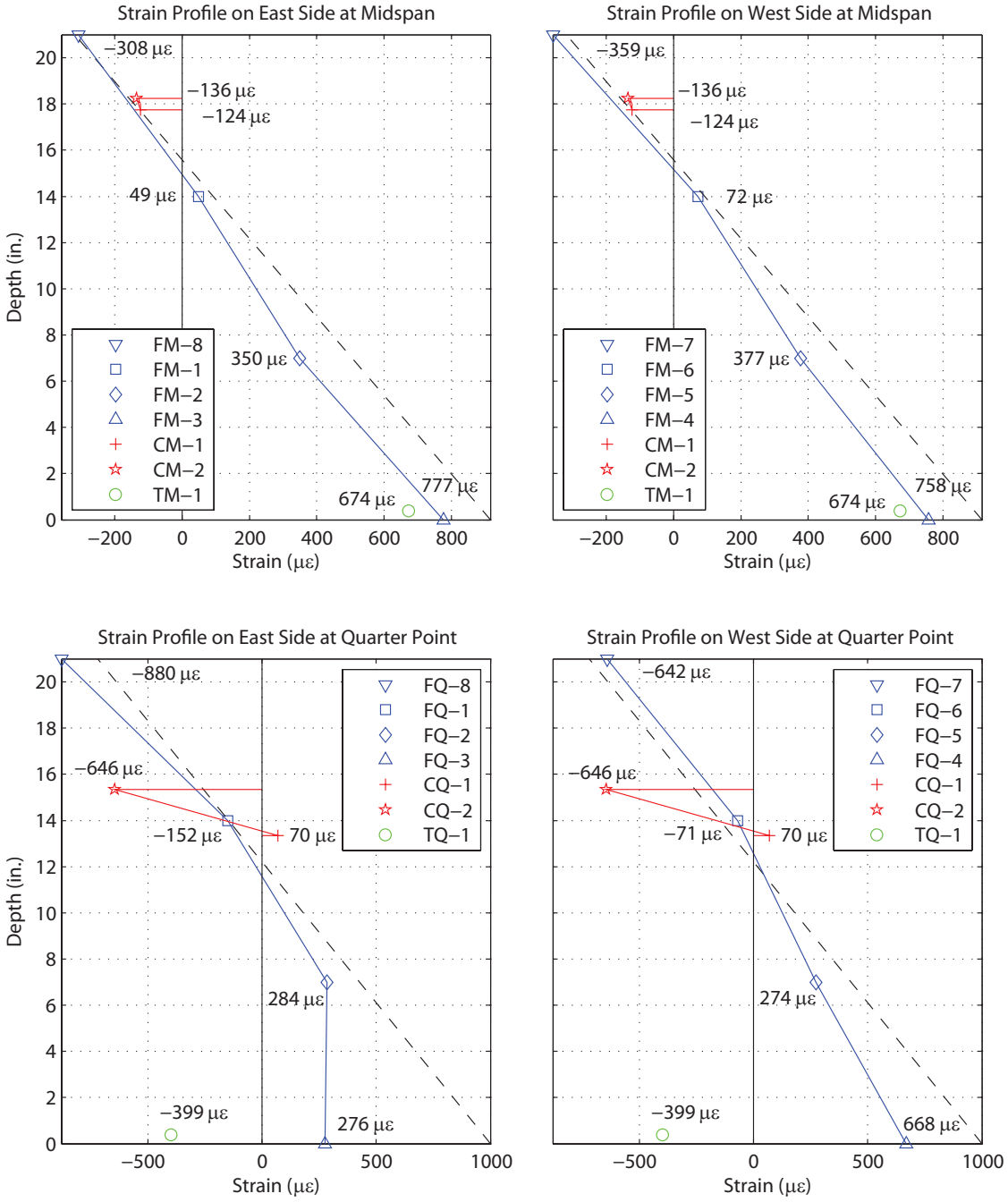
Strain Profile on East Side at Midspan
−308 με
−136 με
−124 με
49 με
350 με
674 με
777 με
FM−8
FM−1
FM−2
FM−3
CM−1
CM−2
TM−1
Depth (in.)
Strain (με)
Strain Profile on West Side at Midspan
−359 με
−136 με
−124 με
72 με
377 με
674 με
758 με
FM−7
FM−6
FM−5
FM−4
CM−1
CM−2
TM−1
Strain (με)
Strain Profile on East Side at Quarter Point
−880 με
−646 με
−152 με
70 με
284 με
−399 με
276 με
FQ−8
FQ−1
FQ−2
FQ−3
CQ−1
CQ−2
TQ−1
Depth (in.)
Strain (με)
Strain Profile on West Side at Quarter Point
−642 με
−646 με
−71 με
70 με
274 με
−399 με
668 με
FQ−7
FQ−6
FQ−5
FQ−4
CQ−1
CQ−2
TQ−1
Strain (με)

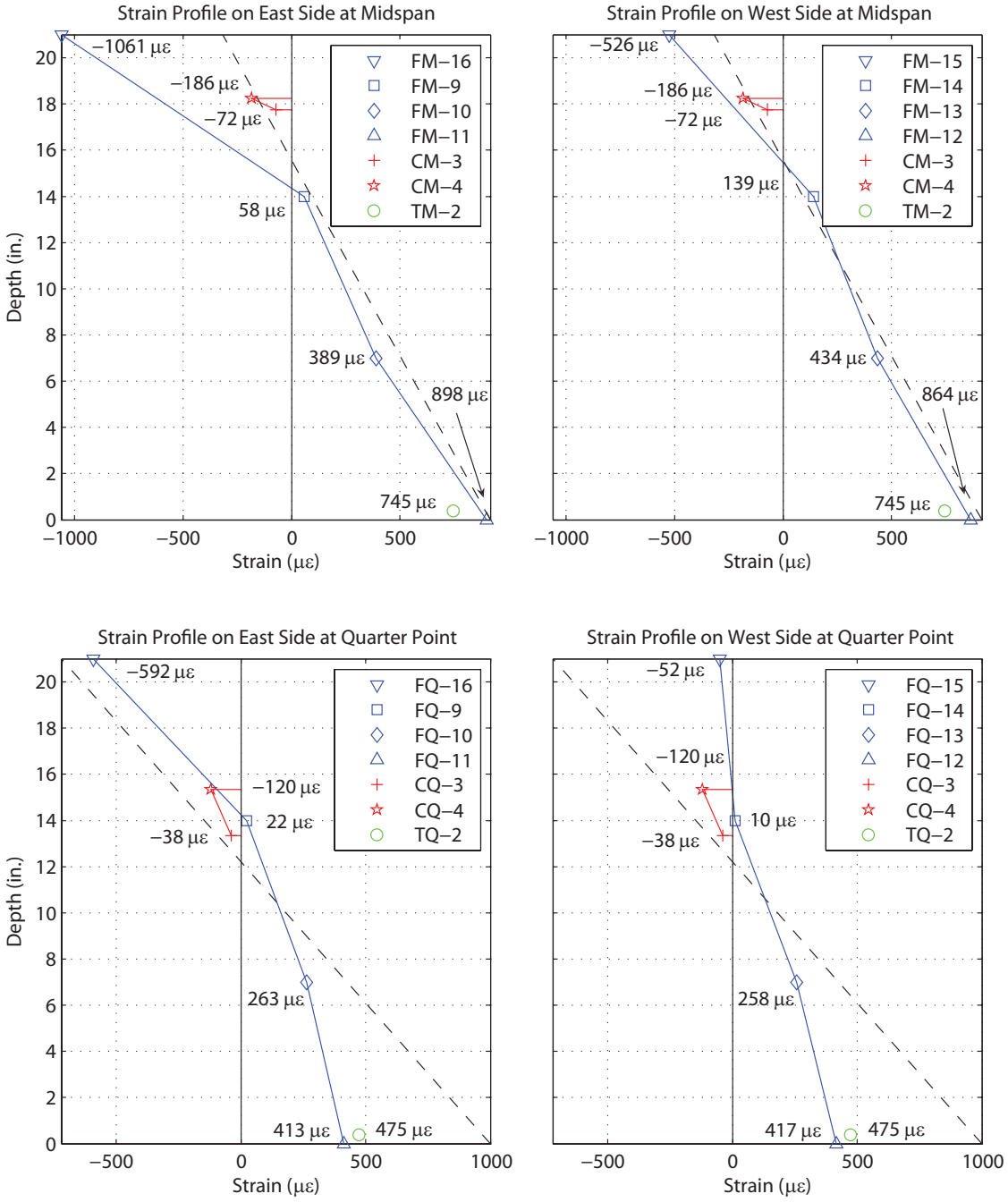
Strain Profile on East Side at Midspan
−1061 με
−186 με
−72 με
58 με
389 με
898 με
745 με
FM−16
FM−9
FM−10
FM−11
CM−3
CM−4
TM−2
Depth (in.)
Strain (με)
Strain Profile on West Side at Midspan
−526 με
−186 με
−72 με
139 με
434 με
864 με
745 με
FM−15
FM−14
FM−13
FM−12
CM−3
CM−4
TM−2
Strain (με)
Strain Profile on East Side at Quarter Point
−592 με
−120 με
22 με
−38 με
263 με
413 με
475 με
FQ−16
FQ−9
FQ−10
FQ−11
CQ−3
CQ−4
TQ−2
Depth (in.)
Strain (με)
Strain Profile on West Side at Quarter Point
−52 με
−120 με
10 με
−38 με
258 με
417 με
475 με
FQ−15
FQ−14
FQ−13
FQ−12
CQ−3
CQ−4
TQ−2
Strain (με)

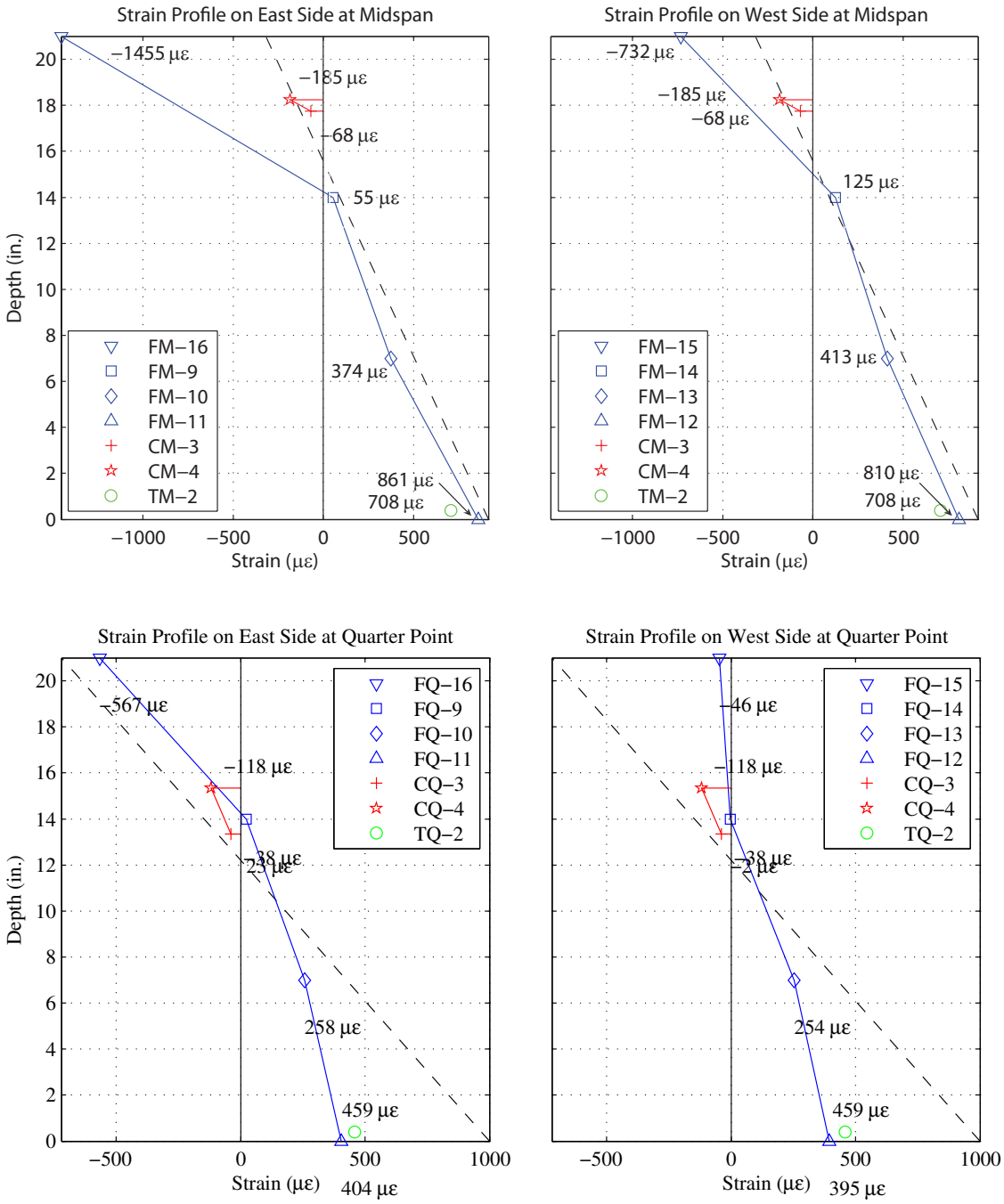
Strain Profile on East Side at Midspan
−1455 με
−185 με
−68 με
55 με
374 με
861 με
708 με
FM−16
FM−9
FM−10
FM−11
CM−3
CM−4
TM−2
Depth (in.)
Strain (με)
Strain Profile on West Side at Midspan
−732 με
−185 με
−68 με
125 με
413 με
810 με
708 με
FM−15
FM−14
FM−13
FM−12
CM−3
CM−4
TM−2
Strain (με)
Strain Profile on East Side at Quarter Point
−567 με
−118 με
38 με
25 με
258 με
459 με
404 με
FQ−16
FQ−9
FQ−10
FQ−11
CQ−3
CQ−4
TQ−2
Depth (in.)
Strain (με)
Strain Profile on West Side at Quarter Point
−46 με
−118 με
38 με
−2 με
254 με
459 με
395 με
FQ−15
FQ−14
FQ−13
FQ−12
CQ−3
CQ−4
TQ−2
Strain (με)

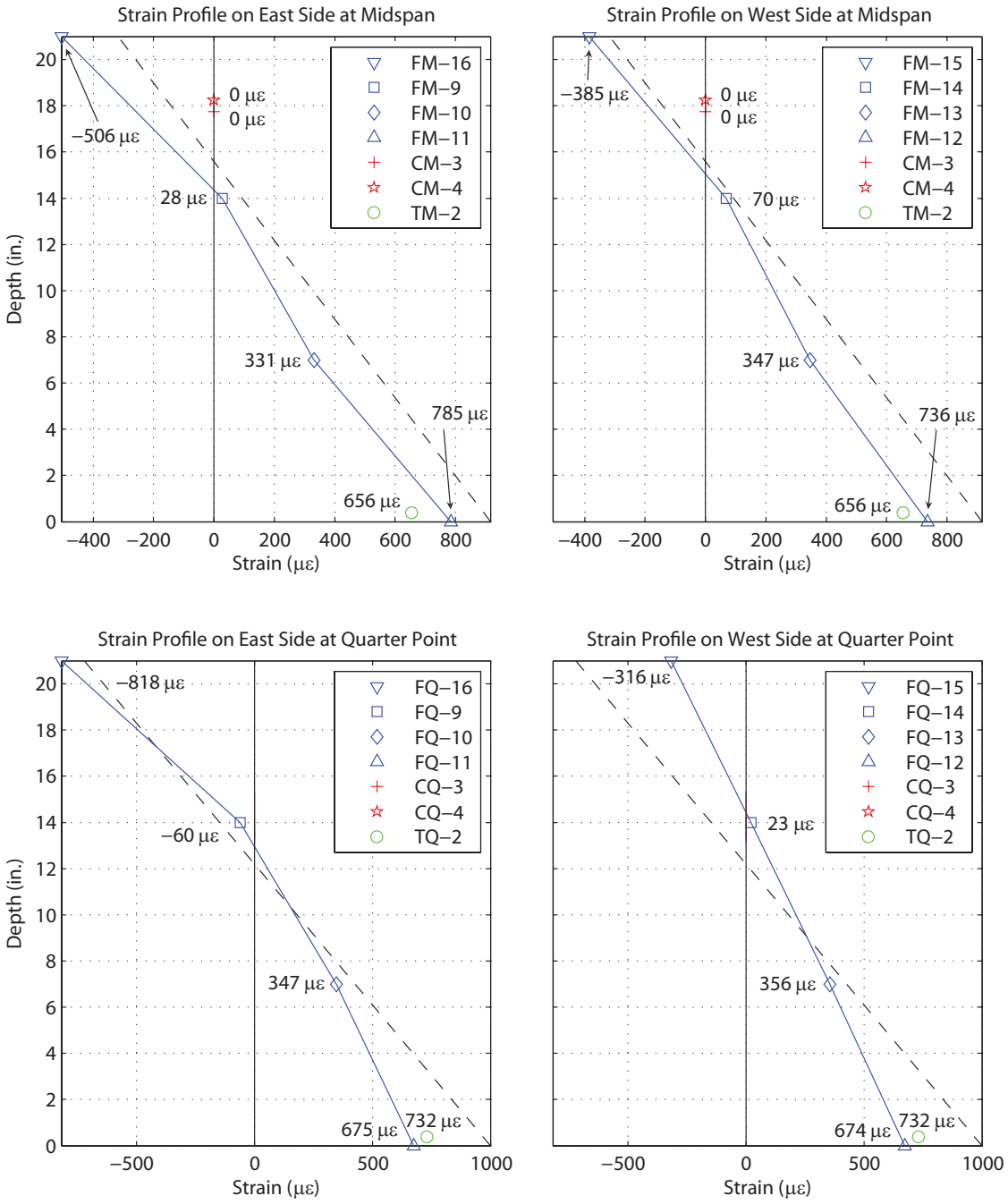
Strain Profile on East Side at Midspan
Depth (in.)
Strain (με)
FM–16
FM–9
FM–10
FM–11
CM–3
CM–4
TM–2
0 με
0 με
−506 με
28 με
331 με
785 με
656 με
Strain Profile on West Side at Midspan
Strain (με)
FM–15
FM–14
FM–13
FM–12
CM–3
CM–4
TM–2
−385 με
0 με
0 με
70 με
347 με
736 με
656 με
Strain Profile on East Side at Quarter Point
Depth (in.)
Strain (με)
FQ–16
FQ–9
FQ–10
FQ–11
CQ–3
CQ–4
TQ–2
−818 με
−60 με
347 με
675 με
732 με
Strain Profile on West Side at Quarter Point
Strain (με)
FQ–15
FQ–14
FQ–13
FQ–12
CQ–3
CQ–4
TQ–2
−316 με
23 με
356 με
674 με
732 με

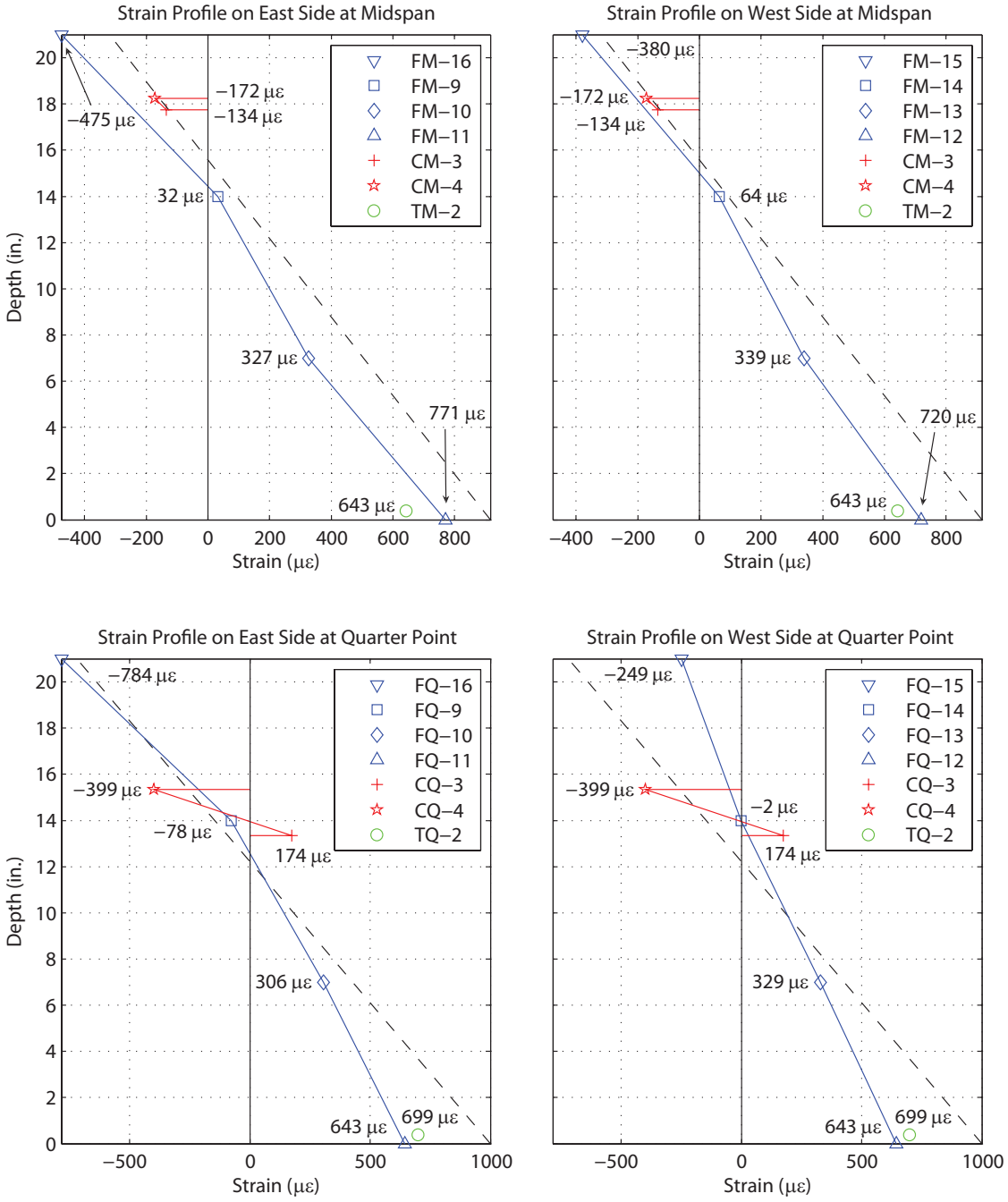
Strain Profile on East Side at Midspan
Depth (in.)
Strain (με)
FM–16
FM–9
FM–10
FM–11
CM–3
CM–4
TM–2
−475 με
−172 με
−134 με
32 με
327 με
771 με
643 με
Strain Profile on West Side at Midspan
−380 με
−172 με
−134 με
64 με
339 με
720 με
643 με
FM–15
FM–14
FM–13
FM–12
Strain Profile on East Side at Quarter Point
−784 με
−399 με
−78 με
174 με
306 με
643 με
699 με
FQ–16
FQ–9
FQ–10
FQ–11
CQ–3
CQ–4
TQ–2
Strain Profile on West Side at Quarter Point
−249 με
−399 με
−2 με
174 με
329 με
643 με
699 με
FQ–15
FQ–14
FQ–13
FQ–12

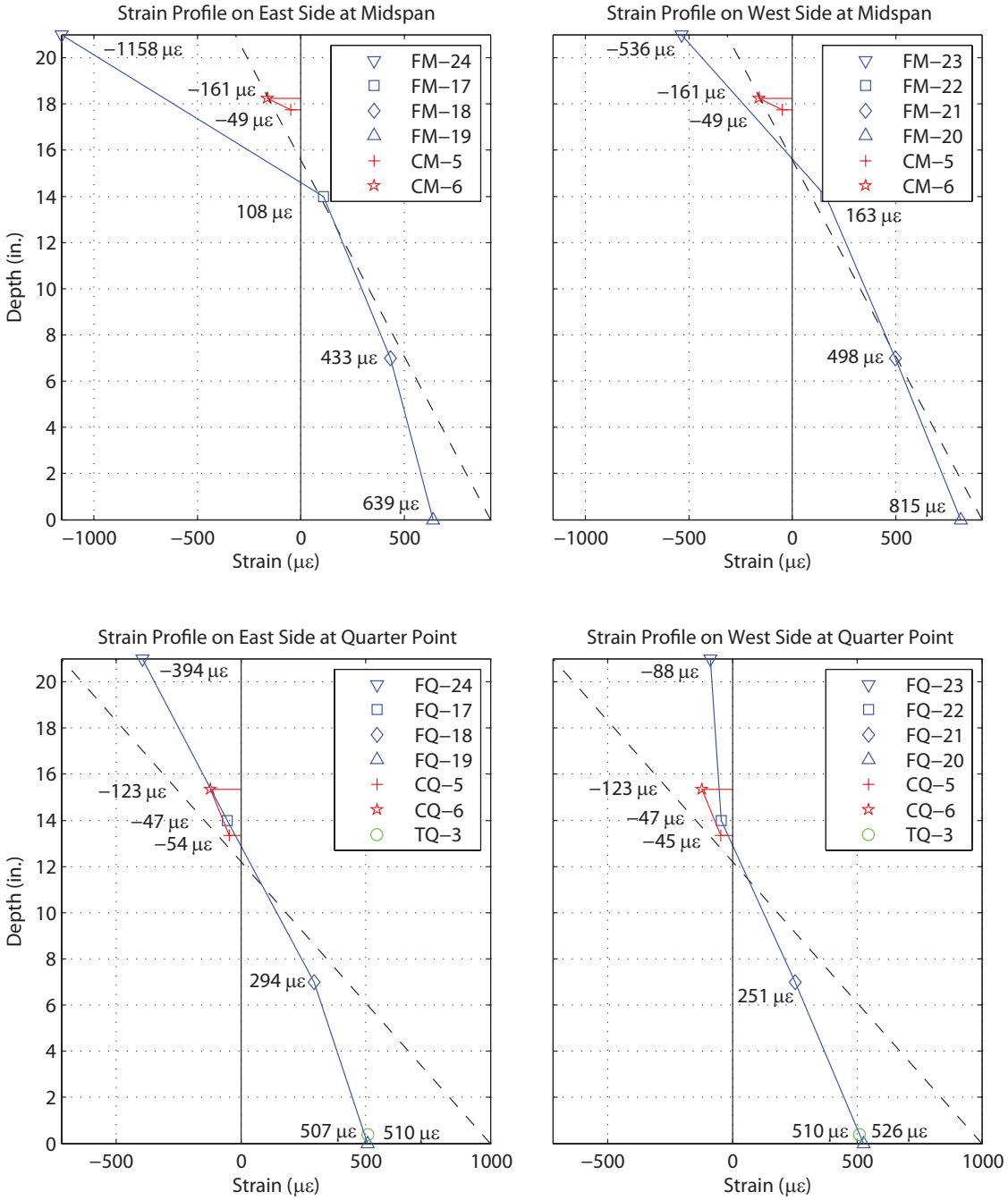
Strain Profile on East Side at Midspan
−1158 με
−161 με
−49 με
108 με
433 με
639 με
FM−24
FM−17
FM−18
FM−19
CM−5
CM−6
Depth (in.)
Strain (με)
Strain Profile on West Side at Midspan
−536 με
−161 με
−49 με
163 με
498 με
815 με
FM−23
FM−22
FM−21
FM−20
CM−5
CM−6
Strain (με)
Strain Profile on East Side at Quarter Point
−394 με
−123 με
−47 με
−54 με
294 με
507 με
510 με
FQ−24
FQ−17
FQ−18
FQ−19
CQ−5
CQ−6
TQ−3
Depth (in.)
Strain (με)
Strain Profile on West Side at Quarter Point
−88 με
−123 με
−47 με
−45 με
251 με
510 με
526 με
FQ−23
FQ−22
FQ−21
FQ−20
CQ−5
CQ−6
TQ−3
Strain (με)

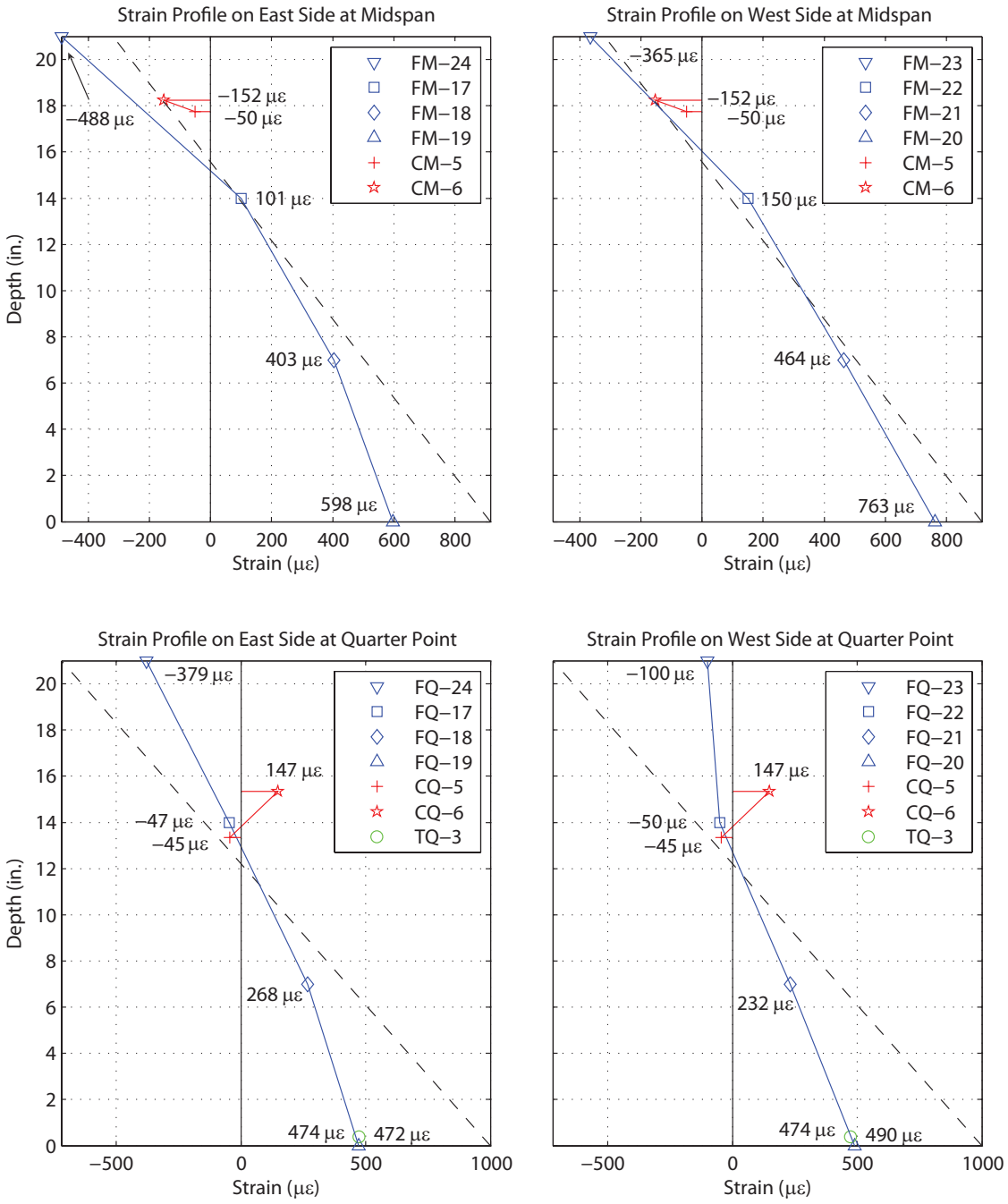
Strain Profile on East Side at Midspan
Depth (in.)
Strain (με)
FM–24
FM–17
FM–18
FM–19
CM–5
CM–6
−488 με
−152 με
−50 με
101 με
403 με
598 με
Strain Profile on West Side at Midspan
FM–23
FM–22
FM–21
FM–20
CM–5
CM–6
−365 με
−152 με
−50 με
150 με
464 με
763 με
Strain Profile on East Side at Quarter Point
FQ–24
FQ–17
FQ–18
FQ–19
CQ–5
CQ–6
TQ–3
−379 με
147 με
−47 με
−45 με
268 με
474 με
472 με
Strain Profile on West Side at Quarter Point
FQ–23
FQ–22
FQ–21
FQ–20
CQ–5
CQ–6
TQ–3
−100 με
147 με
−50 με
−45 με
232 με
474 με
490 με

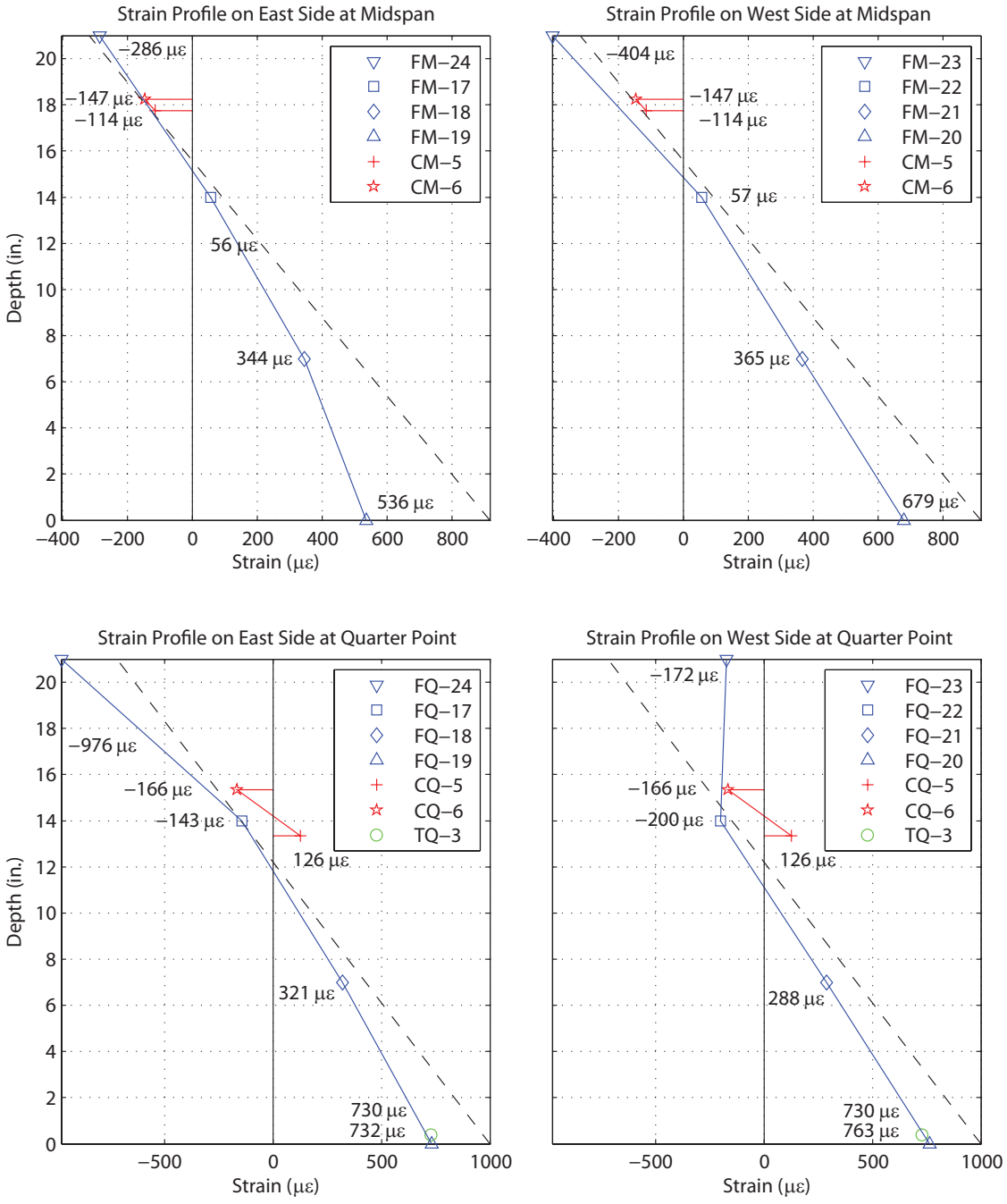
Strain Profile on East Side at Midspan
−286 με
−147 με
−114 με
56 με
344 με
536 με
FM−24
FM−17
FM−18
FM−19
CM−5
CM−6
Depth (in.)
Strain (με)
Strain Profile on West Side at Midspan
−404 με
−147 με
−114 με
57 με
365 με
679 με
FM−23
FM−22
FM−21
FM−20
CM−5
CM−6
Strain (με)
Strain Profile on East Side at Quarter Point
−976 με
−166 με
−143 με
126 με
321 με
730 με
732 με
FQ−24
FQ−17
FQ−18
FQ−19
CQ−5
CQ−6
TQ−3
Depth (in.)
Strain (με)
Strain Profile on West Side at Quarter Point
−172 με
−166 με
−200 με
126 με
288 με
730 με
763 με
FQ−23
FQ−22
FQ−21
FQ−20
CQ−5
CQ−6
TQ−3
Strain (με)

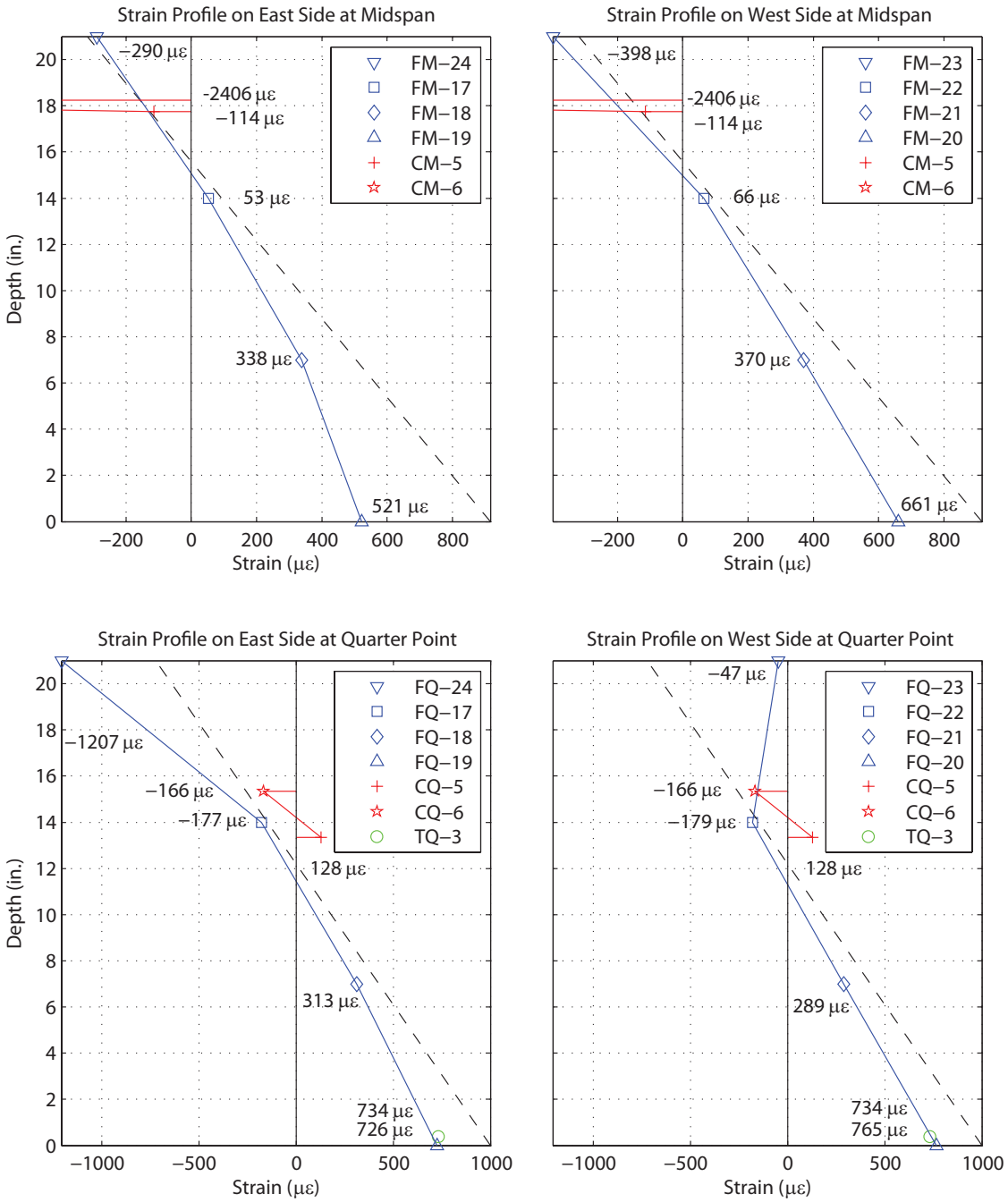
Strain Profile on East Side at Midspan
−290 με
-2406 με
−114 με
53 με
338 με
521 με
FM−24
FM−17
FM−18
FM−19
CM−5
CM−6
Depth (in.)
Strain (με)
Strain Profile on West Side at Midspan
−398 με
-2406 με
−114 με
66 με
370 με
661 με
FM−23
FM−22
FM−21
FM−20
CM−5
CM−6
Strain (με)
Strain Profile on East Side at Quarter Point
−1207 με
−166 με
−177 με
128 με
313 με
734 με
726 με
FQ−24
FQ−17
FQ−18
FQ−19
CQ−5
CQ−6
TQ−3
Depth (in.)
Strain (με)
Strain Profile on West Side at Quarter Point
−47 με
−166 με
−179 με
128 με
289 με
734 με
765 με
FQ−23
FQ−22
FQ−21
FQ−20
CQ−5
CQ−6
TQ−3
Strain (με)

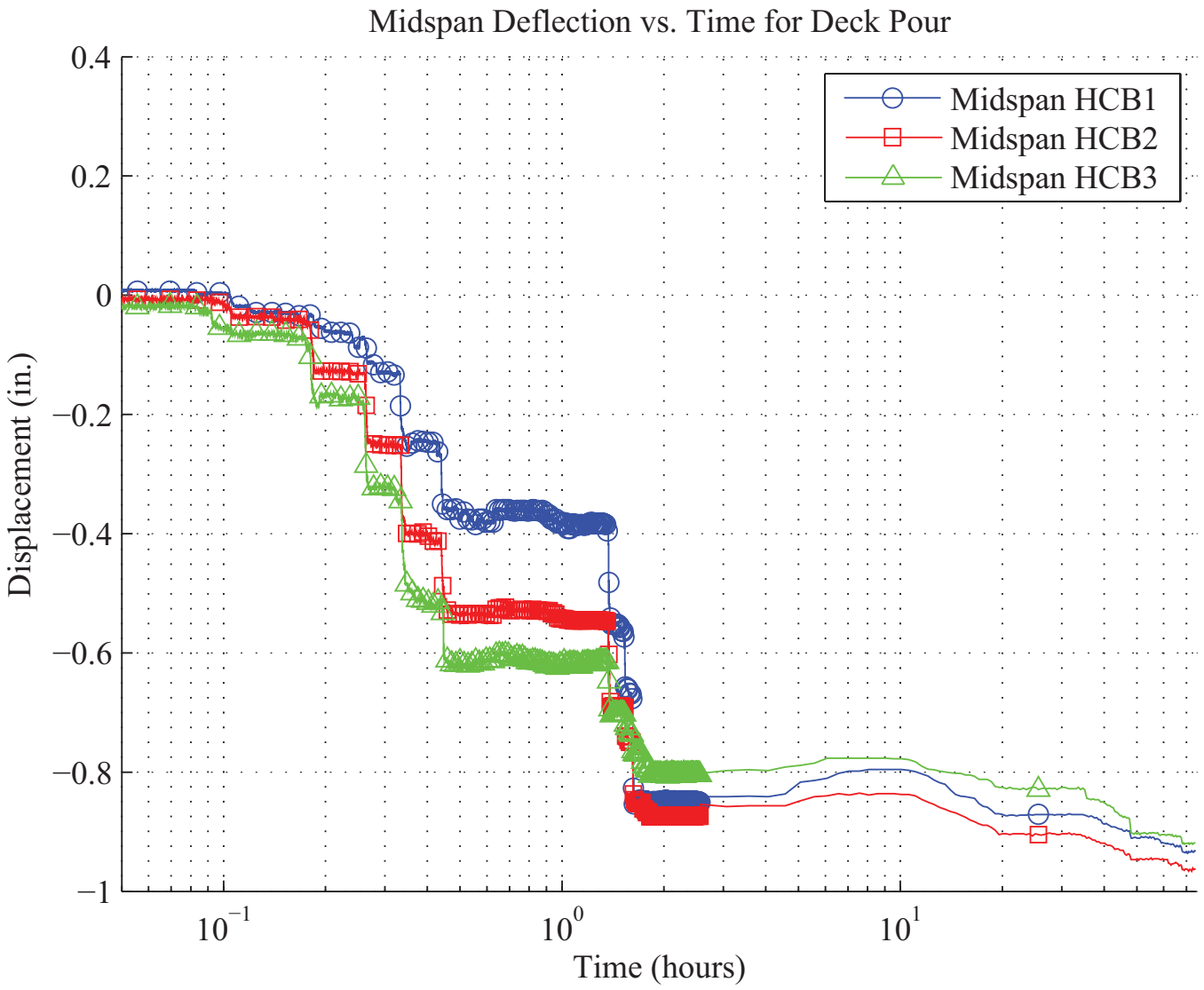
Midspan Deflection vs. Time for Deck Pour
Midspan HCB1
Midspan HCB2
Midspan HCB3
Displacement (in.)
Time (hours)
0.4
0.2
0
−0.2
−0.4
−0.6
−0.8
−1
10^−1
10^0
10^1

Estimated Strains from Deck Pour

x	ybar	Ix	Interior Moment	Bottom Flange Strain	Top Flange Strain	Strand Strain
ft.	in.	in^4	kip*in	με	με	με
0	2.74	3433	0	0	0	0
4.3	7.09	3565	383	246	-482	228
8.6	10.47	5413	681	425	-428	405
10.75	11.67	6540	798	460	-367	440
12.9	12.88	7668	894	484	-305	466
17.2	14.33	9394	1022	503	-234	485
21.5	14.81	10032	1064	507	-212	490
25.8	14.33	9394	1022	503	-234	485
30.1	12.88	7668	894	484	-305	466
32.25	11.67	6540	798	460	-367	440
34.4	10.47	5413	681	425	-428	405
38.7	7.09	3565	383	246	-482	228
43	2.74	3433	0	0	0	0

NOTE: Moments calculated by transforming volume of concrete for interior girder into equivalent uniform load. Uniform load used to calculate moment in simple span. Moment used to calculate strains using M*y/I*E using Hillman model section properties (E=3100 ksi).

Appendix D – Supplementary Phase III Results and Calculations

Phase III Load Locations

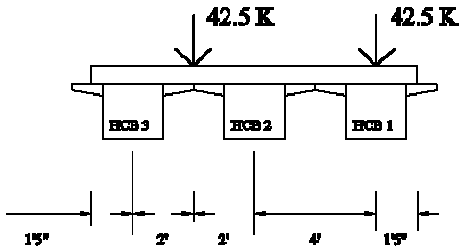

North Elevation View

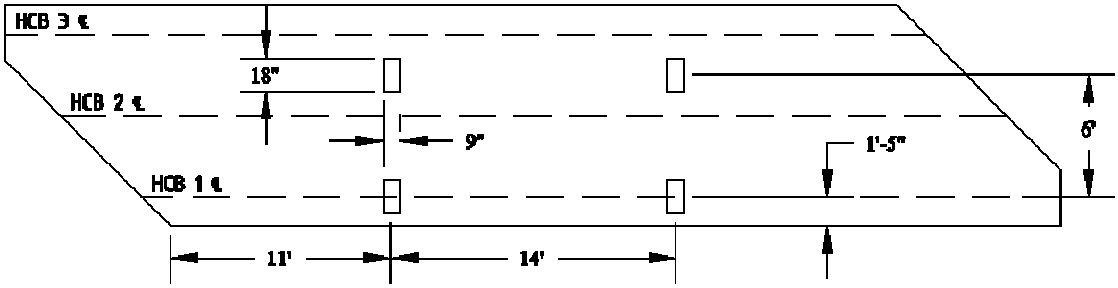

Plan View

Test ST1 and ST2 Load Location

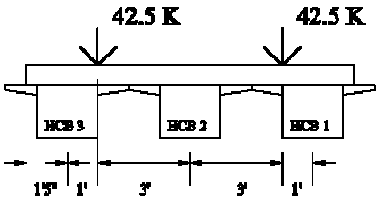

North Elevation View

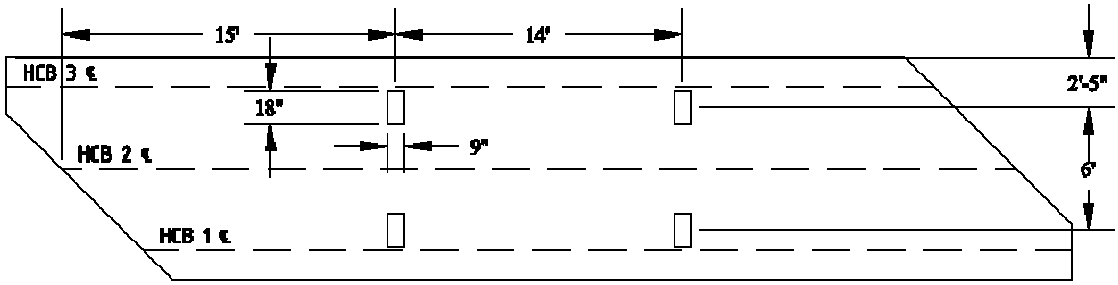

Plan View

Test ST3 and ST4 Load Location

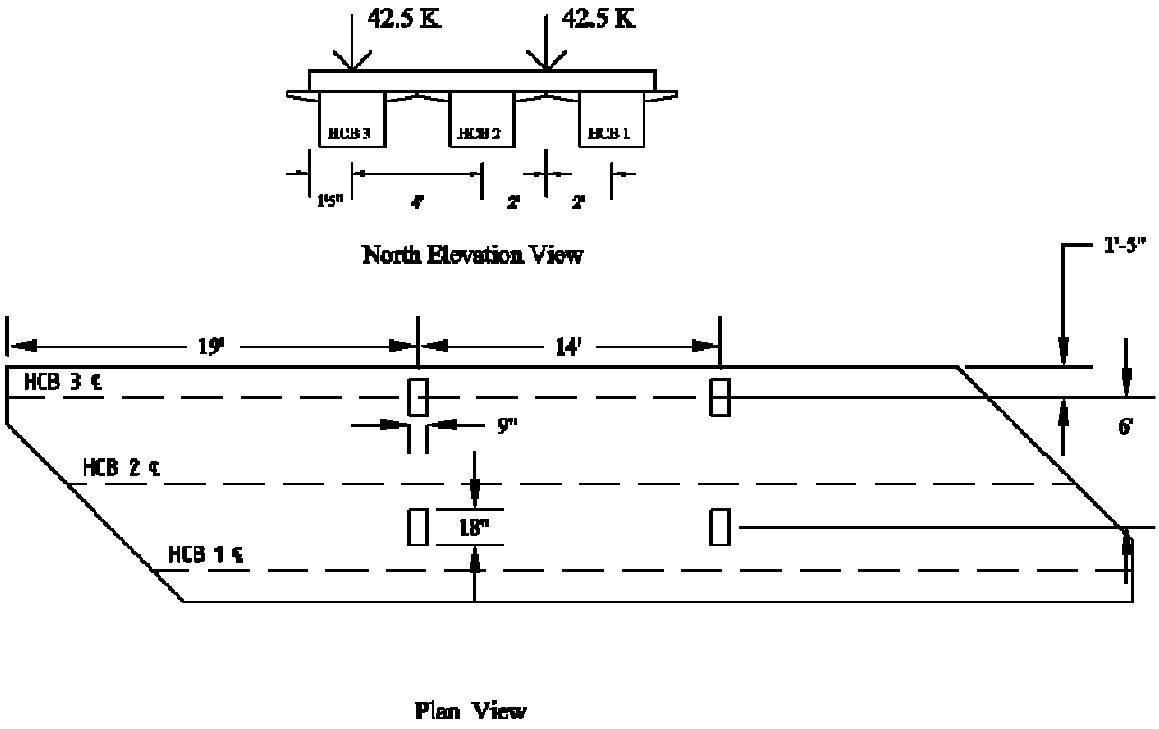

Test ST5 and ST6 Load Location

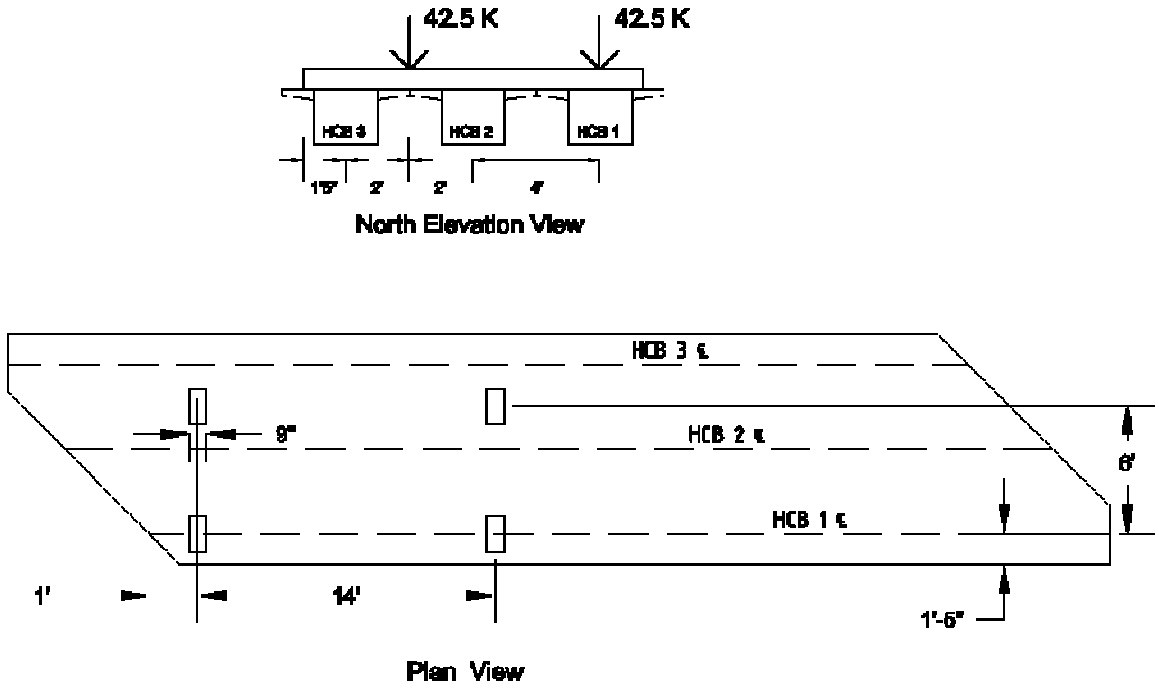

Test ST7 and ST8 Load Location

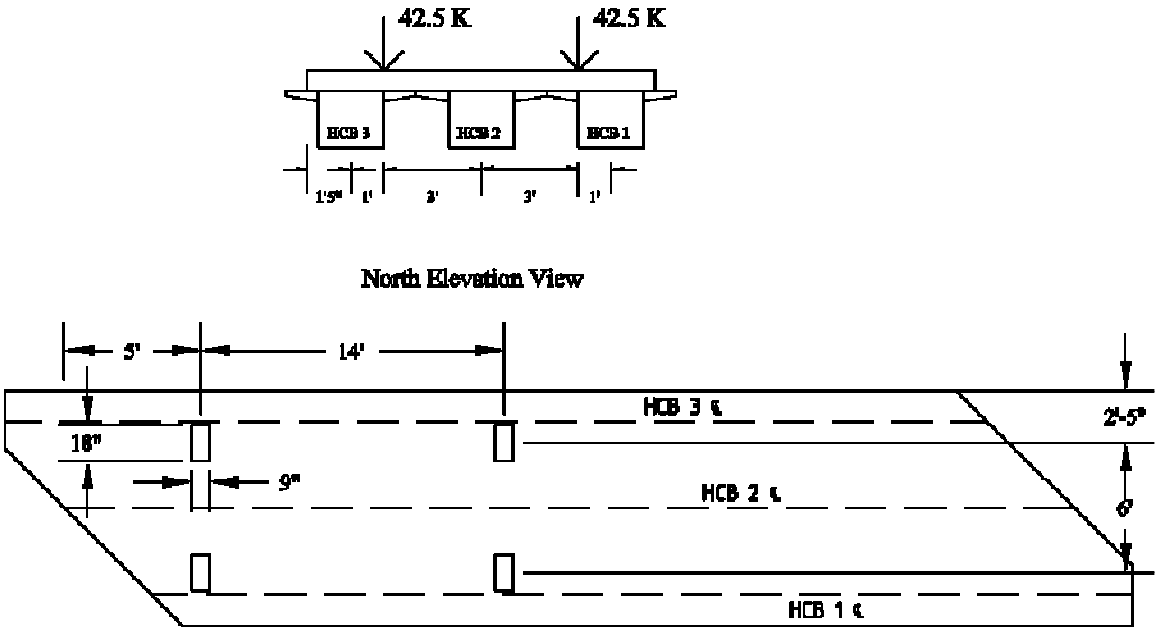

Test ST9 and ST10 Load Location

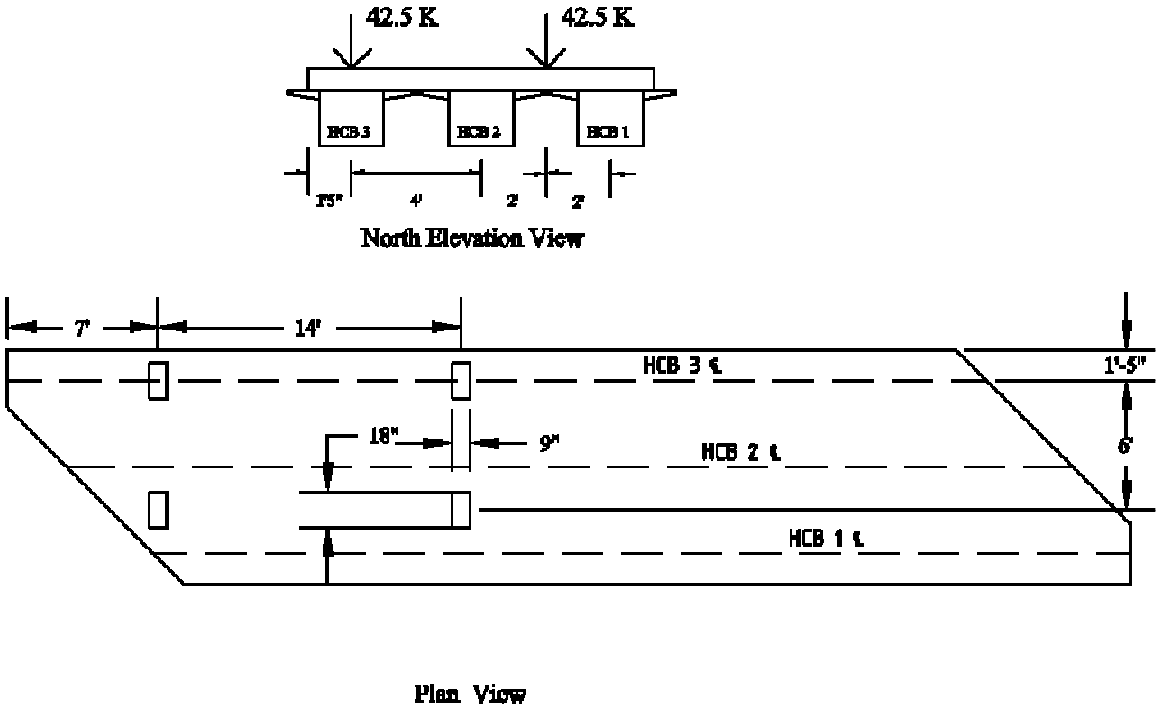

Test ST11 and ST12 Load Location

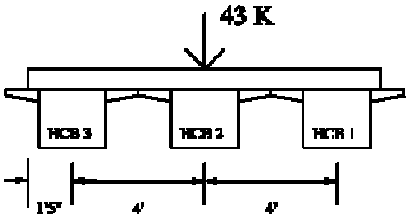

North Elevation View

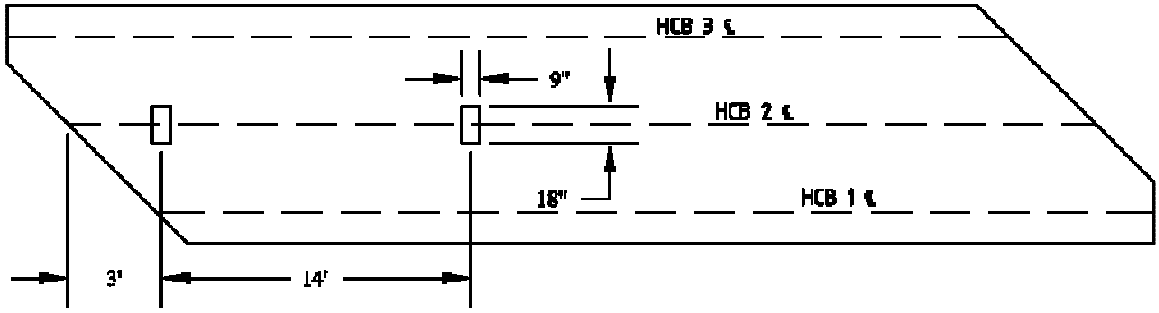

Plan View

Test ST13 and ST14 Load Location

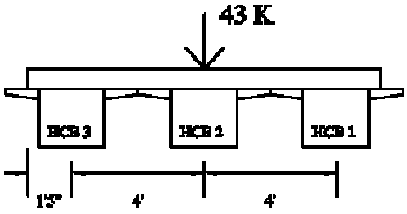

North Elevation View

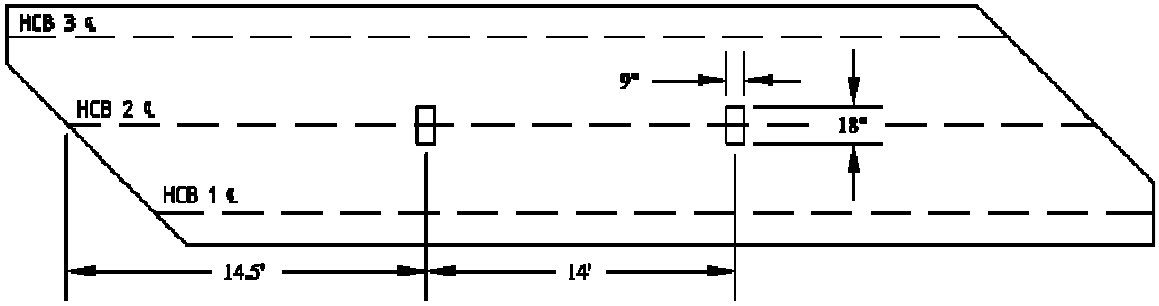

Plan View

Test ST15, ST16, and ST17 Load Location

Load vs. Deflection Plots

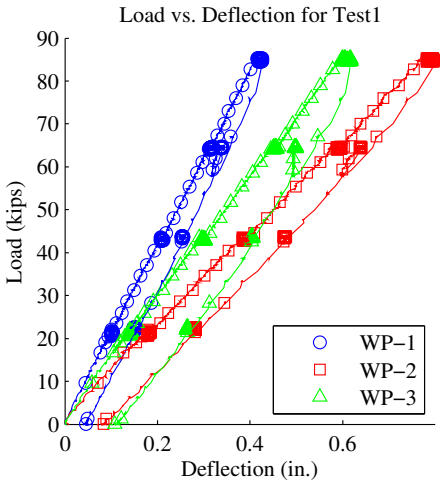

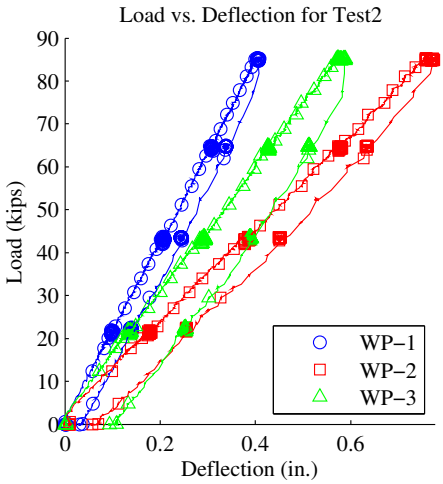

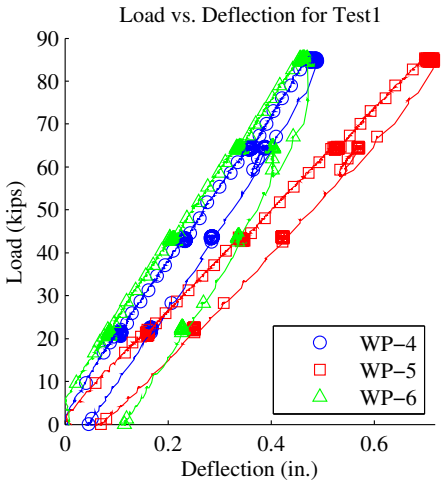

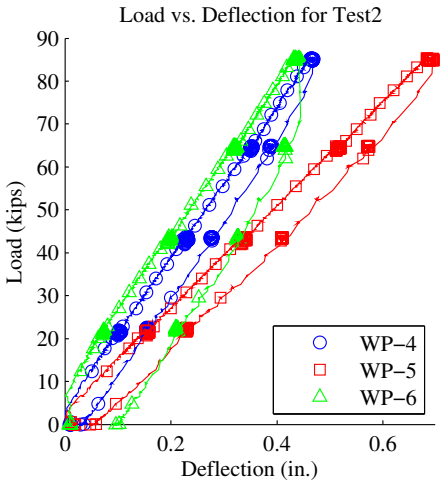

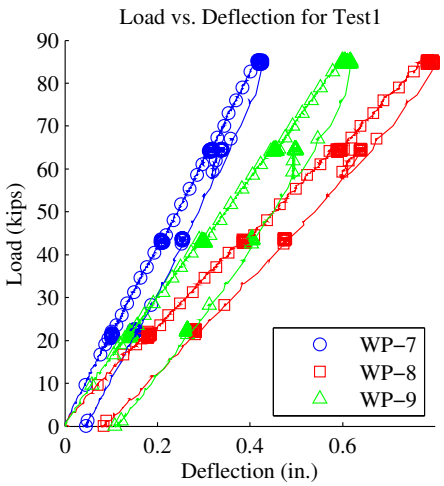

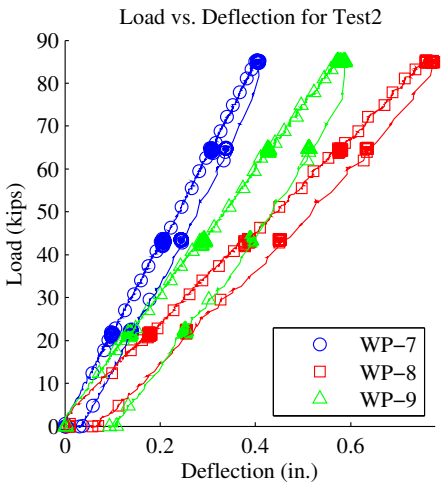

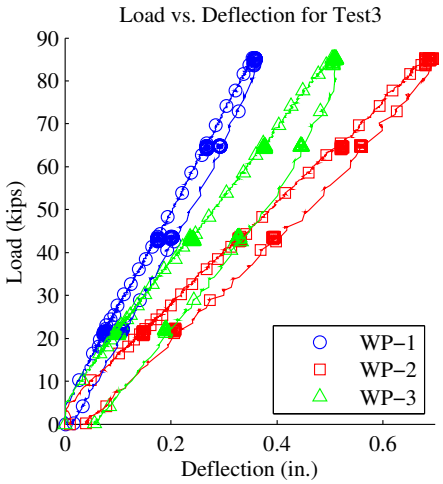
Load vs. Deflection for Test3
Load (kips)
Deflection (in.)
WP−1
WP−2
WP−3

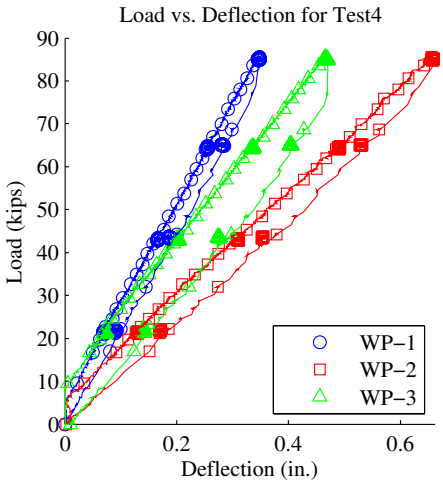
Load vs. Deflection for Test4
Load (kips)
Deflection (in.)
WP−1
WP−2
WP−3

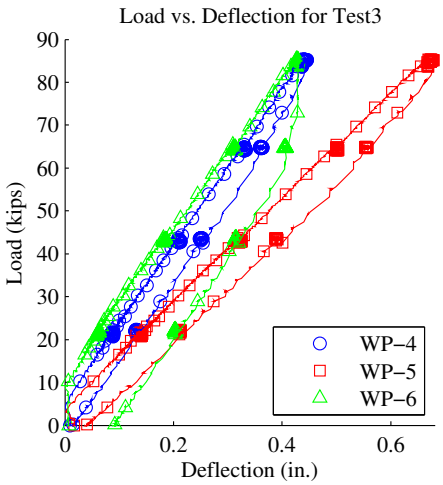
Load vs. Deflection for Test3
Load (kips)
Deflection (in.)
WP−4
WP−5
WP−6

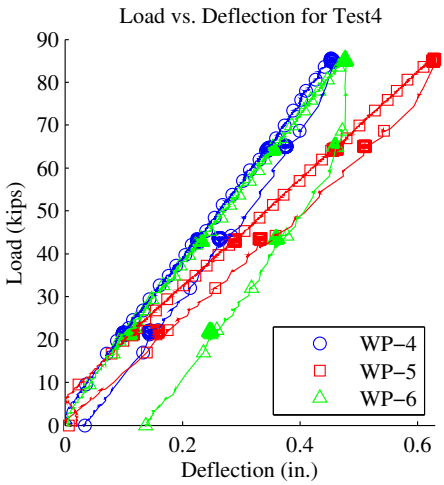
Load vs. Deflection for Test4
Load (kips)
Deflection (in.)
WP−4
WP−5
WP−6

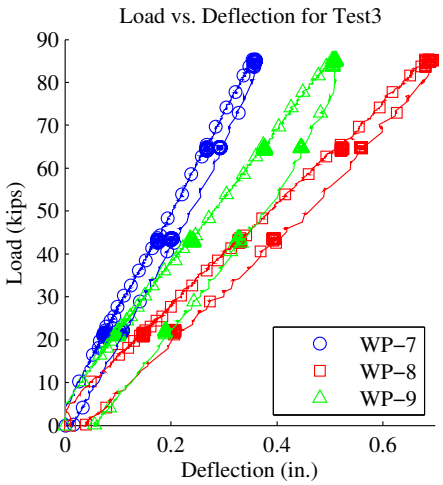
Load vs. Deflection for Test3
Load (kips)
Deflection (in.)
WP−7
WP−8
WP−9

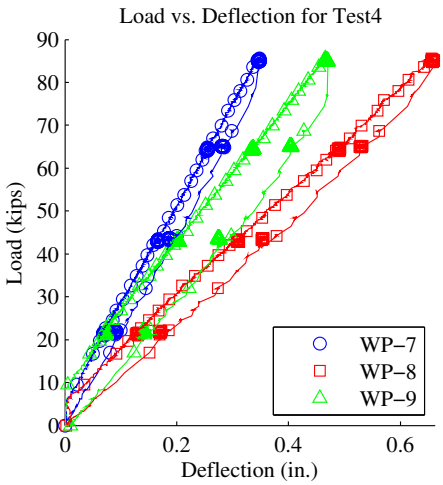
Load vs. Deflection for Test4
Load (kips)
Deflection (in.)
WP−7
WP−8
WP−9

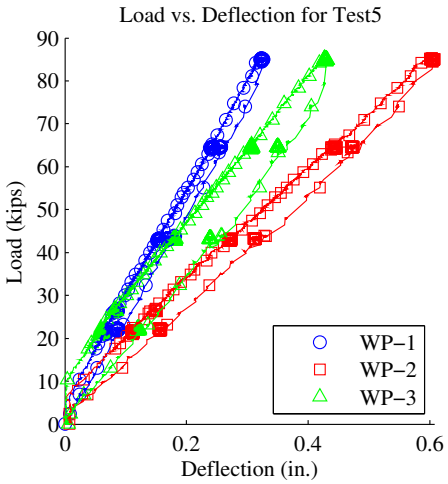
Load vs. Deflection for Test5
Load (kips)
Deflection (in.)
WP−1
WP−2
WP−3

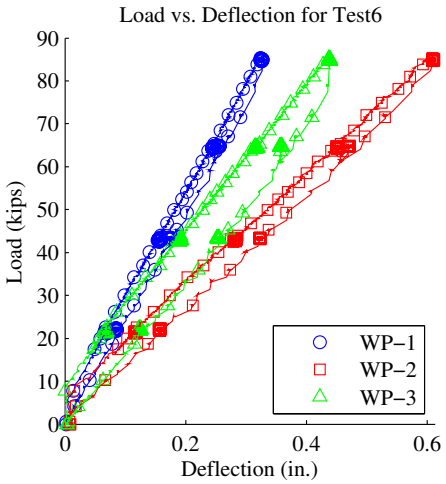
Load vs. Deflection for Test6
Load (kips)
Deflection (in.)
WP−1
WP−2
WP−3

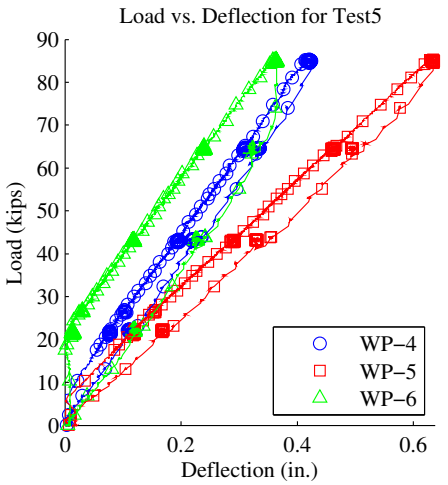
Load vs. Deflection for Test5
Load (kips)
Deflection (in.)
WP−4
WP−5
WP−6

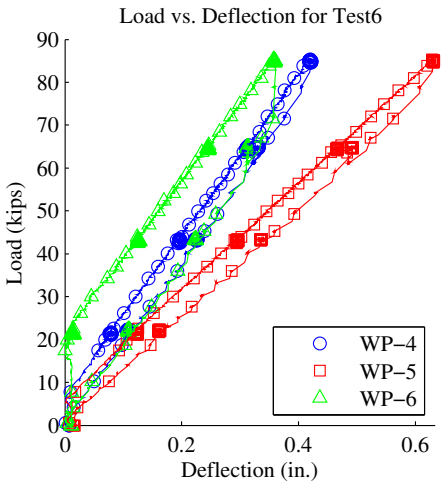
Load vs. Deflection for Test6
Load (kips)
Deflection (in.)
WP−4
WP−5
WP−6

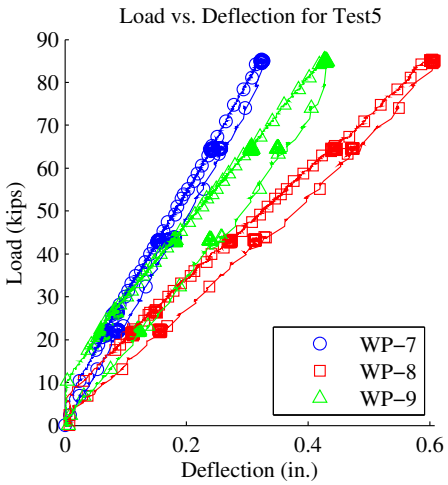
Load vs. Deflection for Test5
Load (kips)
Deflection (in.)
WP−7
WP−8
WP−9

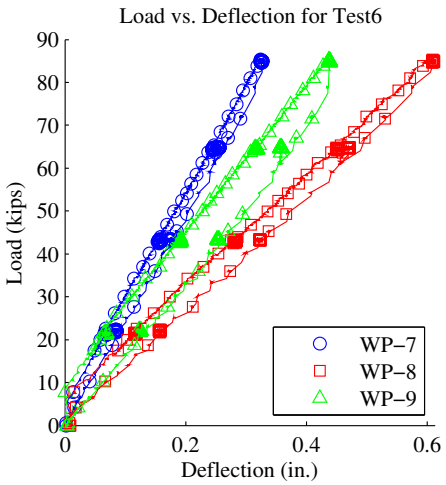
Load vs. Deflection for Test6
Load (kips)
Deflection (in.)
WP−7
WP−8
WP−9

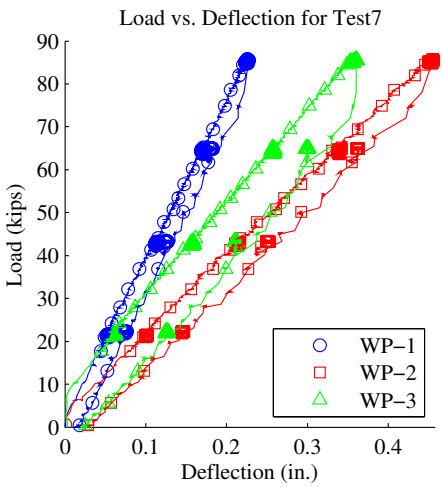
Load vs. Deflection for Test7
Load (kips)
Deflection (in.)
WP–1
WP–2
WP–3

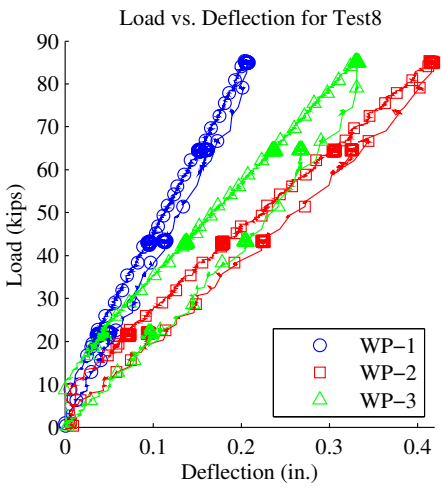
Load vs. Deflection for Test8
Load (kips)
Deflection (in.)
WP–1
WP–2
WP–3

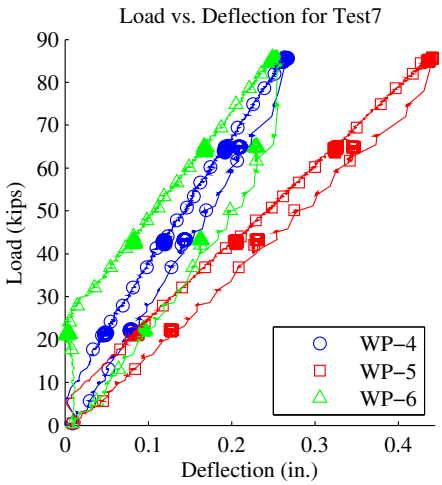
Load vs. Deflection for Test7
Load (kips)
Deflection (in.)
WP–4
WP–5
WP–6

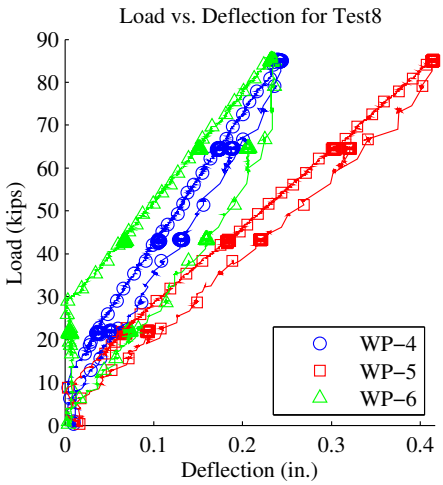
Load vs. Deflection for Test8
Load (kips)
Deflection (in.)
WP–4
WP–5
WP–6

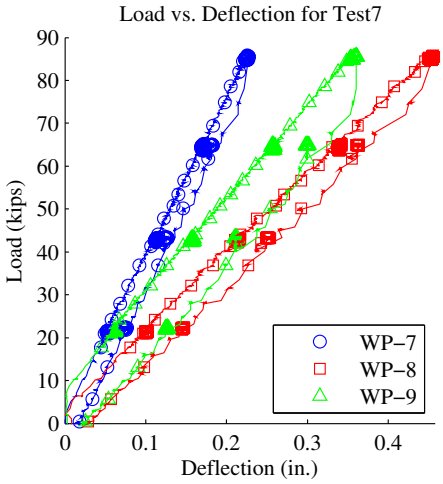
Load vs. Deflection for Test7
Load (kips)
Deflection (in.)
WP–7
WP–8
WP–9

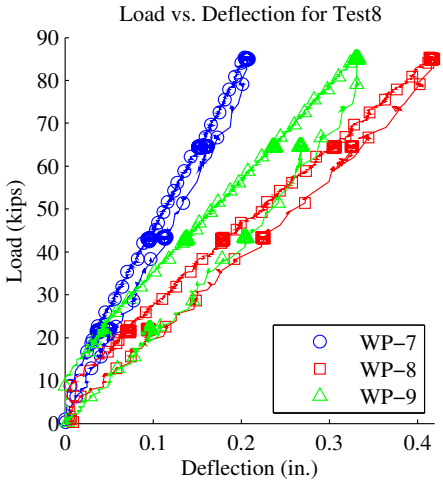
Load vs. Deflection for Test8
Load (kips)
Deflection (in.)
WP–7
WP–8
WP–9

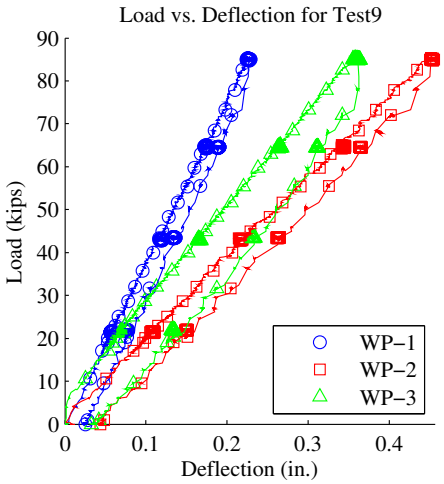
Load vs. Deflection for Test9
Load (kips)
Deflection (in.)
WP−1
WP−2
WP−3

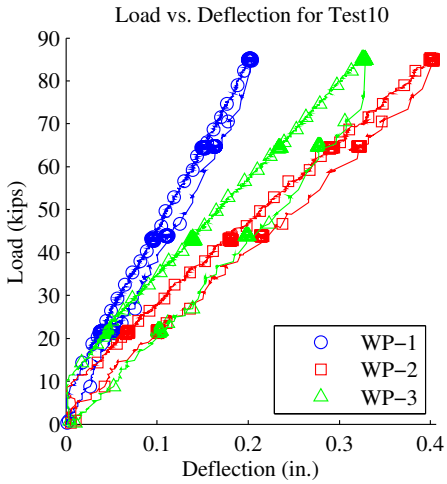
Load vs. Deflection for Test10
Load (kips)
Deflection (in.)
WP−1
WP−2
WP−3

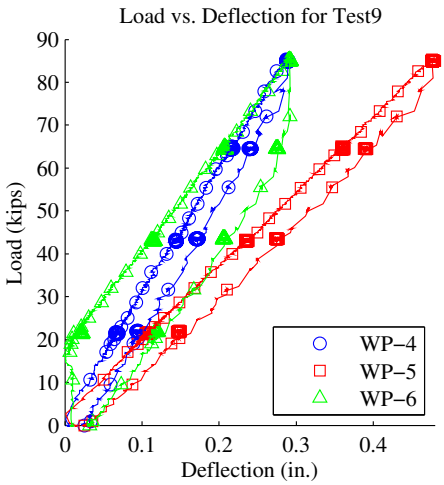
Load vs. Deflection for Test9
Load (kips)
Deflection (in.)
WP−4
WP−5
WP−6

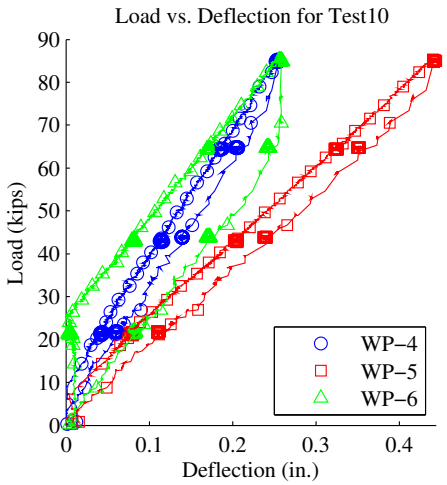
Load vs. Deflection for Test10
Load (kips)
Deflection (in.)
WP−4
WP−5
WP−6

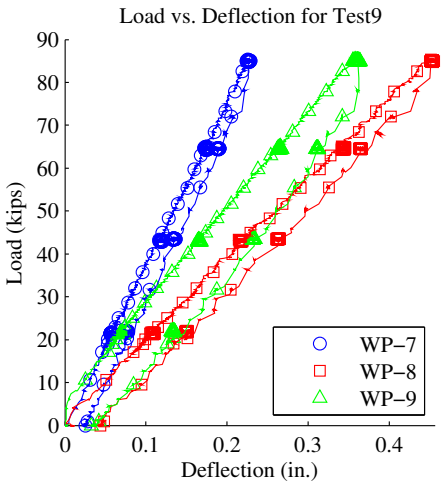
Load vs. Deflection for Test9
Load (kips)
Deflection (in.)
WP−7
WP−8
WP−9

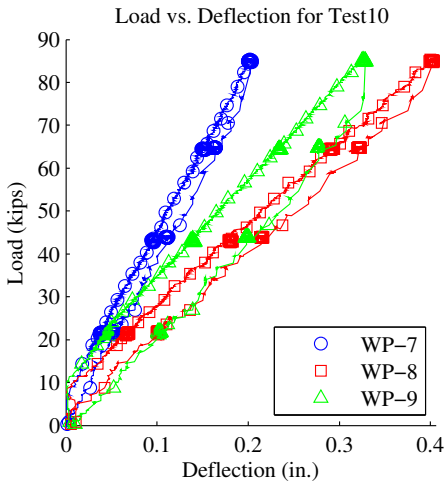
Load vs. Deflection for Test10
Load (kips)
Deflection (in.)
WP−7
WP−8
WP−9

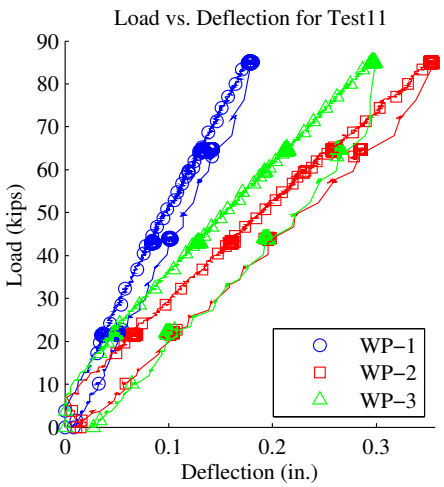
Load vs. Deflection for Test11
Load (kips)
Deflection (in.)
WP–1
WP–2
WP–3

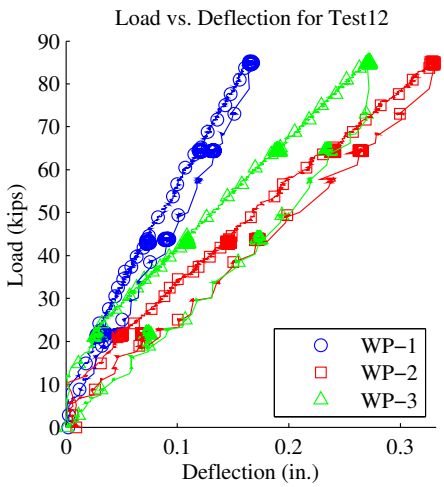
Load vs. Deflection for Test12
Load (kips)
Deflection (in.)
WP–1
WP–2
WP–3

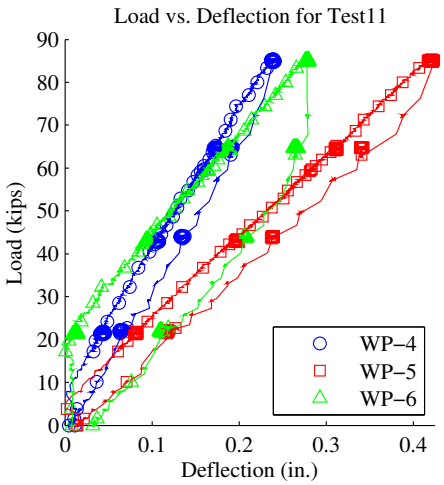
Load vs. Deflection for Test11
Load (kips)
Deflection (in.)
WP–4
WP–5
WP–6

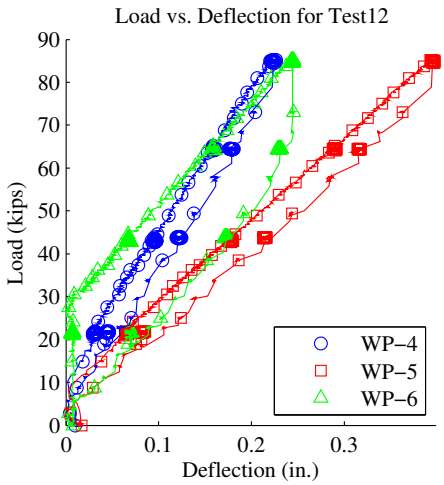
Load vs. Deflection for Test12
Load (kips)
Deflection (in.)
WP–4
WP–5
WP–6

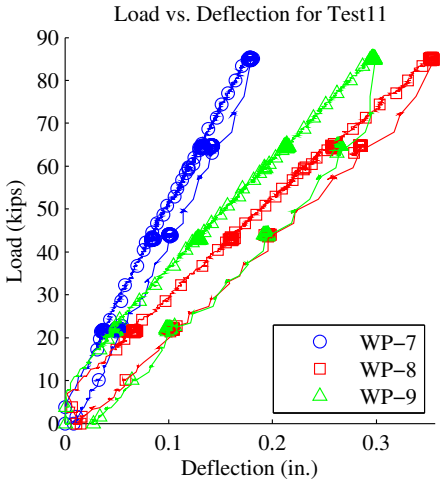
Load vs. Deflection for Test11
Load (kips)
Deflection (in.)
WP–7
WP–8
WP–9

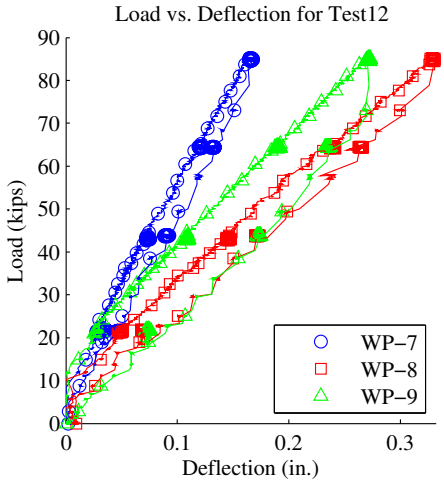
Load vs. Deflection for Test12
Load (kips)
Deflection (in.)
WP–7
WP–8
WP–9

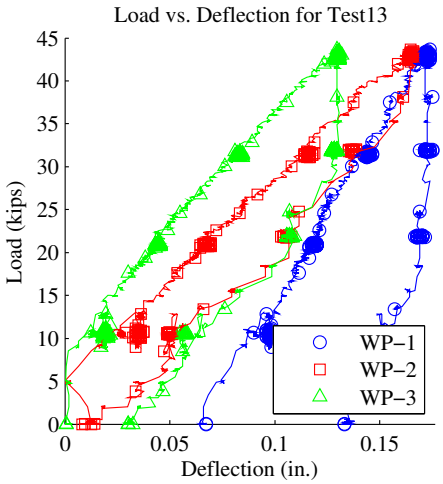
Load vs. Deflection for Test13
Load (kips)
Deflection (in.)
WP–1
WP–2
WP–3

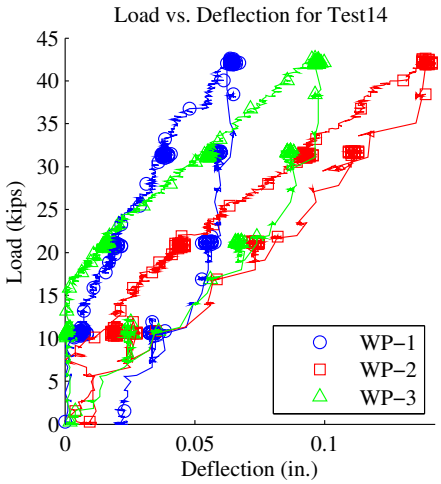
Load vs. Deflection for Test14
Load (kips)
Deflection (in.)
WP–1
WP–2
WP–3

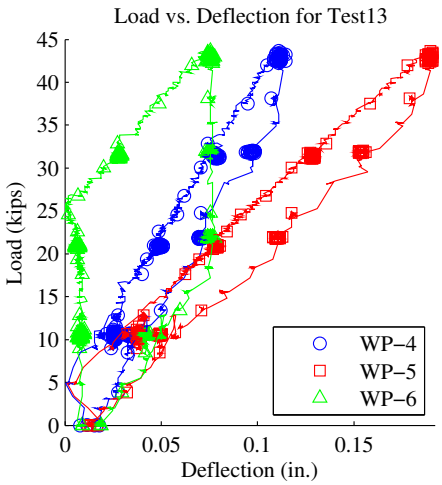
Load vs. Deflection for Test13
Load (kips)
Deflection (in.)
WP–4
WP–5
WP–6

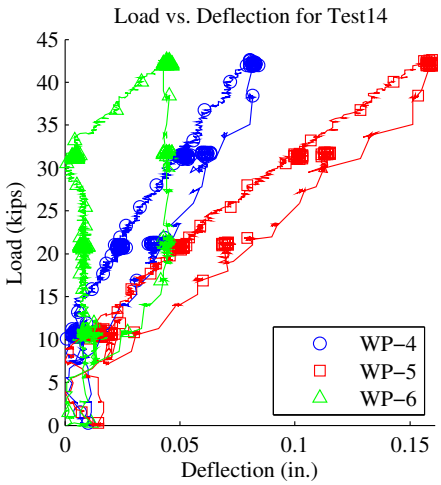
Load vs. Deflection for Test14
Load (kips)
Deflection (in.)
WP–4
WP–5
WP–6

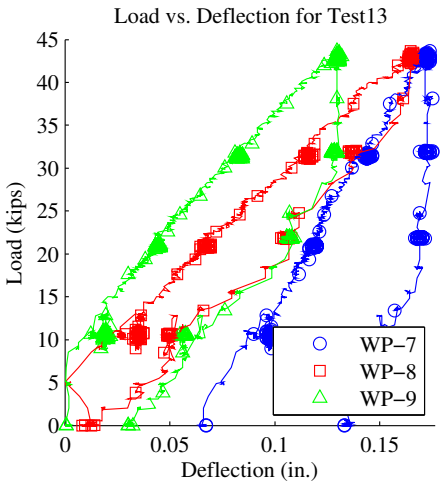
Load vs. Deflection for Test13
Load (kips)
Deflection (in.)
WP–7
WP–8
WP–9

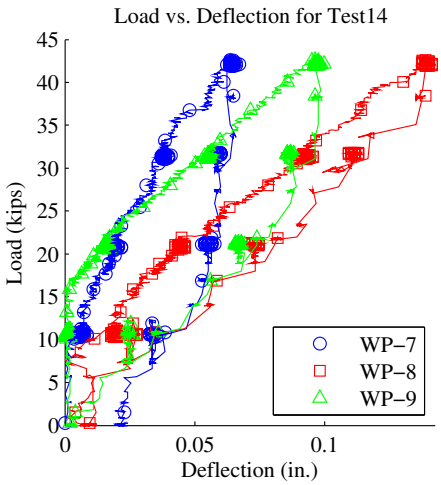
Load vs. Deflection for Test14
Load (kips)
Deflection (in.)
WP–7
WP–8
WP–9

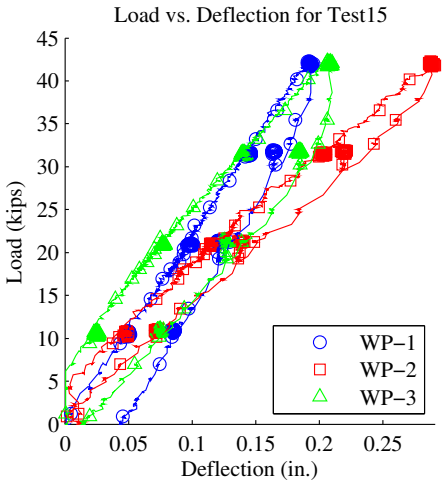
Load vs. Deflection for Test15
Load (kips)
Deflection (in.)
WP–1
WP–2
WP–3

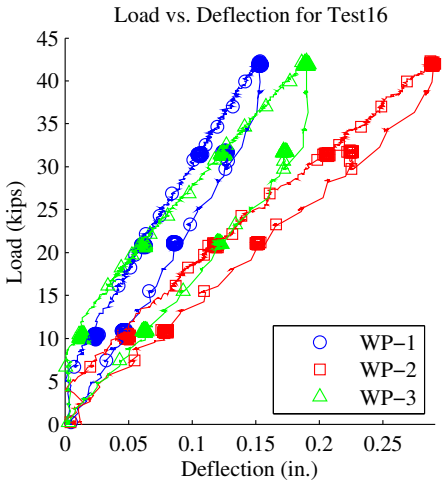
Load vs. Deflection for Test16
Load (kips)
Deflection (in.)
WP–1
WP–2
WP–3

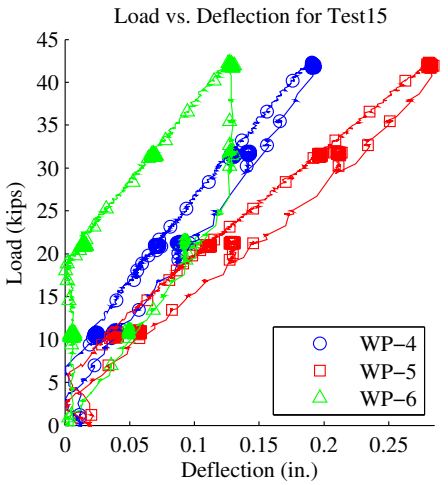
Load vs. Deflection for Test15
Load (kips)
Deflection (in.)
WP–4
WP–5
WP–6

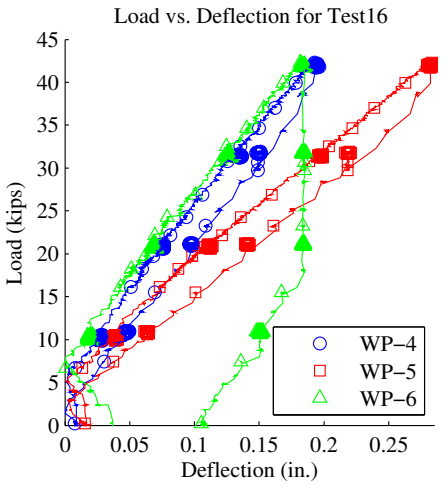
Load vs. Deflection for Test16
Load (kips)
Deflection (in.)
WP–4
WP–5
WP–6

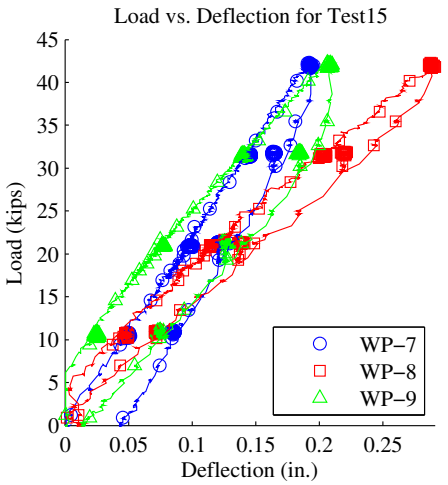
Load vs. Deflection for Test15
Load (kips)
Deflection (in.)
WP–7
WP–8
WP–9

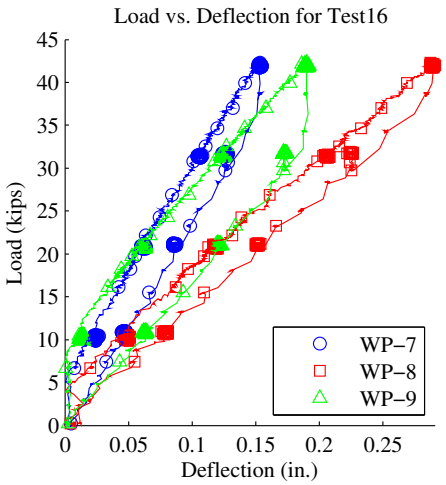
Load vs. Deflection for Test16
Load (kips)
Deflection (in.)
WP–7
WP–8
WP–9

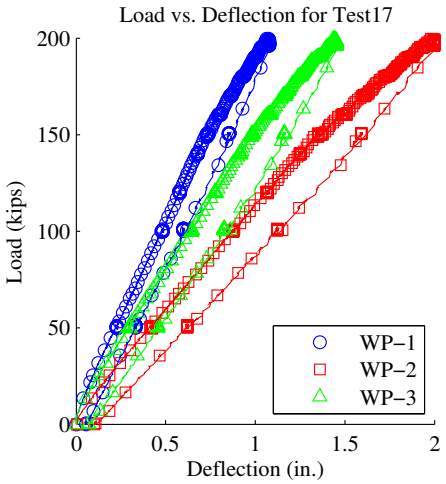
Load vs. Deflection for Test17
Load (kips)
Deflection (in.)
WP−1
WP−2
WP−3

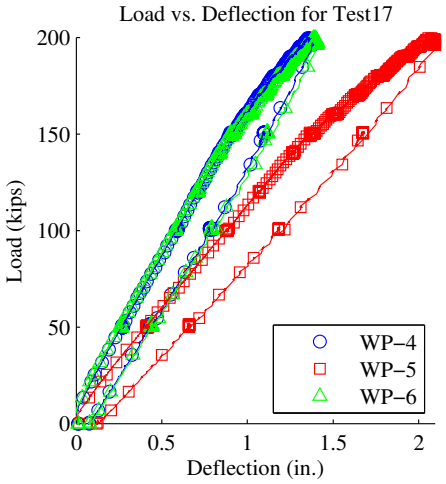
Load vs. Deflection for Test17
Load (kips)
Deflection (in.)
WP−4
WP−5
WP−6

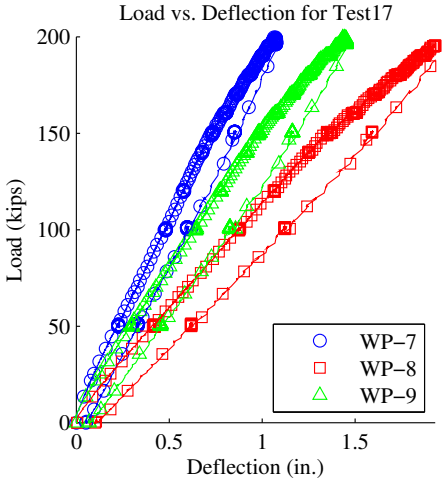
Load vs. Deflection for Test17
Load (kips)
Deflection (in.)
WP−7
WP−8
WP−9

Strand Strain vs. Load

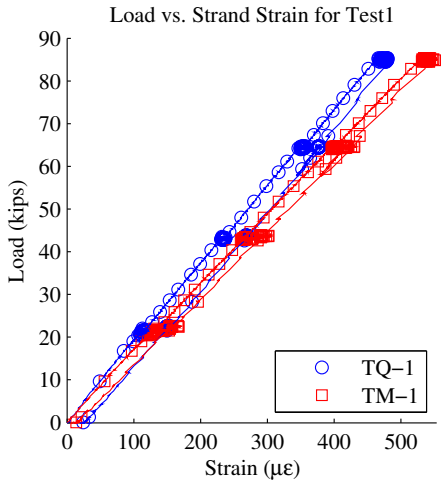

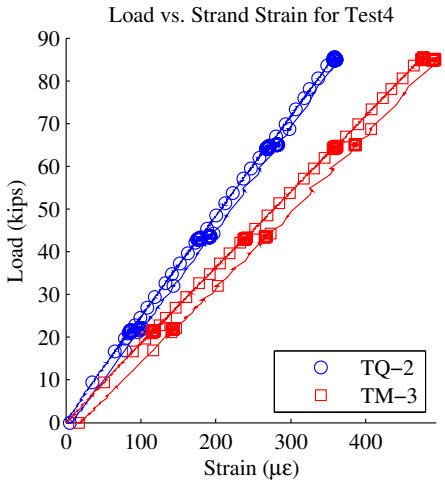

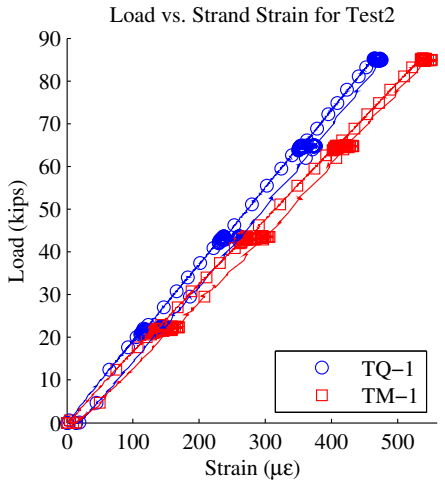

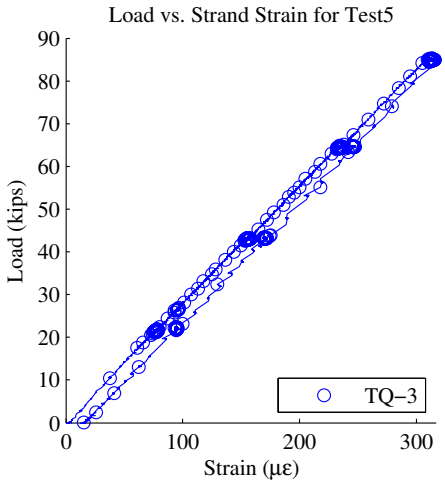

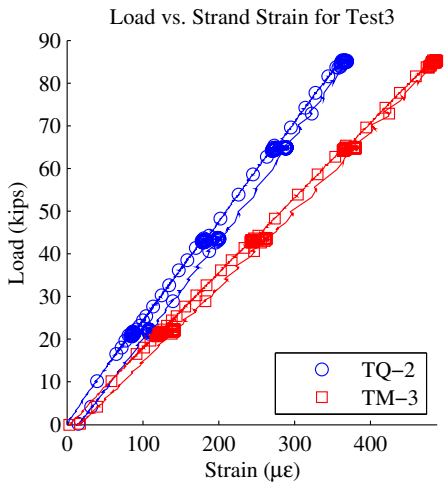

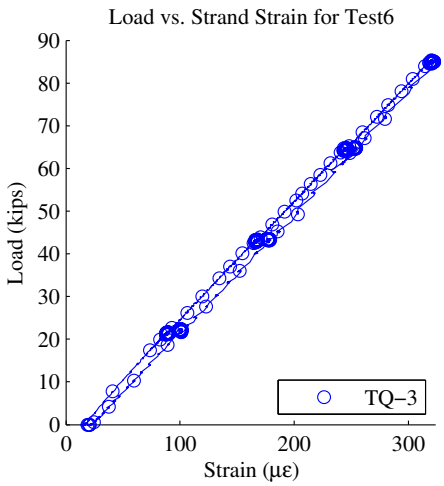

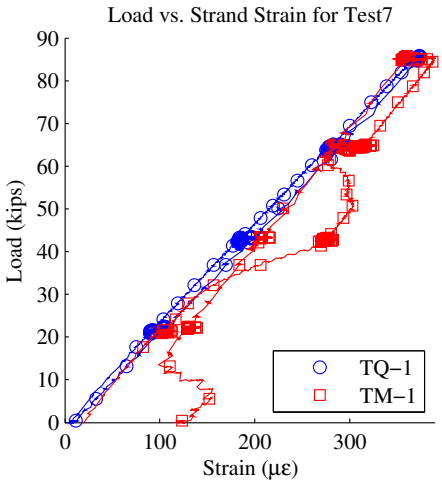
Load vs. Strand Strain for Test7
Load (kips)
Strain (με)
TQ−1
TM−1

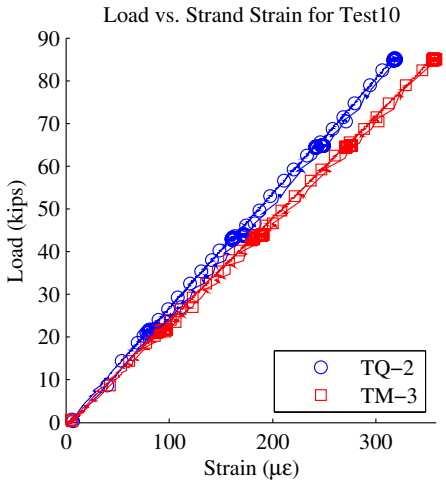
Load vs. Strand Strain for Test10
Load (kips)
Strain (με)
TQ−2
TM−3

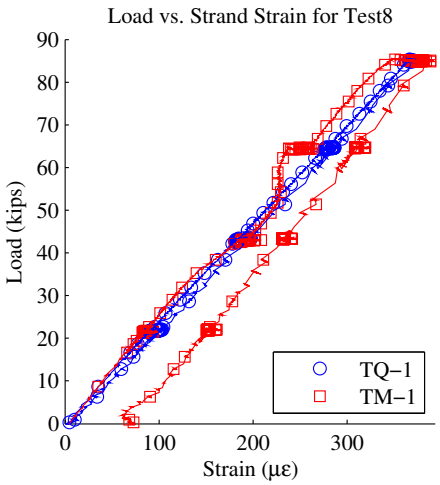
Load vs. Strand Strain for Test8
Load (kips)
Strain (με)
TQ−1
TM−1

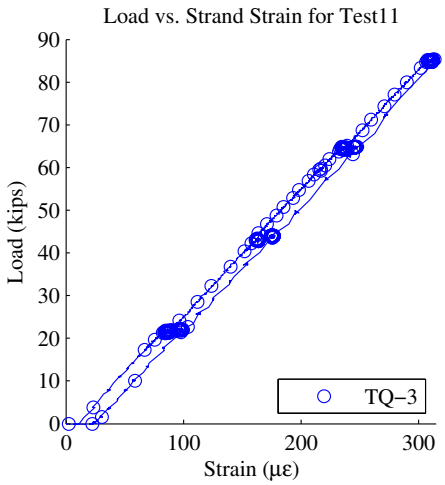
Load vs. Strand Strain for Test11
Load (kips)
Strain (με)
TQ−3

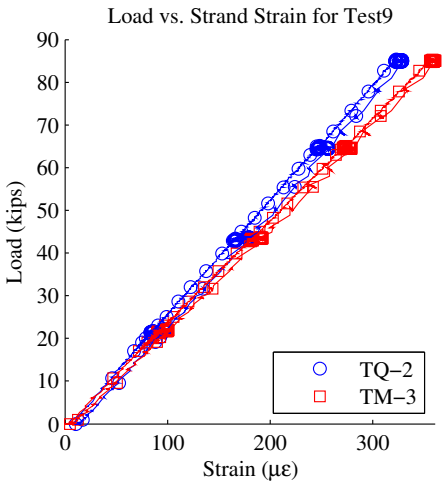
Load vs. Strand Strain for Test9
Load (kips)
Strain (με)
TQ−2
TM−3

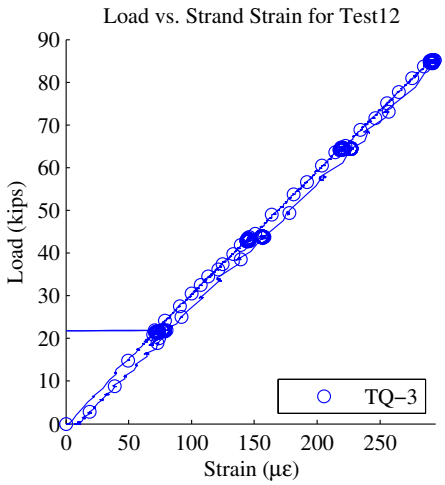
Load vs. Strand Strain for Test12
Load (kips)
Strain (με)
TQ−3

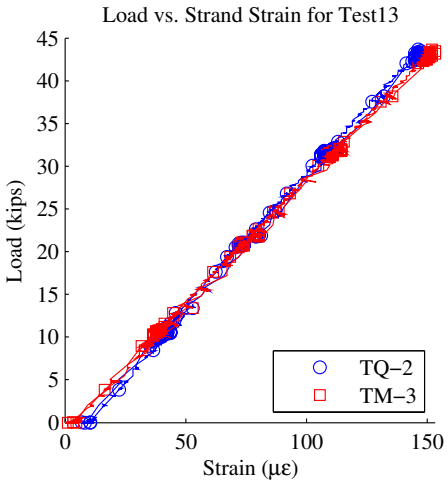
Load vs. Strand Strain for Test13
Load (kips)
Strain (με)
TQ−2
TM−3

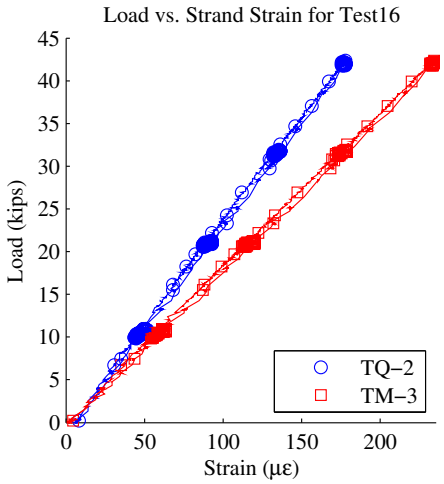
Load vs. Strand Strain for Test16
Load (kips)
Strain (με)
TQ−2
TM−3

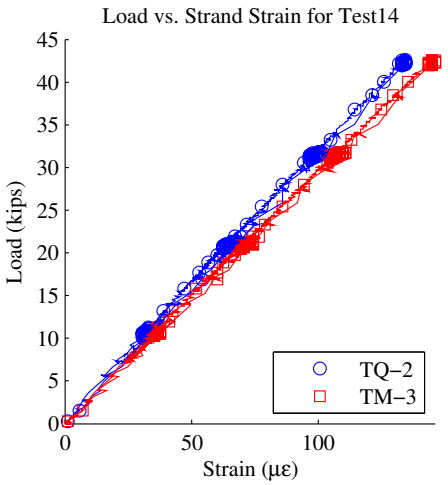
Load vs. Strand Strain for Test14
Load (kips)
Strain (με)
TQ−2
TM−3

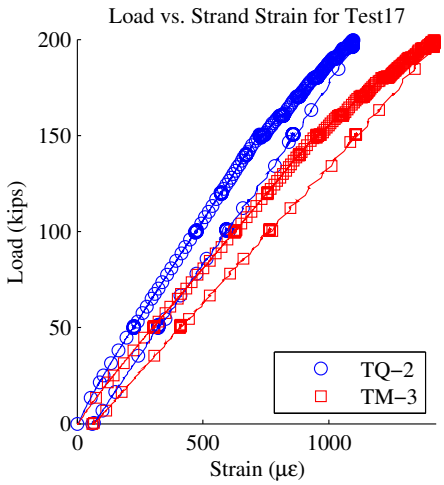
Load vs. Strand Strain for Test17
Load (kips)
Strain (με)
TQ−2
TM−3

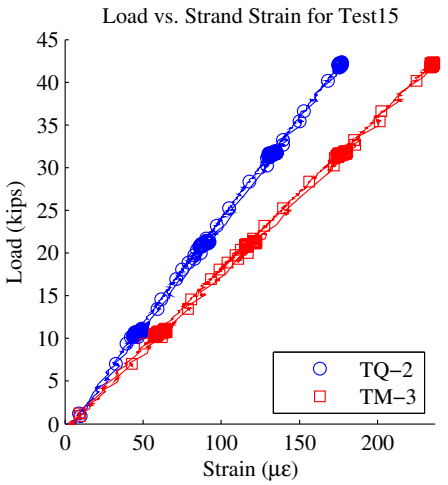
Load vs. Strand Strain for Test15
Load (kips)
Strain (με)
TQ−2
TM−3

Load vs. FRP Bottom Flange Strain

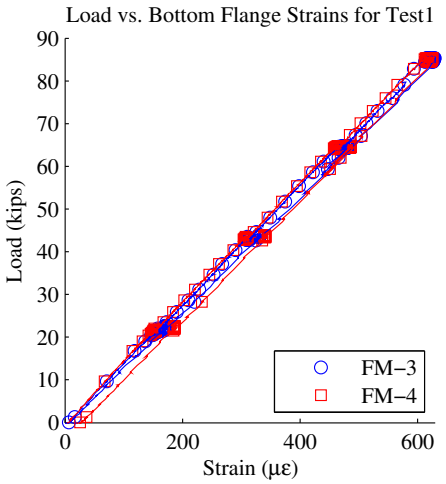

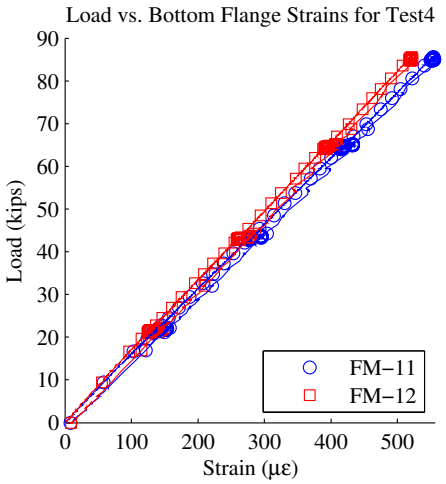

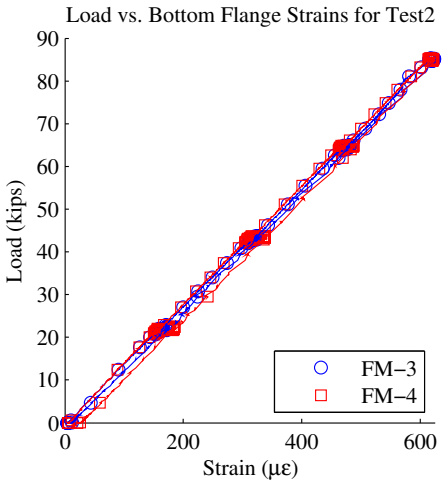

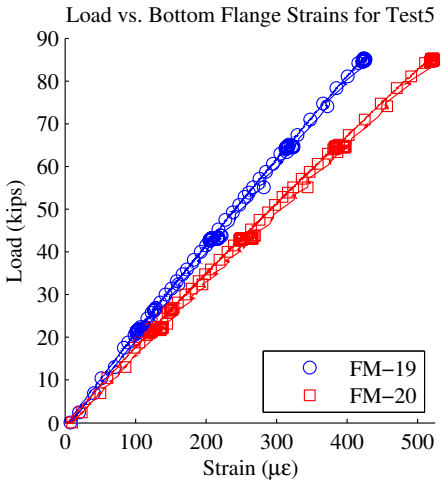

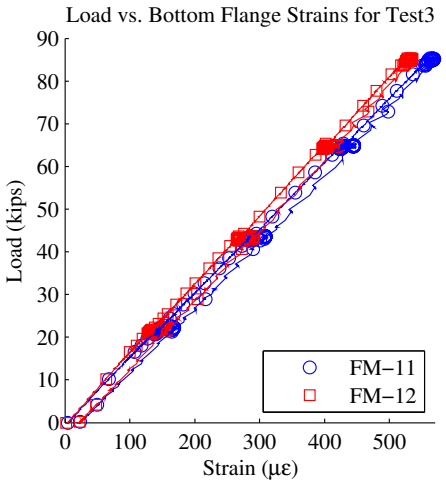

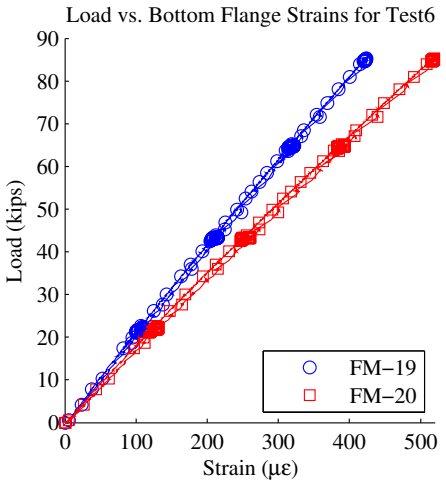

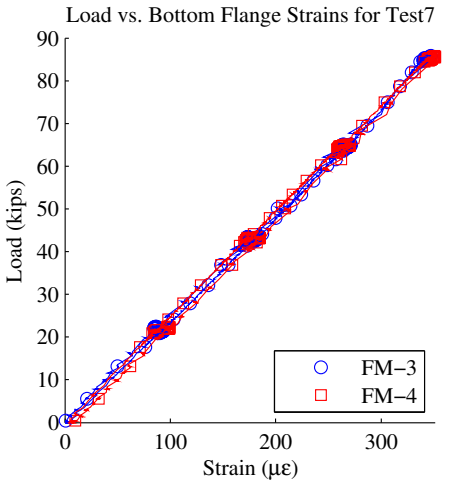
Load vs. Bottom Flange Strains for Test7
Load (kips)
Strain (με)
FM−3
FM−4

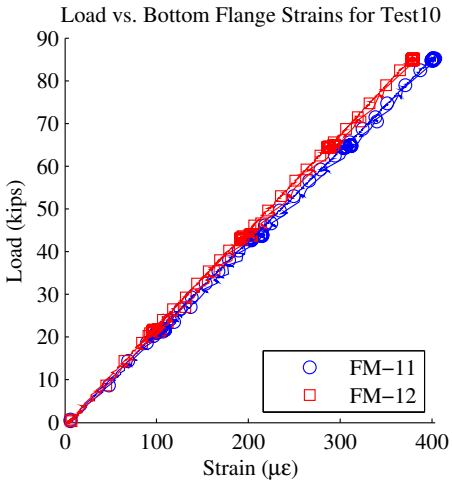
Load vs. Bottom Flange Strains for Test10
Load (kips)
Strain (με)
FM−11
FM−12

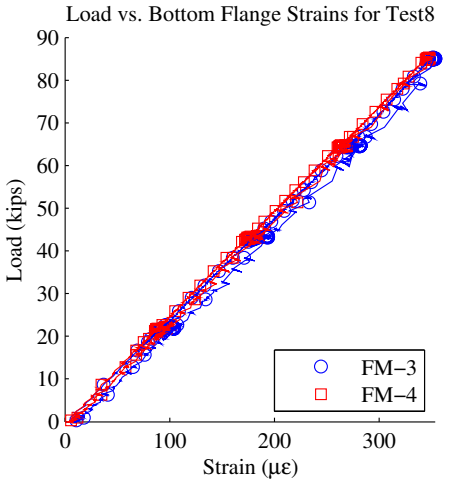
Load vs. Bottom Flange Strains for Test8
Load (kips)
Strain (με)
FM−3
FM−4

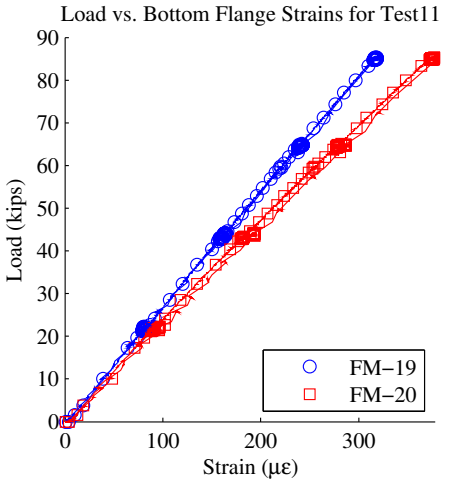
Load vs. Bottom Flange Strains for Test11
Load (kips)
Strain (με)
FM−19
FM−20

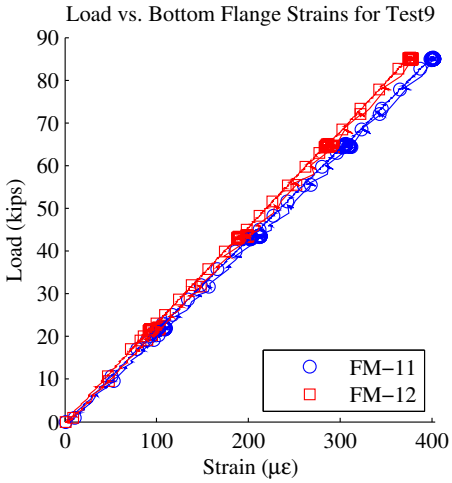
Load vs. Bottom Flange Strains for Test9
Load (kips)
Strain (με)
FM−11
FM−12

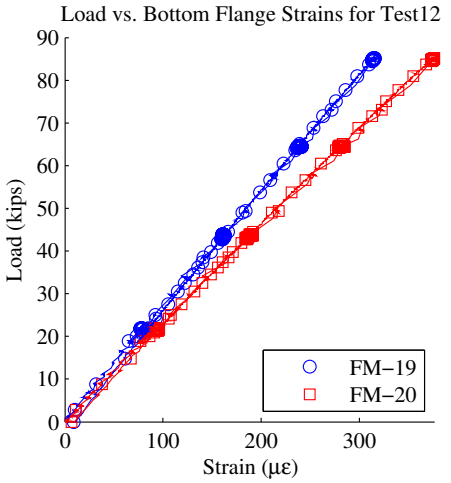
Load vs. Bottom Flange Strains for Test12
Load (kips)
Strain (με)
FM−19
FM−20

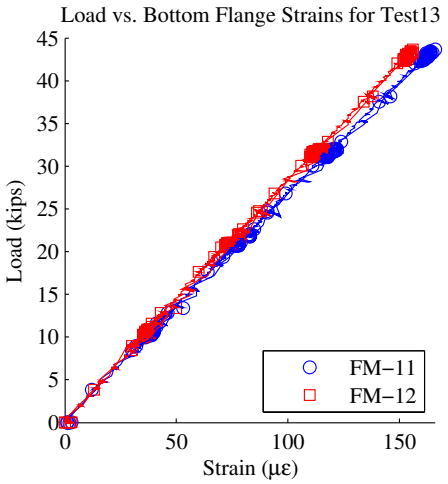
Load vs. Bottom Flange Strains for Test13
Load (kips)
Strain (με)
FM−11
FM−12

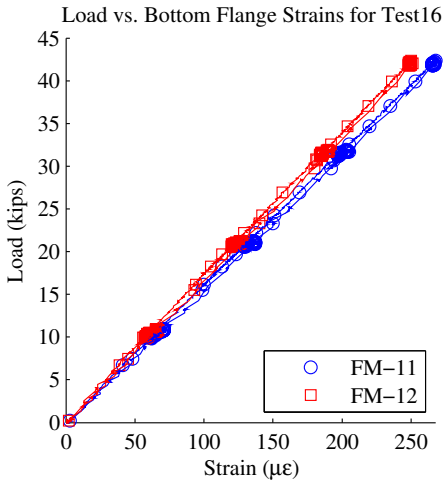
Load vs. Bottom Flange Strains for Test16
Load (kips)
Strain (με)
FM−11
FM−12

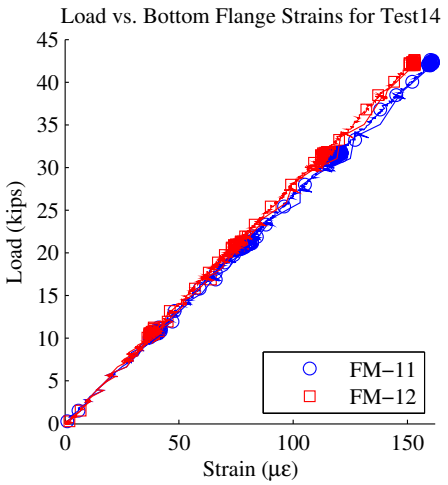
Load vs. Bottom Flange Strains for Test14
Load (kips)
Strain (με)
FM−11
FM−12

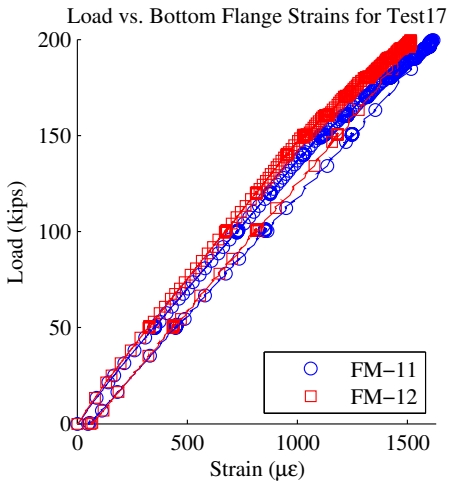
Load vs. Bottom Flange Strains for Test17
Load (kips)
Strain (με)
FM−11
FM−12

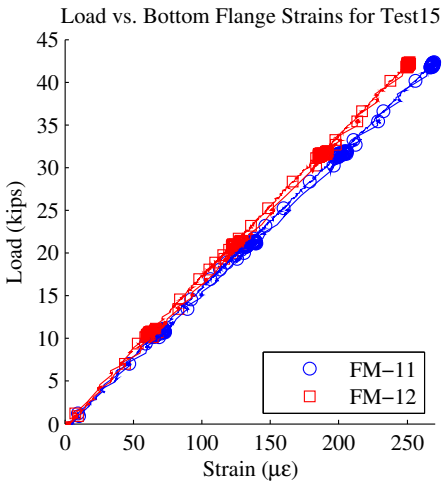
Load vs. Bottom Flange Strains for Test15
Load (kips)
Strain (με)
FM−11
FM−12

Load vs. Concrete Strain

Test 1

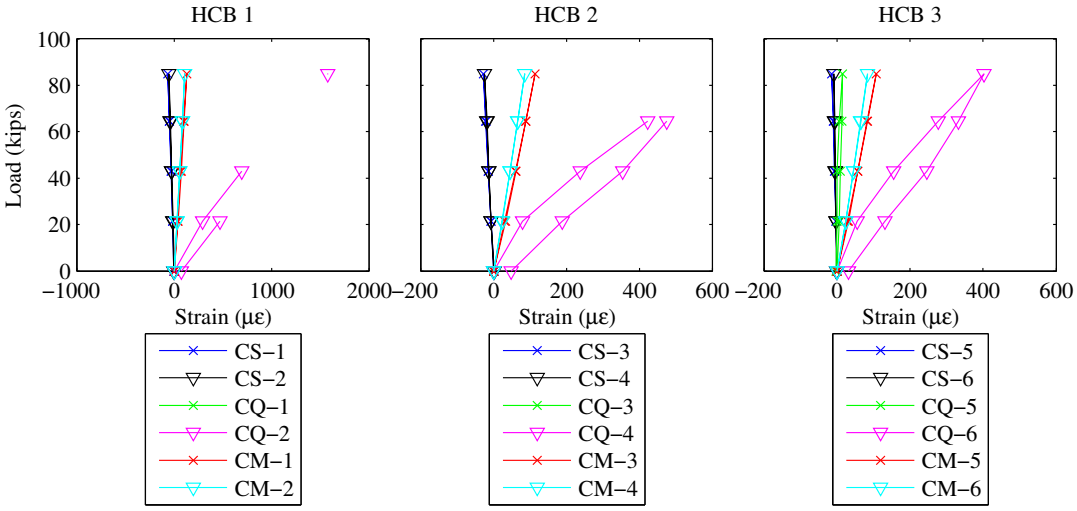

Test 2

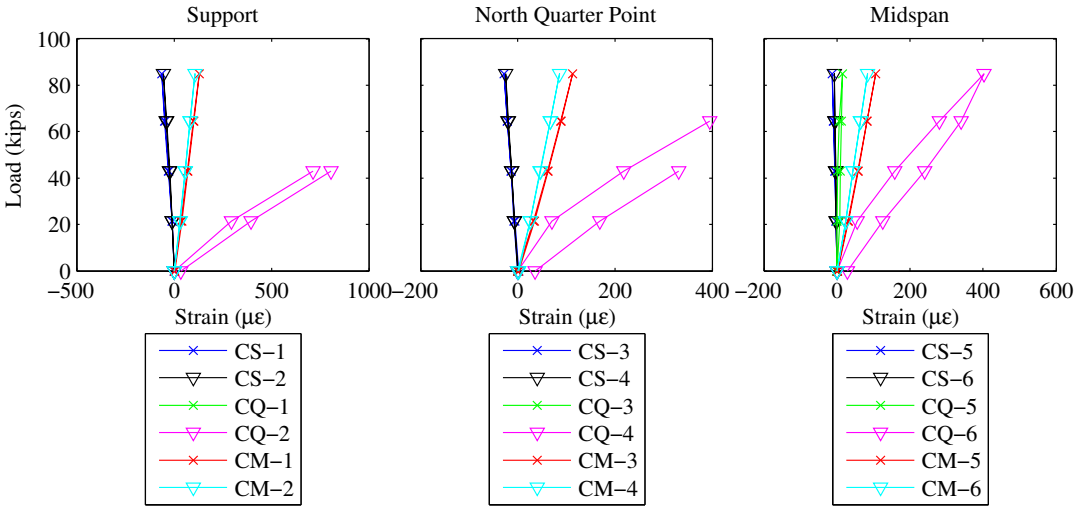

Test 3

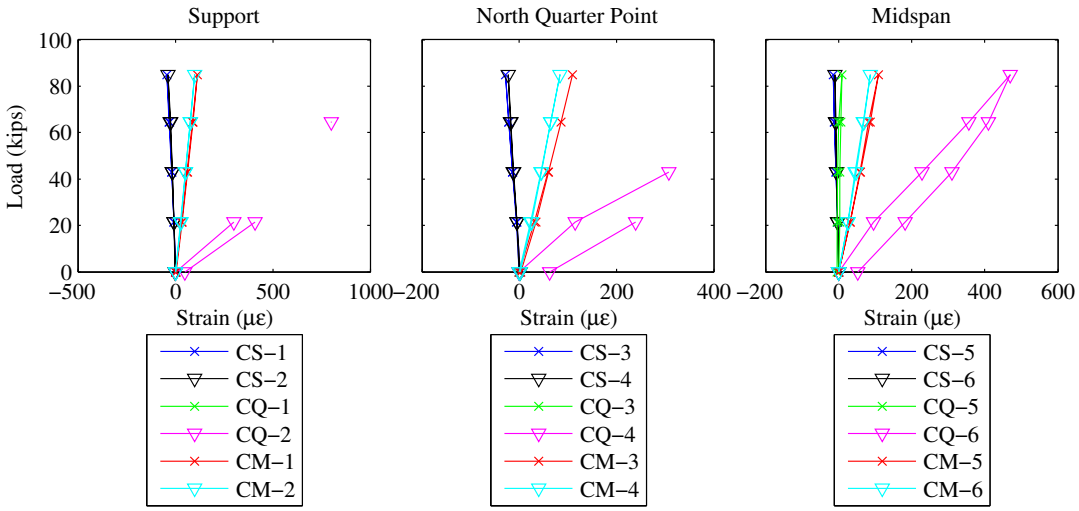
Support
North Quarter Point
Midspan
Load (kips)
Strain (με)
CS–1
CS–2
CQ–1
CQ–2
CM–1
CM–2
CS–3
CS–4
CQ–3
CQ–4
CM–3
CM–4
CS–5
CS–6
CQ–5
CQ–6
CM–5
CM–6

Test 4

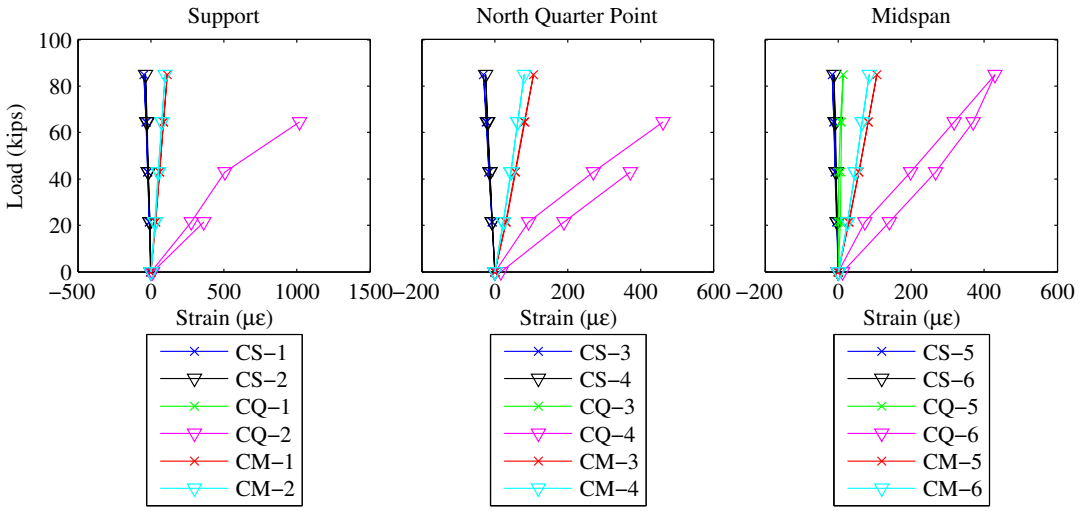
Support
North Quarter Point
Midspan
Load (kips)
Strain (με)
CS–1
CS–2
CQ–1
CQ–2
CM–1
CM–2
CS–3
CS–4
CQ–3
CQ–4
CM–3
CM–4
CS–5
CS–6
CQ–5
CQ–6
CM–5
CM–6

Test 5

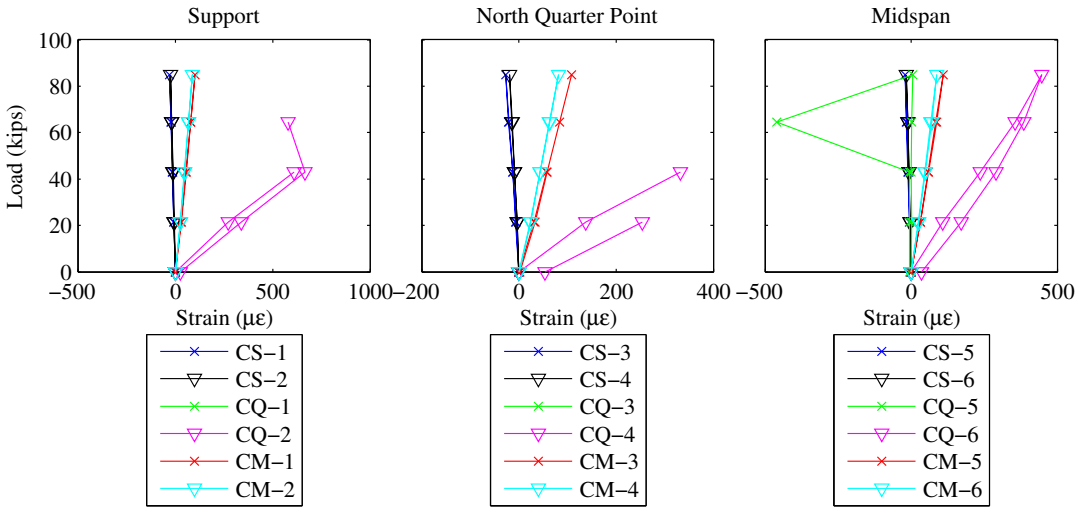
Support
North Quarter Point
Midspan
Load (kips)
Strain (με)
CS–1
CS–2
CQ–1
CQ–2
CM–1
CM–2
CS–3
CS–4
CQ–3
CQ–4
CM–3
CM–4
CS–5
CS–6
CQ–5
CQ–6
CM–5
CM–6

Test 6

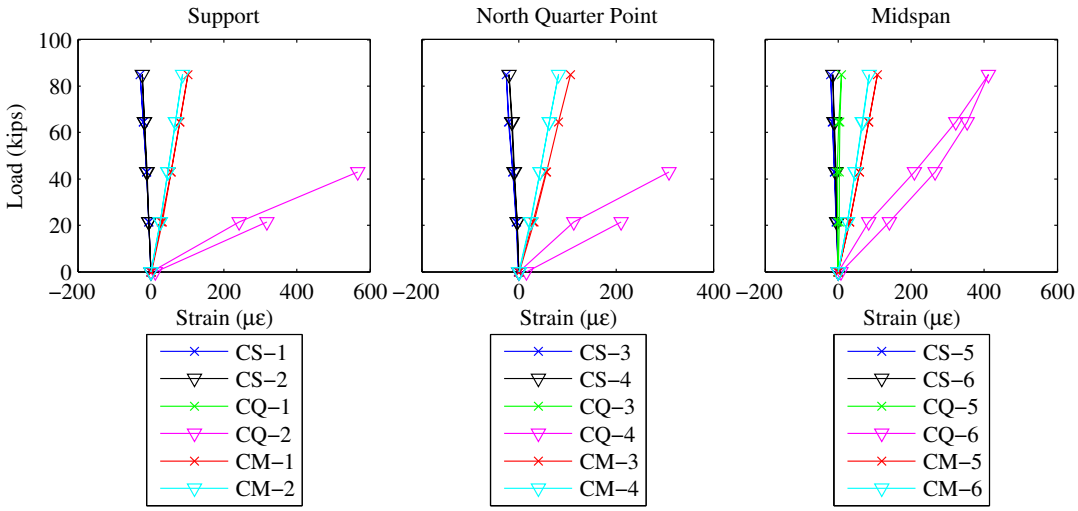
Support
North Quarter Point
Midspan
Load (kips)
Strain (με)
CS–1
CS–2
CQ–1
CQ–2
CM–1
CM–2
CS–3
CS–4
CQ–3
CQ–4
CM–3
CM–4
CS–5
CS–6
CQ–5
CQ–6
CM–5
CM–6

Test 7

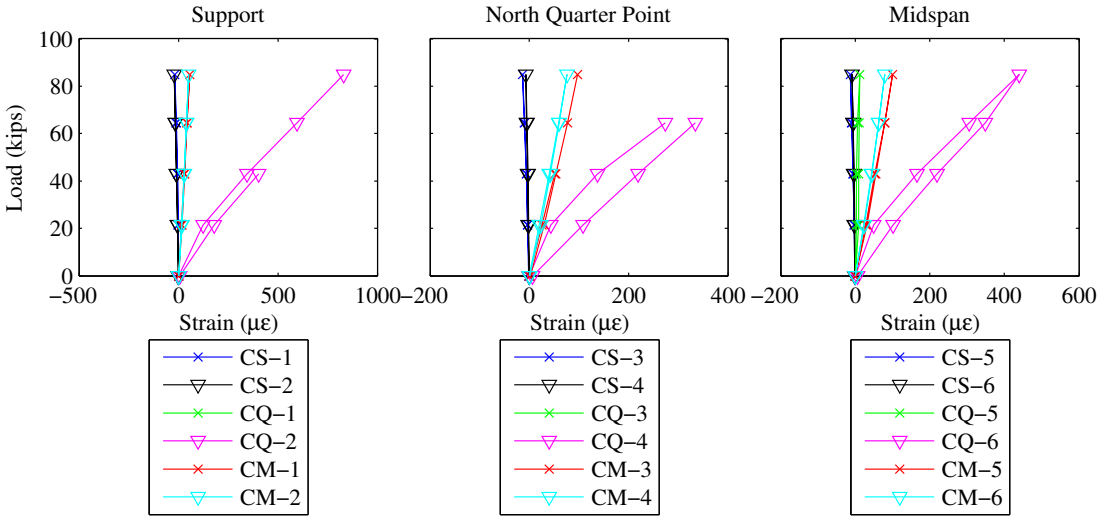
Support
North Quarter Point
Midspan
Load (kips)
Strain (με)
CS–1
CS–2
CQ–1
CQ–2
CM–1
CM–2
CS–3
CS–4
CQ–3
CQ–4
CM–3
CM–4
CS–5
CS–6
CQ–5
CQ–6
CM–5
CM–6

Test 8

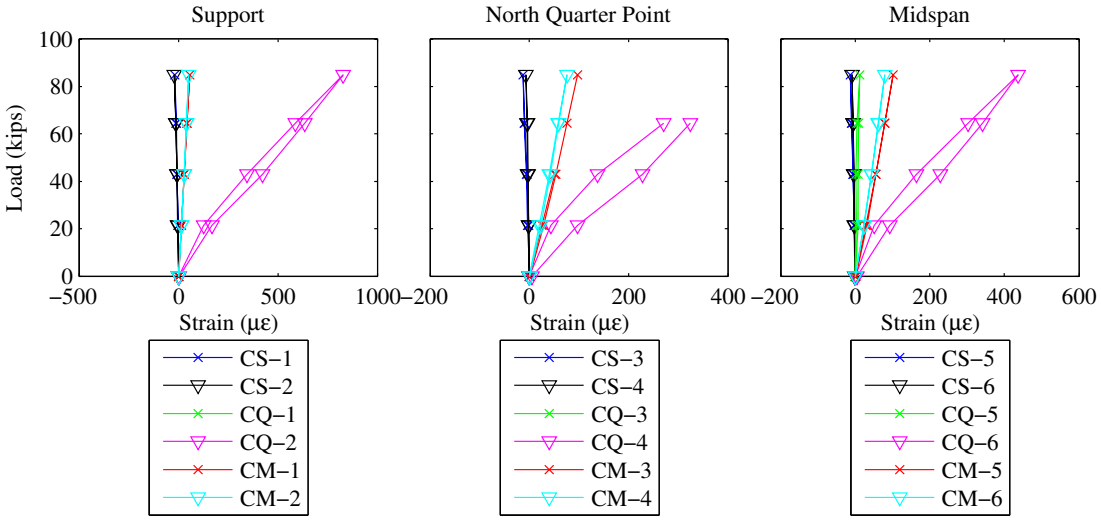
Support
North Quarter Point
Midspan
Load (kips)
Strain (με)
CS–1
CS–2
CQ–1
CQ–2
CM–1
CM–2
CS–3
CS–4
CQ–3
CQ–4
CM–3
CM–4
CS–5
CS–6
CQ–5
CQ–6
CM–5
CM–6

Test 9

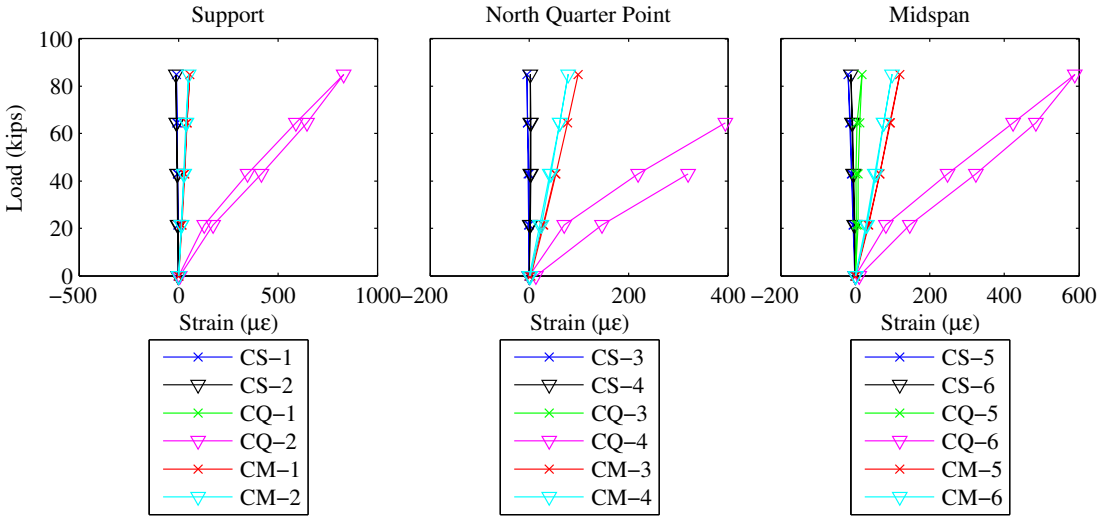

Test 10

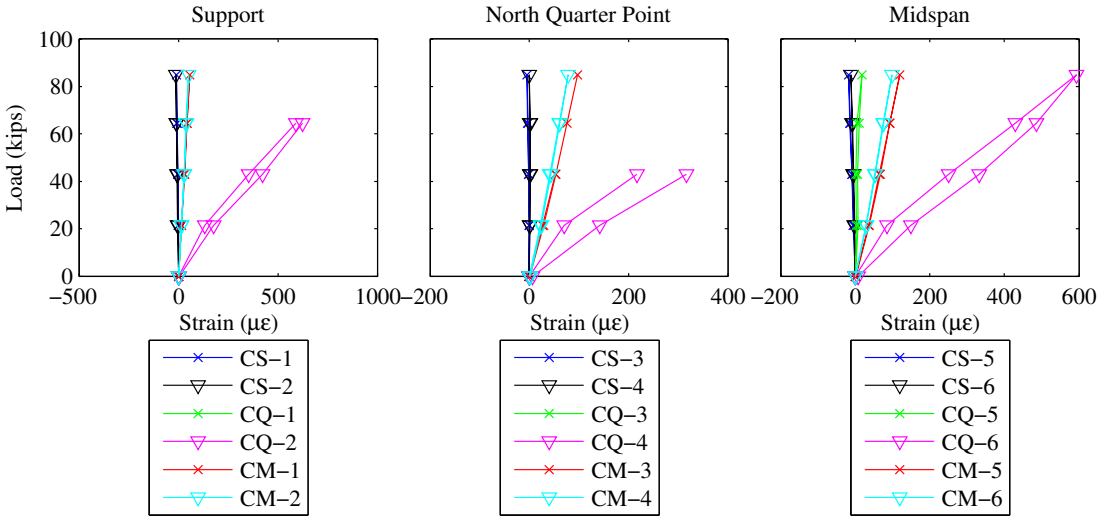

Test 11

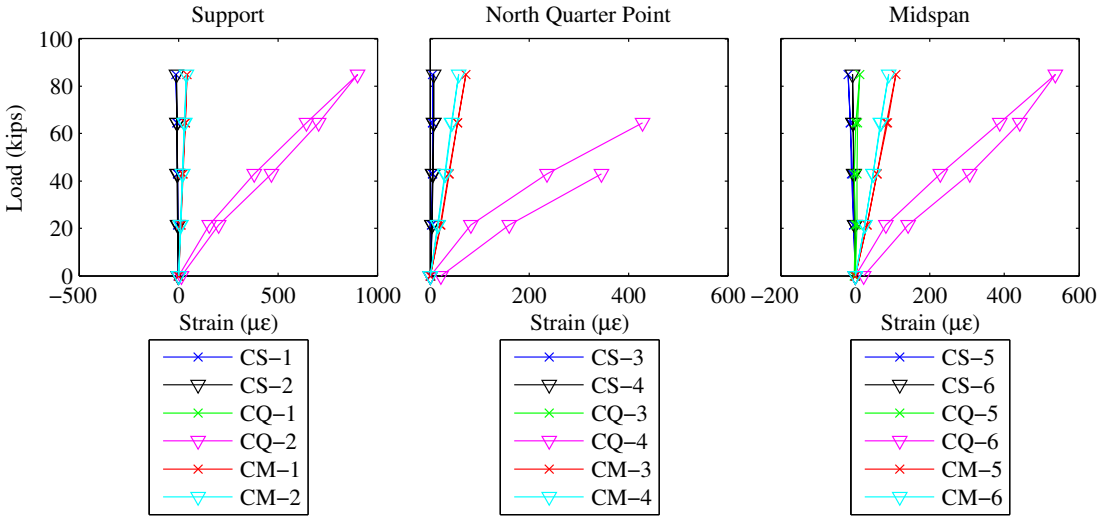

Test 12

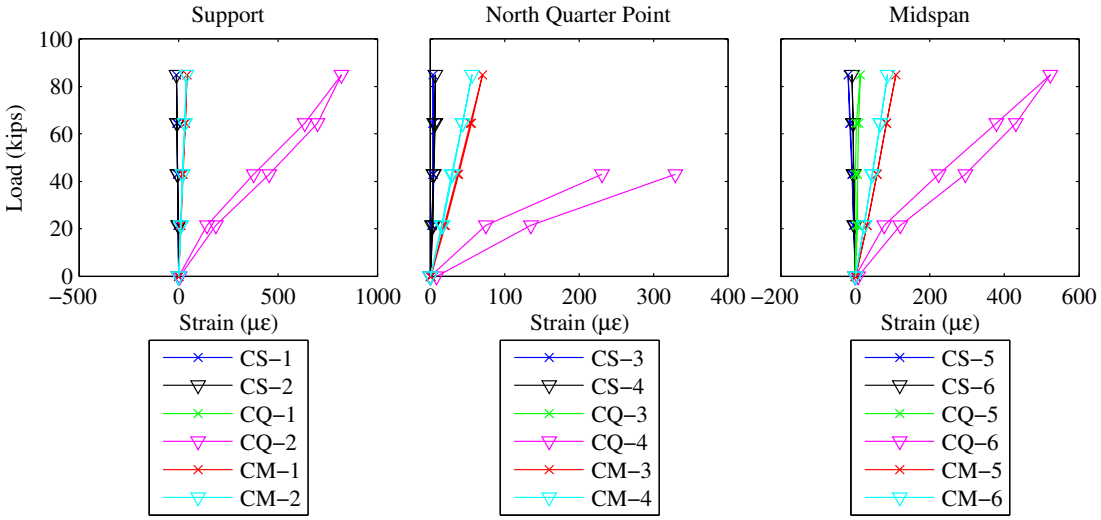

Test 13

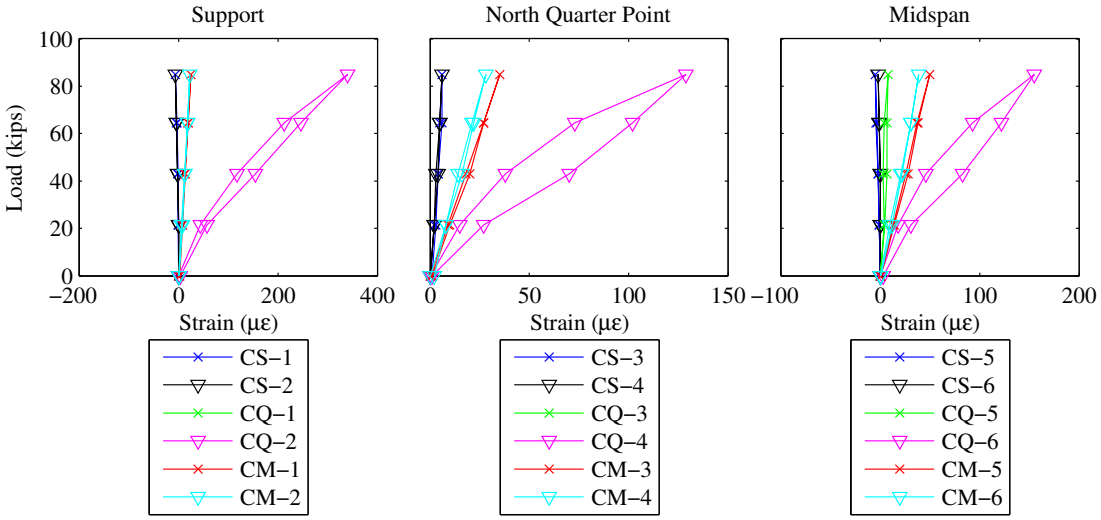

Test 14

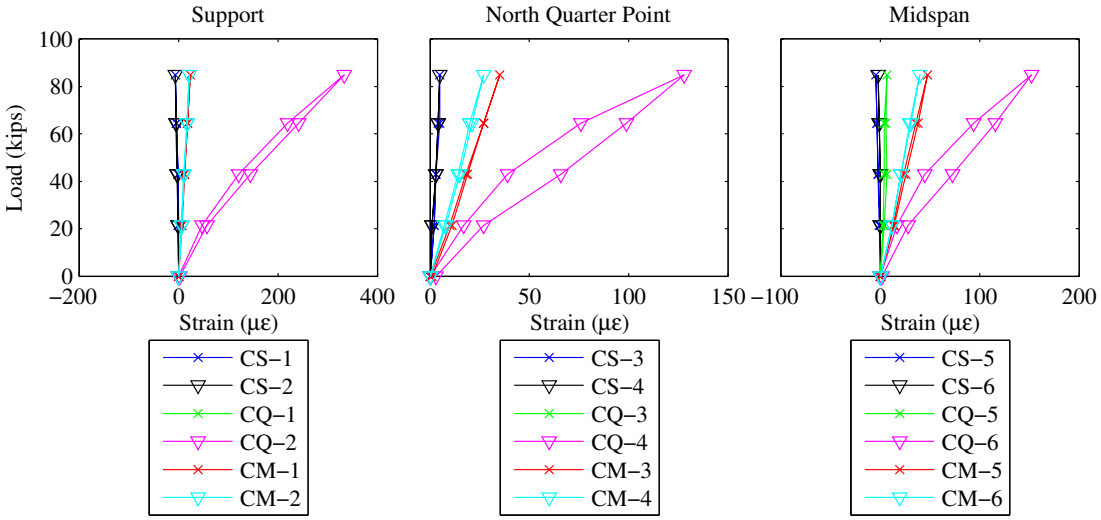

Test 15

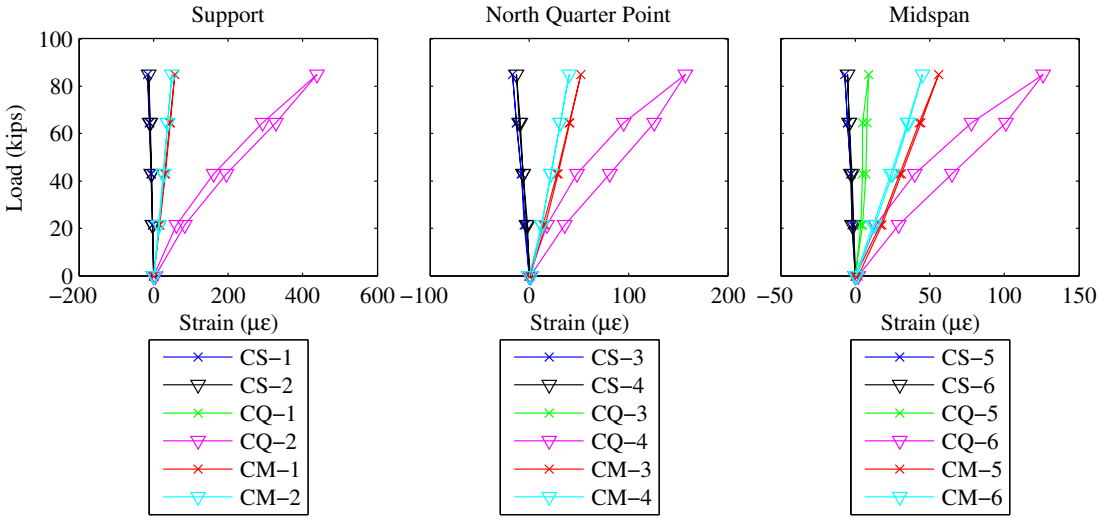

Test 16

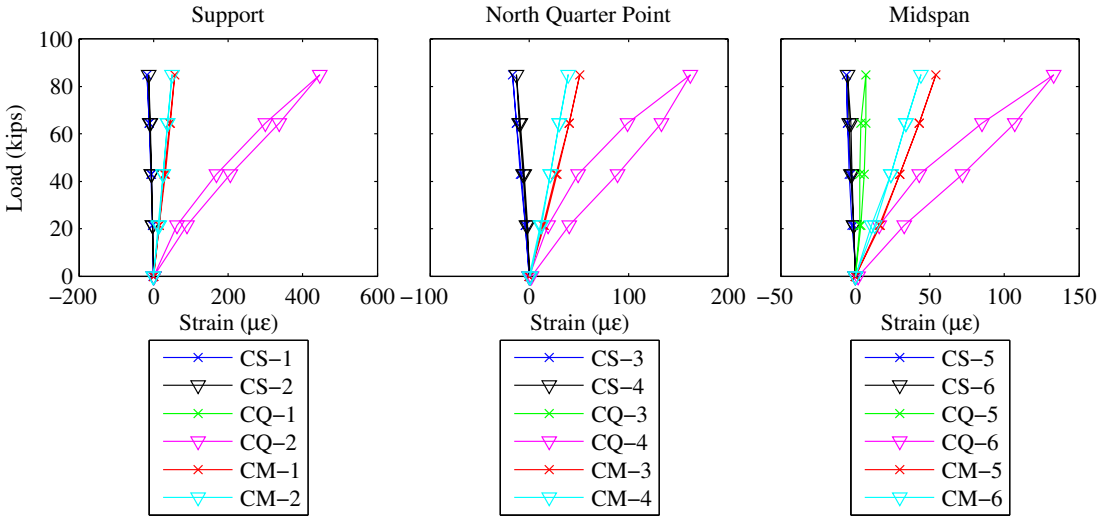

Test 17

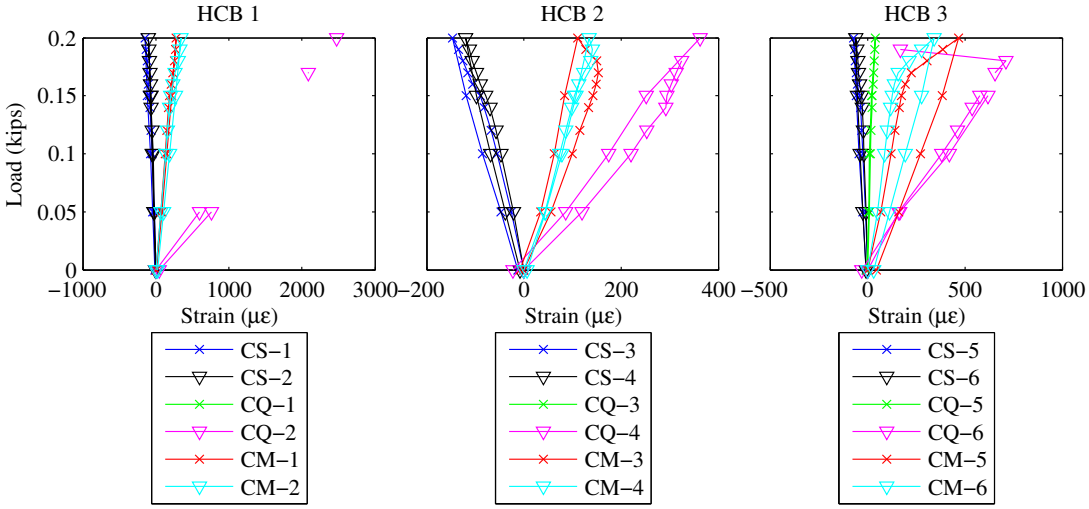
HCB 1
HCB 2
HCB 3
Load (kips)
0.2
0.15
0.1
0.05
0
−1000
0
1000
2000
3000
−200
0
200
400
−500
0
500
1000
Strain (με)
Strain (με)
Strain (με)
CS−1
CS−2
CQ−1
CQ−2
CM−1
CM−2
CS−3
CS−4
CQ−3
CQ−4
CM−3
CM−4
CS−5
CS−6
CQ−5
CQ−6
CM−5
CM−6

Dead Load Reactions

NOTE: Dead load reactions were measured by load cells when the setup was jacked up to put load cells in place. The validity of the load cell readings were difficult to establish for Phase III testing and thus may indicated the values in the below table may be incorrect. The values are presented for information purposes only.

Dead Load Reactions (lbs.)					
HCB 1		HCB 2		HCB 3	
LC-1	LC-2	LC-3	LC-4	LC-5	LC-6
9034	9692	6043	4730	3809	5560

Distribution Factors

Test 1

Deflection and Strain Based (Skewed Direction)

	Deflection-Based				Strain-Based			
Location	HCB 1	HCB 2	HCB 3	Total	HCB 1	HCB 2	HCB 3	Total
North Quarter	0.40	0.31	0.29	1.00	0.39	0.32	0.29	1.00
Midspan	0.36	0.33	0.31	1.00	0.39	0.35	0.26	1.00
South Quarter	0.30	0.35	0.36	1.00				
Average	0.35	0.33	0.32	1.00	0.39	0.33	0.28	1.00

Deflection Based (Transverse Direction)

HCB 1	HCB 2	HCB 3	Sum
0.29	0.28	0.42	1.00

Load Based (Shear)

HCB 1	HCB 2	HCB 3	Sum
0.71	0.14	0.15	1.00

Test 2

Deflection and Strain Based (Skewed Direction)

	Deflection-Based				Strain-Based			
Location	HCB 1	HCB 2	HCB 3	Total	HCB 1	HCB 2	HCB 3	Total
North Quarter	0.40	0.31	0.30	1.00	0.44	0.29	0.27	1.00
Midspan	0.36	0.33	0.31	1.00	0.39	0.35	0.25	1.00
South Quarter	0.29	0.35	0.36	1.00				
Average	0.35	0.33	0.32	1.00	0.42	0.32	0.26	1.00

Deflection Based (Transverse Direction)

HCB 1	HCB 2	HCB 3	Sum
0.36	0.31	0.33	1.00

Load Based (Shear)

HCB 1	HCB 2	HCB 3	Sum
0.79	0.10	0.11	1.00

Test 3

Deflection and Strain Based (Skewed Direction)

	Deflection-Based				Strain-Based			
Location	HCB 1	HCB 2	HCB 3	Total	HCB 1	HCB 2	HCB 3	Total
North Quarter	0.36	0.31	0.32	1.00	0.40	0.30	0.30	1.00
Midspan	0.33	0.33	0.34	1.00	0.37	0.36	0.27	1.00
South Quarter	0.27	0.34	0.39	1.00				
Average	0.32	0.33	0.35	1.00	0.38	0.33	0.29	1.00

Deflection Based (Transverse Direction)

HCB 1	HCB 2	HCB 3	Sum
0.36	0.32	0.32	1.00

Load Based (Shear)

HCB 1	HCB 2	HCB 3	Sum
0.64	0.22	0.14	1.00

Test 4

Deflection and Strain Based (Skewed Direction)

	Deflection-Based				Strain-Based			
Location	HCB 1	HCB 2	HCB 3	Total	HCB 1	HCB 2	HCB 3	Total
North Quarter	0.35	0.36	0.29	1.00	0.39	0.31	0.30	1.00
Midspan	0.34	0.33	0.33	1.00	0.37	0.35	0.28	1.00
South Quarter	0.27	0.36	0.37	1.00				

Deflection Based (Transverse Direction)

HCB 1	HCB 2	HCB 3	Sum
0.36	0.31	0.33	1.00

Load Based (Shear)

HCB 1	HCB 2	HCB 3	Sum
0.61	0.22	0.17	1.00

Test 5

Deflection and Strain Based (Skewed Direction)

	Deflection-Based				Strain-Based			
Location	HCB 1	HCB 2	HCB 3	Total	HCB 1	HCB 2	HCB 3	Total
North Quarter	0.32	0.36	0.32	1.00	0.37	0.32	0.31	1.00
Midspan	0.31	0.33	0.36	1.00	0.34	0.36	0.30	1.00
South Quarter	0.25	0.34	0.41	1.00				
Average	0.29	0.34	0.36	1.00	0.36	0.34	0.31	1.00

Deflection Based (Transverse Direction)

HCB 1	HCB 2	HCB 3	Sum
0.33	0.30	0.36	1.00

Load Based (Shear)

HCB 1	HCB 2	HCB 3	Sum
0.52	0.27	0.20	1.00

Test 6

Deflection and Strain Based (Skewed Direction)

	Deflection-Based				Strain-Based			
Location	HCB 1	HCB 2	HCB 3	Total	HCB 1	HCB 2	HCB 3	Total
North Quarter	0.35	0.30	0.35	1.00	0.37	0.32	0.31	1.00
Midspan	0.31	0.33	0.36	1.00	0.34	0.36	0.31	1.00
South Quarter	0.25	0.34	0.41	1.00				
Average	0.31	0.32	0.38	1.00	0.36	0.34	0.31	1.00

Deflection Based (Transverse Direction)

HCB 1	HCB 2	HCB 3	Sum
0.33	0.31	0.36	1.00

Load Based (Shear)

HCB 1	HCB 2	HCB 3	Sum
0.510724	0.2685221	0.2207539	1.00

Test 7

Deflection and Strain Based (Skewed Direction)

	Deflection-Based				Strain-Based			
Location	HCB 1	HCB 2	HCB 3	Total	HCB 1	HCB 2	HCB 3	Total
North Quarter	0.36	0.34	0.30	1.00	0.40	0.29	0.31	1.00
Midspan	0.34	0.33	0.33	1.00	0.34	0.37	0.29	1.00
South Quarter	0.28	0.33	0.39	1.00				
Average	0.32	0.33	0.34	1.00	0.37	0.33	0.30	1.00

Deflection Based (Transverse Direction)

HCB 1	HCB 2	HCB 3	Sum
0.27	0.35	0.37	0.99

Load Based (Shear)

HCB 1	HCB 2	HCB 3	Sum
0.54	0.28	0.18	1.00

Test 8

Deflection and Strain Based (Skewed Direction)

	Deflection-Based				Strain-Based			
Location	HCB 1	HCB 2	HCB 3	Total	HCB 1	HCB 2	HCB 3	Total
North Quarter	0.34	0.36	0.30	1.00	0.40	0.29	0.31	1.00
Midspan	0.33	0.33	0.34	1.00	0.34	0.37	0.29	1.00
South Quarter	0.27	0.33	0.40	1.00				
Average	0.32	0.34	0.35	1.00	0.37	0.33	0.30	1.00

Deflection Based (Transverse Direction)

HCB 1	HCB 2	HCB 3	Sum
0.26	0.36	0.38	0.99

Load Based (Shear)

HCB 1	HCB 2	HCB 3	Sum
0.54	0.28	0.17	1.00

Test 9

Deflection and Strain Based (Skewed Direction)

	Deflection-Based				Strain-Based			
Location	HCB 1	HCB 2	HCB 3	Total	HCB 1	HCB 2	HCB 3	Total
North Quarter	0.33	0.33	0.34	0.99	0.15	0.40	0.44	0.99
Midspan	0.31	0.33	0.36	1.00	0.31	0.37	0.32	1.00
South Quarter	0.26	0.33	0.40	0.99				
Average	0.30	0.33	0.37	0.99	0.23	0.38	0.38	0.99

Deflection Based (Transverse Direction)

HCB 1	HCB 2	HCB 3	Sum
0.25	0.31	0.43	0.99

Load Based (Shear)

HCB 1	HCB 2	HCB 3	Sum
0.46	0.32	0.22	1.00

Test 10

Deflection and Strain Based (Skewed Direction)

	Deflection-Based				Strain-Based			
Location	HCB 1	HCB 2	HCB 3	Total	HCB 1	HCB 2	HCB 3	Total
North Quarter	0.31	0.35	0.34	0.99	0.36	0.30	0.33	1.00
Midspan	0.30	0.33	0.37	1.00	0.32	0.36	0.32	1.00
South Quarter	0.26	0.32	0.42	0.99				
Average	0.29	0.33	0.37	0.99	0.34	0.33	0.33	1.00

Deflection Based (Transverse Direction)

HCB 1	HCB 2	HCB 3	Sum
0.25	0.31	0.43	0.99

Load Based (Shear)

HCB 1	HCB 2	HCB 3	Sum
0.46	0.33	0.22	1.00

Test 11

Deflection and Strain Based (Skewed Direction)

	Deflection-Based				Strain-Based			
Location	HCB 1	HCB 2	HCB 3	Total	HCB 1	HCB 2	HCB 3	Total
North Quarter	0.28	0.35	0.36	1.00	0.38	0.28	0.33	1.00
Midspan	0.27	0.32	0.41	1.00	0.29	0.35	0.36	1.00
South Quarter	0.24	0.32	0.45	1.00				
Average	0.26	0.33	0.41	1.00	0.34	0.32	0.35	1.00

Deflection Based (Transverse Direction)

HCB 1	HCB 2	HCB 3	Sum
0.16	0.34	0.49	0.99

Load Based (Shear)

HCB 1	HCB 2	HCB 3	Sum
0.36	0.41	0.23	1.00

Test 12

Deflection and Strain Based (Skewed Direction)

	Deflection-Based				Strain-Based			
Location	HCB 1	HCB 2	HCB 3	Total	HCB 1	HCB 2	HCB 3	Total
North Quarter	0.28	0.36	0.35	0.99	0.42	0.27	0.31	1.00
Midspan	0.27	0.33	0.40	1.00	0.29	0.36	0.35	1.00
South Quarter	0.23	0.32	0.44	1.00				
Average	0.26	0.34	0.40	1.00	0.35	0.31	0.33	1.00

Deflection Based (Transverse Direction)

HCB 1	HCB 2	HCB 3	Sum
0.16	0.35	0.47	0.99

Load Based (Shear)

HCB 1	HCB 2	HCB 3	Sum
0.36	0.39	0.24	1.00

Test 13

Deflection and Strain Based (Skewed Direction)

	Deflection-Based				Strain-Based			
Location	HCB 1	HCB 2	HCB 3	Total	HCB 1	HCB 2	HCB 3	Total
North Quarter	0.28	0.39	0.32	0.99	0.21	0.36	0.43	0.99
Midspan	0.29	0.33	0.37	1.00	0.32	0.37	0.30	1.00
South Quarter	0.38	0.25	0.36	1.00				
Average	0.32	0.32	0.35	1.00	0.26	0.36	0.37	0.99

Deflection Based (Transverse Direction)

HCB 1	HCB 2	HCB 3	Sum
0.25	0.34	0.41	0.99

Load Based (Shear)

HCB 1	HCB 2	HCB 3	Sum
0.42	0.37	0.21	1.00

Test 14

Deflection and Strain Based (Skewed Direction)

	Deflection-Based				Strain-Based			
Location	HCB 1	HCB 2	HCB 3	Total	HCB 1	HCB 2	HCB 3	Total
North Quarter	0.26	0.41	0.32	1.00	0.38	0.29	0.33	1.00
Midspan	0.29	0.33	0.38	1.00	0.33	0.37	0.30	1.00
South Quarter	0.23	0.29	0.47	1.00				
Average	0.26	0.35	0.39	1.00	0.35	0.33	0.32	1.00

Deflection Based (Transverse Direction)

HCB 1	HCB 2	HCB 3	Sum
0.25	0.31	0.43	0.99

Load Based (Shear)

HCB 1	HCB 2	HCB 3	Sum
0.42	0.37	0.21	1.00

Test 15

Deflection and Strain Based (Skewed Direction)

	Deflection-Based				Strain-Based			
Location	HCB 1	HCB 2	HCB 3	Total	HCB 1	HCB 2	HCB 3	Total
North Quarter	0.34	0.38	0.28	1.00	0.35	0.34	0.31	1.00
Midspan	0.33	0.32	0.35	1.00	0.37	0.36	0.27	1.00
South Quarter	0.31	0.32	0.37	1.00				
Average	0.33	0.34	0.33	1.00	0.36	0.35	0.29	1.00

Deflection Based (Transverse Direction)

HCB 1	HCB 2	HCB 3	Sum
0.37	0.29	0.35	1.00

Load Based (Shear)

HCB 1	HCB 2	HCB 3	Sum
0.52	0.27	0.21	1.00

Test 16

Deflection and Strain Based (Skewed Direction)

	Deflection-Based				Strain-Based			
Location	HCB 1	HCB 2	HCB 3	Total	HCB 1	HCB 2	HCB 3	Total
North Quarter	0.35	0.34	0.31	1.00	0.38	0.32	0.31	1.00
Midspan	0.33	0.33	0.34	1.00	0.37	0.36	0.27	1.00
South Quarter	0.26	0.34	0.39	1.00				
Average	0.31	0.34	0.35	1.00	0.37	0.34	0.29	1.00

Deflection Based (Transverse Direction)

HCB 1	HCB 2	HCB 3	Sum
0.37	0.29	0.34	1.00

Load Based (Shear)

HCB 1	HCB 2	HCB 3	Sum
0.52	0.27	0.21	1.00

Test 17

Deflection and Strain Based (Skewed Direction)

	Deflection-Based				Strain-Based			
Location	HCB 1	HCB 2	HCB 3	Total	HCB 1	HCB 2	HCB 3	Total
North Quarter	0.35	0.35	0.30	1.00	0.36	0.34	0.30	1.00
Midspan	0.33	0.35	0.32	1.00	0.35	0.36	0.29	1.00
South Quarter	0.28	0.36	0.36	1.00				
Average	0.32	0.35	0.33	1.00	0.36	0.35	0.30	1.00

Distribution Factor Calculation using Lever Rule

Service Test 1 and 2: Wheel line placed directly over HCB 1

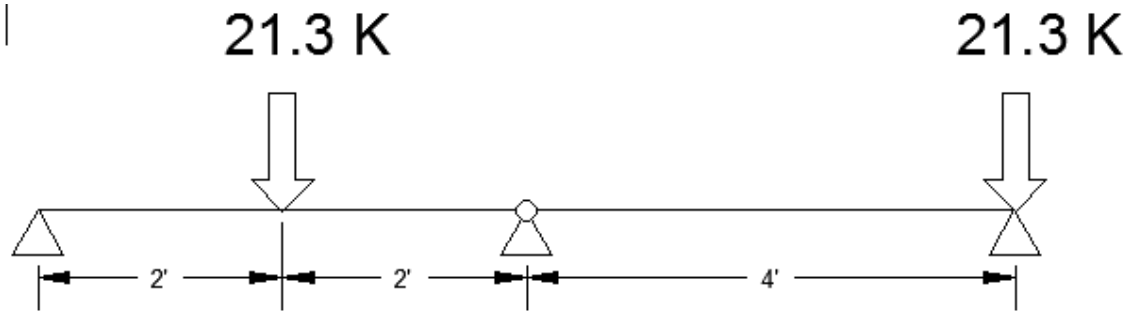

Given Information:

Girder Spacing: $S_b := 4ft$

Axle Spacing: $S_a := 6ft$

Wheel Loading with Dynamic Allowance Factor: $P := 16kip \cdot 1.33 = 21.28 \cdot kip$

Calculations:

Calculate distribution factor for exterior girder using the lever rule. Moments are summed about a hinge placed at the interior beam centerline.

$$DF\_Exterior\_S1 := \frac{\frac{P}{2} \cdot S_b}{S_b \cdot P}$$

$$DF\_Exterior\_S1 = 0.5$$

Calculate distribution factor for interior girder using lever rule. Moments are summed about centerline of HCB 3.

$$DF\_Interior\_S1 := \frac{\frac{P}{2} \cdot 0.5 \cdot S_b}{S_b \cdot P}$$

$$DF\_Interior\_S1 = 0.25$$

NOTE: Distribution factors are the same for Service Test 5 and 6 where wheel line is placed directly over HCB 3

Distribution Factor Calculation using Lever Rule

Service Test 3 and 4: Wheel lines stradling HCB 2

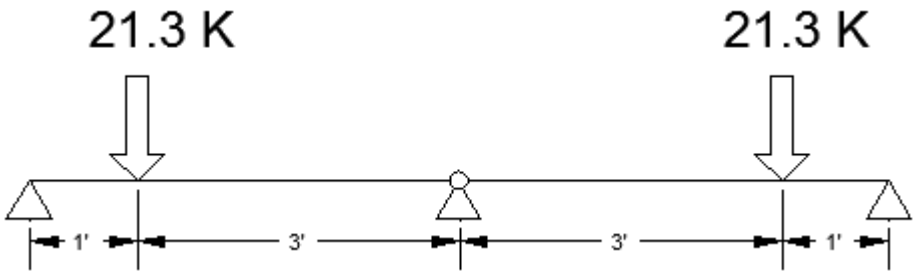

Given Information:

Girder Spacing: $S_b := 4ft$

Axle Spacing: $S_a := 6ft$

Wheel Loading with Dynamic Allowance Factor: $P := 16kip \cdot 1.33 = 21.28 \cdot kip$

Calculations:

Calculate distribution factor for interior girder using the lever rule. Moments are summed about exterior girder centerlines.

$$DF\_Interior\_S3 := \frac{P \cdot 1ft}{P \cdot S_b}$$

$$DF\_Interior\_S3 = 0.25$$

Calculate distribution factor for exterior girders using lever rule. Moments are summed about interior beam centerline.

$$DF\_Exterior\_S3 := \frac{P \cdot 3ft}{S_b} \cdot \frac{1}{2P}$$

$$DF\_Exterior\_S3 = 0.375$$

Distribution Factors for Tests 1 and 2 Control

Distribution Factor Calculation for Spread Concrete Box Girder

Calculations based on 2008 AASHTO LRFD Specifications Section 4.6.2

Input Variables:

Span Length (ft.): $L := 43$

Girder Depth (in.): $d := 21$

Girder Spacing (ft.): $S := 4$

Skew Angle (radians) $\theta := \frac{\pi}{4}$

Distance from Curb to Exterior Girder Centerline: $d_e := 2 - 1.3 = 0.7$

Because three girders are used in test specimen, AASHTO formulas do not apply. Use lever rule.

Distribution Factor Calculation for Exterior Spread Concrete Box Girder

Distribution for Moment for One Lane Loaded

Use Lever Rule Table 4.6.2.2.2d-1

Use multiple presence factor of 1.2 for one lane loaded

$DFM\_Ext_{1\_Lane} := DF\_Exterior\_S1 \cdot 1.2 = 0.6$

$DFM\_Int_{1\_Lane} := DF\_Interior\_S1 \cdot 1.2 = 0.3$

Correction for Skew Angle

$C_{Moment} := 1.05 - 0.25 \cdot \tan(\theta)^{1.5}$ Table 4.6.2.2.2e-1

$C_{Moment} = 0.8$

Correction for Skew Angle

Correct for skew for moment

$DFM\_Ext_1 := C_{Moment} \cdot DFM\_Ext_{1\_Lane} = 0.48$

$DFM\_Int_1 := C_{Moment} \cdot DFM\_Int_{1\_Lane} = 0.24$

Distribution for Shear for One Lane Loaded

Use Lever Rule Table 4.6.2.2.3b-1

Use multiple presence factor of 1.2 for one lane loaded

$DFS\_Ext_{1\_Lane} := DF\_Exterior\_S1 \cdot 1.2 = 0.6$

$DFS\_Int_{1\_Lane} := DF\_Interior\_S1 \cdot 1.2 = 0.3$

Problem (cont.)

Correction for skew in obtuse corner

$$C_{Shear} := 1 + \frac{\sqrt{\frac{L \cdot d}{12}}}{6 \cdot S} \cdot \tan(\theta)$$ Table 4.6.2.2.3b-1

$C_{Shear} = 1.361$

$DFS\_Ext_1 := C_{Shear} \cdot DFS\_Ext_{1\_Lane} = 0.817$

$DFS\_Int_1 := DFS\_Int_{1\_Lane}$

Distribution Factors for Interior Girder

$DFM\_Int_1 = 0.24$

$DFS\_Int_1 = 0.3$

Distribution Factors for Exterior Girder

$DFM := DFM\_Ext_1 = 0.48$

$DFS := DFS\_Ext_1 = 0.817$